UNIVERSITY OF EAST ANGLIA

Lagrangian studies, circulation and mixing in the Southern Ocean

by

Christos Mitsis

A thesis
submitted in partial fulfilment of the
requirements for the degree of
Doctor of Philosophy
in the
School of Environmental Sciences
University of East Anglia

August 2013

Declaration of Authorship

I, Christos Mitsis, declare that this thesis titled, 'Lagrangian studies, circulation and mixing in the Southern Ocean' and the work presented in it are my own. I confirm that:

- This work was done wholly or mainly while in candidature for a research degree at this University.
- Where any part of this thesis has previously been submitted for a degree or any other qualification at this University or any other institution, this has been clearly stated.
- Where I have consulted the published work of others, this is always clearly attributed.
- Where I have quoted from the work of others, the source is always given. With the exception of such quotations, this thesis is entirely my own work.
- I have acknowledged all main sources of help.
- Where the thesis is based on work done by myself jointly with others, I have made clear exactly what was done by others and what I have contributed myself.

Signed: _____

Date: _____

"I to the world am like a drop of water
That in the ocean seeks another drop,
Who, falling there to find his fellow forth,
Unseen, inquisitive, confounds himself."

William Shakespeare

English poet and playwright (1564 -1616)

"There is a pleasure in the pathless woods
There is a rapture on the lonely shore
There is society, where none intrudes,
By the deep sea, and music in its roars:
I love not man the less, but Nature more..."

George Gordon Byron

English poet (1788-1824)

Abstract

Oceans play a vital role as one of the major components of Earth's climate system. The study of oceanic processes and the complexity inherent in dynamic flows is essential for understanding their regulatory character on the climate's variability. A key region for the study of such intrinsic oceanic variability is the Southern Ocean. In the form of a wind-driven, zonally unbounded, strong eastward flow, the Antarctic Circumpolar Current (ACC) circumnavigates the Antarctic continent connecting each of the ocean basins. The dynamics of the ACC, which is characterised by the absence of land barriers, apart from when crossing Drake Passage, have long been a topic of debate [*Rintoul et al.*, 2001].

The main interests of this study focus on inferring and mapping the dynamic variability the ACC exhibits by means of transient disturbances [*Hughes*, 2005] (such as mesoscale eddies) and subsequent mixing from Lagrangian trajectories. The distribution of eddy transport and intensity, the mixing of conservative quantities and flow dynamics through to the interaction of eddy kinetic energy, mean flow and topography are examined.

The sparseness of observations in the Southern Ocean and the necessity to understand the role of the oceanic circulation in the climate by a holistic approach highlights computational ocean circulation models as indispensable. In the context of this study, output from the run401 of the Ocean Circulation and Climate Advance Model (OCCAM) 1/12° ocean model, developed at the U.K. National Oceanography Centre, is utilised. In order to deduce the temporal and spatial variability of the flow dynamics, as well as its vertical distribution, simulation of monthly releases of passive particles using different schemes (i.e. cluster or linear alignment) on isobaric and isoneutral surfaces was conducted. An analysis of the Lagrangian trajectories reveals the characteristics of the dynamics that control the flow and depict regions of enhanced eddy activity and mixing. The model's ability to simulate real oceanic flows is established through comparison with a purposeful release of the tracer CF_3SF_5, which is conducted as part of the DIMES experiment (http://dimes.ucsd.edu/).

We find that topography plays a fundamental role in the context of Southern Ocean mixing through the association of high EKE regions, where the interaction of vortical elements and multi filamented jets in non-parallel flows supports an effective mechanism for eddy stirring, resulting in the enhanced dispersion of particles. Suppression of mixing in regions where the flow is delineated by intensified and coherent, both in space and time, jets (strong PV gradients) signifying the separation of the flow in differentiated kinematic environments, is illustrated. The importance of a local approximation to mixing instead of the construction of zonal averages is presented. We present the caveats of classical diffusion theory in the presence of persistent structures and find that

values of 1000-2000 m^2 s^{-1} for the cross-stream diffusivity are characteristic of the eddy stirring intensified regions. These coincide spatially, in general, with the distribution of high EKE and where the mean flow is not effective as a transport barrier, though, no scaling analogy is found with EKE values. We are not able to depict an increase of diffusion at a steering level as proposed by the critical layer theory. By spatially mapping the flow dynamics of the ACC through the computation of particle spatial occurrences in a 17 year period, the role of coherent structures in time, which also control the tracer distribution, are linked to kinematic boundaries which under certain 'stagnation' area conditions for vortical and elliptical elements, create the necessary conditions for eddy stirring proliferation.

Thesis supervisors: Prof. Andrew Watson (UEA), Prof. Dave Stevens (UEA), Prof. Michael Meredith (BAS)

Thesis examiners: Prof. Alberto Naveira Garabato (NOC) (external), Prof. Karen Heywood (UEA) (internal)

Acknowledgements

Research is driven by personal aspirations and fulfilled in the minds of many. Most of the time is about getting rather than giving [*Einstein*, 1955]. While at University of East Anglia, UEA, (and sometimes British Antarctic Survey, BAS), I've met, talked, and listened to people, to whom I am most grateful for their different perspectives.

Above all, I am grateful to my supervisors Mike Meredith (BAS), Dave Stevens (UEA) and Andy Watson (UEA) (alphabetic order) for their insightful help, advice and guidance but most of all for their patience - I am mostly grateful to them though because they gave me the chance to add one of the best experiences in my life curriculum so far - a Southern Ocean cruise for two months, probably onboard one of the most emblematic and beautiful research ships, James Clark Ross, which was from my perspective the essential experience of this fellowship.

A big thank you to all those onboard her, the crew and captain, the scientists and colleagues. It was pure enjoyment.

This PhD project was a EU Marie Curie Early Stage Training Fellowship fund at UEA and BAS. My sincere compliments, to everybody involved in organising and running the FAASIS project (Fellowships in Antarctic Air-Sea-Ice Science).

I thank all of the authors on this thesis's bibliography list. Their work has been the ultimate drive to attempt to achieve at least something to stand up as decent. In certain stages they served as the re-awakening incentive to complete this thesis. The same stands for all those passionate speakers on seminars and workshops.

And last but not least, to all those, family, friends, strangers, that helped, even without sometimes being aware of, to achieve this work and to Her...

Contents

List of Figures

Abbreviations

AABW	**A**ntarctic **B**ottom **W**ater
AAIW	**A**ntarctic **I**ntermediate **W**ater
ACC	**A**ntarctic **C**ircumpolar **C**urrent
ACCE	**A**tlantic **C**irculation and **C**limate **E**xperiment
ACW	**A**ntarctic **C**ircumpolar **W**ave
ACoC	**A**ntarctic **Co**astal **C**urrent
ALACE	**A**utonomous **L**agrangian **C**irculation **E**xplorer
ARGO	**A**utonomous **A**rray for **R**eal-time **G**eostrophic **O**ceanography
AVISO	**A**rchiving **V**alidation and **I**nterpretation of **S**atellite **O**ceanographic data
BAS	**B**ritish **A**ntarctic **S**urvey
CSIRO	**C**ommonwealth **S**cientific and **I**ndustrial **R**esearch **O**rganisation
CTD	**C**onductivity **T**emperature **D**epth
CFL	**C**ourant-**F**riedrich-**L**ewy stability criterion
DIMES	**D**iapycnal and **I**sopycnal **M**ixing **E**xperiment in the **S**outhern Ocean
EKE	**E**ddy **K**inetic **E**nergy
FSLE	**F**inite **S**cale **L**yapunov **E**xponent
FTLE	**F**inite **T**ime **L**yapunov **E**xponent
GCM	**G**eneral **C**irculation **M**odel
GEBCO	**G**eneral **B**athymetric **C**harts of the **O**ceans
GPE	**G**ravitational **P**otential **E**nergy
HYCOM	**HY**brid **C**oordinate **O**cean **M**odel
IBCSO	**I**nternational **B**athymetric **C**hart of the**S**outhern **O**cean
IPV	**I**sentropic **P**otential **V**orticity
KE	**K**inetic **E**nergy
LCDW	**L**ower **C**ircumpolar **D**eep **W**ater
MIT	**M**assachusetts **I**nstitute of **T**echnology

MITgcm	**MIT g**eneral **c**irculation **m**odel
MKE	**M**ean **K**inetic **E**nergy
MOC	**M**eridional **O**verturning **C**irculation
NADW	**N**orth **A**tlantic **D**eep **W**ater
NATRE	**N**orth **A**tlantic **T**racer **R**elease **E**xperiment
NetCDF	**Net**work **C**ommon **D**ata **F**orm
NOC	**N**ational **O**ceanography **C**entre
OCCAM	**O**cean **C**irculation and **C**limate **A**dvanced **M**odelling
OGCM	**O**ceanic **G**eneral **C**irculation **M**odel
OW	**O**kubo **W**eïss parameter
PE	**P**otential **E**nergy
PF	**P**olar **F**ront
POP	**P**arallel **O**cean **P**rogram
PV	**P**otential **V**orticity on isoneutral surface n
QG	**Q**uasi **G**eostrophic
RAFOS	SOFAR reverse
SAFN	**S**ub **A**ntarctic **F**ront **N**orth
SAFS	**S**ub **A**ntarctic **F**ront **S**outh
SACCF	**S**outhern **A**ntarctic **C**ircumpolar **C**urrent **F**ront
SAM	**S**outhern **A**nnular **M**ode
SeaWiFS	**Sea**-viewing **Wi**de **F**ield-of-view **S**ensor
SOFAR	**SO**und **F**ixing **A**nd **R**anging
SOL	**S**outhern **O**cean **L**agrangian experiment
SOSE	**S**outhern **O**cean **S**tate **E**stimation
T/S	**T**emperature / **S**alinity
UCDW	**U**pper **C**ircumpolar **D**eep **W**ater
UEA	**U**niversity of **E**ast **A**nglia
WOCE	**W**orld **O**cean **C**irculation **E**xperiment
XBTs	e**X**pendable **B**athy **T**hermographs

Physical Constants

Acceleration due to gravity, g (in m s^{-2}) as a function of latitude ϕ and height z (in m)

$$g = (9.98032 + 0.005172\text{sin}^2\phi - 6e - 5sin^2 2\phi)(1 + z/\alpha)^{-2}$$

Time, in seconds (s), minutes (min = 60s), hours (hr = 3600s), days (days = 86,400ss), years ($yr = 3.1558 \times 10^7 s$)

Properties of Seawater, the reader is referred to *Gill* [1982], Appendix Three

Radius of sphere with the same volume as the Earth, $\alpha = 6371$ km

Rotation rate of Earth, $\Omega = 7.292 \times 10^{-5} s^{-1}$

Symbols

ω	angular frequency	rads^{-1}
α	radius of the Earth	km
φ	longitude	radians
ϑ	latitude	radians
γ^n	neutral density	kg m^{-3}
$\Delta\Phi$	geopotential anomaly	m^3 kg^{-1} Pa == m^2 s^{-2} == J kg^{-1}
S	salinity (psu)	dimensionless
T	*in situ* temperature	$Celsius$ $^\circ C$
θ	potential temperature	$Celsius$ $^\circ C$
p	pressure	decibars dbar(1dbar=10^5 dyn cm^{-2})
ν	kinematic viscosity	m^2 s^{-1}
u	zonal component of velocity vector	cm s^{-1}
v	meridional component of velocity vector	cm s^{-1}
w	vertical component of velocity vector	cm s^{-1}
$\mathcal{U}$	horizontal velocity (u,v)	cm s^{-1}
$\mathcal{L}_d$	first baroclinic Rossby radius of deformation	km
$\mathcal{L}_e$	characteristic eddy length scale	km
$T_{L,E}$	*Lagrangian*, *Eulerian* integral time	days
$\mathcal{E}$	enstrophy	s^{-2}
κ_∞	*absolute* diffusion	m^2 s^{-1}
$\overline{\mathcal{D}^2}$	*relative* dispersion	km^2
κ_τ	*relative* diffusion	m^2 s^{-1}
$\mathcal{OW}$	Okubo-Weïss parameter	s^{-2}
$\mathcal{S}_\kappa$	suppression mixing coefficient	dimensionless
Sv	Sverdrup transport	10^6 m^3 s^{-1}

Dedicated to anyone who might extract a useful note ...

Chapter 1

Introduction

1.1 Introduction

Antarctic Circumpolar Current. Overturning circulation. Stratification. Baroclinicity-barotropicity. Eddies. Mixing. Stirring. Diffusivity. Vorticity. Jets. Transport barriers. CO_2 sinks. Climate. Life. These are probably some of the most frequent subjects in any study regarding ramifications of oceanic circulation in the Southern Ocean. The role of the oceans is vital being one of the essential regulators of Earth's climate system and subsequent ecosystems' health [IPCC Fourth Assessment, *Solomon et al.*, 2007]. It is argued by many and noted by even more that Gaia's future may involve us or not but it is not bounded by our existence [*Lovelock*, 1991; *Lenton and Lovelock*, 2000; *Watson*, 2004; *Lovelock*, 2008]. The opposite, though, is fundamentally true. Alfred Worden[1], when in space, quoted impulsively 'Now I know why I am here. Not for a closer look at the moon, but to look back at our home, the Earth'. It is our ethical duty to try to understand, elucidate and preserve Gaia [*Lovelock*, 2008] in order to decipher warning signals of our equivocal existence [*Hodell et al.*, 2001].

1.1.1 The Antarctic Circumpolar Current dynamics

Oceanic processes and the complexity inherent in dynamic flows are intrinsic features of the Antarctic Circumpolar Current (ACC). In the form of a wind-driven zonally unbounded strong eastward flow [*Gille*, 1999; *Gille et al.*, 2001], the ACC circumnavigates the Antarctic continent connecting each of the ocean basins (Fig. 1.1) with a nominal net baroclinic transport[2] of 137 ± 7.8 Sv [*Cunningham et al.*, 2003]. A mechanically instigated oceanic circulation, (Fig. 1.2), through wind stress and tides, and its counterpart induced expression of eddy formation and evolution [*Munk*, 1950] with accompanied

[1] Alfred Worden is an astronaut that flew on Apollo 15 Moon mission in July−August 1971.
[2] Baroclinic transport relative to the bottom.

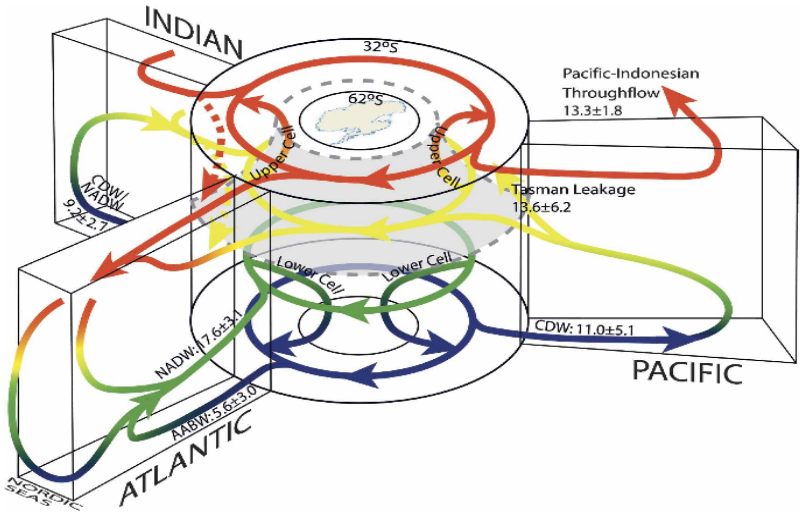

FIG. 1.1: Graphical illustration of the global overturning circulation in the Southern Ocean delineating major water mass exchanges and transformations. Density ranges. Red: upper, $\gamma^n = 27.0$; yellow: intermediate, $\gamma^n = 27.0 - 27.6$; green: deep, $\gamma^n = 27.6 - 28.15$; blue: bottom, $\gamma^n > 28.15$. Gray surface with dashed edges is $\gamma^n = 27.6$ at 32°S, separating upper and lower cell transformation in the Southern Ocean and dashed arrows indicating a westward exchange from Indian-to-Atlantic at approximately 30°E. Illustrated is the net overturning circulation, with integration performed across the respective ocean basin. [Image after *Lumpkin and Speer* [2007] with an adapted format from *Schmitz* [1996]].

energetic transformations are still not fully reconciled [*Huang and Wang*, 2003; *Wunsch and Ferrari*, 2004; *Ferrari and Wunsch*, 2009; *Meredith et al.*, 2011a].

Baroclinity and transport are inextricably related in the ACC [*Stammer*, 1998; *Tilburg et al.*, 2002; *Smith*, 2007; *Thompson*, 2010; *Lu and Speer*, 2011] (see also *Gill* [1982], *Rintoul et al.* [2001] and *Marshall and Radko* [2003] for a review of baroclinic instability and the subsequent effect on the 'residual' circulation). Modelling studies in the Southern Ocean though, indicated that the process responsible for the fast response of the ACC to changes in the zonal wind stress is barotropic in nature and topography controlled [*Webb and Cuevas*, 2007][3].

In a generic approximation of the ACC circulation[4] (a detailed discussion on energy balances, exchange and transformations is given by [*Huang*, 2004; *Wunsch and Ferrari*, 2004; *Ferrari and Wunsch*, 2009, 2010]), wind stress energy input is translated to a geostrophic surface current and a surface drift (*Ekman* drift). This is associated with an increase in gravitational potential energy (GPE), expressed through the upward tilting of isopycnals, through energy dissemination by *Ekman* pumping, as seen in figure 1.2.

[3] An oversimplified analogous in the atmosphere can be related to the *Charney-DeVore* model [Chapter 10, section 6, *Low Frequency Variability*, *Holton*, 2004], where the way topographically forced Rossby waves interact with the zonal mean flow is examined.

[4] Wind stress, tidal energy dissipation, buoyancy forcing, surface heat flux, atmospheric loading, bottom form stress are the main components of energy inputs and transformation mechanisms.

The GPE is depleted through baroclinic instability with an ensuing eddy kinetic energy (EKE) transformation compensating for the isopycnal tilting.

Tidal energy dissipation is the dominant source inaugurating bottom mixing. Tthe interaction of tidal flows with topography leads to deep diapycnal mixing due to generation and breaking of internal waves. The interaction of the mean flow and eddies with topography could also result to the generation of internal waves [*Marshall and Garabato*, 2008].

Turbulent mixing Turbulence-induced mixing is an important factor for water-mass modifications. The fundamental characteristics of oceanic flows, from the perspective of their dynamic extent, capacity in mixing and exchanging of water properties, can be approached in the context of diapycnal and isopycnal eddy diffusivity.

Diapycnal eddy diffusivity as a measurement of vertical mixing exhibits substantial spatial variability across different oceanic environs. According to the depth of the water column, the energetic regime and the topography relief over which water masses flow, quantification of diapycnal mixing exhibits a range of values with variance reaching an order of magnitude.

Munk [1966] computed the average vertical diffusivity for the ocean to be in the $\mathcal{O}(10^{-4})$ m^2 s^{-1}. A reconfirmation of their straightforward calculation was provided by *Munk and Wunsch* [1998] for the majority of the ocean deeper than 1000 m, taking also into consideration the exhibited high spatial variability. Among several approximations, *Marshall et al.* [2002] suggested that heat radiated down from the surface Ekman layers is not vertically diffused but is arrested through baroclinic instabilities and laterally advected by the ensuing eddies. Enhancement of vertical turbulent mixing then, when not associated with flows over rough topography, is confined at the surface mixed layer. *Ledwell et al.* [1993] had obtained a value of $1.2 \pm 0.2 \times 10^{-5}$ m^2 s^{-1} from measuring the concentration of SF_6 (sulphur hexafluoride) for five months during their experiment in the Atlantic, west of the Canary Islands, where they injected 139 kg of their chemical tracer at a depth of 310 m. *Wunsch and Ferrari* [2004] signify the role of vertical mixing in maintaining the oceans' stratification and regulating the global thermohaline circulation. Energetic dissipations and transformations are important in cases of deep overflow. They also argue towards an intensified diapycnal mixing over rough topography. Enhancement of vertical turbulent mixing ($> 10^{-4}$ m^2 s^{-1}) over rough topography has also been reported by *Polzin et al.* [1997]; *Ledwell et al.* [1999]. Enhanced diapycnal mixing over the abyssal Southern Ocean in the Scotia Sea basin has been also identified by *Heywood et al.* [2002]. Derived diffusivity was in the range of $39 \pm 10 \times 10^{-4}$ m^2 s^{-1}. The establishment of a positive connection between rough topography and high mixing rates was further strengthened from the study of *Naveira Garabato et al.* [2004].

Their estimated vertical mixing over the rough bathymetry of Scotia Sea resulted in remarkably high values in the range of 10^{-3} - 10^{-2} m^2 s^{-1} near the sea floor. One of the proposed mechanisms for the intensification of turbulent mixing over small-scale topography was the dissipation of internal waves energy by breaking [*Naveira Garabato et al.*, 2007; *Nikurashin and Ferrari*, 2010; *Naveira Garabato*, 2010]. In the open ocean pycnocline though, observations are suggestive of low diapycnal mixing values ($0.1-0.2\times10^{-4}$ m^2 s^{-1}) [*Watson and Ledwell*, 2000][5].

On the contrary, mixing along isopycnal (isoneutral) surfaces is a far more important constituent, since demand on GPE is minimum [*Huang*, 2004, 2010; *Nycander*, 2011]. *Hallberg and Gnanadesikan* [2001] discuss the role of diapycnal fluxes and transient and stationary eddies on the maintenance of the density structure in the ACC. Stratification and baroclinity, mainly associated with upwelling (south) and downwelling (north) of water masses, led to the depiction, on a meridional vertical section, of the zonally integrated streamfunction of the so called *Deacon* cell. The structure of the *Deacon* cell was attributed to meandering of the ACC, suggesting that it is mainly a horizontal projection of gyre circulation along tilted isopycnals in the east-west direction [*Döös and Webb*, 1994] rather than elevated diapycnal fluxes. The dominance of oceanic mesoscale eddy kinetic energy and its spatio-temporal distribution in respect of: topography; horizontal intensity and vertical extent of the ACC's circulation fronts; unrestricted flow; and response to wind-energy flux are still under vigorous scrutiny regarding their unfolding path of contribution in the overturning circulation and climate [*Rintoul et al.*, 2001]. In the Southern Ocean circulation framework, nested mostly in the context of adiabatic approximation, lateral mixing along isopycnals is concentrated on the balance between eddy versus the mean flow components [e.g. *Gent and McWilliams*, 1990; *Griesel et al.*, 2010]. The eddy induced contribution to the meridional overturning circulation (MOC) relates to the relative spatial and temporal distribution of eddy dynamics, as do the isopycnal potential vorticity (PV) and eddy diffusivity [*Naveira Garabato et al.*, 2011].

Topography, baroclinity and mixing With the characteristic absence of topographic barriers above 2000 m at the latitudinal band of 45-55°S, the dynamics of the ACC have long been a topic of debate. *Rintoul et al.* [2001], among others, noted that the absence of topographic barriers and the inability to balance zonal pressure gradients demonstrates the inadequacy of the Sverdrup approximation in the context of this zonally unbounded flow. A detailed representation of topography in numerical circulation models is a prerequisite for realistic transports and the representation of mixing processes [*Olbers et al.*, 2007]. Interaction of the flow with topography [*Lu and Speer*, 2011]

[5]Favouring the assertion of low diapycnal mixing in the ocean interior, in light of the realization of the DIMES experiment tracer release in the ACC and west of Drake Passage, first evaluated results on diapycnal mixing rates [*Ledwell et al.*, 2010] indicate values as low as $(1.3\pm0.2)\times10^{-5}$ m^2 s^{-1} for an annual average over the tracer's dispersion area.

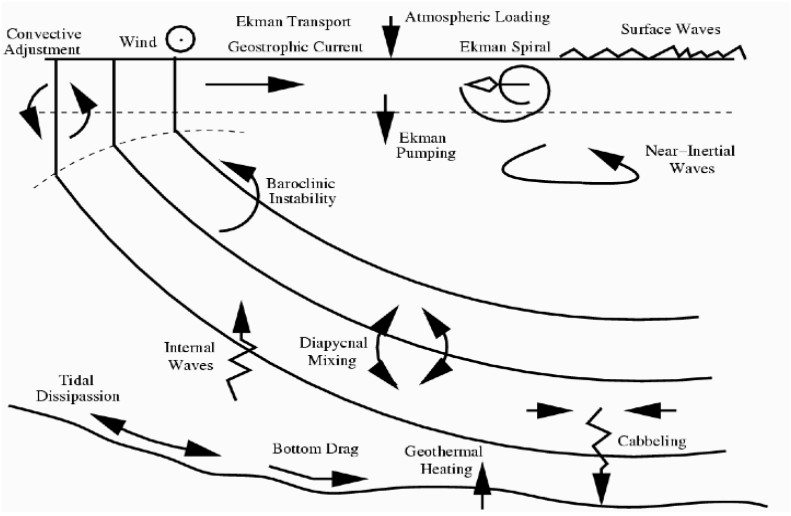

FIG. 1.2: Schematic of mechanical energy diagram. [Image after *Huang* [2004]].

with expressions such as jet formation [*Thompson*, 2010], vertical turbulence intensification [*Polzin et al.*, 1997; *Naveira Garabato et al.*, 2004], EKE [*Gille et al.*, 2000b], internal waves dissipation [*Nikurashin and Ferrari*, 2010] and topographic steering [*LaCasce*, 2000] have all been suggested and being debated. Many were re-confirmed, either partly or unequivocally, by observational and modelling studies (a detailed review of observational and modelling records in the Southern Ocean focusing on the Drake Passage is given by *Meredith et al.* [2011b]). The role of eddies in a whole host of processes has yet to be clearly established.

The ACC's jet structure One of the most important characteristic features of the ACC, regarding ocean dynamics and transport of tracers, are its front/jet structures [*Orsi et al.*, 1995]. Exhibiting a vertical coherency through the water column [*Sokolov*, 2002; *Thompson*, 2010], the ACC associated fronts (Fig. 1.3), their co-interaction and spatial disposition and circulation pattern arrangements were examined in connection with plankton blooms [*Pollard et al.*, 2007; *Williams and Follows*, 2003], (Fig. 1.4), as were mixing inhibition - upwelling and the general relationship to climate indexes [*Pahnke and Zahn*, 2005; *Watson and Naveira Garabato*, 2006; *Le Quéré et al.*, 2009]. The frontal structure of the ACC is multi-filamented rather than coherent circumpolar fronts. The structure has been observed in satellite and drifter-derived dynamic topography, geostrophic velocity [*Maximenko et al.*, 2009; *Sokolov and Rintoul*, 2009a,b], sea-surface temperature gradients (SST) [*Hughes et al.*, 1998] and simulated in Oceanic General Circulation Models (OGCMs) [*Hughes and Ash*, 2001]. The frontal structure is the combined result of locally controlled barotropic and baroclinic instabilities emerging through the interaction of EKE and mean flow dynamics with topography [*Thompson*,

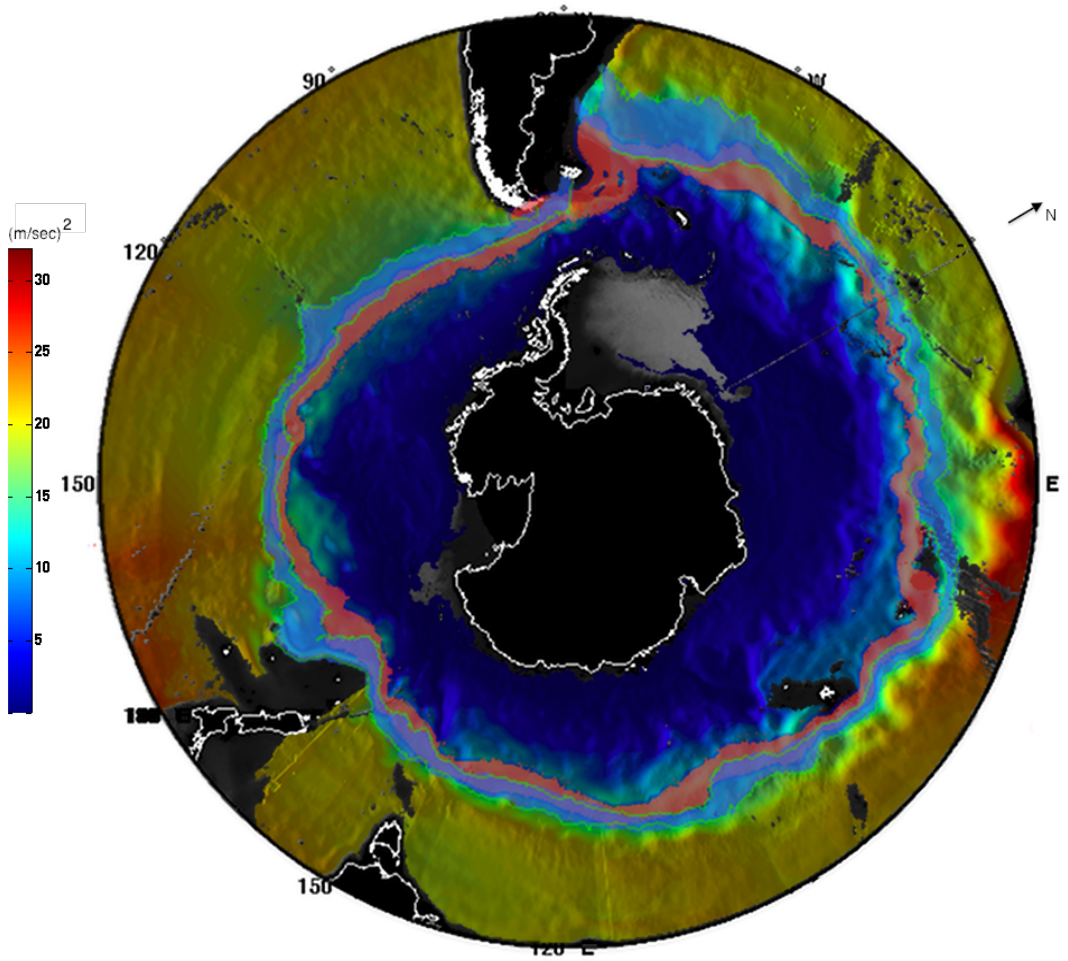

FIG. 1.3: Graphical representation of ensembles of the two main dynamic fronts of the ACC, the Sub-Antarctic (SAF) (light blue) and Polar Front (PF) (light red), superimposed on geopotential anomaly (m^2 s^{-2}) for neutral density surface $\gamma^n = 27.9$ in OCCAM 1/12° General Circulation Model (GCM). Fronts' ensembles are produced from weekly interpolated positions of altimetry sea level anomaly data, covering the period 1992-2010 (see *Sallée et al.* [2008a]). [Coastline, depicted in white, from GEBCO.]

2010; *Thompson et al.*, 2010]. Their subsequent control of mixing extent and intensity through their role as barriers of transport and/or pathways for tracers is still ambiguous.

The role of eddies The features of oceanic flows dominating oceanic energy are the mesoscale eddies. With a radius scale of $\mathcal{O}(100$ km), mesoscale eddies, more than likely the result of non-linear effects [*Venaille et al.*, 2011], owe their existence on locally emerging baroclinic instabilities interacting with the mean flow [*Gill et al.*, 1974]. *Chelton et al.* [2007, 2011], analysing sea surface height (SSH) fields from satellite altimeters, comment on their universal census and nonlinearity[6] suggesting baroclinity as the norm

[6]The *Chelton et al.* [2011] characterization of nonlinearity is based on a ratio measuring the circum-average rotational speed U to the translation speed c of coherent mesoscale features, with values $U/c > 1$ depicting vortex formations.

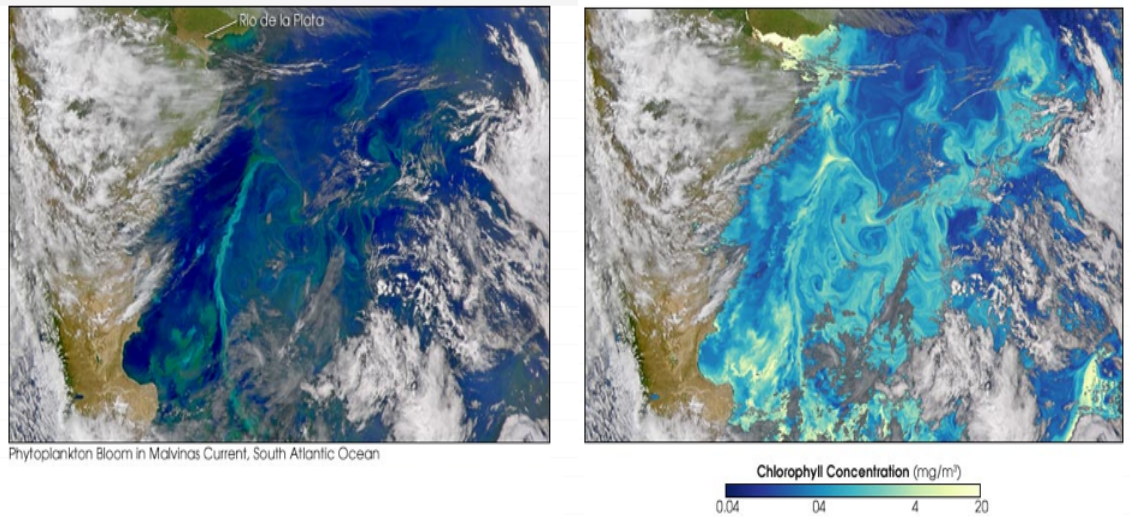

FIG. 1.4: Satellite image on December 6, 2004 from the Sea-viewing Wide Field-of-view Sensor (SeaWiFS) probe. The Malvinas Current transfers cold water following the Sub-Antarctic Front of the Antarctic Circumpolar Current. This northward jet entering the Argentina Basin along the coast of South America meets the south-flowing Brazil current. The convergence of the two currents of different thermodynamic properties leads to the emergence of filamented regions of downwelling and upwelling. The influx of nutrients provided by the upwelling displacement induces phytoplankton growth and concentrations increase. Left image is natural colour with depicted blooms of marine plant life in blue and green. Right top image illustrates chlorophyll concentrations in shades of blue (lower values) to yellow (higher). [Images provided by the SeaWiFS Project, NASA/Goddard Space Flight Center, and ORBIMAGE].

of the World Ocean [*Wunsch*, 1997]. An estimate of the eddy to mean flow ratio is of $\mathcal{O}(100)$ for the surface distribution [*Stammer*, 1998] outlining their importance as the major energy containing structures. Vortices contribute to water mass transport, to set the conditions for water mass homogenization by the mixing of properties such as heat and nutrients, and are relevant not only to fluid dynamics and climate but also to the marine ecosystem [*Lee and Williams*, 2000; *Goodwin et al.*, 2009]. In the Southern Ocean circulation framework, nested mostly in the context of adiabatic approximation[7], lateral mixing along isopycnals focuses on the eddy versus the mean flow contributions [e.g. *Gent and McWilliams*, 1990; *Griesel et al.*, 2010]. The eddy induced contribution in the meridional overturning circulation (MOC) [*Wunsch and Ferrari*, 2004; *Lumpkin and Speer*, 2007], (Fig. 1.1), relates to the relative spatial and temporal distribution of eddy-mean flow dynamics. It is due to the imperative role of eddies in the general oceanic circulation and climate that we need to have a reliable representation of their effect in our simulation efforts of climate projections and ocean states. As the whole spectrum of eddy scales is still unresolved we establish various parameterization schemes based

[7]Refers to the gradual change of external conditions as an adiabatic process and thus, that the time scale of a perturbation controls the ability of a system to react to and accommodate that same perturbation.

on theories of how the intensity of EKE, time-mean flow and topography interact with each other. We will try to address this connection utilising an explicitly eddy resolving model and present our results in a context that will add new information delineating the role of eddies in the complex Southern Ocean dynamics.

Summary In this set-up, being a key region of the global oceanic conveyor belt, water mass formation and transformation, the relative balance of mixing processes and the capture of CO_2 have extensively been discussed but not fully resolved yet. Mostly because of the scarcity of observations (a gap now partly filled by satellites and the ARGO observational system network), theory establishment and branching evolved in close association computational power [*Willebrand and Haidvogel*, 2001] and advances in observational techniques [*Davis*, 1991]. Our understanding of the Southern Ocean fluid dynamics seems to follow numerical simulations' resolution with the implementation of less parameterizations. Fewer parameterizations result in more realistic simulations where the fundamental constituents of a dynamical system are allowed to interact, as in coupled atmospheric-oceanic models. However numerical integrations with increased complexity would be meaningless without observations, since the modelled dynamical system is still far from reality. The World Ocean Circulation Experiment (WOCE) was conceived with the recognition of the importance of observations in a system as complex as the oceans . Apart from the provision of data on a scale previously not attempted, it signified the need for multidisciplinary perspectives and international collaboration in deciphering this critical component of Earth's climate.

While the ACC related studies have identified that the interaction of topography, mean-flow and eddies[8] are key factors for turbulent mixing, the results are not consonant with one another. In the section to follow the various theories regarding Southern Ocean mixing are addressed.

1.2 What are the main questions regarding Southern Ocean mixing? Eddy stirring or mixing, or both?

Stirring is defined as the spatial distortion of fluid particles by the combined processes of stretching and eddying [*Davis*, 1991]. The process is an inescapable consequence of the vortex contribution, given the inadequacy of a theoretical time-mean background velocity field to produce progressively finestructure filaments of fluid elements. Nonetheless, dispersion by itself only requires random displacements, as described by *Taylor* [1921] in examining particle motion in stationary and homogeneous turbulence regimes. Hence,

[8]Eddies induced by local instabilities (barotropic and/or baroclinic) affect mixing conditions at their generation sites or at remote sites during their propagation as transient disturbances of the mean flow.

the end-process of stirring a passive tracer, in a fluid dynamics context, is mixing by small scale diffusion [*Abernathey et al.*, 2010]. Elaborating more on the stirring versus mixing sequence, eddy stirring of a passive tracer field precedes with a progressive scale reduction down to that of an ideal approximation of a point vortex system [*Provenzale*, 1999] of transient nature. Filamentation of the tracer patches through a strain mechanism induced by the velocity field ensues until width scales are sufficiently small to allow a full diffusion process. In the sense above, illustration of the stirring to mixing evolution would require multiple particle-based measurement methods [*Davis*, 1991]. It is still not clear whether the ACC associated mixing can be characterized by one dominant process.

1.2.1 Stirring versus mixing

Are stirring and mixing two disparate processes associated with clearly identifiable regimes or they are both part of the dynamical evolution of a mixing environment alternating their dominant character? Geostrophic stirring appears to be the dominant mechanism for the generation of thermosaline T/S finescale structure below the thermocline, contrary to the common view that ascribes the generation of T/S finestructure primarily to internal wave or double diffusive turbulence [*Smith and Ferrari*, 2009]. The mesoscale forcing sets the rate of stirring at the submesoscale in the ocean interior, while it sets both the rate of stirring (through mesoscale strain) and mixing (through modifications of convection and shear instabilities at fronts) at the ocean surface [*Taylor and Ferrari*, 2009, 2010]. The efficiency of stirring against mixing, as a diagnostic for different flow regimes, was suggested on a basis of a direct computation of gradients of tracer distribution without the previous knowledge of background diffusivity values or strain rate estimation [*Lee et al.*, 2009].

Two fundamental questions concerning most underlying processes of geophysical flows, that also apply in a stirring-mixing context, are outlined below.

First, what would be the time evolution of this stirring-mixing system? *Garrett* [2006] associated a fairly quick stirring to mixing transgression with a relatively small *Prandtl*[9] number, Pr, allowing the act of diffusion at the scale of the turbulent eddies. On the contrary a large Pr introduces a finite time lag in order for the eddy induced strain effect to produce the 'permitting' diffusion. Further fluctuations in the passive tracer spatial clustering is expected with time evolution and dispersal of the produced filaments and vortices.

Second, what would be the spatial distribution of a stirring-mixing system and how does it relate to the temporal and spatial variation of the velocity field and the potential

[9]The *Prandtl*, number is a non-dimensional measure of the ratio of the kinematic viscosity ν to the thermal diffusivity α, $Pr = \frac{\nu}{\alpha}$, with low (high) values denoting strong conductive (convective) transfer.

vorticity (PV) distribution associated with the observed ACC's jet structures? Spatial distribution of eddy stirring in the Southern Ocean, with respect to jet intensity, is under consideration [*Abernathey et al.*, 2010; *Griesel et al.*, 2010; *Naveira Garabato et al.*, 2011; *Sallée et al.*, 2008b; *Shuckburgh et al.*, 2009a; *Waugh and Abraham*, 2008], and its role as an indicator of eddy diffusivity maxima and minima is still debated. Theoretical considerations of eddy stirring characterization in geophysical flows are along the following lines: eddy stirring as quasi-homogeneous turbulence, associated to predictions of enhanced eddy stirring in jet cores; linear waves in a parallel shear flow, expressed as enhanced eddy stirring on jet flanks and below jet cores; weakly nonlinear waves in a parallel shear flow, with eddy stirring inhibited in jet cores; aspects of wave propagation in non-parallel shear flows, suggesting that eddy stirring continues to act in jet cores; and the law of the wall, with eddy stirring being suppressed in the vicinity of a topographic boundary, [*Naveira Garabato et al.*, 2011]. These theoretical considerations led to the formation of various groups of studies aiming to interpret the Southern Ocean mixing in the context of EKE, time-mean flow and bottom topography interaction. Our approach, with the utilization of Lagrangian particles in order to represent stirring by the stretching and compression of their trajectories, aims to further investigate ACC mixing and the hypotheses presented in the next section.

1.2.2 The ACC mixing hypotheses

The diverging ACC mixing hypotheses, founded on the theoretical considerations regarding eddy stirring in geophysical flows, are outlined in the following representative groups of studies:

The first one [*Holloway*, 1986; *Visbeck et al.*, 1997; *Sallée et al.*, 2008b] denotes that high EKE is analogous to an invigoration of eddy diffusivity. *Sallée et al.* [2008b] analyse surface Lagrangian trajectories and conclude that maxima in EKE are related with intensified eddy diffusivities in the most energetic regions. Similarly, *Waugh and Abraham* [2008] suggest that a connection exists between eddy stirring (quantified as finite-time Lyapunov exponents (FTLEs) representations) and regions of intensified EKE, using satellite-altimeter data for derived surface geostrophic currents. In the northern hemisphere *Lankhorst and Zenk* [2006] favour this hypothesis in their analysis of 89 eddy resolving RAFOS and MARVOR[10] type floats. Their suggestion was that much of the intensified mixing can be related to eddy activity, especially cyclonic, with a pronounced presence in the subpolar region of the northeastern Atlantic.

The second group, represented by studies of [*Killworth*, 1997; *Smith and Marshall*, 2009; *Abernathey et al.*, 2010], embrace the idea of a Rossby wave critical layer existence where eddy diffusivity is enhanced. The mechanism proposed is that mixing is enhanced

[10]The MARVOR float is a multi-cycle RAFOS type float, developed by IFREMER and MARTEC.

when the mean eastward zonal flow speed has a similar magnitude to the westward Rossby wave phase speed.

A third perspective allowing for mean flow intensity when considering eddy diffusivities was introduced by *Shuckburgh et al.* [2009a]. They indicated that characterisations of eddy diffusivities in regions of strongly varying mean flow, such as the Southern Ocean is, based solely on EKE approximations are subject to inadequacies. *Naveira Garabato et al.* [2011] examined eddy stirring in the aforementioned theoretical context with an analysis of repeated hydrographic sections and altimetric observations. They adhere to an eddy stirring formalism as weakly nonlinear waves, with eddy diffusivity in direct analogy to the mixing length l'[11] and suppression of eddy stirring within jets. Mean to eddy flow interactions [*Stammer*, 1998; *Hughes and Ash*, 2001] are delineated with the depiction of non-coherent, local reorganised barriers in the flow [*Sokolov*, 2002]. In the context of isentropic potential vorticity (IPV) gradients *Thompson et al.* [2010] examined the generation, effectiveness and persistence of regional frontal jets. They also deduced the fundamental role of topography on the ACC's jet structure.

In this study an improved Lagrangian scheme is employed in order to resolve the spatio-temporal scales associated with eddy-mean flow dynamics. The fundamental role of topography, in the Southern Ocean's isopycnal horizontal and vertical mixing variation, is depicted by the association of high EKE regions, where the interaction of vortical elements and multi filamented jets in non-parallel flows provide the mechanism for eddy stirring resulting in enhanced dispersion of particles. Suppression of mixing in regions where the flow is delineated by intensified and coherent, both in space and time, jets (strong PV gradients) signifying the separation of the flow in differentiated kinematic environments will be illustrated. We discuss the importance of a local approximation to mixing instead of the construction of zonal averages and detach the ACC mixing from a circumpolar latitudinal variation. We will investigate how cross and along stream diffusivity variation, approached in terms of classical diffusion theory, falls into one or more of the above contexts and present the caveats of classical diffusion theory in the presence of persistent structures. We will illustrate, by spatially mapping the flow dynamics of the ACC through the computation of particles' spatial occurrences during a period of 17 years, coherent structures in time that regulate the tracers distribution.

[11] The mixing length used by *Naveira Garabato et al.* [2011] differs from a simple approximation with the eddy length scale $\mathcal{L}_e$.

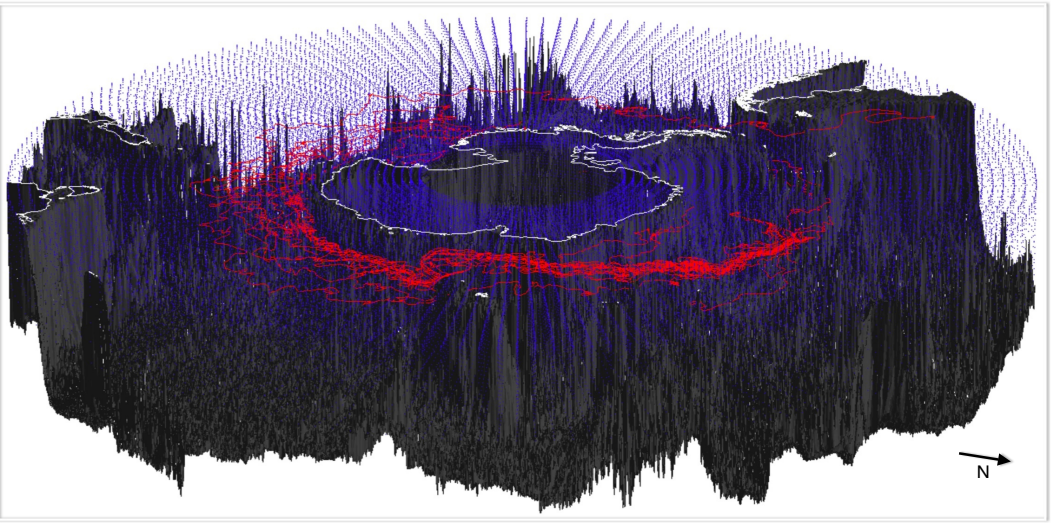

FIG. 1.5: A perspective 3D illustration of OCCAM's 1/12° model bathymetry (vertically exaggerated) with Eulerian grid nodes (blue dots) superimposed. Also shown, are selected Lagrangian trajectories (red lines) for a release on neutral density surface $\gamma^n = 27.76$ as computed from the model's output. The grid points are equally spaced every 1° in the horizontal and 1/4 of OCCAM's 1/12° model nominal resolution in the vertical. Lagrangian trajectories have the advantage of sampling space in time and representing the evolution of kinematics in space over Eulerian points sampling temporal variations of quantities at specific locations.

1.3 Why Lagrangian trajectories? The combination with a Eulerian representation of kinematics.

1.3.1 Definitions. Eulerian versus Lagrangian representations.

Let us consider a parcel of fluid in a kinematic geophysical flow, evolving in time, with the flow's initial time being t_0 and position of the fluid parcel $\mathbf{x_0}$ at that time. Evolution of the flow produces a fluid parcel displacement which is a consequence of the flow characteristics itself and initial position $(\mathbf{x_0}, t_0)$. A Lagrangian approximation to flow (or *material* point of view [*Vallis*, 2006a]) is the observational method that samples space in time and evolution of kinematics and flow structures in space. However, an Eulerian observation in time relates to a fixed point in space. So, it actually samples the rate of change of the respective quantity evolving both in time and space but at a specific location (e.g an oceanographic mooring is an Eulerian instrument)[12], (Fig. 1.5).

An assumption is made that a particle can serve as an adequate representation for a fluid parcel if scaling arguments are adopted regarding the grid resolution of the numerical simulation. The geometric space of sequential particles' displacements constitutes the particle's trajectory and a direct representation of travel history and streamline evolution. As such, observing the evolution of fluid flows reduces to the observation of

[12] A review on Lagrangian and Eulerian representations of kinematic flows is given by *Price* [2006].

the particles' trajectories representing discrete material fluid parcels. If $\mathbf{x}$ the position vector of a particle in a Cartesian space system and $\mathbf{x}_0$ the particle's position at time $t = t_0$ (or initialization), then the trajectory $\mathbf{X}$, would be the geometric set of the trails of the position vector at the instances observed

$$\mathbf{X} = \mathbf{x}(\mathbf{x}_0, t).$$

Accordingly, the particle's velocity (Lagrangian) is just the time derivative of the position $\mathbf{x}(\mathbf{x}_0, t)$ with

$$\mathcal{U}_L = \frac{\partial \mathbf{x}(\mathbf{x}_0, t)}{\partial t}$$

since the geometric space $\mathbf{X}$ is dependent on initial position $\mathbf{x}_0$. In a fixed point reference observation system (Eulerian), the velocity at a point $\mathbf{x}$ in space $\mathcal{U}_E(\mathbf{x}, t)$, with (x,y,z) fixed coordinates, at time t would be exactly equal to the particle's Lagrangian one $\mathcal{U}_L$ while passing from the same point $\mathbf{x}$ at time t (Of course one has to pre-order the coincidence of the spatial 'resolution' of a fixed point in space and of a passing one or else that both points represent the same material volume).

Even though the equality at instant time t seems trivial, considering the evolution of Lagrangian trajectories in geophysical flows both in time and space in connection with the Eulerian fixed point properties is ambiguous. Chaotic advection [*Pierrehumbert*, 1991] characterizes any dynamical system described with any simple streamfunction $\psi(x, y, t)$ denoting the velocity $\mathcal{U}(x, y, t) = (u(x, y, t), v(x, y, t))$ through the equations $u = -\partial_y \psi(x, y, t)$ and $v = \partial_x \psi(x, y, t)$. Even in the simple case where the streamfunction ψ, being a nonlinear function of x and y, varies periodically with time, the system can exhibit chaotic behaviour. The result is the emergence of *Lagrangian chaos* where even non-complex background Eulerian velocity fields generate Lagrangian trajectories which are quite unpredictable [*Boffetta et al.*, 2001] as a consequence of nonlinearities in the velocity field. Therefore, a simple connection between the Eulerian properties and the Lagrangian time evolved trajectories is difficult to establish since turbulent and complex flows can result from similar trajectories aso simple flows. That leaves us with only one choice if we aim to decipher flow characteristics and depict mixing potential in geophysical flows: Lagrangian statistics.

A logistics problem? *Davis* [1991] considered the size of the oceans and the economic repercussions of a fully (highly dense) maintained Eulerian observational network. In a numerical context, it can be clearly understood by considering the illustration in figure 1.5. A full Lagrangian experiment, both in spatial and temporal scales, as the one formulated in this thesis has the potential to depict the underlying dynamics of the ACC and the general Southern Ocean oceanic flow. Considering the temporal resolution for

the Lagrangian particles to be equal to 1 day[13] and for the Eulerian case to be the 5 day means from the model's output, the whole simulation period results in 6204 and 1241 time-events respectively. Releasing 2000 particles every 5 degrees of longitude results in ≃9e+08 individual position events. For a grid resolution of 1/12° and a spatial extent from 35-90°S and 0-360° of longitude, the Eulerian space representation is 518×4320 grid points. Excluding the land area and taking into consideration the isoneutral surface geometry, $\sim 25\%$ of the whole, the number of individual events ends up at almost 40% of the respective Eulerian representation. So, full coverage of the flow dynamics takes less than half the computational data requirements using a Lagrangian approach.

1.4 Neutral density definition and caveats

A neutral density isosurface is a concept of an ideally depicted three-dimensional Euclidean space surface. Following *Eden and Willebrand's* [1999] terminology of *neutral trajectory*, the envelope of local neutral surface elements tangent to the 3D neutral paths at each point in the fluid form a neutral surface. A fundamental 'conceptual' property inherent in the isopycnal or neutral density surface definition, is that a fluid parcel's minute displacement following a path on the neutral density two-dimensional manifold results in no residual buoyancy potential bequeathed to it. *McDougall* [1987] stated the notion as "...Neutral surfaces are defined so that small isentropic and adiabatic displacements of a fluid parcel on a neutral surface do not produce a buoyancy restoring force on the parcel". The isentropic characterisation complies with homogeneous[14] mixing. In reality though the norm of neutral density surface mixing is not to be homogeneous absolutely.

Continuity of a fluid, eloquently described by Euler in *Principia Motus Fluidorum* [*Euler*, 1756/7][15], distills into the fact that fluid parcel movements on an isopycnal surface should be examined from the perspective of pairs of particles. *Huang* [2010], in the context of compressibility of fluid particles, corroborates that such a displacement is more than possibly accompanied by a GPE residual. Depending on the density difference or the potential compressibility factor between the two fluid particles interchanging positions, GPE can be positive or negative. On a larger scale of baroclinic instability, the role of geostrophic eddies to rectify the isopycnals' tilting is associated with a vertical

[13] In fact, the temporal resolution of a Lagrangian approximation is both controlled by the background temporal resolution of the Eulerian field, as nominated from the model's output, and the numerical advection scheme employed. In the numerical scheme in this study, this is equal to 8640 seconds but only positions respective of 1 day travel time are retained (see Chapter 2).

[14] Here, homogeneous mixing refers solely to the physical aspects of an isentropic surface and not to a regime where the presence of transport barriers and spatial separation of the flow kinematics do indeed differentiate mixing potential.

[15] '...I shall posit that the fluid cannot be compressed into a smaller space, and its continuity cannot be interrupted. I stipulate without qualification that, in the course of the motion within the fluid, no empty space is left by the fluid, but it always maintains continuity in this motion'.

flux of potential vorticity [*Marshall*, 2000]. The vertical displacement of an isopycnal surface is followed by a subsequent release of the integrated GPE over the 2D manifold (isosurface). The result is a flux of energy that augments lateral mixing on a common neutral density coordinate reference level. This GPE opposing the isentropic character of neutral surface mixing is lost though, through turbulent dissipation and formation of internal waves [*Huang*, 2010].

Nonetheless, formulation of the OGCM employed in this study is contingent on an incompressible fluid approximation and so is the tracking algorithm employed in the Lagrangian particles' trajectories depiction. So, assumption of isentropic lateral mixing, that is on isoneutral surfaces, is adopted. Additionally, the microstructure of turbulent dissipation energetics and vertical scale of internal waves are not resolvable in the z-coordinate of OCCAM 1/12° grid structure. *Jackett and McDougall* [1997] developed a complete definition of a neutral density surface based on its spatial distribution and accompanying approximations. The neutral density variable γ^n is a function of salinity S, *in-situ* temperature T and pressure p at the geospatial longitudinal and latitudinal coordinates of the fluid parcel under investigation.

1.5 Why and why not OCCAM 1/12°...-Evaluation studies

The Ocean Circulation and Climate Advanced Modelling (OCCAM) model is a primitive equation numerical model developed and run by the National Oceanography Centre (NOC), Southampton, [*Gwilliam*, 1995; *Lee et al.*, 2002; *Coward and De Cuevas*, 2005] (see Chapter 3 for detailed references) available in three grid resolutions of 1°, 1/4° and 1/12°. Numerous evaluation studies exist mainly for the 1/4° grid resolution [*Drijfhout et al.*, 2003; *Lee and Coward*, 2003; *Thorpe et al.*, 2007; *Döös et al.*, 2008 among others]. Here, reference is made to those considering the 1/12° version with emphasis on the Southern Ocean.

Lee et al. [2007] investigated eddy-induced transport of temperature and salinity tracers, with a view to two distinct mechanisms: advective and diffusive transport. They computed different eddy diffusivity values for tracer transport in comparison to that for advective transport by the residual velocity component. Their result, supporting the existence of significant separation for tracer transport by eddy diffusion versus that by eddy advection, questions the validity of a common eddy diffusivity parameterization for both the eddy advection and diffusion processes in climate modelling.

Screen et al. [2008] identified an agreement between the 1/12° model spatial distribution of mean EKE values and those derived from satellite altimetry. Further examining the relationship between EKE and SAM index, they found that in both the 1/12° and

1/4° versions of OCCAM and in the satellite estimates, a positive correlation exists between SAM events and EKE variations. A time lag of 2-3 years, in agreement with a previous study of *Meredith and Hogg* [2006], was detected with the maximum EKE response in the models being consistent with the satellite data. A difference in the increased magnitude was also found with the satellite based computations illustrating an enhanced EKE intensification relative to the 1/12° model.

Lee et al. [2009] examined effective eddy isopycnic diffusivity from point release tracer scenarios closely resembling the North Atlantic Tracer Release Experiment (NATRE). They also introduced 'stirring efficiency', a measure of the efficiency of stirring against mixing, in order to indicate different flow regimes. They inferred that convergence of all different diffusivity computations in their study should occur at a value of 1000 m^2 s^{-1} at the final diffusion stage (not reachable by all of the various computations at the same time scale). In comparison with the lower resolution of OCCAM 1/4°, the 1/12° model was found to be about 10 times more efficient in terms of the tracers' stirring. They suggested that a discrepancy with the real ocean stirring efficiency values would be indicative of an intrinsic deficiency in models with large numerical diffusion, such is the 1/12° model, or a combination of the weak strain rate and large explicit diffusion, found in the 1/4° version.

Renner et al. [2009] in an evaluation of three global ocean models in the Weddell Sea concluded that the 1/12° version of OCCAM captures the general features of the Weddell Sea hydrography, though with several deviations from the observations. An underestimation of the magnitude of an asymmetric pattern associated with bottom water formation in the southern and western Weddell Sea was detected. An overestimation of the ice cover extent was also discussed, though the observations and the annual cycle of the ice cover extent in the model are in agreement when considering short time scales. An out of equilibrium mixed layer depth with an increasing depth trend was noted in the central Weddell Sea attributed to erroneous surface fluxes in the area. Transport of the ACC in the Drake Passage region was stable through the majority of the examined period.

A comparison study of total kinetic energy (TKE) computed from four global eddy permitting-resolving ocean models runs with a global dataset of moored current meter records was provided by *Scott et al.* [2010]. TKE was computed throughout the vertical extent of the water column. In general, the models in an eddying-regime with TKE compared reasonably well with observations, though, at individual mooring sites considerable scatter was found that was comparably larger than the computed statistical uncertainty. OCCAM simulations of TKE in the top 300 m is in agreement within a factor of 2 with the current meter record but appears to be significantly weaker at greater depths. In detail, the OCCAM 1/12° was estimated to be $\sim$ 1.5 times too weak at 300

m depth, about 2 times too weak at 3000 m, and around 3 times too weak at 4000 m. It was mentioned that data assimilation improved the model-observation comparison, especially below 2000 m as seen with the HYCOM model. Even though the dataset comprising the current meter records numbered around 5000, their spatial coverage cannot be considered as uniform in the Southern Ocean and results from this area should be interpreted with caution. Exceptions are the Drake Passage, the Greenwich meridian section, the Agulhas Retroflection area and the region between the Southwest Indian ridge and Kerguelen Island (see figure 1 in *Scott et al.* [2010]).

We need to point out that the primary scope of this study is not to evaluate the performance of OCCAM 1/12° but to examine the dynamics of a specific dynamic environment, namely the ACC, and deduce useful ideas regarding mixing in complex geophysical flows. Inference with respect to the underlying connection of eddies, mean flow and bottom topography is attempted based on the fact that OCCAM 1/12° reproduces the broad detail of ACC dynamics and that of an oceanic dynamical system. Our aim is not to 'glorify' the computed eddy diffusivity values as 'real' but to facilitate a way of reasoning, through our experimental scheme, that would justify, reject or even merge one or more of the proposed mixing theories in the Southern Ocean.

1.6 Outline of thesis

This thesis primarily concerns eddy stirring and mixing in the Antarctic Circumpolar Current (ACC) with respect to jet-vortex interaction and consequent formalization of dispersion regimes. Diffusivity is only approximated on an isoneutral density framework through a Lagrangian perspective of Eulerian time-varying velocity fields. The main approach is simulations of conceptual particle trajectories on selected isoneutrals, computed from the *run401* of GCM OCCAM 1/12° output. The focus is particularly on diffusion estimates from particles' time derivative of dispersion including the relationship with local distributions and evolution of potential vorticity. Eddy stirring processes are also discussed within the context of previous studies and by computation of space effective probability densities.

In this introductory chapter a brief description of the ACC dynamics is attempted. The founding theoretical factors of the simulation scheme employed in this study, such as neutral density and the Lagrangian representation of flow kinematics, are defined. The importance of Lagrangian studies in geophysical flows is revisited and prevalent mixing theories outlined. Reference to previous studies utilising the same model were made and the scope of this thesis was outlined.

Chapter 2 provides a description of the numerical model output used and the background computations and assumptions taken into consideration. The Lagrangian tracking algorithm is described and release schemes explained. Flow separation is discussed and its role in particle advection and diffusion schemes outlined. Various methodologies applied are more often presented in the respective chapters with a brief bibliographic introduction and ensuing discussion.

Chapter 3 provides an introduction to ACC dynamics from a Lagrangian perspective. It illustrates the advantages of Lagrangian studies to decipher and represent flow characteristics and establishes a connection between particle occurrence probabilities and dynamical systems theory. It sets the background for the diffusivity calculations discussed in Chapter 4 and provides a qualitative assessment of particle dispersion in the ACC. It provides a suggestion about a potential effective eddy stirring mechanism based on the spatial distribution of kinematic boundaries. Finally, a simulation of a real time experiment, the Diapycnal and Isopycnal Mixing Experiment in the Southern Ocean (DIMES), is presented on both an isobaric and isopycnal framework for comparison reasons.

In Chapter 4, diffusivity in the ACC, in the context of classical diffusion theory, is computed. Estimated diffusivities are presented and discussed in relation to mixing theories and in relation to flow characteristics and spatial variability.

Chapter 5 describes the fundamental structure of mixing with numerical simulations and presents a non-parallel flow mechanism as responsible for the distributions depicted in the previous chapters. The role of coherent vortices, topography, potential vorticity gradients and mixing suppression by the mean flow are analysed.

Appendix A lists additional calculations and accompanying illustrations to respective sections in the main text. Appendix B describes the DIMES experiment and corresponding simulations.

Chapter 2

OCCAM, datasets, numerical tracking scheme and fundamentals

2.1 OCCAM 1/12° model

2.1.1 Model formulation

The Ocean Circulation and Climate Advanced Modelling (OCCAM) model is a primitive equation numerical model developed and run by the National Oceanography Centre (NOC), Southampton [*Gwilliam*, 1995; *Lee et al.*, 2002; *Coward and De Cuevas*, 2005]. The model is based on the Bryan-Cox-Semtner type [*Bryan*, 1969; *Semtner*, 1974; *Cox*, 1984] rigid lid global ocean general circulation model and the Modular Ocean Model (MOM)[*Pacanowski*, 1995], but with the inclusion of improved advection schemes, both horizontal and vertical, sea-ice model, a mixed layer and a free surface after *Killworth et al.* [1991] and *Webb et al.* [1998]. The sea-ice model dynamics are built upon the elastic-viscous-plastic scheme described by *Hunke and Dukowicz* [1997], while the thermodynamics is based on that of *Semtner* [1976]. A complete description of the sea-ice model can be found in *Aksenov* [2002]. There are five primary variables archived from the model runs: potential temperature θ, salinity S, the u and v vectors of the horizontal velocity and sea surface height *ssh*.

The primitive equations The primitive equations, so called during the inception of numerical modelling due to their effective numerical integration, are a set of nonlinear differential equations [*White*, 2003]. Their implementation is aimed to adequately describe the state of the ocean in conjunction with the equation of state and boundary conditions. A modification of the Navier-Stokes equations, in the form of momentum

conservation, conservation of mass and a thermodynamic equation with the fundamental assumption that the ocean is incompressible, the applied Boussinesq approximation neglects small density variations in the presence of horizontal pressure gradients. In the vertical momentum equation the assumption that the vertical motion is much smaller compared to the horizontal, requires the pressure gradient term to balance the gravitational term (hydrostasis) resulting to the relation:

$$\frac{\partial p}{\partial z} = -\rho g \tag{2.1}$$

where p the pressure, z the vertical coordinate, ρ is the density and g the gravitational acceleration. The horizontal momentum equation in a rotating frame for a viscous fluid is:

$$\frac{D\mathbf{u}}{D\mathbf{t}} + 2\mathbf{\Omega} \times \mathbf{u} + w\frac{\partial \mathbf{u}}{\partial \mathbf{z}} = -\frac{1}{\rho}\nabla_z p + \nu\nabla^2\mathbf{u} - \nabla\mathbf{\Phi} \tag{2.2}$$

where $\mathbf{u}$ is the horizontal velocity $\vec{\mathbf{u}}(u,v)$, $\mathbf{\Omega}$ is the angular velocity of the rotating frame, ∇_z the horizontal gradient term (at constant z), ν is the kinematic viscosity ($\nu = \mu/\rho$, where μ is the viscosity) and $\mathbf{\Phi}$ the geopotential as a sum of the gravitational potential and the centrifugal potential (for related work on this topic see *ch.4*, *Gill* [1982]) representing the applied body forces (per unit mass). For the scales of motion involved in oceanic circulation the kinematic viscosity term is replaced by a diffusion term $\mathbf{D}_u$ [*Webb et al.*, 1998], following *Bryan* [1969], denoting that smaller scale motions are parameterized by a turbulent viscosity approximation. This is a necessity if a constant density fluid is to reach equilibrium as viscosity is the only way for the dissipation of the mechanical energy provided to the system [see p.74 *Gill*, 1982]. The mass conservation (or continuity) equation is

$$\frac{D\rho}{Dt} + \rho\nabla \cdot \boldsymbol{\upsilon} = 0 \tag{2.3}$$

where $\boldsymbol{\upsilon}$ the three dimensional velocity vector $\vec{\boldsymbol{\upsilon}}(u,v,w)$, which in the case of an incompressible fluid reduces to:

$$\nabla \cdot \boldsymbol{\upsilon} = 0 \tag{2.4}$$

The shallow-layer fluid approximation surmises that the fluid layer depth is small compared to the radius of the earth.
The thermodynamic equations and the accompanied equation of state can be described after *Vallis* [2006b] by

$$\frac{D\theta}{Dt} = Q_\theta, \quad \frac{DS}{Dt} = Q_S \tag{2.5}$$

where θ is potential temperature, S is salinity, Q_θ are dissipation and forcing of θ and Q_S dissipation and forcing of S.
The equation of state has the form

$$\rho = \rho(T, S, p) \tag{2.6}$$

where T is the temperature and p the pressure at level z, which in turn defines the calculation level of the hydrostatic pressure, $-\rho_0 gz$, with ρ_0 the reference density.

OCCAM grid The OCCAM model is split into two parts, called Model 1 and Model 2 (see figure 2.1). Model 1 uses a standard latitude-longitude grid and covers the Pacific, Indian and South Atlantic oceans while Model 2 covers the North Atlantic and Arctic oceans and uses a rotated grid which has its poles on the Equator in the Indian and Pacific oceans. It is oriented to match Model 1 at the Equator in the Atlantic. The two models are connected with a simple channel model of the Bering Strait. The necessity for the split of a potentially globally uniform latitude-longitude grid lies in the convergence of the meridians near the poles. This leads to a singularity at the pole and reduced grid spacing close to the pole and hence high computational cost to maintain numerical stability [*Webb et al.*, 1998; *Coward and De Cuevas*, 2005].

In order to solve the oceanic primitive equations OCCAM uses the finite differences method on a horizontal Arakawa-B grid [*Lee et al.*, 2002]. The Arakawa-B grid (see figure 2.2) locates velocity grid points at the corners of tracer grid boxes. There is a horizontal offset of half grid point with respect to the three-dimensional grid that is formed by the tracer points. Such a scheme has been regarded as the optimal solution in models where the horizontal resolution is greater than the Rossby radius of the ocean and so the most efficient in depiction of the higher vertical modes [*Webb et al.*, 1998]. Different horizontal resolutions of 1°, 1/4°, 1/8° and 1/12° exist, while the vertical resolution has been increased from 36 to 66 levels [*Coward and De Cuevas*, 2005; *Webb and Cuevas*, 2007]. The 66 z-level structure is of varying thickness with 14 vertical levels dedicated to the upper 100 metres of the ocean. The variation of thickness is between 5 m for the top level to 208 m at the bottom. A scheme of partial bottom cells has also been introduced in order to achieve a realistic approximation of topography [*Pacanowski and Gnanadesikan*, 1998]. The version of the model with horizontal resolution of 1/12° is employed within this thesis. This corresponds to a constant latitudinal grid spacing of approximately 9.26 km and a longitudinal spacing varying from 7.6 km at 35°S to 2.4 km at 75°S and thus resolves mesoscale eddies with diameters at least two to three times the

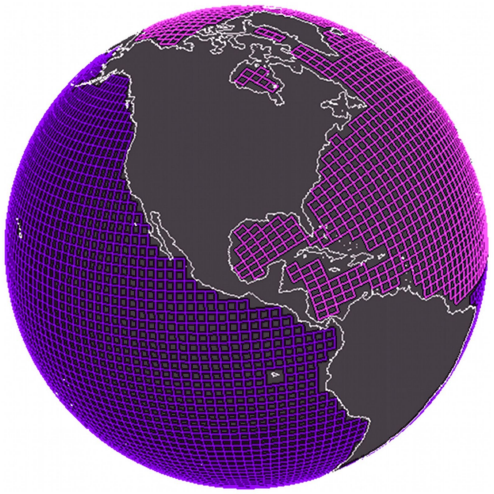

FIG. 2.1: Depiction of the OCCAM 1/12° model grid constituting of Model 1 (purple) covering the Pacific, Indian and South Atlantic Oceans and the rotated Model 2 (magenta) extending over the North Atlantic and Arctic Oceans (figure from *Stark and Marotzke* [2003]).

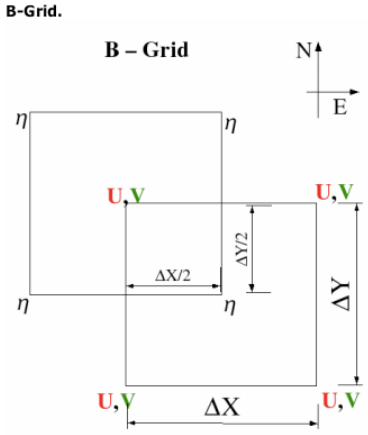

FIG. 2.2: Schematic representation of a B grid with the $\tilde{\mathbf{u}}(u, v)$ velocity grid points located 1/2 grid point offset from the tracer (η) grid points [Reproduced from OceanographersNet].

distance between grid points (for eddy scales in the Southern Ocean see *Chelton et al.* [2011]). The longitudinal resolution is calculated as a function of latitude as, *lonres = R*cos(latitude)*dxrad*, where R is the radius of the Earth ($\simeq$ 6370 km), *latitude* is in radians and *dxrad* is the horizontal resolution of the OCCAM 1/12° model in radians also, i.e. 1/12° * π/180.

Advection and diffusion Horizontal and vertical advection for both the tracer and velocity fields are determined by the MSQ (Modified Split-Quick) scheme after *Webb et al.* [1998] and *Webb and Cuevas* [2007]. OCCAM employs the non-local 'K

profile parameterization' (KPP) mixed layer of *Large et al.* [1994], while isopycnal mixing, implemented using the scheme of *Griffies et al.* [1998] in the version 1/4°, is no longer applicable. No explicit horizontal mixing is present in the 1/12° version. Velocity dependent biharmonic diffusion is implicitly induced into the advection scheme. A background vertical diffusion is explicitly defined with diffusivity of 0.5 $cm^2\ s^{-1}$, while harmonic eddy viscosity parameterization with coefficients $1cm^2\ s^{-1}$ and 50 $m^2\ s^{-1}$ is used in the vertical and horizontal direction respectively, [*Lee et al.*, 2007].

2.1.2 Surface forcing

Momentum forcing for the coupled sea ice-ocean model was introduced by the application of six-hourly 10 m height atmospheric fields provided by the National Centre for Environmental Predictions (NCEP). Surface fluxes were supplied from the National Centre for Atmospheric Research (NCAR) reanalysis, period 1985-2004. The implementation by *Large et al.* [1997] of coupled freshwater and heat fluxes through the utilization of an explicit evaporation/latent heat flux, led to the adjustment of the density flux in order to be consonant with more substantial surface boundary conditions [for related work on this topic see *Large and Nurser*, 2001]. A bulk formulae after *Large and Pond* [1982]; *Large et al.* [1997] was used for the calculation of downward sensible and latent heat. Evaporation is computed by dividing latent heat, Q_{lat}, by latent heat of vaporization, L_e. Surface specific humidity and sea surface temperature are from the model level 1 while air temperature, and atmospheric specific humidity from the six hourly 2 m height atmospheric fields from the same NCEP reanalysis [*Kalnay et al.*, 1996]. Sea level pressure (SLP) forcing was the combined result of the interpolated product of the NCEP reanalyses six-hour SLP in space and time at each model timestep and the model's level 1 pressure. The International Satellite Cloud Climatology Project (ISCCP) provided monthly averaged cloud fraction [*Rossow and Schiffer*, 1991], updated with climatological data for the period 1992-2004. ISCCP data with a constant albedo of 7% were also used to compute the short wave radiation. Monthly averaged incoming solar radiation for the period 1984-1991 was after *Bishop and Rossow* [1991] diurnal data, with gaps filled by the ISCCP climatology (for details see *Lee et al.* [2007]). Net long wave radiation is calculated after the bulk radiation formula of Berliand & Berliand, [*Coward and De Cuevas*, 2005]. The long wave radiation formulation for the sea ice follows *Marshunova* [1966], (for related work on this topic see *Aksenov* [2002]; *Aksenov et al.* [2007]). The two-band approximation of *Paulson and Simpson* [1977] was used to compute the pervasive solar radiation accompanied with a global consistent Jerlov Ib water type assumption. The model uses monthly precipitation after *Spencer* [1993] derived from the Microwave Sounding Unit (MSU) satellite data with the integration of observational data climatology for the later years [*Xie and Arkin*, 1996].

2.1.3 Topography and initialization of the model

The model topography (see figure 2.3) is the result of integration of three different bathymetries. The primary dataset consists of the bathymetric model (v*6.2*) of *Smith and Sandwell* [1997], spanning 72°N to 72°S with a spatial resolution of 2-minutes. North of 72.0°N the Smith & Sandwell ocean floor topography was conjoined with the International Bathymetric Chart of the Arctic Ocean (IBCAO) dataset by *Jakobsson et al.* [2000]. The U.S Digital Bathymetric Data Base 5-minute data (DBDB5) was used south of 72°S. In order to avoid conflict between the free surface model and variable bottom box [*Pacanowski and Gnanadesikan*, 1998], a minimum depth of two model levels was imposed [*Coward and De Cuevas*, 2005]. The model bathymetry was engineered so key straits and sills were open and at the correct depth [*Thompson*, 1995] but no further smoothing was applied. Straits between 8 and 16 km wide were opened up to two model cells while straits less than 8 km wide were closed.

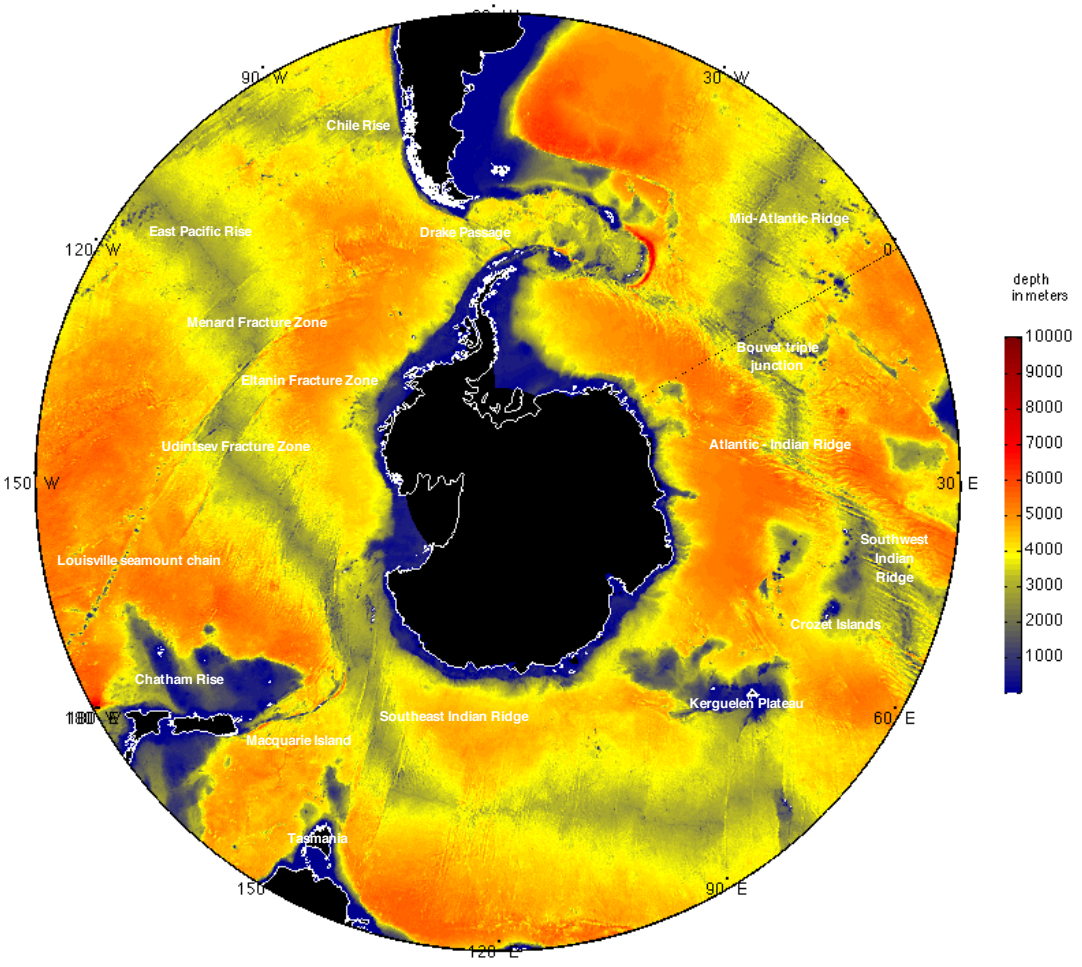

FIG. 2.3: OCCAM 1/12° model bathymetry illustrated in colour scale around the continent of Antarctica. [Coastline, depicted in white, from GEBCO].

For most of the world's oceans the World Ocean Circulation Experiment - Special Analysis Centre (WOCE SAC) climatology [*Gouretski*, 1996] was employed for the initial potential temperature and salinity fields. In the Arctic a merged product of *Steele et al.* [2001] consisting of the Arctic Ocean Atlas [Arctic Climatology Project(1997,1998)] and the World Ocean Atlas 1998 series data [*Antonov et al.*, 1998; *Boyer*, 1998] was used. Only the simulated surface salinity was relaxed to the monthly climatological values on a time scale equivalent to 30 days for the top 20 m induced from the discharge of surface flux and fresh water [*Webb et al.*, 1998; *Lee et al.*, 2007]. Data from the Ice and Snow Atlas after *Romanov* [1995] were utilised for the initialization of the sea-ice and snow cover in the model's Arctic regions. Values of 1.50 m and 0.15 m were applied respectively to sea-ice and snow south of 62.5°S in the vicinity of Antarctica and 0.10 m of sea-ice north of 79°N in the Arctic, with the cover in each affected grid cell to be 99%.

2.1.4 OCCAM 1/12° model data output

The OCCAM 1/12° model data output are employed for the initialization and evolution of the Lagrangian experiments developed as part of this thesis. The primary variables stored, after the integration of the model, for off-line implementation in the tracking code, are θ, S, u and v and *ssh*. Sea-ice extent is also part of the data examined. In this thesis, we make use of the model *run401* data output covering the period from 1988 to 2004-5 (i.e. model days 1095 to 7300) excluding the first three years of the initial spin-up. Time varying fields are the result of online averaged data at 5-day intervals while stationary[1] fields, as the 11- and 17-year velocity fields employed as part of the experimental context of this work, are computed off-line by estimating the statistical mean of the 5-day velocity fields over the whole aforementioned periods respectively. Velocity components on isobaric levels have been extracted for 4 out of the 66 levels defining the vertical resolution of the OCCAM 1/12° model [*Coward and De Cuevas*, 2005]. Model levels 2 and 38 with respective depths of 8 and 1252 m have been chosen for the reproduction of isobaric Lagrangian trajectories. Model level 2 files range from model day 1095 to 7300 while the final utilized model day is 5140, approximately calendar year 1996, for model level 38. Salinity and potential temperature are preserved at their entire vertical extent as they were used for the computation of the isoneutral surfaces. These are denoted in four classes of neutral density γ^n 27.9, 27.96, 28.06 and 28.16 covering the whole period from 1988 to 2004-5 apart from class 27.9 (this is the value of neutral density γ^n nominated for the Diapycnal and Isopycnal Mixing Experiment

[1] A field is defined as stationary, when its distribution is time independent and hence if the time variable t is shifted, its joint probability distribution remains invariable i.e. for definite $\tau \geq 0$ it holds that $\{\tilde{\mathbf{v}}(\tau + t, x); t \geq 0, x \in \mathbf{R^d}\}$ and $\{\tilde{\mathbf{v}}(t, x); t \geq 0, x \in \mathbf{R^d}\}$ have homogeneous distributions [*Carmona and Rozovskii*, 1999].

in the Southern Ocean (DIMES), see Appendix B) where only the period from 1991 to 1997 (model days 3275 to 5500) is represented.

2.2 Lagrangian particle tracking method

2.2.1 Introduction

A particle tracking algorithm is employed in order to investigate Lagrangian trajectories off-line[2]. The scheme has been modified from a previous version developed by *Thorpe et al.* [2002, 2004]. Adaptation of the model was focused on improving efficiency, calculation speed, large matrix manipulation and accommodating the technical data requirements to serve both the isobaric and isopycnal simulation release modes.

In order to determine the particle's trajectory inside each grid box the velocity vector components are required at the particle's position. The zonal and meridional components (u, v) are determined by a bilinear interpolation of the four surrounding grid points in the time-varying velocity field. The former of two sequential 5-day mean velocity files (see 2.1.4) added to the two 5-day fields' gradient, constitutes the time-varying velocity field for each 5-day simulation period. No slip is allowed at the boundaries. Stranded particles are no longer considered. Particles are neutrally buoyant. As a consequence, no vertical displacement is possible in an isobaric release and no neutral density surface relocation during an isopycnal one. Their character is passive so as to only react to the underlying ocean dynamics and not interact with or in any way modify them.

A timestep of 2880 s (48 min) has been chosen to define the temporal resolution of the scheme. The timestep conforms with the stability criterion of Courant-Friedrich-Lewy and performs adequately in the context of Southern Ocean's circulation as reproduced by OCCAM 1/12° model.

The algorithm is employed for the advection of Lagrangian particles with 5-day mean velocity fields, for the aforementioned periods, on various model levels and surfaces of constant neutral density γ^n. A mean velocity field covering the same period is also used.

Diffusion in the algorithm is not explicitly managed. Instead, in order to represent diffusion a random walk pattern is introduced with the mean velocity field and omitted when the time-varying velocity fields are employed.

2.2.2 Description of the particle tracking algorithm

The particle tracking algorithm used is adapted from *Thorpe et al.* [2004]. Both the horizontal advective and diffusive components of a two dimensional passive particle

[2]The advantage of an off-line calculation is the possibility to compute many more trajectories than it would be possible with a simultaneous processing with the OGCM integration.

movement are embodied in the scheme.

Advection The advection component is based on a two dimensional second-order two stage scheme employed in the numerical analysis of differential equations. This is an explicit second-order, $O(\Delta t^2)$, *Runge-Kutta* finite-difference method which is related to the forward *Euler* method, designated here by the general formula: $y_{n+1} = y_n + hf(t_n, y_n)$, where h is the step size and the additional implementation of the midpoint corrector method. A particle's position at step *n+1* is based on the initial estimation of the particle's location at a forward timestep of $\Delta t/2$ and the subsequent calculation of the position based on the interpolated velocity (see Appendix C) at particle's position at step *n+1/2* (2.8). In our case, denoting $\boldsymbol{s}_n$ the particle position instead of $\boldsymbol{y}_n$ and replacing $\boldsymbol{f}(t_n, y_n)$ by $\mathbf{u}_n$, denoting the velocity at the specified position $\boldsymbol{s}_n$, the two stage scheme employed can be described by:

$$\mathbf{s}_{n+1/2} = \mathbf{s}_n + \frac{\Delta t}{2}\mathbf{u}_n(\mathbf{s}_n) \tag{2.7}$$

$$\mathbf{s}_{n+1} = \mathbf{s}_n + \Delta t \mathbf{u}_{n+1/2}(\mathbf{s}_{n+1/2}) \tag{2.8}$$

The advective component $\mathbf{u}$ in all of the aforementioned derivations is obtained from the 5-day mean velocity fields of OCCAM 1/12° *run 401*. In each position $\boldsymbol{s}$, the velocity is bilinearly interpolated from the four surrounding grid points on the B grid, which provide the initial conditions for the deduction of the intermediate particle's positions. The computed velocity is defined as the sum of the gradient[3] between two sequential fields multiplied by the discretization resolution in the algorithm and added to the velocity field commencing the nominal 5-day period between the respective pair of files. In that way, the derived quantity is mapped with respect to the number of steps and the difference in velocity between two sequential files. The gradient is in essence analogous to the reciprocal of the number of steps defined in the algorithm. The number of steps commensurate with the timestep used, Δt (see equations (2.7) and (2.8)) and thus the timestep in effect introduces and controls the artificial horizontal resolution of the tracking scheme.

Diffusion The effect of diffusion is approximated with the introduction of a random walk pattern after *Evans and Noye* [1995]. It is defined as the addition of a horizontal random increment, which is characterized by an arbitrary orientation, to the advection term. Large scale eddy diffusivity is inferred to be of the same order as the deduced isotropic diffusion in the scheme employed by *Thorpe et al.* [2004]. A value of $D_h = 100$

[3]If $\boldsymbol{U}_1$ and $\boldsymbol{U}_2$ are two sequential velocity fields separated by 5 days, then the gradient would be, $grad\mathbf{U} = (\mathbf{U}_2 - \mathbf{U}_1)/nsteps$, where *nsteps* is the temporal discretization resolution, dependent on the *timestep* used and the period represented in each velocity field, *filestep*, which in our case is 5 days.

$m^2\ s^{-1}$ has been assigned as appropriate following *Olbers and Wenzel* [1989]. Employing a value of 100 $m^2\ s^{-1}$ for the horizontal diffusion might seem contrary to the formulation of the OCCAM 1/12° [*Coward and De Cuevas*, 2005]. *Thorpe* [2001] estimated that the alteration of the value of D_h in a range of percentages between 50% and 500% does not result to any significant alteration of the trajectories computed [*Thorpe et al.*, 2004].

Equation (2.8) describes a particle's position at discrete timesteps but with the absence of the effect of diffusion $\boldsymbol{W}_r$. In the case of a stationary velocity field where variability requires to be introduced, the effect of diffusion has to be included, and equation (2.8) becomes:

$$\mathbf{s}_{n+1} = \mathbf{s}_n + \Delta t \mathbf{v}_{n+1/2}(\mathbf{s}_{n+1/2}) + \mathbf{W}_r \tag{2.9}$$

The meridional and zonal components of the random walk are $W_{r_j} = d_{rw} cos\Theta$ and $W_{r_i} = d_{rw} sin\Theta$, respectively. The random walk distance is given by, $d_{rw} = \sqrt{12 D_h \Delta t R_n}$, while the direction Θ is defined as, $\Theta = 2\pi R_n$, where R_n is output from a uniformly random number generator in the range (0,1). This number generator is the *swb2712*, which is a modified Subtract-with-Borrow generator, similar to an additive lagged Fibonacci generator with lags 27 and 12, and with a period of approximately 2^{1492} [*Marsaglia and Zaman*, 1991].

2.2.3 Implications of the CFL stability criterion on the timestep

In order to ensure stability of the numerical integrations the information inherent in the context of the analytical solution has to be accessible to the scheme forming the numerical solution. Thus, in essence the domain of determination of the differential equation being a subset of the difference equation's domain[4]. By using an explicit scheme in the trajectory tracking algorithm, we are constrained to a necessary criterion that has to be met which in general does not suffice for the convergence of the numerical and analytic solutions but in our case proves adequate. The *Courant-Friedrich-Lewy* (CFL) stability criterion, after *Courant et al.* [1928], is employed to examine if the previous principle is violated; according to it the travel time for a perturbation (such as a wave) between two adjacent grid points should be greater than the timestep in the numerical scheme which simulates the passive conveyance of a particle due to that same perturbation. The advective *Courant number* ν, which is contingent on the finite difference method [for related work on this topic see *Courant et al.*, 1967; *Döös*, 2008], is defined by:

[4] *Definition:* Domain of dependence of an explicit finite difference scheme for a given mesh point is the set of mesh points that affect the value of the approximate solution at the given mesh point [*Heath*, 2002].

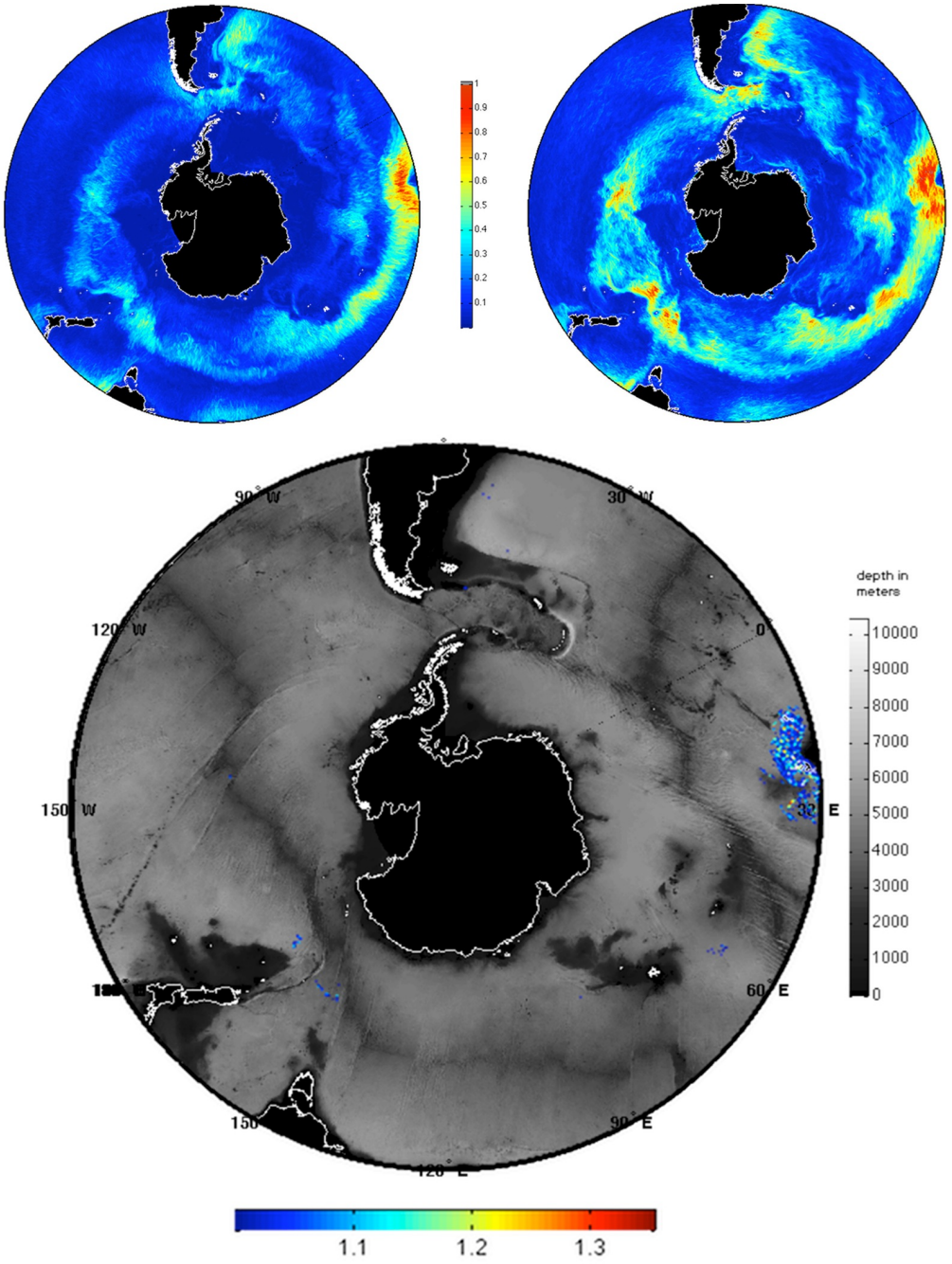

FIG. 2.4: The *Courant-Friedrich-Lewy* stability criterion for the three substantial conditions representing the velocity's components interrelation for OCCAM 1/12° model level 2. The upper left panel depicts the *Courant number* ν for the meridional velocity component. The upper right panel for the zonal velocity component. The bottom image illustrates the violation of the CFL criterion for the case of an omnidirectional velocity field, with the jet coloured pixels representing regions where the *Courant number* $\nu > 1$. The time scale of the illustration extends from model day 1095 to 7300. A timestep of 2880 seconds ($\simeq 0.033$ *day*) is used in the derivation of the CFL criterion. [Coastline, depicted in white, from GEBCO. Bathymetry from Smith & Sandwell (v6.2, 1997)].

$$\frac{|\mathbf{u}|\Delta t}{\Delta x} = \nu \tag{2.10}$$

where $\mathbf{u}$ is the velocity or the advection parameter, Δt the timestep and Δx the horizontal resolution or spatial interval in the direction of the velocity propagation. For advection in one dimensional flow the CFL condition is satisfied if $\nu \leq 1$.

For a two dimensional flow following *O'Brien* [1986] (see p.181) the approach here is rather heuristic. Owing to the fact that the grid resolution differs in the zonal and meridional directions, our selection of timestep is justified by depicting three cases delineating the relation of the latitudinal and longitudinal velocity vectors' magnitudes. The first two conditions conform with the mono-directional expression of the velocity vector. These are the cases of either exclusively zonal or meridional velocity. The third condition applies when both constituents of the velocity field, the zonal and meridional components, are taken into account. Examining the advection components at model level 2 (8 m depth), being the only isobaric surface layer in the extent of this study, we adhere to an increasing towards the surface[5] vertical distribution of velocity for both the isobaric and isopycnal layers selected here. The timestep used is 2880 seconds or $\simeq 0.033$ days. In the case of a prominent meridional flow by combining the maximum $\tilde{\mathbf{v}}$ velocities for the period covering model days 1095 to 7300, the *Courant number* ν (2.10) satisfies the stability criterion $\nu \leq 1$, (see figure 2.4 (upper left panel)). When the dominant flow is zonal, the CFL stability criterion is violated in minor regions of 1-2 grid cells in the vicinity of Agulhas Retroflection south of Africa at the northern boundary of the ACC as illustrated in figure 2.4 (upper right panel). In the condition where the velocity vector is omnidirectional, which in fact embraces the former two cases, we use a modified relationship after *O'Brien* [1986] in order to consider the fulfilment of the stability criterion. The *Courant number* is calculated for each model day, for the aforementioned period, based on:

$$|\mathbf{u}|\frac{\Delta t}{\Delta x} + |\mathbf{v}|\frac{\Delta t}{\Delta y} \leq 1, \tag{2.11}$$

and the regions where the CFL criterion is not met are depicted in figure 2.4 (bottom panel). The contravention of the CFL criterion does not compromise the simulation results, though. The regions that exhibit the CFL criterion violation extend beyond the area of interest with regard to the spatial distribution of the computed particle trajectories.

The residency of the CFL criterion violation events in time space terms weights their effect in introducing errors in the simulation of the trajectories. This is depicted by

[5] *Davis* [1991] in his review study refers to *Swallow and Worthington* [1961] depicting a velocity inversion associated with a counter current in the Gulf Stream.

the calculation of their frequency (temporal term) as also their maximum continuous occurrence in specific regions (spatial term). The left panel of figure 2.5 depicts the frequency of the CFL criterion violation for a simulation period of approximately 17 years. Frequency in the range of 0.01 to less than 0.03 $days^{-1}$ dominates the region of interest. Thus, the events exceeding the CFL criterion upper bound value (2.11) occur for about 12 to 33 days (by definition not necessarily consecutive) for the whole period of 17 years. The right panel of figure 2.5 illustrates the maximum continuous occurrence of violation episodes. The majority of the temporal maximum continuous occurrence is between 10 and 20 days (or 2 to 4 sequential 5-day average velocity fields) and their spatial distribution are consistent with the dominant frequency values on the left panel. It can be concluded that few, if any, CFL violation events occur in the region of interest during the simulation period. The equivalence between the frequency and maximum continuous incidents values suggest that the dominant frequency events exhibit a singular character as far as their replication during the period of the 17 years. This clearly depicts the ephemeral character of such events and provides confidence in the simulation results with regard to the CFL criterion for the timestep chosen.

The importance of this analysis lies in the potential of a particle trajectory alteration due to the misinterpretation of the advective discretization resolution (i.e. as introduced from the utilization of the specific particle tracking algorithm timestep parameter). In order to control the introduced error, any particle entering the specified region during the occurrence of a CFL violation episode is excluded from the analysis procedure in chapters 4, 5 and 6. The decision is based on the postulation that even small differences in initial particles' positions can lead to quite divergent trajectories. In the equivalent context of *Lagrangian chaos* [*Artale et al.*, 1997; *Aurell et al.*, 1997; *Lacorata et al.*, 2001] small displacements place the particles on neighbouring streamlines with the potential of different momentum provision. In a chaotic advection regime this could result in significantly disparate trajectories of initially adjacent ones [*LaCasce*, 2008]. Similarly, an inaccurate discretization resolution (as depicted by the CFL criterion violation) will result in an inconsistent future spatial distribution with regard to the underlying dynamics. Particles are conveyed faster than the information of the advection field. Their spatial-temporal distribution culminates in disagreement with the respective state phase of the velocity field.

The timestep of 2880 s that was employed in the particle trajectory tracking scheme in this thesis satisfies the CFL criterion. Longer timesteps, as for example 5760 s, were also evaluated. Performing the analysis presented above revealed violation of the CFL criterion in extensive areas spread out through our whole simulation geographical area and thus were rejected. In the following section, in order to further justify our selection of timestep, a comparison of 2 more timesteps based on computation efficiency and

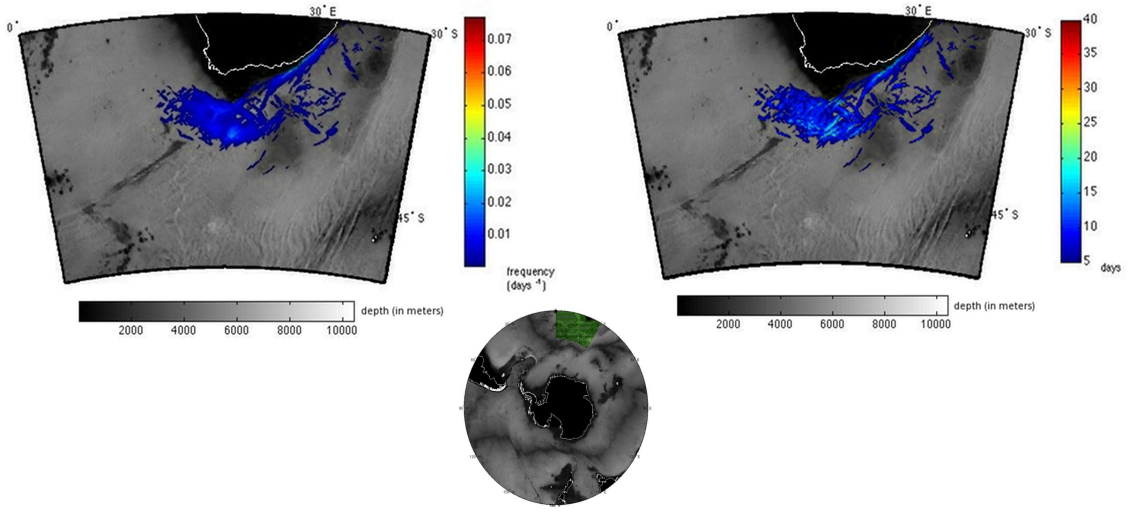

FIG. 2.5: The frequency of the *CFL* criterion violation is depicted in the left panel for the green outlined region as seen on the image. The dominant colour of dark blue is representing a frequency of approximately 5 days per the simulation period. The right panel illustrates the maximum continuous occurrence of the *CFL* criterion violation events (in days). Stationarity in space and continuity in time of the events obviously do not constitute a restricting issue of the timestep used in the simulation of the particles' trajectories. The minimum value of 5 days represents actually one event for the whole period of study. Recall that the velocity fields employed in the context of this thesis were 5 day means.

representation of the underlying dynamics of the advection field is presented.

2.2.4 Comparison of timesteps, Δt

Computational efficiency, both in terms of calculation speed and data output volume, is dependent upon the size of the timestep used. This leads to the question: What is the biggest timestep that can be used to sufficiently adhere to the underlying dynamics? This is addressed in two distinct contexts. Apart from the provisos imposed by the stability criterion, as described in detail in 2.2.3, a timestep regulates the fidelity of the approximation to the circulation, the expression of the underlying dynamical system. The flow structure, conveyed as the velocity field, controls the passive movement of the particles. A particle's displacement at a specific position is the result of the computed velocity (see paragraph 2.2.2 p.27 for definition) at that same position. The temporal discretization resolution[3] regulates the incremental amount of momentum added to the particle at each simulation step. It becomes clear that even with the same velocity field and the exact initial spatial coordinates for the starting position, the trajectories of two particles employing two different timesteps, will exhibit differences. This is fully consistent with the inherent spatial and temporal variability in dynamical flows [*Düing*, 1978;

Wunsch and Ferrari, 2004; *Wiggins*, 2005]. Since a trajectory is defined as the illustration of a particle's sequential displacement positions, it essentially maps the evolution of the computed velocity field. The remaining concern is that the spatial variability the dispersion of two simulated trajectories exhibit (i.e. in the case of examining individual particle trajectories simulated with two different timesteps from the same initial position) could be examined from the perspective of a particle's velocity or the distance covered by a particle.

2.2.4.1 Distance as a measure of similarity

In order to define a valid comparison criterion in the justification process of timestep selection the following approach is adopted. Three possible timesteps of 1440, 2880 and 8640 s, are considered here. It is noted that the CFL stability criterion in the area of investigation is a prerequisite for the compared timesteps[6]. Differences of incremental particle distance covered, dispersion of individual particles and comparison of their separation times for the three timesteps in question are calculated. A scheme of 200 linearly aligned particles was released on the isobaric level 38 (1252 m depth) of the OCCAM $1/12^{\circ}$ model, as seen in figure 2.6. The period under examination spans model days 1095 to 2485, approximately 4 years of simulation.

The incremental distance difference approach is based upon the idea of contrasting the velocity of a particle released under two different timesteps. Each timestep, as mentioned already, constitutes a direct analogue of the temporal step resolution in the simulation scheme. The analysis is necessarily performed on a comparable time scale. The estimate is executed on sequential steps on the temporal resolution of the largest timestep in the procedure; i.e. when comparing the distance covered for example by particle with ID 58 using the timesteps 1440 and 2880, the comparison time scale is 2880 s. In figure 2.7, comparison of individual particle trajectories between the three timesteps mentioned above can be seen. All releases initiate at model day 1095. The images depict the residual incremental distance difference for each particle between the 1440 and 2880 and the 2880 and 8640 timesteps, respectively. Negative values suggest a longer distance covered for a particle released with the largest timestep. The colour range distribution in the top image suggests a higher degree of similarity between the two releases for the majority of the particles. Nevertheless, in both juxtaposed pairs in figure 2.7, the differences events' pattern i.e. the temporal distribution of detected and prominent residual values with respect to associated particles, presents a topological similarity in the two diagrams. This suggests, that the fundamental structure of the

[6]Timestep 8640 s does not satisfy the CFL criterion in most of the high energetic regions at model level 2 (8 m depth) and in many at model level 38 (1252 m depth). It is used here as a mean for inferring trajectory sensitivity among the compared timestep pairs and because it was chosen in previous studies (see *Thorpe et al.* [2004]).

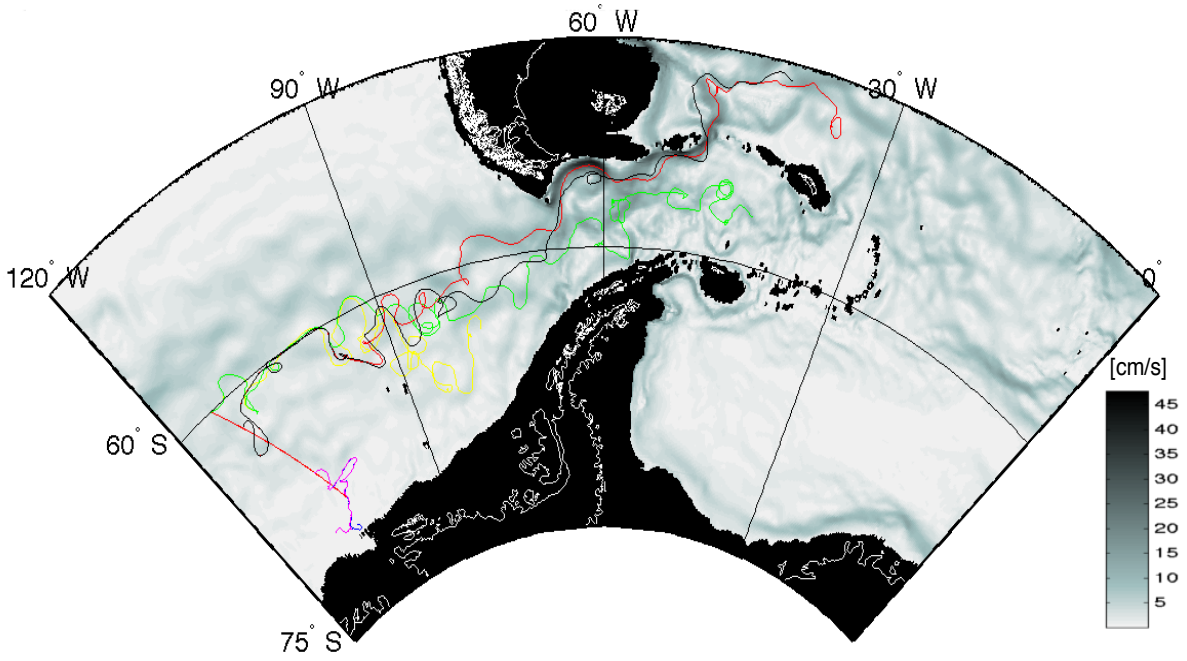

FIG. 2.6: Trajectories of selected particles illustrate the comparison of timesteps 1440 and 2880 s. Particles with ID 2 (yellow:1440, green:2880), 45 (red:1440, black:2880) and 150 (blue:1440, magenta:2880) are shown. Mean velocity field for the period 1095-5140 model days for level 38 in OCCAM 1/12°].

velocity field responsible for the advection of the particles is depicted at adjacent times by all timesteps in the comparison process. The characterisation "adjacent times" is conferred as the direct result of the temporal approximation detail to the source of trajectory variability i.e. the velocity field, which is common in all releases, as previously discussed.

A similar pattern appears in figure 2.8, where differences in dispersion distances among individual particles released under different timesteps are illustrated. Difference values are higher for the pair 2880-8640 with more particles favouring this discrepancy as can be seen by contrasting the upper and lower panel. Separation of particles, in general, occurs later for the timestep pair 1440-2880 than that of 2880-8640, denoted by the transition of dark blue to lighter colours. Most particle trajectories diverge after a time lag of 200 to 300 days. The initialization of the trajectory divergence exhibited is not uniformly distributed. Particles 2 and 3 for example, initially on the northern part of the linear alignment in figure 2.6, exhibit higher differences among the smaller timesteps but after 2 1/2 years of travelling (see also Fig. 2.6, particle ID 2, yellow:1440, green:2880). As in figure 2.7, minimum difference values for almost the whole examination period are depicted for particles with IDs >147. These particles are initially positioned in the southward quarter of the particle release scheme (Fig. 2.6), south of the main core of the ACC. This coincides with the noted quiescent region below 65°S and well westward

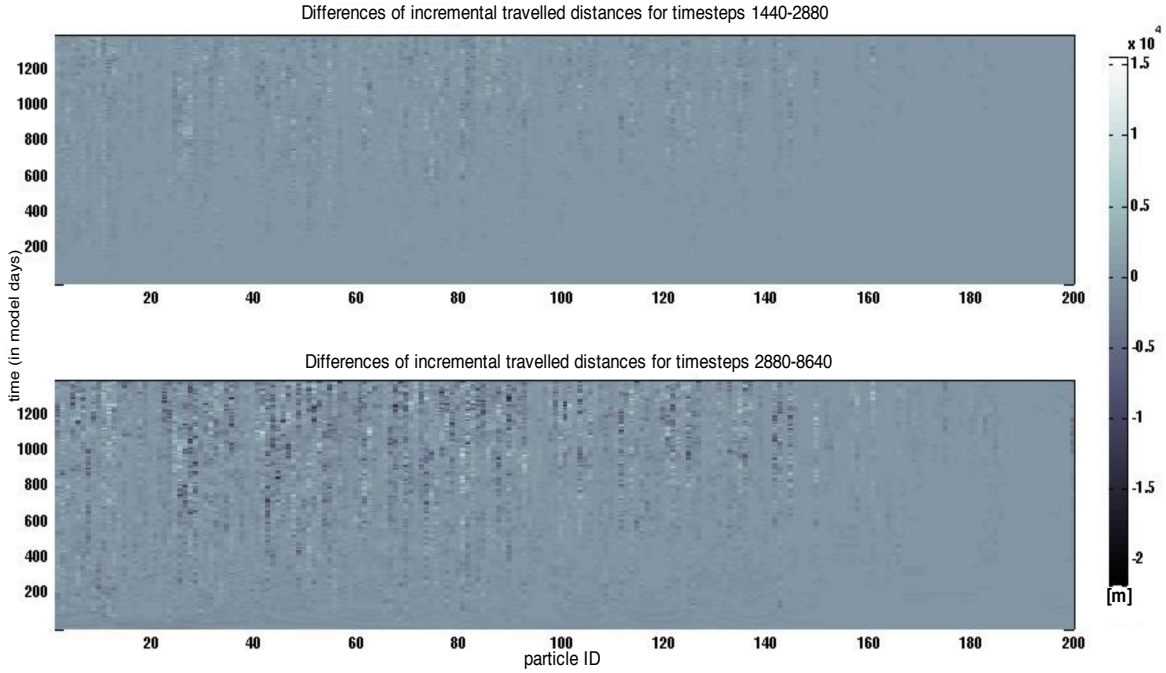

FIG. 2.7: Differences of incremental distance covered by individual particles between releases under different timesteps. The upper panel illustrates comparison of timesteps 1440 and 2880 s. The lower one depicts differences between releases with timesteps 2880 and 8640 s. The comparison period extends from model days 1095 to 2485. The vertical axis denotes the particle travel time in days while the horizontal axis denotes the particles' ID increasing in the north - south direction, as seen in figure 2.6. Distance is in metres.

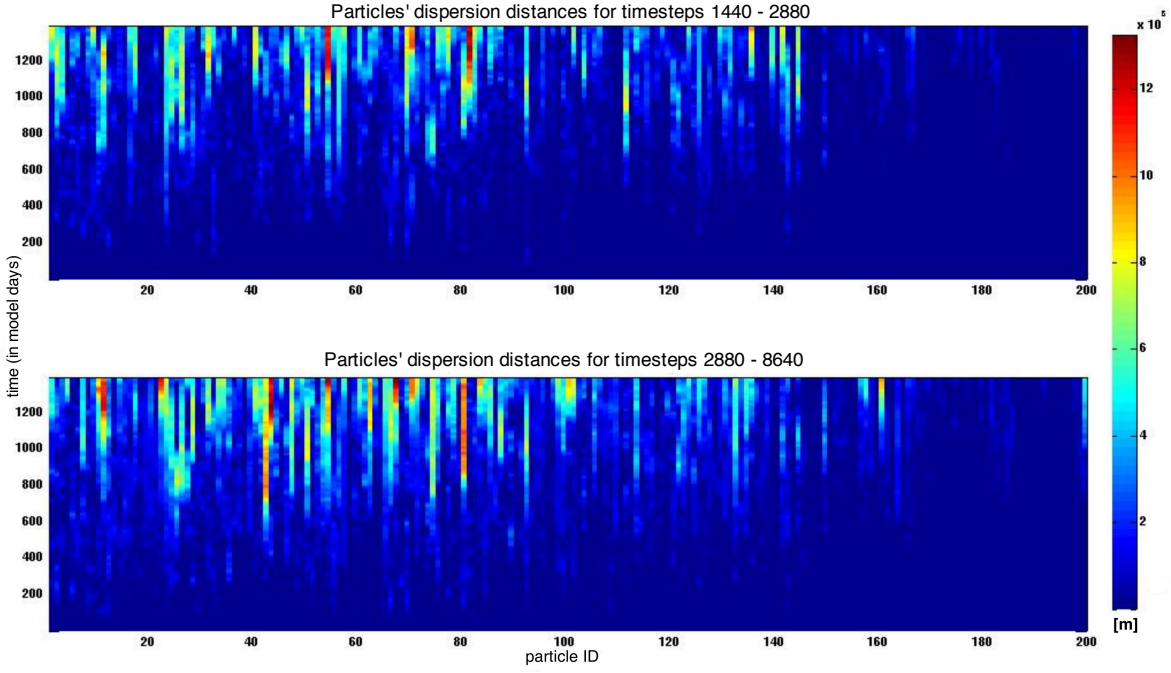

FIG. 2.8: Dispersion distance of individual particles between releases under timesteps 1440, 2880 and 8640 s. The upper panel illustrates comparison of timesteps 1440 and 2880 s. The lower panel depicts differences between releases with timesteps 2880 and 8640 s. The comparison period extends from model days 1095 to 2485. Axis as in figure 2.7.

of the energetic environment of Drake Passage. A relatively 'dormant' area exhibiting small velocity gradients from both a temporal and spatial perspective, is expected to impart minimum variability to the temporal discretization resolution. A higher degree of trajectory homogeneity among the two timesteps is exhibited. At the same time, ∼12% of the particles (ID > 170) do not record separation distances larger than 157 km for the whole period examined. Particle separation distances greater than ∼ 65 km are recorded in a similar pattern. The dispersion difference recorded is not monotonic though. For specific particles, trajectories appear to converge after a period of separation (Fig. 2.6 (particle ID 45, red:1440, black:2880). Bifurcation occurs at 85°W 62°S and trajectories merge again at 65°W 58°S in the area of Drake Passage.

Extrema in individual particles' comparison dispersion distances, especially after 2 years of travelling time, suggests a particle's transverse history through regions of substantially different energetic character for the two timesteps. It is expected small displacements in space to grow in time [*Lorenz*, 1963], where the displacement reinstates a significant imbalance in the available energy to a particle. In figure 2.9, growth of averaged particle distances is plotted against time. Distance D is calculated at specific time intervals among positions $\vec{X}$ of a particle released under two timesteps, 1440 and 2880 s. The mean d_t is taken for all particles n at every time interval t and plotted with respect to travel time

$$\mathbf{d}_t = \frac{1}{n}\sum_{i=1}^{n} D(X_{1440it} - X_{2880it})$$

Particle trajectories appear coherent for a specific period of time. In figure 2.10, the empirical cumulative density function for the displacement of particles' positions between releases with timesteps 1440 and 2880 s can be seen. Density distribution of the displacements is examined in five transient times. After 100 days of travel almost 92% of the particles display consistent trajectories under the compared releases. The median is 490.45 metres and the mean $\simeq$ 6.7 km. The median remains below the 1 grid point latitudinal resolution of 9.24 km for more than a year of particle motion. Almost 60% of the particles exhibit minor displacements after 500 days with a median of ∼11 km. After 2 years, 50% of the sample is below the value of 73 km increasing to 354 km when travel time extends to approximately 3 years. That indicates that we should not expect the replication of trajectories, under the various timesteps examined, to hold for periods long enough or in regions where the velocity field is characterized spatially as highly variable. Additionally, the demonstrated variability of the simulated dynamic system is of lower resolution than the temporal one introduced by the respective timestep during the simulation scheme of the Lagrangian particles. This leads to minimum differences as mentioned (see Fig. 2.6 particle ID 150, blue:1440, magenta:2880).

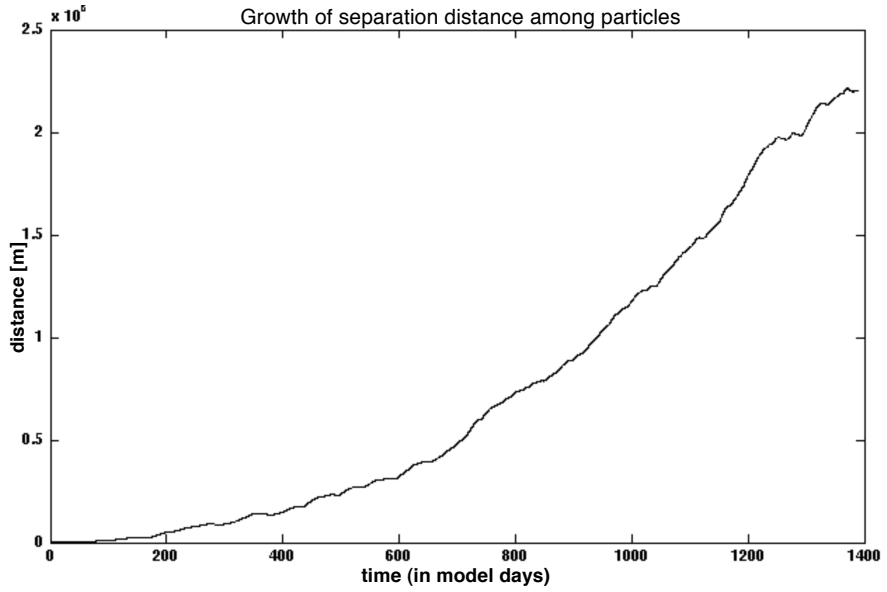

FIG. 2.9: Averaged distance, derived from individual particles released under timesteps 1440 and 2880 s, with respect to travel time t. The simulation period extends from model days 1095 to 2485.

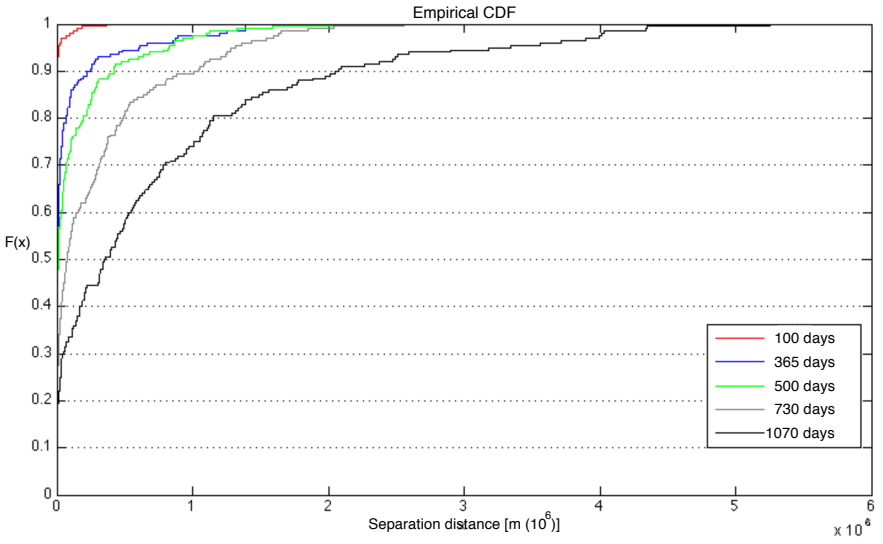

FIG. 2.10: Empirical cumulative density function for five travel times of particles' displacements (in metres). See text for description. Timesteps under comparison are 1440 and 2880 s. The simulation period extends from model days 1095 to 2485.

Concluding remarks Based on the differences exhibited in the simulated particle trajectories when utilising different timesteps, evidence for the most appropriate choice is summarised in the following. A higher degree of similarity has been justified for timesteps 1440 and 2880 s than that of 2880 and 8640 s, both from a transit particle velocity and separation distance perspective.

Displacements among trajectories of individual particle simulations under two timesteps show an exponential growth with time. This result is consistent with the nonperiodic flow of *Lorenz* [1963] in the context of chaotic dynamical systems and geophysical flows in general.

Particle population similarity for different travel times is depicted by the empirical cumulative density function in figure 2.10. For a minimum of 365 days of particles' transient time almost 80% reproduce the velocity field indistinguishably for timesteps 1440 and 2880 s. Is it wise to expect the extension of homogeneity of trajectories in longer time scales when using different temporal resolutions? If we consider the behaviour of a chaotic dynamical system then the answer is no. As mentioned above, in a chaotic dynamical system we expect small differences to grow with time. In our comparison experiment a time scale of 365 days for exhibited minima in displacements is considered satisfactory.

Two practical reasons control whether a timestep shorter than 1440 s should be employed or 1440 s itself. First, computational efficiency. Since the 2880 s timestep does not violate the CFL criterion there seems no valid reason to increase the temporal discretization resolution of the tracking algorithm. Already, any demonstrated variability at temporal scales shorter than 5 days is deduced from the oversampling of the 5-day mean velocity fields. It was mentioned earlier that the simulated dynamical system is of lower resolution than the temporal one introduced through the respective timestep during the simulation scheme of the Lagrangian trajectories. The second reason has to do with the nature of geophysical flows as explained in the previous paragraph. What would make sense though, is to compare the performance of the different candidate timesteps when simulating actual floats (i.e. ARGO or ALACE). Still, from the perspective of a chaotic dynamical system various uncertainties arise.

In agreement with the dynamic context of a time varying modelled velocity field, the choice to not compare the performance of the selected timestep when simulating deployed floats or drifters, with their actual trajectories, was made. Even though comparison with float trajectories is possible and theoretically may help guide the choice of timestep, however, this is impractical for two reasons: (1) most floats (i.e. the type of ARGO (float with highest census in the Southern Ocean), ALACE) follow an operational procedure where they detach from their chosen deployment level periodically, in order to surface and report data. As noted by *Gille and Romero* [2003], displacement of ALACE floats

by surface intensified currents and wind drag, during the transmitting phase, results in a probable failure to 'rejoin the same streamline or water mass on consecutive dives'. And (2) small differences in starting conditions and forcings will lead to divergent trajectories anyway. Initial conditions at the exact time of the real ocean state are also impossible to be reproduced to perfectly match. And even if possible, no model aims to fit to a perfect, faultless, set of assimilated data since it would compromise its validity in the representation of a dynamically consistent future modelled ocean state. Two possibilities remain: first, search for resembling dynamical conditions i.e. geopotential anomaly and velocity vector; second, by performing monthly or even quasi-monthly releases in order to capture variability and compare trajectories ensembles with a real float's path. In both cases, no exact replication of trajectories is expected since initial and transient conditions differ.

2.3 Simulation *modus operandi*

In the context of this thesis, simulations of passive particle Lagrangian trajectories with the implementation of the described tracking algorithm, under two distinct experimental regimes, employing namely an ***isobaric*** and an ***isopycnal*** method respectively are performed. An ***isobaric*** approach infers the offline use of the integrated tracers and velocity at levels of constant pressure. OCCAM's model output data are stored on isobaric levels so no further manipulation or interpolation is required for the data and the algorithm. An ***isopycnal*** method, requires the estimation of the topology (or geometry) of an isoneutral surface (or vertical distribution of isoneutral density adaptive grid points). Even though an isopycnal model is a better choice for the representation of the deep basin dynamics, at the time of this thesis OCCAM 1/12° was the only available solution with the highest-resolution, eddy-resolving and model run over a lengthy period (though not lengthy enough for interannual variability examination) in the Southern Ocean. Further details on the computation of the isopycnal surfaces and the implementation of the tracking algorithm for this scheme are presented next.

2.3.1 Implementation of the code in an isobaric and isopycnal scheme

The isobaric method In the isobaric method no modification is required of the input data. As a corollary, the algorithm employed here considers only 2-dimensional (2D) velocity fields and it is adequate to use the grid point values of the OCCAM 1/12° model output without any transformation. Tracer fields in certain parts of the analysis to follow have been translated to the velocity grid by bilinear interpolation. Recall that OCCAM 1/12° model uses a B-grid (Fig. 2.2) where the velocity grid points are offset in the zonal and meridional directions by half grid point respectively, that is 1/24° in

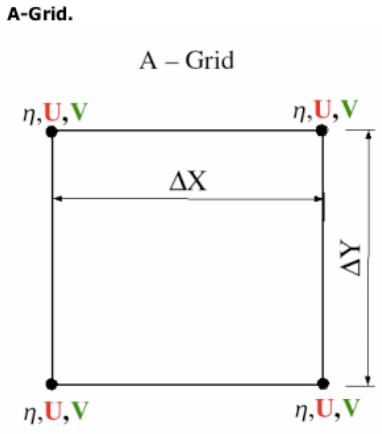

FIG. 2.11: Schematic representation of an A grid with the $\tilde{\mathbf{u}}(u, v)$ velocity and the tracer (η) are defined on the same grid points [Reproduced from OceanographersNet].

terms of the model's horizontal resolution. The translation results in an A-grid (Fig. 2.11) in an arrangement where both the tracer and the velocity are allocated the same grid points.

Optimization of the code for parallel computing, in order to increase the number of particles available for release and achieve efficient simulation in an adequate time scale, was undertaken.

The isopycnal method In the isopycnal method, calculation of the geometry of specified neutral density surfaces is required. This requires the interpolation of the 3D tracer field on to a 2D surface. In detail, the adopted approach is deconstructed in defining the depth of the neutral density surface and then interpolating in the vertical direction to deduce the velocity at that depth. The end product of this procedure is a horizontal velocity field mapped on an isoneutral surface. As such, the particles are simulated on a surface that is advected up and down by the vertical velocity. That means that the isopycnal method utilised here does not allow for any parameterization of diapycnal mixing and thus particles released on an isoneutral density surface do not migrate to adjacent density stable surfaces. However, in our adiabatic approximation the tracking of particles in specific regions ends when the surface itself ceases to exist in those areas due to formation or upwelling of denser water. The velocity mapping described reduces the cost of performing a 3D simulation of Lagrangian trajectories. The projection of a volumetric geometry, as is an isopycnal layer, on a hypothetical horizontal surface defined by the interpolated velocity vector redefines the 3D problem as a 2D one. This allows us to adapt the tracking algorithm described for the isobaric method without further adjustments in the fundamental core of the code.

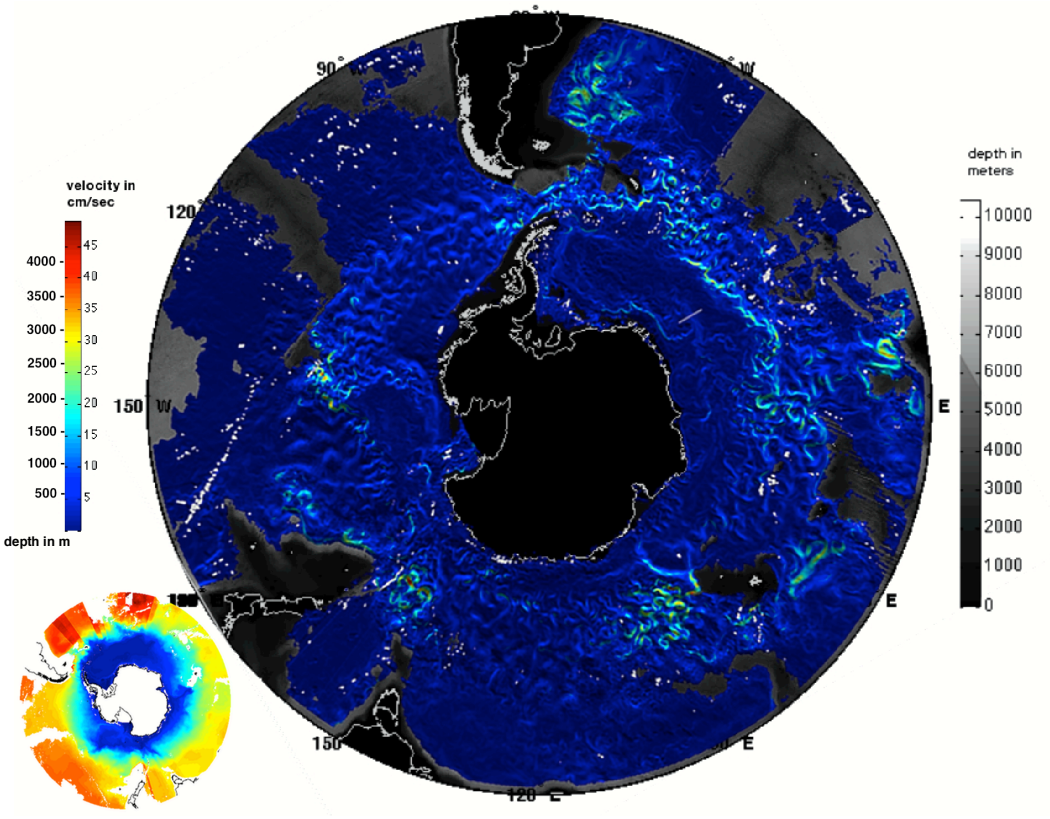

FIG. 2.12: Computed velocity on isoneutral density surface γ^n=28.06. The figure illustrates velocity (cm s^{-1}) for model day 3275 of OCCAM 1/12 ° GCM. Also seen, is average depth of the isoneutral surface for the whole model run of 17 years. Based on the exhibited spatial depth variability a comparison with an isobaric level would not be valid.

2.3.1.1 Computation of the velocity field on the isopycnal surfaces

The computation of a velocity field on an isopycnal surface necessitates the estimation of the designated 3D geometry in Euclidean space. Definition of the neutral density γ^n of a water parcel at a specific geographical location entails the use of salinity S, *in-situ* temperature T and pressure p at the same geographical coordinates [*Jackett and McDougall*, 1997]. The corresponding output data in OCCAM model are practical salinity S, potential temperature θ with respect to the ocean surface in $^{\circ}C$ and pressure p in *dbar*. Tracer values are mapped to the velocity grid by bilinear interpolation (i.e. values are re-distributed from a B-grid to an A-grid stencil formulation, see figures 2.2 and 2.11). In order to derive *in-situ* T from potential θ temperature we employ the Seawater Equations (v*3.2*) by the Commonwealth Scientific and Industrial Research Organisation (CSIRO) Marine and Atmospheric Research. Temperature is referenced in the International Temperature Scale 1990 (ITS-90). Derivation of the neutral density γ^n is performed as a function of $\{S, T, p, longitude, latitude\}$, at an arbitrary grid point

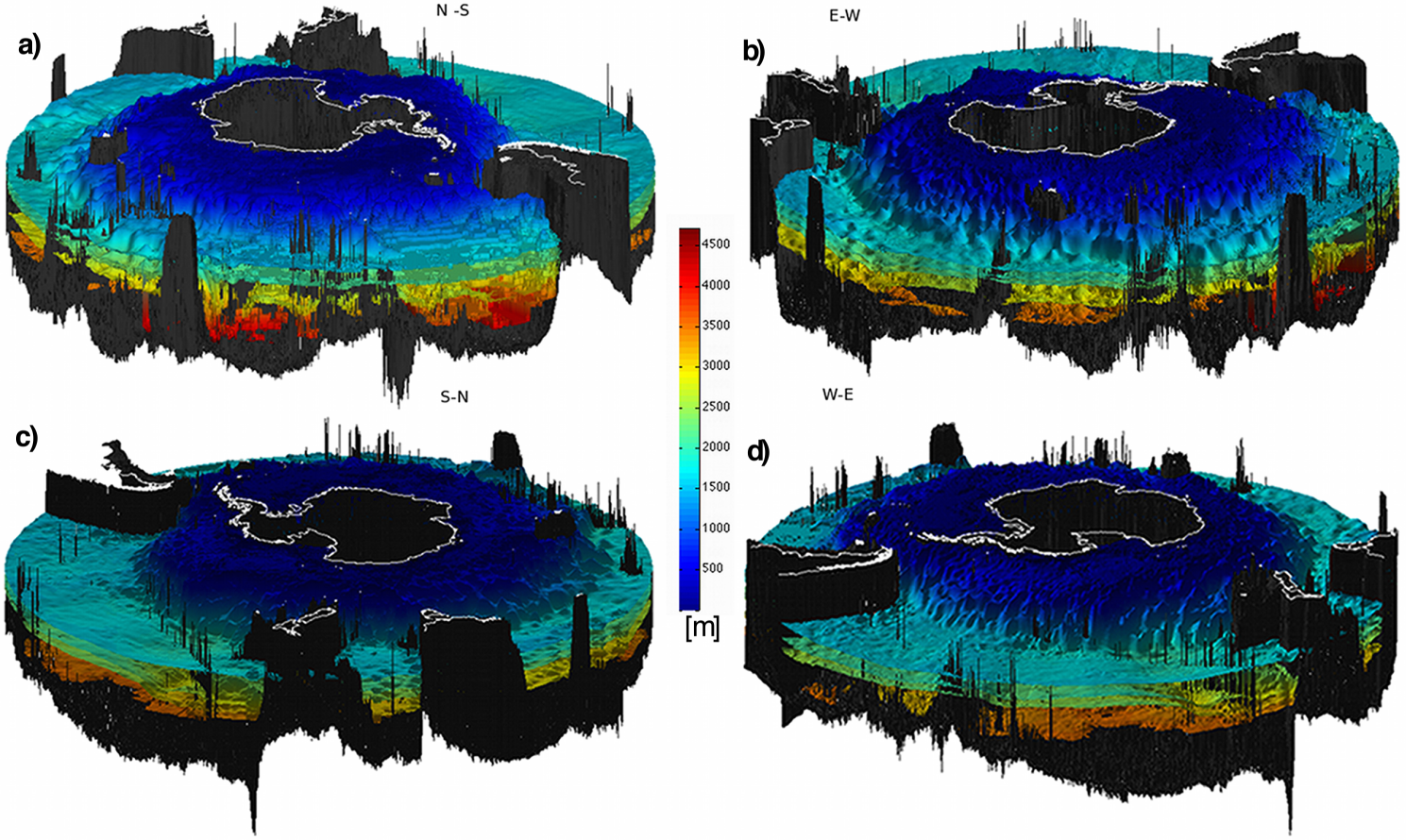

FIG. 2.13: Illustration of the geometry of all isoneutral density surfaces. The model day is 3315[a] of OCCAM 1/12 ° GCM. The panels a) - d) depict different orientations N-S, E-W, S-N and W-E respectively. In the context of the simulation experiments in this thesis, computation of velocity was limited to five different isopycnal surfaces, namely γ^n = 27.76, 27.9, 27.96, 28.06 and 28.16, which are illustrated here as layers in the 3D representations from lighter (top) to denser (bottom) (see Chapter 4 for details on selection). The selection was considered the optimum for investigating the dynamics of the ACC, partly because of the existence, of concordant in nature, of oceanographic experiments and hydrographic data (i.e. DIMES etc). The circumpolar variation of the isoneutral density surfaces' geometry is depicted in four, meridional and zonal, directions. Colour scale denotes depth in m of neutral density surfaces.

[a]Integration model day 3315 was considered the 'dynamic equivalent' (similar synoptic dynamic conditions) with the DIMES experiment tracer release day

in OCCAM model with the geographical coordinates ($longitude, latitude$), with the implementation of the neutral density surfaces software contributed by Dr David Jackett and Dr Trevor McDougall (CSIRO Division of Oceanography). The neutral density code employs the 1980 Equation Of State of water (EOS80), with salinity referenced in the 1978 Practical Salinity Scale (IPSS-78) and temperature in the 1968 International Temperature Scale (IPTS-68). A NetCDF library is utilized as a reference prelabeled global dataset of γ^n, being contingent on the spatial distribution of salinity and temperature from climatological datasets [*Jackett and McDougall*, 1997]. The computation routine used demands the calculation of neutral density on hydrographic casts on latitudinal slices. Estimation of the depth of specified neutral density values, and respectively of the isopycnal surfaces' vertical locations, is performed by linear interpolation. The horizontal velocity is then obtained at the same vertical location by linearly interpolating velocity from neighbouring grid points in the vertical direction. The result of the procedure is the projection of 2D interpolated velocity fields mapped on a 3D neutral density γ^n surface (Fig. 2.12 and 2.13).

2.3.2 Selection criteria of isoneutral surfaces

The isoneutral surfaces selection was based on the geometric characteristics of neutral density γ^n profiles in selected sections of the ACC around Antarctica, taking into consideration the *Gouretski and Koltermann* [2004] climatology (see figures 2 - 3, Appendix A for selected meridional sections). The main selection criteria allowing examination of eddy dynamics were slope and vertical extent.

The lighter isopycnal is computed so as to not be intruded upon by the highest bathymetric features. The second neutral density value is being chosen for its middepth range (Figs. 2 - 3, Appendix A). A third one endeavours to unveil the direct effect of topography in particles' trajectory alteration. The denser isoneutral surface is, from this study's perspective, the most coherent representation of the deepest possible isosurface engulfing the ACC's meridional extent. The isoneutral surfaces have γ^n equal to 27.76, 27.96, 28.06 and 28.16, respectively. A fifth isopycnal surface of neutral density $\gamma^n = 27.9$ was selected for the DIMES experiment analysed in chapter 5.

Accordingly, the behaviour of particles where isopycnals outcrop is also of interest. Does a particle experience a translation of its kinetic energy by an equal amount to GPE? Calculation of the Brunt -Väisälä frequency and interpolation of it on the isoneutral for the whole period of study indicates a statistically stable stratification. In the AAIW formation region, as depicted in figure 2.14 with a red arrow, the isoneutral 27.76 is absent. Tracking of any particle entering or already into the region stops since particles are not allowed to migrate to different isoneutrals.

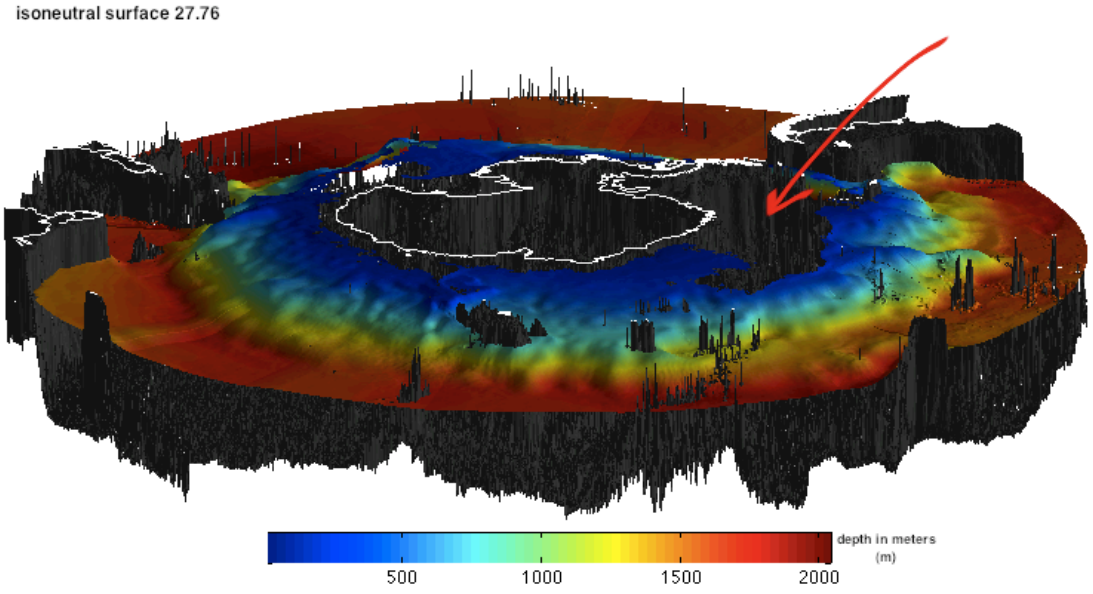

FIG. 2.14: Graphical 3D representation of isoneutral surface with density $\gamma^n = 27.76$. Spatial distribution of neutral density surface is averaged for a period of 17 years covering model days 1095 to 7300. Red arrow indicates a region of neutral density $\gamma^n = 27.76$ surface absence. It designates an area of deep water formation, as the AABW and CDW modes are, for the aforementioned period in the region of Weddell Sea. Vertical coordinate has been exaggerated for both the bathymetry and the isoneutral surface for illustration purposes. Colorbar denotes depth in metres.

2.3.3 Rate of isoneutral surfaces' vertical displacement

By definition, an isoneutral density surface is also an isentropic one for small displacements of particles when considering an incompressible fluid flow [*McDougall*, 1987]. As a consequence diapycnal mixing and diffusion have no impact on a particle's density and on its computed timestep scaled displacement. In the generalised context of the ACC's circumpolar energy balance though, eddy vertical fluxes do have the potential of influencing the vertical coordinate and spatial geometry of an isoneutral surface. Thus, a particle trajectory on a longer time scale is prone to alteration since the mapping of the horizontal velocity is performed on a different vertical level.

What is of interest then is the rate of the vertical displacement or w component of velocity. In figures 2.16 - 2.17, spatial distribution of maxima and minima in the vertical velocity component is illustrated. Only the lighter and denser isoneutral surfaces selected in this study, γ^n equal to 27.76 and 28.16, respectively, are presented. Comparing figures 2.16 and 2.17, it is evident that the magnitude of w resides in the same range between the two isoneutral surfaces. Examination of the downward and upward components' values exposes a balance in magnitude between the two, on the denser surface. Upward velocity appears significantly augmented with respect to values of downward displacement rates on the isoneutral surface 27.76. In figure 2.18, mean

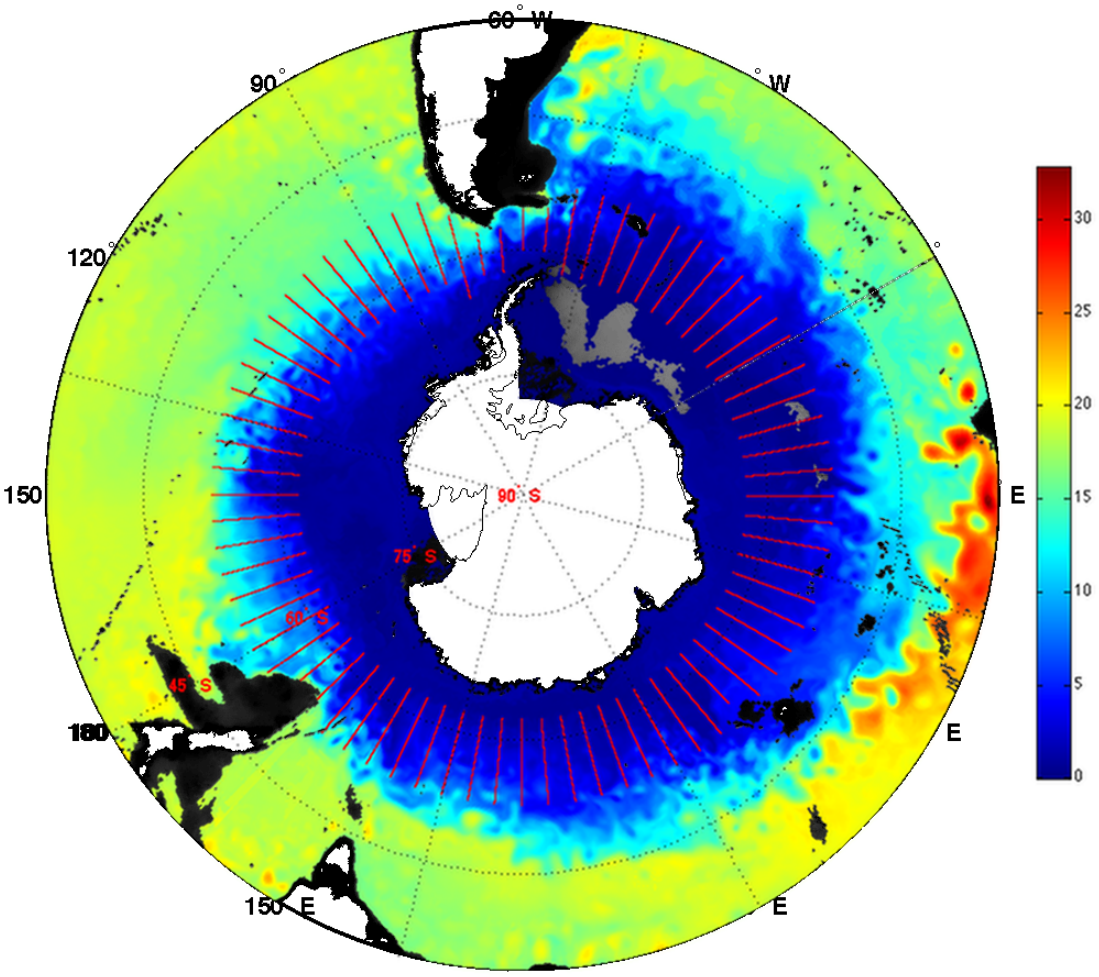

FIG. 2.15: Graphical representation of the passive particle linear alignment release scheme on neutral density $\gamma^n = 27.76$ superimposed on geopotential anomaly ($m^2\ s^{-2}$) at the day of release (model day 1095). Geopotential anomaly is computed on isoneutral surface 27.76 with respect to the surface. Longitudinal spacing among different release locations is 5 degrees. In the meridional direction latitudinal range is controlled by the geometry of the neutral density surface at the time of release but in general extend from 52.5° to 62.5°S . Its latitudinal spatial distribution, in certain locations, is confined by the outcropping bathymetry and/or excluding homogeneous density regions as regions of AABW formation (delineated by a grey patch in the Weddell Sea area).

absolute velocity for all isoneutral surfaces in the SOL experiment is illustrated. Could a relationship be established connecting downward velocity with the restoring mechanism of isopycnals tilting and the opposite procedure of upward displacement direction with introduction of baroclinic instability in the system? The velocity spatial distribution in figure 2.18 corresponds with the high EKE distribution in the ACC and thus clearly can be associated with the baroclinic instabilities generating the eddy regimes over and downstream of large scale bottom topography (Fig. 2.3).

Adopting as frame of reference a universally stable stratified ocean where unstable

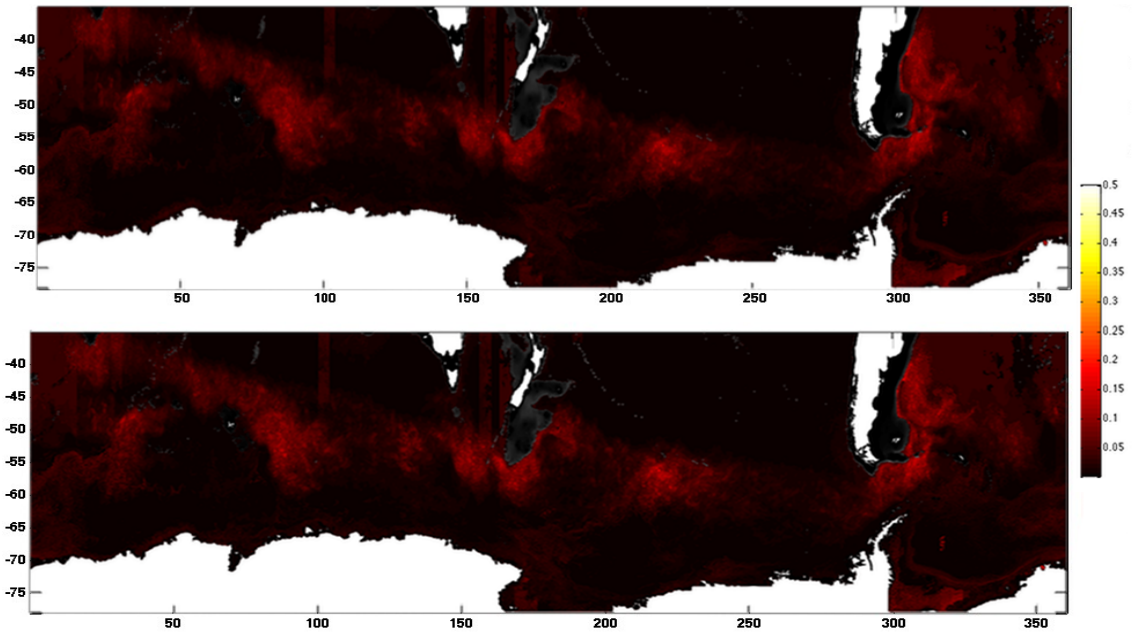

FIG. 2.16: Maxima of vertical velocity component w in (cm s^{-1}) for model days period 1095 to 7300 on isoneutral surface γ^n=27.76. Upper panel: Downward vertical velocity component. Lower panel: upward vertical velocity component. The ACC approximate path and the resemblance with EKE spatial distribution can be seen in figure 2.23. White areas depict land while grey shaded regions the underlying bathymetry. The meridional linear bands of homogeneous colour seen in several regions are due to spatio-temporal grouping of maxima misrepresenting variability and should not taken into account.

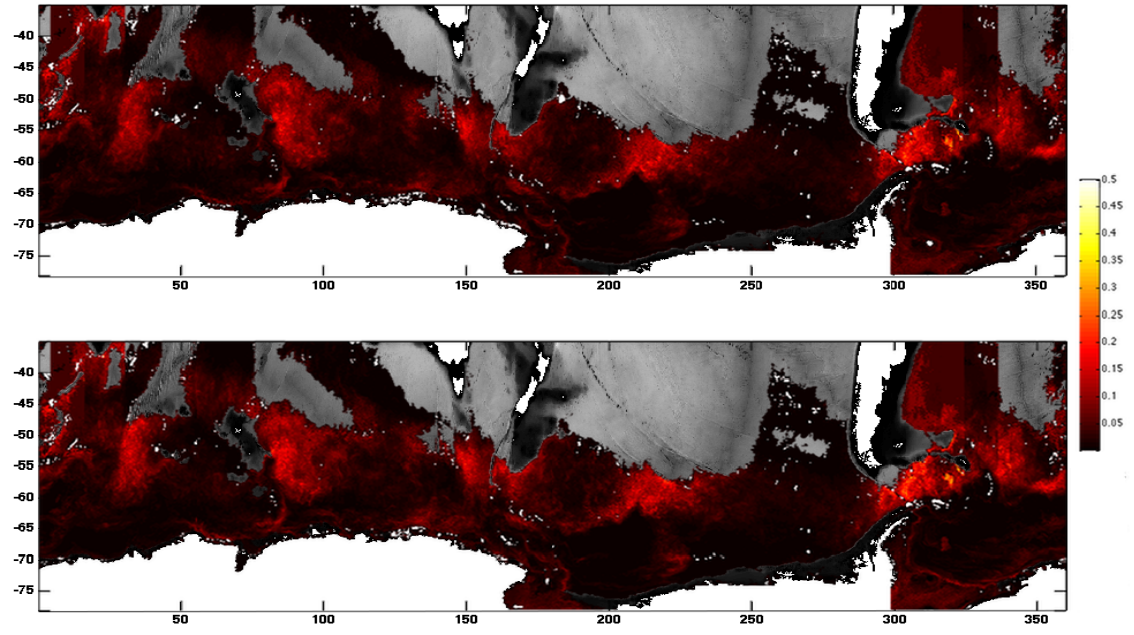

FIG. 2.17: Same as in Fig. 2.16 but on isoneutral surface γ^n=28.16. Upper panel: Downward vertical velocity component. Lower panel: upward vertical velocity component. A more coherent signal applies for both the downward and upward maxima.

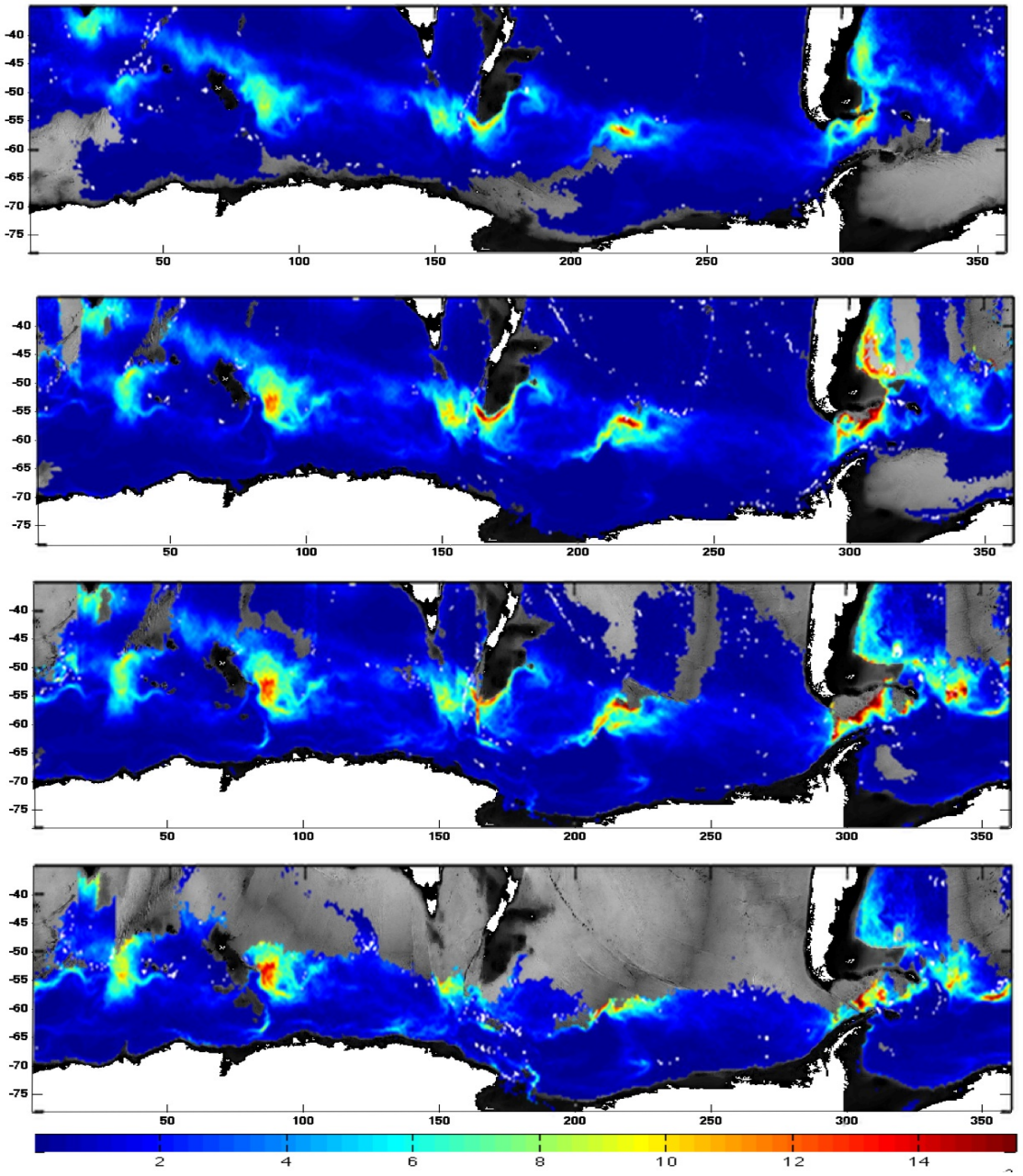

FIG. 2.18: Mean absolute vertical velocity component w for isoneutral surfaces 27.76, 27.96, 28.06 and 28.16 (from top to bottom panels). Velocity is in 10^{-3} (cm s^{-1}). Period covered spans from model day 1095 to 7300.

regions constitute rare ephemeral exceptions [*Wunsch and Ferrari*, 2004], and a maintained through a set of forcing functions mean zonal flow [*Olbers et al.*, 2007], one expects the mean horizontal velocity to decrease from the surface to depth [*Munk*, 1950; *Wunsch*, 1997]. In response to this vertical distribution the ratio of vertical to horizontal components of velocity should appear larger as long as vertical velocity remains within the same magnitude range irrespective of depth. Indeed, as seen in figure 2.19 for isoneutral surface $\gamma^n = 27.76$ the maximum ratio of vertical to horizontal velocity components

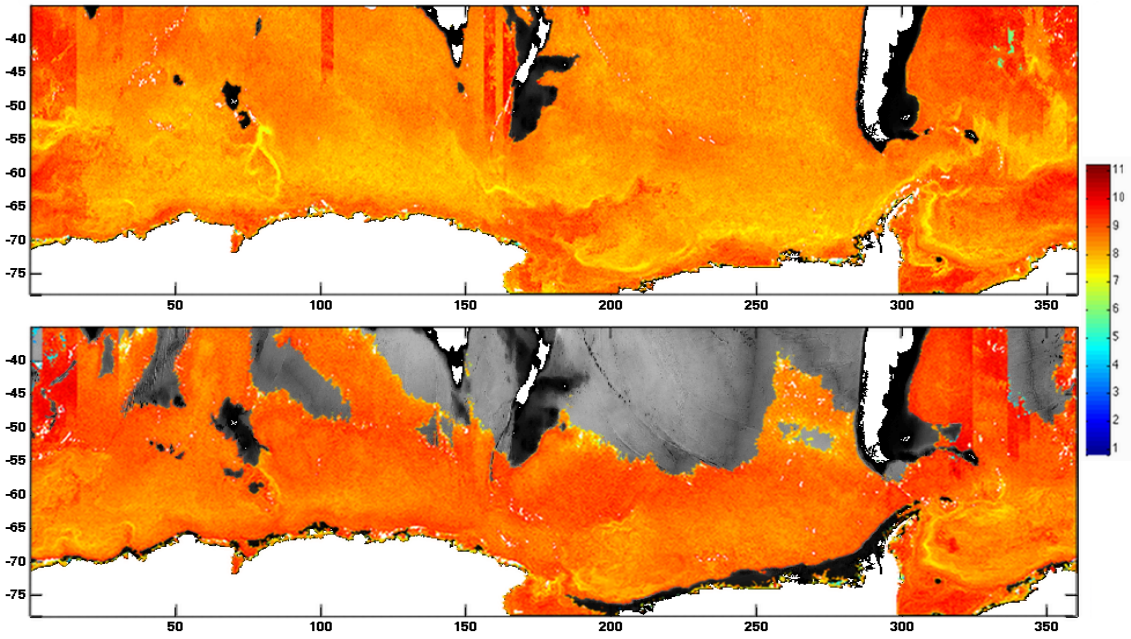

FIG. 2.19: Maximum ratio $(log_{10}, 10^{11})$ of vertical to horizontal velocity components for isoneutral surface 27.76 (upper panel) and 28.16 (lower panel). Period covered spans from model day 1095 to 7300.

is 0.0055, minimum 4.13×10^{-12} with a mean of 4.56×10^{-5} and a standard deviation of 5.46×10^{-5}. Accordingly, for isoneutral surface $\gamma^n = 28.16$ the maximum $w/\mathcal{U}$ ratio, where $\mathcal{U}(u,v)$ is the magnitude of the horizontal velocity component, is 0.016 with a mean value of 8.2×10^{-5} and a standard deviation of 8.4×10^{-5}. The minimum is an order of magnitude smaller than the estimation derived for the neutral density 27.76 isopycnal. The maximum rate of an isoneutral's vertical displacement is significantly smaller than its horizontal velocity. The flow in fact is not incompressible but can be approximated as such given the computed magnitudes for the vertical and horizontal velocity components aforementioned. Assuming an incompressible flow in the horizontal direction (2.4), fluid particles diverging horizontally along particular directions should maintain the mass balance with fluid receipt along other directions. In that sense, stretching of conserved fluid quantities, motion is considered to be quasi-geostrophic due to the synoptic scale of the observed features referenced here, can be linked to mixing [*d'Ovidio et al.*, 2004].

In the incompressible flow assumption here the pseudo-horizontal Eulerian velocity $\mathcal{U}_{E_n}$ is approximated to be non-divergent, $\nabla \cdot \mathbf{u} = 0$. The computed close to zero vertical velocity and a constant density, by construction of the isopycnal simulations, are associated with a unit volume (Green's integral relation) accompanying a moving fluid parcel which is assumed as pre-conditionally valid [*McWilliams*, 2006]. Under an isopycnal particle movement framework this could be extended to the whole fluid.

2.3.4 Release scheme configuration

Two release schemes, multiple and single in time releases respectively, are employed in the context of this study in line with the two main Lagrangian simulation experiments performed.

In the DIMES experiment, each monthly release is constituted by a cluster of 2500 particles, with a homogeneous spatial distribution of $\sim$ 500 m initial separation distance. The location and initialization of the numerical simulations were based on the climatology on site immediately following the injection date [*Ledwell et al.*, 2010] (see also Appendix B.6.1).

The set-up of the main, single in time, release scheme formulated in this Lagrangian trajectories study, hereinafter the Southern Ocean Lagrangian (SOL) experiment, is described as follows. Simulations were conducted on four isoneutral surfaces covering the full zonal extent of the Southern Ocean. The latitudinal range of the linearly aligned releases aims to reasonably capture the meridional extent of ACC. In figure 2.15, the release scheme is illustrated superimposed on a snapshot of geopotential anomaly[7] for model day 1095. 2000 particles are released at model day 1095 every 5 degrees in longitude, with an initial linear alignment resulting in 576,000 particles for the four isoneutral surfaces. Particles' initial spacing is equivalent to 0.005 degrees which, based on OCCAM's 1/12° model latitudinal grid resolution, is equivalent to approximately 556 m in the meridional direction. The spatial resolution chosen is not expected to yield additional information with regard to the representation of the underlying dynamics as long as particles are located in the same grid cell. However, the resolution employed is valid for the calculation and subsequent spatial identification of alternative trajectories when considering Lagrangian statistics. The high density of released particles introduces more degrees of freedom in the configuration of different groups of particles initialized at slightly different initial conditions. The latitudinal range of the releases, from -52.5 to -62.5 degrees, is chosen so that they represent cross-sections of the ACC and the local extent of its major characteristic frontal jet formations. This formulation establishes a Lagrangian context of comparative analysis of particle trajectories under spatially differentiated energetic environments.

[7]Geopotential anomaly (or dynamic-height anomaly) $\Delta\Phi$ at a grid point (i,j) is computed as the

$$\Delta\Phi(i,j) = \int_{P_{1_{(i,j)}}}^{P_{2_{(i,j)}}} \delta \, dp$$

where δ is the *specific volume anomaly* and P_1, P_2 the respective pressure surfaces at the point of interest. $\Delta\Phi$ is calculated for all 66 isobaric z-levels of OCCAM 1/12° model and interpolated on the isoneutral surfaces estimated vertical coordinates. Computation is with respect to the top surface layer in OCCAM 1/12° model vertical level parameterization and thus $P_{2_{(i,j)}}$ is $\sim$ 3 dbar (see *Coward and De Cuevas* [2005] for detailed description of OCCAM's z-level definition).

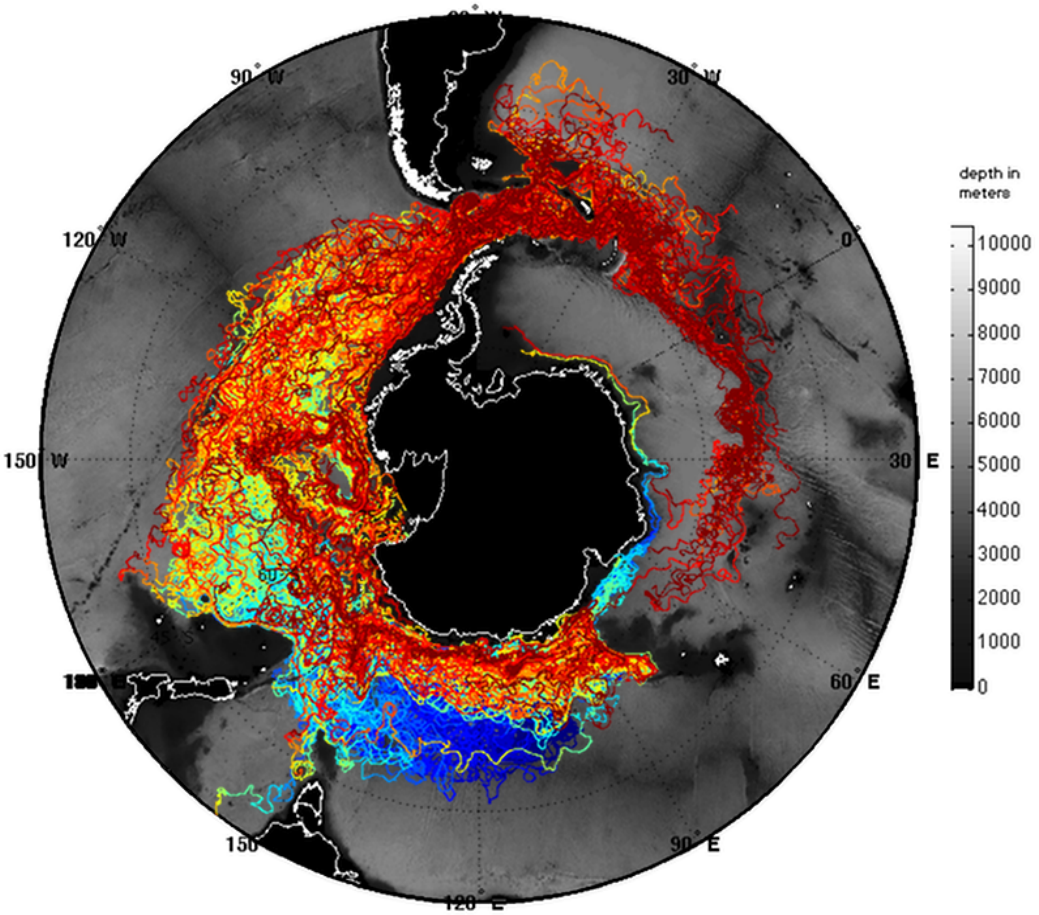

FIG. 2.20: Particles' simulated trajectories on isoneutral surface 27.96 colour coded with respective year of travel (blue, first - dark red, last). Spatial distribution of trajectories is indicative of particles varying and uncorrelated dispositions with time evolution. Travel time is for a period of $\sim$ 17 years covering model days 1095 to 7300.

In figure 2.20, 'spaghetti' trajectories time evolution for a single release on the selected isoneutral surface γ^n=27.96 are illustrated. Particles are advected for a period of 17 years taking advantage of OCCAM's hindcast spanning from model day 1095 (January 1988) to 7300 (December 2004). This characterises all releases in the context of the SOL experiment. Particles get stranded when reaching land or when neutral density, in the next timestep of the numerical calculation, increases due to formation of denser water in the surrounding area. In Chapter 4, the role of PV gradients in excluding particles from entering these regions will be presented.

At certain regions of interest, i.e. eddy intensified, weak and strong mean flow areas, a more detailed release scheme is devised. Particles are released on a grid of doubled spatial density, i.e. with 1/24° spacing, compared with the OCCAM's 1/12° model grid resolution. Travelling time is set to 90 days which proves adequate to delineate material lines emerging in a dynamical system approximation.

2.4 Eddy kinetic energy

2.4.1 Does a separation in time variant and invariant velocity components exist?

The importance of EKE in the analysis of mixing processes, turbulent diffusion, tracer and marine ecosystems evolution and in fact nearly every aspect of ocean energetics investigation is highlighted in almost every complete approach of ocean dynamics related studies. Its derivation though, in a Eulerian and/or Lagrangian framework, is prone to assumptions that can introduce significant errors in the ensuing results. Eulerian observational data are usually the product of moorings and repeated ground tracks of satellite altimeters. Lagrangian observational data are imparted mainly by floats and drifters. On the other hand, output from OGCMs has the advantage of spatial density that is absent or even non-existent in a form of a universal Eulerian observational dataset. A recently completed international effort resulted in an almost globally spatial coherent Lagrangian dataset through the ARGO system. The spatio-temporal coverage though, still constitutes an important impediment. EKE derives from the estimation of the residual flow i.e. the time-variable component of the velocity field, related to eddy transports and the mean velocity component is a time invariant, stationary mean.

Evaluation of EKE per unit mass, $1/2(u'u'+v'v')$, where u', v' are the horizontal eddy velocity components (or $1/2(\overline{\mathcal{U}^2}-\overline{\mathcal{U}}^2)$, where $\mathcal{U}$ is the projected horizontal velocity (u, v) on the isoneutral surface), requires an advective-diffusive formalism of a tracer C

$$\frac{\partial}{\partial t}\mathcal{C}+\langle\mathcal{U}\rangle\cdot\nabla\mathcal{C}=-\nabla\cdot\langle\mathcal{U}'\mathcal{C}'\rangle\equiv\nabla\cdot(\kappa\nabla\mathcal{C})$$

for the velocity field representation, where the mean $\langle\mathcal{U}\rangle$ and residual flow $\mathcal{U}'$ are assumed well separated in time [*Taylor*, 1921; *Davis*, 1991; *LaCasce*, 2008; *Ferrari and Wunsch*, 2009].

Does such a decomposition of velocity components really exist and if not how good an approximation is it and under what time scales is it statistically valid? *Davis* [1991] in his review paper on Lagrangian ocean studies, assumed that separation of the mean and eddy components of velocity over specific time scales is a valid approximation. On the contrary, *Zang and Wunsch* [2001] found no evidence of such separation existence from their computation of power spectrum densities of low frequency oceanic variability in the Northern hemisphere. A gap in their velocity spectrum would justify the separation of mean and eddy kinetic energetics. *LaCasce* [2008] agrees that no evidence exists that would justify interruption of velocity power spectra. *Ferrari and Wunsch* [2009] in their analysis of power spectrums of moorings' instruments identified a geostrophic eddy band related to sub-inertial scales, and in succession of a white noise flat spectrum region at

low frequencies, but generally admit (see the review work of *Ferrari and Wunsch* [2010]) that no robust evidence for a spectra partition among forced motions and turbulent cascades exists.

Zhurbas [2003] assumed a decomposition of the flow in residual and invariant components for even an inhomogeneous mean. His approach though, required the satisfaction an isotropic mean shear criterion over the averaging bin size in his calculation in order for the residual field not to inherit mean shear characteristics that have the prospects of altering and even dominating diffusion through shear dispersion.

Bauer et al. [2002], analysing a set of drift buoys from 1976-1996 in the tropical Pacific Ocean, adopted the notion of a spectral gap existence in Lagrangian velocities but with sufficiently long time lags in the velocity autocorrelation function. This allowed them to decompose tracer transport into mean (resolved) and eddy (unresolved) motions. Their estimation of the mean field is based on an optimized bicubic spline method resulting in a continuous spatially variable mean aiming to avoid the effects of strong mean shear flow on particle dispersion.

Veneziani et al. [2004] used a local Eulerian spatially dependent mean, where EKE distribution would satisfy homogeneity criteria in both dynamical and statistical characteristics. Their notion was towards a valid decomposition when considering a weak mean flow and a well defined mesoscale turbulent field. Still, the conclusion was drawn that in highly inhomogeneous and nonlinear areas, their approach is potentially problematic.

Sallée et al. [2008b] computed a seasonal mean from the Global Drifter Program (GDP) experiment and an approximate lifespan of 10 years. This might be problematic regardless of the extensive averaging period since the mean is still seasonally variable and thus does not satisfy the time-stationarity criterion in the hypotheses of a valid existent flow decomposition. A 7-year mean irrespective of seasonal trends was devised for the virtual drifters simulation in their experiment.

Griesel et al. [2010] calculated the residual velocity $\mathbf{u}'$, in the autocorrelation equation of *Taylor* [1921], from numerical floats by subtracting a spatially varying Eulerian one year period time mean velocity from each individual float. They then projected each residual float velocity locally across and along the spatially varying Eulerian time mean velocities. By construction, this ensured that the cross-stream dispersion by the mean is zero.

Lu and Speer [2011] comparing mixing efficiency M_e, cumulative probability density functions (CDF), *relative* dispersion and the Finite Scale Lyapunov Exponent (FSLE), conclude that limitations may exist in reflecting the role of jets as mixing barriers, possibly due to the difficulty in specifying the mean flow, for the *relative* dispersion and FSLE methods.

Based on the fact that our time-averaged Eulerian velocity field is not homogeneous

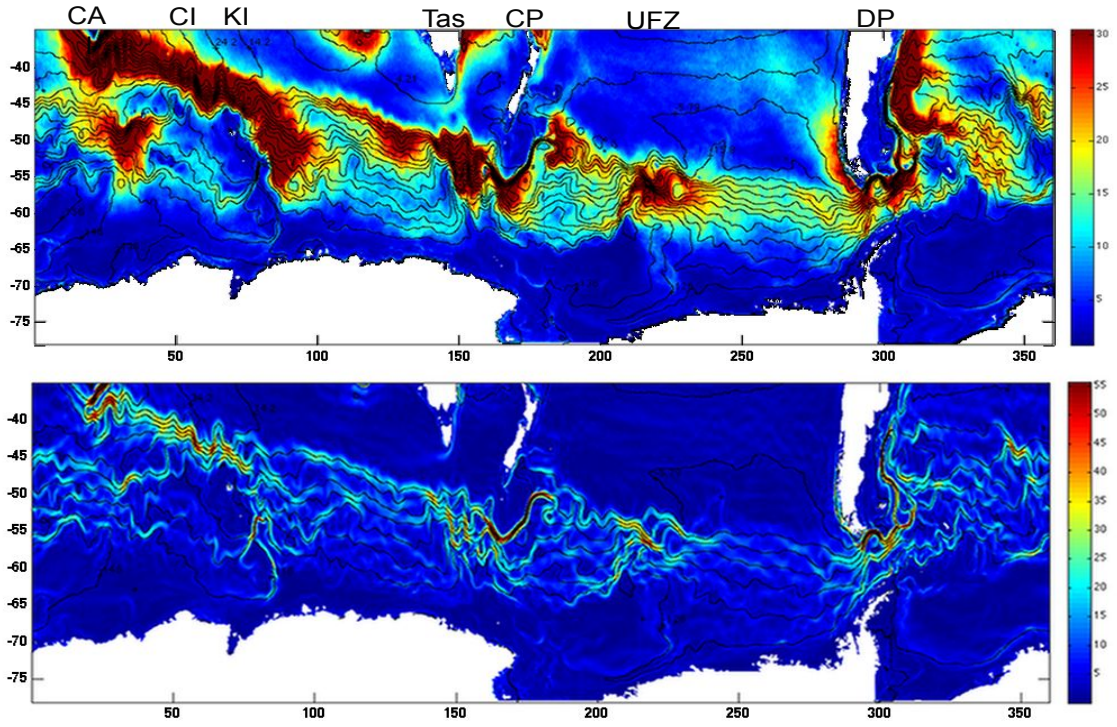

FIG. 2.21: Root mean square residual surface geostrophic velocity, $|\overline{\mathbf{u}'_g}| = \sqrt{2\overline{EKE}}$ (top panel) and mean surface geostrophic velocity, $|\overline{\mathbf{u}_g}|$ (bottom panel) in cm s^{-1}. Overlying, contours of mean dynamic topography with spacing of 10 and 20 cm respectively (top-bottom). Averaged period of dynamic topography from model days 1095 to 7300. Colour scale constrained for comparison with V_{rms} velocity diagrams mapped on isopycnals (see following figures). Regions of interest, topographic prominent areas related with stationary eddies (see text), are denoted as: CA, Cape Agulhas; CI, Crozet Island;KI, Kerguelen Island;Tas, Tasmania; CP, Campbell Plateau; UFZ, Udintsev Fracture Zone; DP, Drake Passage. White areas depict land. For computation of quantities see Appendix A.

in space (Fig. 2.21, bottom panel), subtracting a spatially invariable mean value from each particle's velocity in order to get the residual flow and subsequent displacement, does not suffice for a reliable eddy field representation. In order to account for non-stationarity and inhomogeneous eddy statistics a spatially varying mean needs to be estimated from the spatially inhomogeneous Eulerian velocity time series.

2.4.2 The separation of the mean and eddy components

The degree of completeness of the flow decomposition in variant (residual) and invariant (mean) components is one of the main issues in the context of eddy diffusion approximations. Determining at what degree the flow separation is successful is quite important for the robustness of the absolute diffusivity computation in the context of classical diffusion theory.

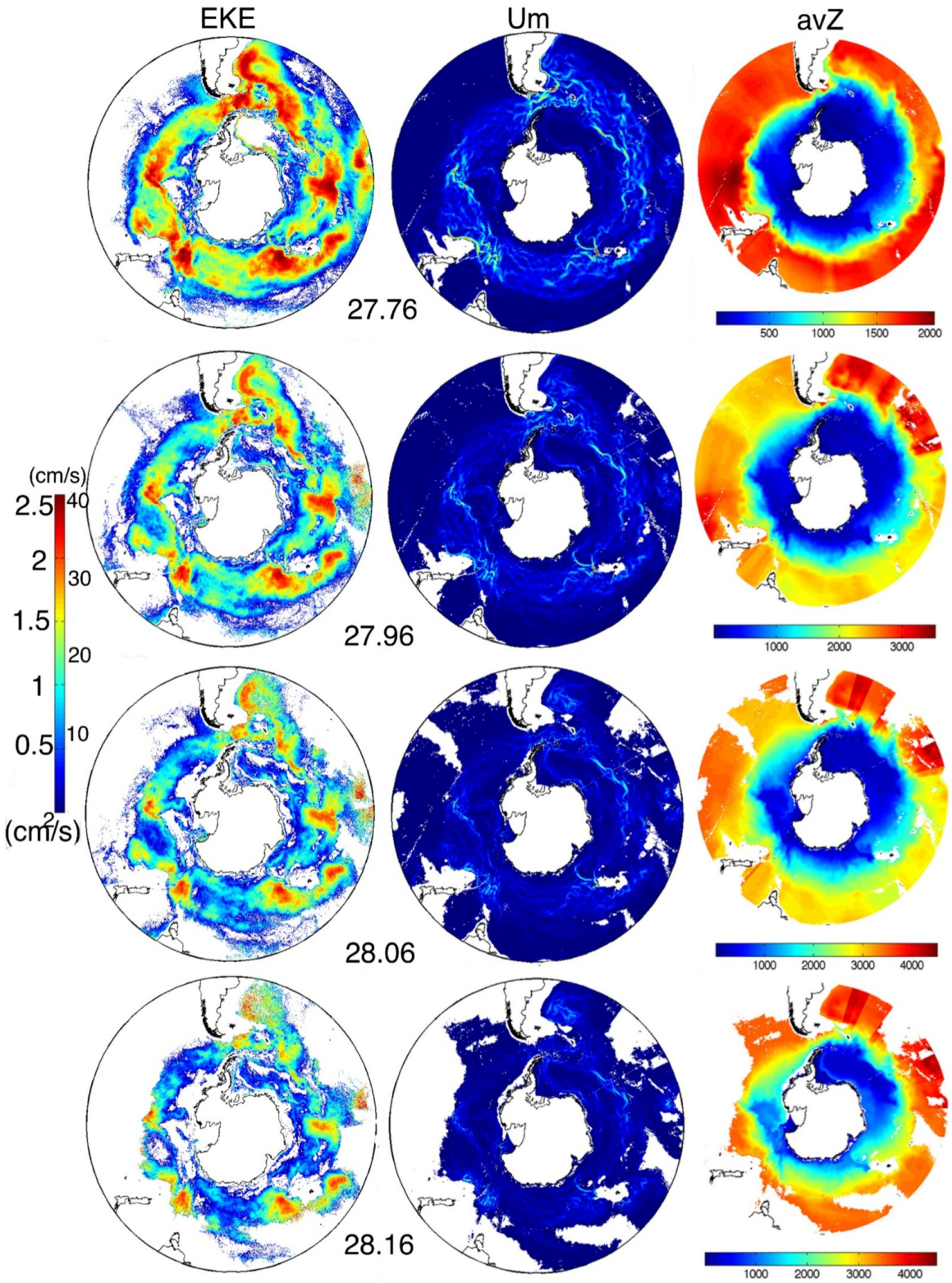

FIG. 2.22: EKE $0.5\mathcal{U}_{rms}^2$ (cm^2 s^{-1}), $\mathcal{U}_m$ velocity (cm s^{-1}) and average depth (m) for all isoneutral surfaces.

In common with the conventional approach, the separation of velocity[8] is written as

$$\mathcal{U}(x, t_0 + \tau) = \overline{\mathcal{U}}(x, \tau) + \mathcal{U}'(x, t_0 + \tau),$$

with the fluctuation term $\mathcal{U}'$ denoting the residual flow contribution, $\mathcal{U}$ representing the instantaneous velocity with constituents (u, v) and τ the time period, assuming the mean $\overline{\mathcal{U}}$ retains no memory of initial conditions. The completeness of this separation is solely a statistical result and not a natural one, considering the nature of geophysical flows and dynamical systems in general. So, if accepted it is always accompanied with a degree of uncertainty, which is dependent on homogeneity, stationarity and fluctuations' variance over the spatio-temporal scales examined. In a rephrase from *Kraichnan* [1961][9], an intrinsic uncertainty of stochastic perturbations due to limited availability of velocity time series is of fundamental importance. Thus, a flow decomposition can only approach completeness when the mean flow is computed over temporal scales that exceed even low frequency variability. Depending on the time averages constructed and flow characteristics and regime, a certain amount of the residual motion is potentially persistently present in the time-mean invariant component.

In order to reduce the possibility of remnant mean shear in our flow decomposition, we compute the mean and residual velocity components over a period of 17 years (Fig. 2.21 - 2.22)[10]. Shorter periods were also examined for evaluation purposes in order to justify that a complete resolution between the stationary space dependent and non-stationary inhomogeneous parts of the velocity field does not exist for time scales less than 5 years. In figure 2.23 the derived EKE for averaging periods of 2 and 5 years still retains detailed jet structure characteristics rendering the separation 'incomplete'.

An additional issue concerns the nature of dynamics represented by the decomposition product. The unresolved component of the velocity field can be further separated in standing (owing their generation to the interaction of the time-varying flow with topography and asymmetric forcing resulting in a meandering time-mean flow) and transient eddy (as the difference of the instantaneous velocity field and the time-mean flow) components [*Hallberg and Gnanadesikan*, 2001; *Olbers et al.*, 2004].

[8]The expansion of the afore motion separation in a *Reynolds decomposition* prescript reveal the elaborative *closure problem* of turbulence [*Kraichnan*, 1961] in which the emerging *Reynolds stresses*, $-\rho\langle u'v'\rangle$ are attempted to a connection with the mean flow through time-averaging of the equations of motion (Reynolds-averaged Navier-Stokes equations). (Note: In an isopycnal context assuming that density ρ remains constant *Reynolds stresses* reduces to the term $-\langle u'v'\rangle$. The brackets denote an *ensemble* average which in fact is an average over realizations and in ergodic flows should converge to the time-average).

[9]*Kraichnan*, 1961 isolates the turbulence *closure problem* in the evolving complexity to derive a future mean velocity distribution even when considering simple initial distributions.

[10]Notation and overlying dynamic topography were selected for a comparison with *Naveira Garabato et al.* [2011] figures 1 (a.-b.) of surface flow, derived from mean dynamic topography of *Maximenko and Niiler* [2005], and EKE, computed from satellite altimetry data (AVISO gridded altimetry product), covering the same geographically bounded region of the Southern Ocean.

Subtracting a velocity spatially varying time-mean denoted as $\langle \mathbf{u} \rangle$ from the instantaneous velocity value $\mathbf{u}$, either Eulerian or Lagrangian, would result to the formalism of the residual component, based on the above definitions, of the transient eddy contribution $\mathbf{u}'$. The differentiation of eddy kinematics based on the hypothesised separation on different time scales leads to a differentiation in aspects of dynamic regimes application. In that context, stationary eddies distribute zonal momentum downward in the water column and succeed transient eddies, emerging through baroclinic instability, when topographic scales are larger than the Rossby radius of deformation [*Treguier and McWilliams*, 1990]. *Lee et al.* [2007] provided a procedure to compute the transient eddies effect in a Eulerian context from OCCAM 1/12° model output.

In this study we do not venture into a decomposition of the respective contributions for the stationary or standing eddies. The residual velocity component here is defined as the difference of the instantaneous velocity field and a time-mean spatially variable circulation as,

$$\mathbf{u} = \langle \mathbf{u} \rangle + u' \tag{2.12}$$

The spatially variable mean velocity, derived in a Eulerian framework, serves as the background mean for the Lagrangian computed residual velocity and ensuing computation of the cross- and along-stream components. The role of EKE in particle trajectories dispersion in an isopycnal context is examined on a Lagrangian trajectory analysis framework. A spatially inhomogeneous mean from the time-varying Eulerian velocity field mapped on selected isoneutral surfaces is computed for the whole simulation period of 17 years. In the context described above, we postulate that this is the most valid time scale for the decomposition of mean and eddy components of the flow with the velocity dataset in our disposal.

2.4.3 Is the invariant component actually invariant?

Performing a release where advection is maintained only with the invariant component (a time-independent flow with a zero phase velocity), it is of interest to observe the corollaries of the flow decomposition approximation. In figure 2.24 a cluster of particles, in the context of the DIMES experiment tracer release (see B.6, Appendix B), is advected with the mean velocity field, constructed as previously described, for a period of 2185 days at 255.5° longitude and ~ 60°S. For comparison reasons the trajectories evolution with the instantaneous velocity component is also plotted with respect to recorded geopotential anomaly during the particles travel time. The differences are quite obvious. Mean flows appear non-dispersive with good approximation while the instantaneous component exhibits great spatial variability in close proximity to the release location.

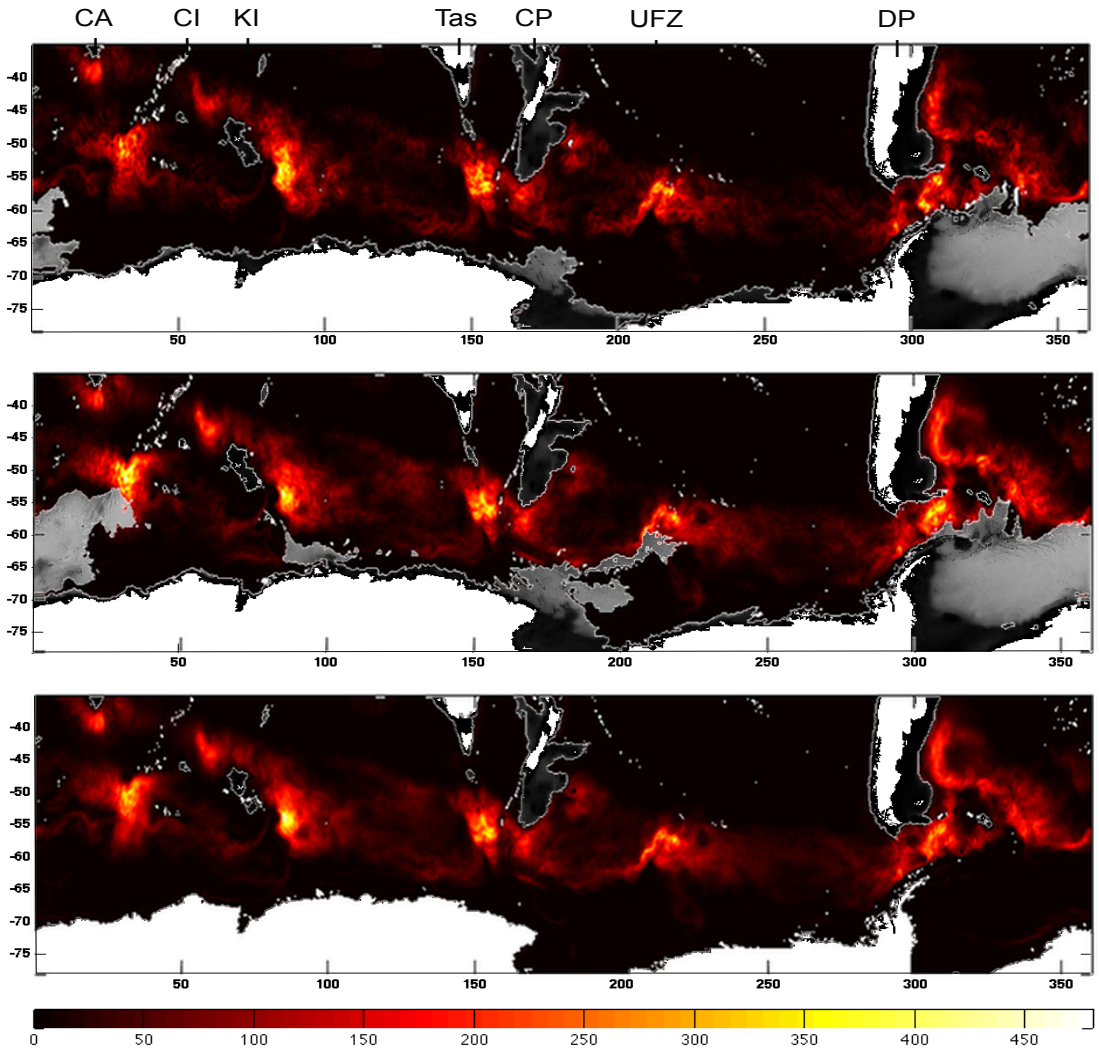

FIG. 2.23: Mean EKE per unit mass, $1/2(\overline{\mathcal{U}^2} - \overline{\mathcal{U}}^2)$, for isoneutral surface 27.76. A stationary spatially inhomogeneous mean of 2, 5 and 17 years is used in the respective images from top to bottom panels. The filamented structure of local enhanced jets and strong vortices are still visible on the top two panels suggesting that the decomposition of the flow to mean and eddy (stationary) components is not complete. $\mathcal{U}$ is the horizontal velocity with (u,v) components. EKE is in (cm s^{-1})^2. The longest period covered spans from model day 1095 to 7300. Regions of interest, topographic prominent areas related with stationary eddies (see text), are denoted as: CA, Cape Agulhas; CI, Crozet Island;KI, Kerguelen Island;Tas, Tasmania; CP, Campbell Plateau; UFZ, Udintsev Fracture Zone; DP, Drake Passage. White areas depict land while grey shaded regions the underlying bathymetry.

Since the flow is time-invariant and spatially stationary with non-parameterization of a diffusion coefficient (Fig. 2.24, a), particle trajectories should be bound to follow closed streamlines. Examining the variability of along-streamline recorded geopotential anomaly during particles travel time we find instead, particles not to follow closed streamlines when advected with the time-invariant component. We evaluate the probability density functions (pdfs) of geopotential anomaly $\Delta\Phi_n$ differences, computed as

the algebraic sum of the value at initialization minus that value at each sequential 5 day interval position (Fig. 2.25). The differences (Fig. 2.25, right panel) exhibit dependence on time lag which translates to alteration of initial values at specific locations. The first section, with a temporal scale of 600 model days from initialization, equivalent to the mean travel time of particles from DIMES release location to Drake Passage (Fig. 2.24, a - blue and cyan coloured trajectories segments), exhibits minimum variance, in agreement with a trajectory almost free of meanders. A topography steered trajectories' evolution, with an enhanced meandering appearance as the particles progress further east from South Georgia (Fig. 2.24, a - 4th year of travel-yellow colour) is depicted. At this longitude (time lag $\sim$ 1000days), the probability density of $\Delta\Phi_n$ and PV differences, are illustrated clearly more variant (Fig. 2.25, top right panel). The ensuing distribution, regarding travel time longer of 2000 model days (red-magenta coloured segments, eastward of 10° E) has maximum variance and associated with strong mean flow meandering over the Atlantic Indian Ridge (Fig. 2.3). This increase in the pdfs distribution is related to entrance in the EKE intensified region (30°) (Fig. 2.23). The evolution of $\Delta\Phi_n$ differences is indicative that the mean velocity field is by no means in geostrophic equilibrium.

Simple non divergent conceptual models have exhibited similar results for Eulerian time-independent, nonzero, mean flows [*Regier and Stommel*, 1979][11]. Based on particles' initial distribution, *Regier and Stommel* [1979] found that trajectories evolution is not consonant with a closed streamline alignment, considering that the mean flow is not perturbed in any way. So, apparently the dispersion exhibited is either the result of inherent divergence[12] in the time-mean velocity field and/or a consequence of the numerical advection scheme (see Chapter 2 section 2.2).

It is clear up to now that flow decomposition is always accompanied with a degree of uncertainty. Mainly dependent on homogeneous and stationary statistics, the spatio-temporal scales examined are crucial to a computation 'free' of the effects of fluctuation components. While this is important in determining eddy diffusivity based on single particle statistics, deciphering underlying dynamics of the flow does not always require the above assumption (see Chapter 4). In the sections to follow we will present how Lagrangian statistics have the ability to depict flow characteristics without the requirement of flow decomposition.

[11] *Regier and Stommel* [1979], in their early theoretical ventures to study approximations of Lagrangian representations of geophysical flows, devised a streamfunction as a sum of a constant velocity and eddies, in the form of square cells advected with a constant phase speed. Releases in their eddy geometry space exhibit similarities with our mean flow component advection results.

[12] Elaborating on the kinetic energy equations of the mean motion [*George*, 2006], a 'turbulence production' divergent term (Reynolds stresses product with the velocity gradient) emerges signifying the transfer of kinetic energy from (to) the mean flow towards (from) the fluctuation component. The mean flow is considered incompressible and thus non-divergent.

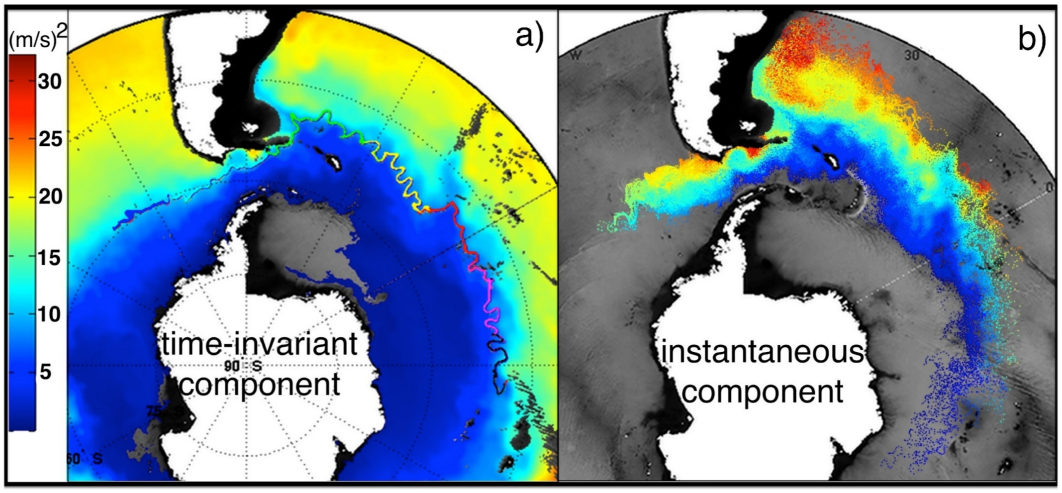

FIG. 2.24: Trajectory evolution of a cluster of particles advected with a) the time invariant and b) instantaneous component of the velocity on isoneutral surface $\gamma^n = 27.9$ for a period of 2185 model days. DIMES release at 255.5°E is depicted as a meandering jet-like current. Different colours of trajectory segments denote year of travel (blue-first year, black-last). Background field in a) is mean geopotential anomaly (m^2 s^{-2}) for the same period of 2185 days. Particle positions in b) are colour-coded with 5-day mean geopotential anomaly linearly interpolated at the respective positions.

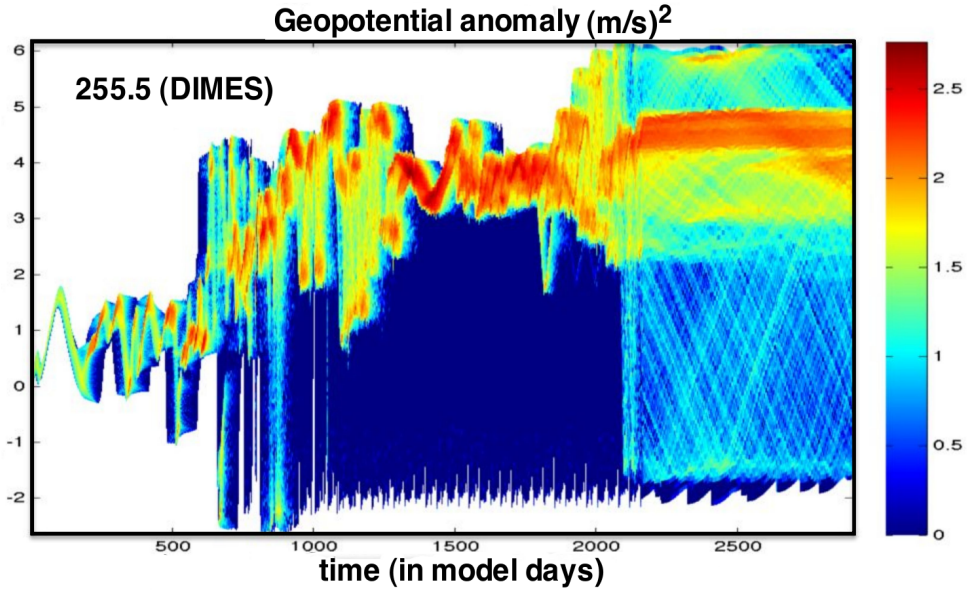

FIG. 2.25: PDFs of interpolated geopotential anomaly (m^2 s^{-2}) (the difference is the algebraic sum of the value at initialization minus that value at each sequential 5 day interval position) (in log_{10} scale) on particles' positions, for advection with the time invariant component of the velocity on neutral density $\gamma^n = 27.9$ surface. The period covered is from 3275 to 5500 model days and releases concern initializations at 255.5° of longitude. Colours in logarithmic scale denote absolute numbers of events.

Summary In this chapter, we presented the model and described thoroughly the particle tracking scheme employed and our approach in translating the isobaric model output to an isoneutral context, which is where the core simulation experiments of this study reside.

Concerns addressed were in relation to the capture of the dynamics from the release scheme employed and an efficient vertical representation of the ACC.

This study focuses on the description of mesoscale energetics by means of diffusion characterization based upon Lagrangian descriptive statistics of particle trajectories. Its foundation lies on taking advantage of the potential of Lagrangian trajectories to sample space in time and capture the evolution of the flow with a release scheme that adequately produces the spatio-temporal coverage needed for robust Lagrangian statistics.

Chapter 3

Flow characteristics of the ACC from a Lagrangian perspective.

3.1 Introduction

The ACC is one of the main corridors of thermohaline circulation in the global ocean system being a major pathway of exchange between ocean basins. However, there is still an ongoing debate concerning eddy mixing and transport inhibition in the ACC. In this chapter we present the advantages of a *Lagrangian* approximation of flow characteristics and present a background qualitative assessment of ACC dynamics. Dispersive regimes and transport barriers are examined with particle probability density functions (normalised by release). The connection between the derived distributions with material curves and persistent dynamical features (i.e. coherent vortices-hyperbolic trajectories) is also presented. Turbulent flows exhibit a complicated spatial and temporal structure rendering the quantitative power of the dynamical systems Lagrangian approach problematic [*Haller and Yuan*, 2000]. We employ the Finite Scale Lyapunov Exponent method as a useful alternative which serves as a comparison tool to particles' probability distributions spatial structure. Asserting local flow characteristics, without being impaired by the visualisation of particles' positions 'chaotic' time evolution from distant regions, is attempted through travel time-constrained longitudinal releases. Apart from delineating flow characteristics and deciphering an effective mechanism for eddy stirring in the ACC with respect to local regimes and particles' distributions during the early stages of their travel, the flow's Lagrangian descriptive statistics aim to describe the dynamics context for diffusion computation in Chapter 4.

3.2 ACC: Barrier or blender ?

Introduction The role of the ACC as a barrier or blender is addressed here by deciphering the structure of kinematic boundaries and advection pathways in the flow. We present both non-local and local approximations by regulating the travel time series length of passive particles. It is obvious that the evolution of particle dispersion in oceanic, and in general in geophysical flows (even when considering periodic time-dependent perturbations[1]) presents a 'chaotic' image with time progression as a consequence of dispersion itself. Therefore, in our computations, the time scale is of fundamental importance in deciphering relevant distributions with regard to underlying dynamics in an equivalent temporal frame.

Our approach is founded on a simple question: 'What are my chances as a particle visiting specific locations in the ACC and, by extension, the Southern Ocean?', which is a direct corollary of *Davis* [1991] assertion that the release location is important for the future evolution of particles' positions.

3.2.1 ACC flow characteristics depicted from particles' spatial distributions

Following *Davis* [1991], a Lagrangian approach to transport is naturally constructed on the passive particles representation of kinematics which is adequate only if particles are proxies for molecules. As such, $P(\mathbf{x}, t|\mathbf{a})$ is, among others, the probability density of molecular particles' (fluid unit parcels) positions. Thus, probability density functions (PDFs) can actually serve as visualisers of oceanic transport capacity, since when considering synoptic to large scales, statistics of numerical molecular displacement (excluding molecular diffusion scales) are approximate to those of advected passive particles.

Computation of PDFs of specific particles would be problematic, since the calculation is dependent on the initial location [*Taylor*, 1921] and on immediate vicinity dynamics. The same is probably true if we calculate the PDFs of particles' locations based on specific releases. In both cases, each computed probability – apart from a function of time – is fundamentally regulated by the release location (in both a vertical and horizontal dependence context). In the SOL experiment, each of the longitudinal releases is associated with a different representation of local dynamics. This is fundamentally true due to space anisotropy as far as it considers particles in the same release (different latitude at initialization) and time partitioning with regard to the temporal distance from a point in space for each of the different longitudinal releases. Thus, each initialization of the particles' entrance into the system constitutes a separate probability space.

[1] In fact, chaotic behaviour as a consequence of the dynamical systems analysis of transport is founded on infinite time periodic systems [*Haller and Yuan*, 2000; *Wiggins*, 2005], and caution is needed when adapting this frame in an aperiodic finite time scale context.

How can a combined probability then be constructed considering all releases' dynamic distributions?

In figure 3.1, the index P_{EOS} is illustrated for the whole simulation period of ∼17 years for isoneutral surfaces 27.76, 27.96, 28.06 and 28.16. When considering multiple releases, the effective occurrence index is based on an algebraic sum as

$$P_{EOS(x|t_0+\tau)} = \sum_{n=1}^{N} EO_{r_n(x|t_0+\tau)}$$

, with $n = 1, 2, 3, ..., N$ being the number of releases. ${EO_{r_n}}^2$ is the number of effective occurrence events per release r_n, constructed as

$$EO_{r_n}(x|t_0+\tau) = \frac{\mathcal{N}_x^{events}(x|t_0+\tau)}{\mathcal{N}_{gridpoints}}$$

, with $\mathcal{N}_x^{events}$ the number of recorded occurrences of particles at each specific grid point $x = (j, i)$ and $\mathcal{N}_{gridpoints}$ the number of active locations[3] for the respective period τ and release r_n (Fig. 3.2). What we measure is space-sampling capacity within a spatio-temporal dynamics context, since occurrence events are scaled with the spatial extent (Fig. 3.2) of each release for the respective travel time. This means that a region with a specific number of events $\mathcal{N}$ and a spatial extent $\mathcal{A}$ will be characterized by a smaller effective occurrence index number with regard to a region with the same $\mathcal{N}$ events and a spatial extent $\mathcal{B} < \mathcal{A}$. Since in all isoneutrals the same numbers of particles are released, less dispersive releases will have higher indexes. Barriers in transport, since particles are unable to cross them, are delineated with high contrast concentrations at their flanks (e.g a common feature in all isoneutrals can be seen in the vicinity of the Ross Sea 170-210°E and around 65°S). Local regimes, though, cannot be used for comparison between different isoneutrals based on their index numbers. A qualitative assessment in this case is made by examining the spatial homogeneity of the respective regions' index numbers.

Two points of note with regard to the distributions depicted are as follows: First, the isoneutral surface geometries for γ^n, equal to 27.76 (the Weddell Sea area, 300-10°E and poleward of 65°S is exempt) and 27.96, do not impose a latitudinal spatial constraint on the particles' potential positions, as is the case for the 28.06 and 28.16 isopycnals. Second, remnants of the linear releases' initial locations can be seen in certain places denoting an analogously higher occurrence number related to a comparatively

[2]Bins are defined with respect to OCCAM's 1/12° grid.

[3]An event is an occurrence of a particle in a specific grid point at time $t_0 + \tau$, either repetitively or not, with τ denoting a period of travel time τ. The number of active locations is basically the number of grid points visited by a specific release r_n for the respective travel period τ, thus defining the spatial extent of the effective isoneutral surface (manifold of potential geometric representations of a single point with neutral density γ^n) which is dependent on the initialization of the release, both in time and space, the travel time of the Lagrangian particles and the flow dynamics for the respective isoneutral.

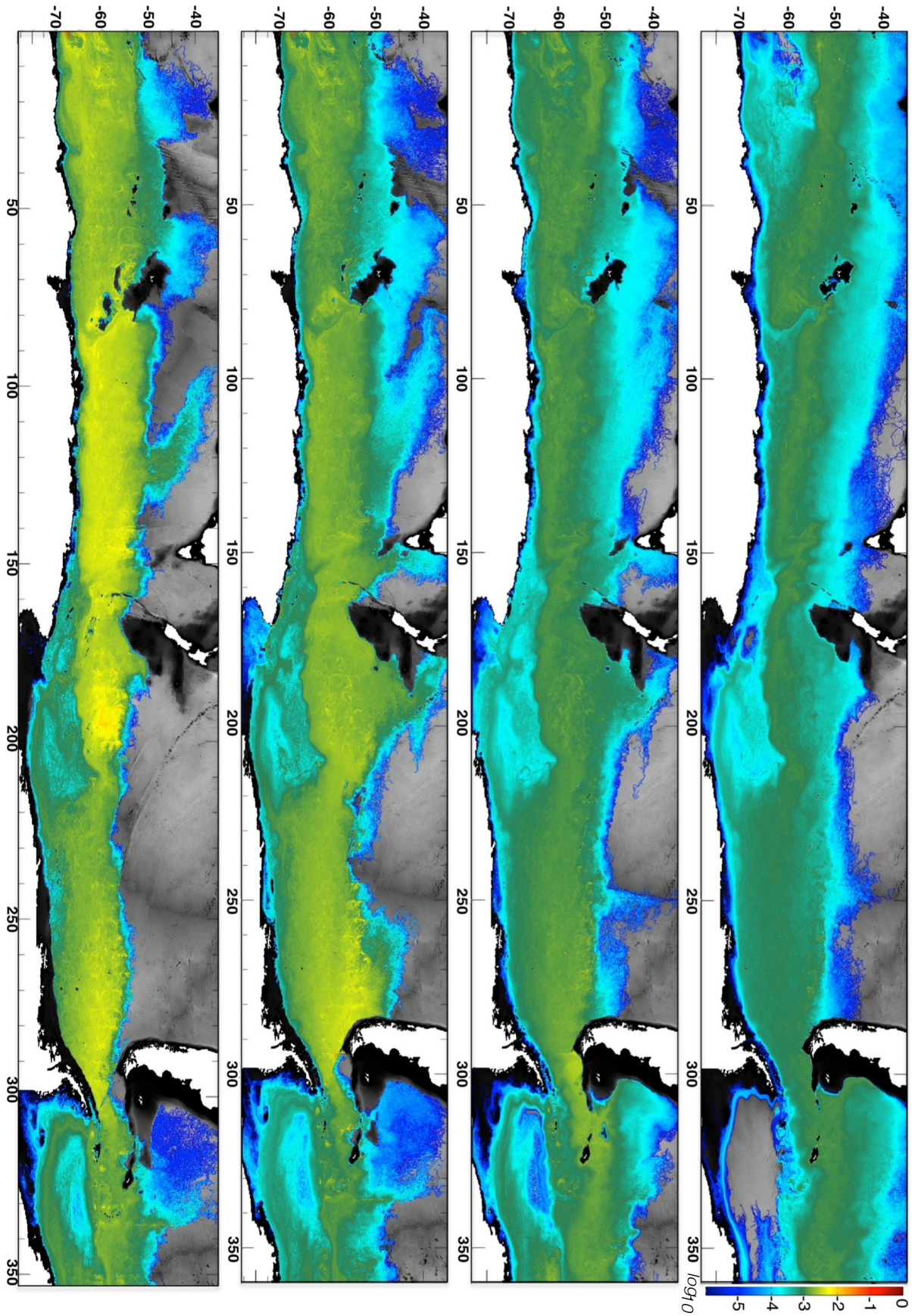

FIG. 3.1: Effective occurrence index (see text for details) for all longitudinal releases on isoneutral surfaces 27.76, 27.96, 28.06 and 28.16 (top to bottom) for the entire simulation period.

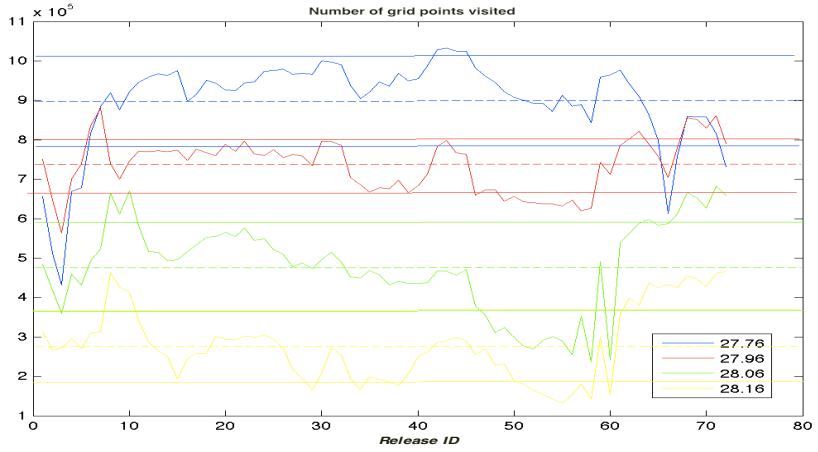

FIG. 3.2: Number of grid points visited in each longitudinal release for every isoneutral surface in the SOL experiment. Also shown are the mean (dashed lines) and standard deviation (solid) estimates.

reduced local velocity regime (Fig. 2.22), and thus discrepancies in the representations favour locations close to initialization. A generic trend of P_{EOS} index values, to increase through transition to denser isoneutral surfaces, is depicted. This occurs because of a reduction in the spatial extent and a decrease in available kinetic energy (Fig. 2.22-bottom panels, Appendix A).

Well-defined structures, associated with high occurrence values, delineate transport corridors as particles' preferred advection pathways. There is the impression of a gradually more dispersive flow with a transition to deeper isopycnals from the perspective that prominent features are less obvious. The main ACC core, between the PF and SACCF (Fig. 4, Appendix A, values of geopotential anomaly 12.4 and 3, respectively), coincides with values above 10^{-3} and a well-portrayed spatial distribution for the top two isoneutrals. Certain distinct features associated with strong PV gradients (Fig. 8) remain remarkably coherent on the various isosurfaces. The most prominent of these include the northern limit of the Ross Sea recirculation gyre, the topographic high associated with the east end of the South-east Indian Ridge (SW of Macquarie Island, 150°E 50°S) and the Kerguelen Plateau (KP, 80°E 50-60°S) transport barrier effect. Transition into areas with a higher degree of spatial homogeneity coincides with the most energetic residual field representations in this band. It is therefore sensible to expect the absence of large scale 'organized' structures in the areas where mixing occurs. The persistence of small-scale filamented structures over a 17 year period demonstrates that kinematic environments are unable to smooth out 'extreme' occurrence events as a result of the stirring of particle trajectories during the initial stages of the releases (Fig. 16, Appendix B). Distributions for these areas tend to become more spatially extensive with an increase in density. See for example the regions at 50-60° westward of KP, 180-200°

eastward of Campbell Plateau and 250-280° eastward of the Eltanin Fracture Zone, all of which are associated with low KE (Fig. 2.22).

It is interesting to examine whether or not restrictions, imposed by the geometry of neutral density surfaces on the spatial distribution of the respective index, favour certain locations. A comparison of the distributions on the respective isopycnals (Fig. 3.2) depicts four prominent differences, associated first with the northward excursions at 120°E on the northern side of the South-east Indian Ridge in connection with the UCDW and LCDW delineated on all isoneutrals, but which more noticeable on the 28.06 and 28.16 due to isopycnal surface geometry constraints, and second with a northward excursion at 150°E Tasmania (Tas) in the density range of the UCDW [*Iudicone et al.*, 2008]. Both of these flow divergences are associated with the area's 'Tasman leakage' outflowcharacteristic, with water flowing from the Pacific Ocean into the Indian Ocean via the East Australian Current running to the south of Australia [*Speich et al.*, 2002; *Döös et al.*, 2008]. The feature at 150°E is present on the 27.96 and 28.06 isoneutrals, but it is completely absent from the 27.76 and 28.16. The absence from the lighter isoneutral is not due to an isoneutral surface geometry restriction but to a flow constraint. For the third difference, a northward excursion at 180-200°E, east of New Zealand and northward of the Campbell Plateau is seen only on the 27.96 and 28.06 surfaces. This feature is again associated with a flow constraint on the 27.76 isoneutral and a geometry restriction on the 28.16 isoneutral. Fourth, the northward divergence associated with the Menard Fracture Zone at 115°W and extended up to 40°S following the East Pacific Rise is only seen on the 27.76 and 27.96 neutral density surfaces. The aforementioned divergence has an eminent alignment with the topographic ridge on the 27.96 and disappears completely on denser isoneutrals. A weak enhancement on E-W spatial coverage to the northward extension on the west side of the South American continent can be seen on all isoneutrals, but it is more obvious on the 28.06. This is probably associated with the Peru current.

All meridional jet structure excursions (Fig. 3.1) can be linked to the topographic steering of jets. This is apparent in the South-east Indian Ridge and in both of the KP jet structures. Topographic steering is even more of a regulatory factor in all of the other discrepancies previously mentioned. Both the spreading east of Tasmania and the encircling of the Chatham Rise NE of New Zealand are actually controlled by the topographic highs. 'Escape' pathways at topographic gap locations are definitely found at the extent of the Louisville seamount chain and at 120°-130°E, affecting only the denser surface (Fig. 2.3). The role of topographic gaps in providing passages for particle movements (Fig. 3.3) has been discussed previously [*Gille et al.*, 2004; *Whitehead*, 2005]. The meridional extent of high values' distributions on the 27.76 isoneutral, for the same region of the Chatham Rise, is constrained by the SAF, with the full extent actually following the Sub-Tropical Front (STF) [*Tilburg et al.*, 2002]. This transport

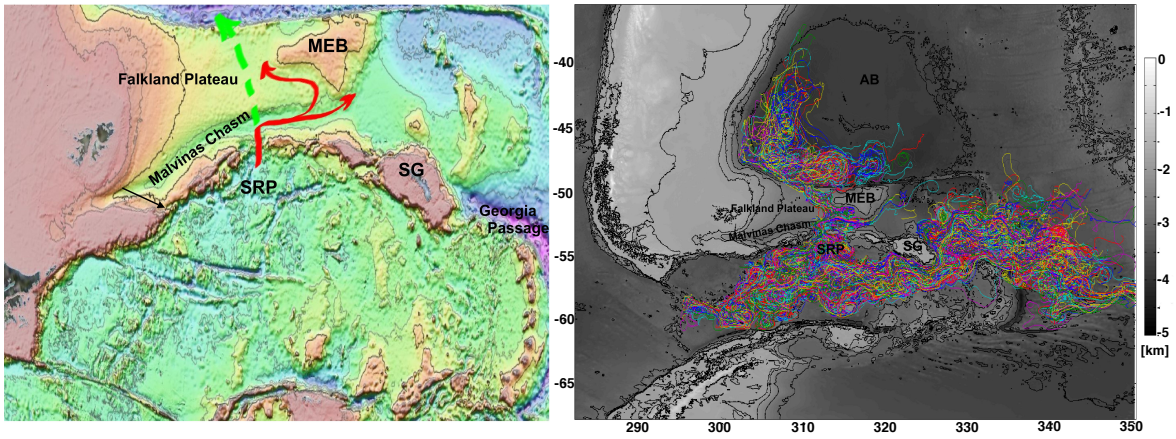

FIG. 3.3: (left panel) Main trajectory paths for particles crossing through the Shag Rocks Passage (SRP). Particles on isoneutral surface 28.06 cross the Malvinas Chasm and move over the Falkland Plateau (green and north-westward red arrow) entering the Argentina Basin further north (not shown here). Trajectories on the isoneutral 28.16, controlled by bathymetric features, follow the Malvinas Chasm to the east (eastward - red arrow) and enclose the Maurice Ewing Bank (MEB) with a delineated westward-stirred flow. A small number of particles follow the west flank of the MEB but fail to cross the Falkland Plateau (northward - red arrow). The green and eastward branches of red arrows coincide with a jet transferring PF waters to the north [*Arhan et al.*, 2002] and the climatological position of the PF, respectively (see also Fig. 1 from *Naveira Garabato et al.* [2003]). The black arrow indicates the entrance location of a deviating flow observed only for releases on isoneutral 27.76; (right panel) selected trajectories for releases at 295, 300 and 310 degrees of longitude on isoneutral surface 28.06 for an enlarged region. Trajectory time length is 800 days. The bold line denotes the isobath of 2000 m. Above: isobaths of 1000 and 500 m; below: 3000, 4000, 5000m; South Georgia (SG). [Bathymetry after IBCSO].

barrier, imposed by the frontal structure present, ceases to exist on the denser isopycnals (except for the 28.16), at least as far as specific areas are concerned. Perhaps a transition to a more barotropic organization of the flow is performed in this instance. The chaotic isotropic distribution of occurrence intensity values east of Chatham Rise signifies an equivalent mixing characterization. Pathways to particle movement provided by small PV gradient 'tongues' are depicted (Fig. 8). The Ross Sea recirculation gyre especially is delineated with a 'closing' circulation with a transition to denser isopycnals, which signifies the diminishing of large-scale barriers in transport, an action which is distinctive of the lighter isopycnals. The Antarctic Coastal Current (ACoC) is pictured on all isoneutrals with a characteristic vortex in the proximity of the northern tip of the Antarctic Peninsula.

The distributions discussed above clearly depict the restriction of particle dispersion while maintaining higher index values in the main path of the ACC (between the PF and SACCF). This meridional transport inhibition is reduced with a transition to denser isoneutrals where, though, isoneutral geometry is not a restricting factor. This is not a

surprising outcome, especially if we associate inhibition of mixing with the fast advection of eddies by the mean flow and, as such, the diminishing of their effectiveness in redistributing particles in space [*Ferrari and Nikurashin*, 2010]. In a reverse analogy, mean flow reduces in line with depth (Fig. 2.22), and eddies gradually become more effective in particle dispersion. Our mapping of the effective occurrence index does not provide any insights into the mixing mechanism of the ACC. It just gives us a general perspective on how the ACC flow regulates particle dispersion, the intensity of this control and the localization of this transport inhibition. Gaining further insights into the eddy stirring process, and where it is most effective, requires deciphering flow dynamics while retaining local regimes' characteristics.

3.2.2 Advection pathways, stagnation areas and transport inhibition

When accounting for flow dynamics and mixing potential in geophysical flows, one has to delineate advection pathways and transport inhibition, homogenization rates within a specific region and mixing regions, which are defined as areas bounded by impermeable or weakly permeable barriers to transport [*Pierrehumbert and Yang*, 1993]. In order to delineate advection pathways, complementary stagnation areas and transport inhibition in a local regime framework, we will define a probability density index in accordance with the occurrence index presented in section 3.2. Each particle release constitutes a different probability space. The discontinuity of occurrences evolution can thus be counterbalanced by the induction of probability analysis to a point in space rather than a single particle one. In this way, we do not measure the preference of a specific particle to visit a specific point but rather the probability of a specific point in space 'attracting' a particle. Space is partitioned in bins coinciding with the grid boxes on the OCCAM $1/12^\circ$ model grid. Hence, the total probability Q of each point in space to record an event after a period τ of travel time is constructed according to equation (3.1).

$$Q(x, t_0 + \tau) = \sum_{n=1}^{N} Qr_n(x, t_0 + \tau) \tag{3.1}$$

with $x = (j, i)$ and $n = 1, 2, 3, ..., N$ as the release ID. $Qr_n(x, t_0 + \tau)$ is the computed effective probability density function at x for each release r_n for the period $[t_0 \quad t_0 + \tau]$, defined as

$$Qr_n(x, t_0 + \tau) = SCP_{r_n} \cdot \int P_x(x_0, t_0 | x, t_0 + \tau)\, dt$$

, with SCP_{r_n}[4] the space capacity potential of each release r_n defined as

[4] A higher number indicates a more dispersive kinematic environment for the specific release and temporal resolution from a global perspective.

$$SCP_{r_n}(t_0+\tau) = \frac{\mathcal{N}_{gridpoints}(t_0+\tau)}{\mathcal{N}_{particles}(t_0+\tau)} \tag{3.2}$$

and

$$P_x(t_0|x,t_0+\tau) = \frac{\mathcal{N}_x^{events}(t_0+\tau)}{\sum_{i=1}^{\mathcal{N}_{gridpoints}} N_x^{events}(t_0+\tau)}$$

the probability density of each visited grid box (i,j) over the same period $\forall x_0' \in X$ where X the geometric space of all initial particles' locations x_0'. We will first discuss the results referring to the mappings of the whole set of releases and then focus in the following paragraphs on the DIMES region.

Considering multiple releases for a reduced period of time, which is adequate enough to allow particle advection in order to cover the initial zonal spatial distance among the initializations, provides an insightful view into local regimes' dynamics. In figures 3.4 and 3.5, we attempt to assess such single time release formulations. We choose a time lag of 91 days from initialization, in order to retain details of initial distributions and to delineate qualitatively a mixing time lag in which a relative homogenization stage of particle distribution has been reached [*Veneziani et al.*, 2004; *Sallée et al.*, 2008b; *Griesel et al.*, 2010]. We assume that both the spatial and temporal scales of the mesoscale eddy field are resolved within this time scale [*Chelton et al.*, 2007, 2011]. Also presented is the mean geopotential anomaly $\Delta\Phi$ (J kg^{-1}), for the same period, in order to delineate the relationship between the probability of occurrence distribution and mean flow streamlines. General agreement on high probability density values, exhibiting a continuous space-persistent filamented structure, with $\Delta\Phi$ contours exists in locations where a clear connection with PV gradient distribution can be established (Fig. 8, Appendix A). The space continuum of the probability index among the different initializations depicts the coherence of advection pathways for the particles.

It is useful to see how probability index distributions (Figs. 3.4 and 3.5) depict flow characteristics. Intuitively, in a dispersive regime the tendency for particles is to reorganise in an 'isotropic' manner at different positions, at each instant in time, in the absence of large-scale transport barriers (e.g the release at 215.5°E, Fig. 16-bottom panels, Appendix A) and as a response to the barriers' time evolution and interaction (merge-collapse-intensification) in space. Embracing such a mixing process[5], patterns in the computed probability index in an effective space context (from a particle occurrence viewpoint) should provide a connection between dispersion, stagnation and 'end-point' organization. Based on the distributions depicted (Figs. 3.4 and 3.5), eddy-intensified regions (Fig. 2.22) are positively correlated with more homogenized, higher probability index values (> -3.5, log_{10} scale). This is expected, since in eddy-intensified regions

[5]Mixing is considered the consequence of jet-filament formation and vortix spatial density in a holistic perturbed dynamic system. Focus here is on expressing the dynamics and not the background mechanism.

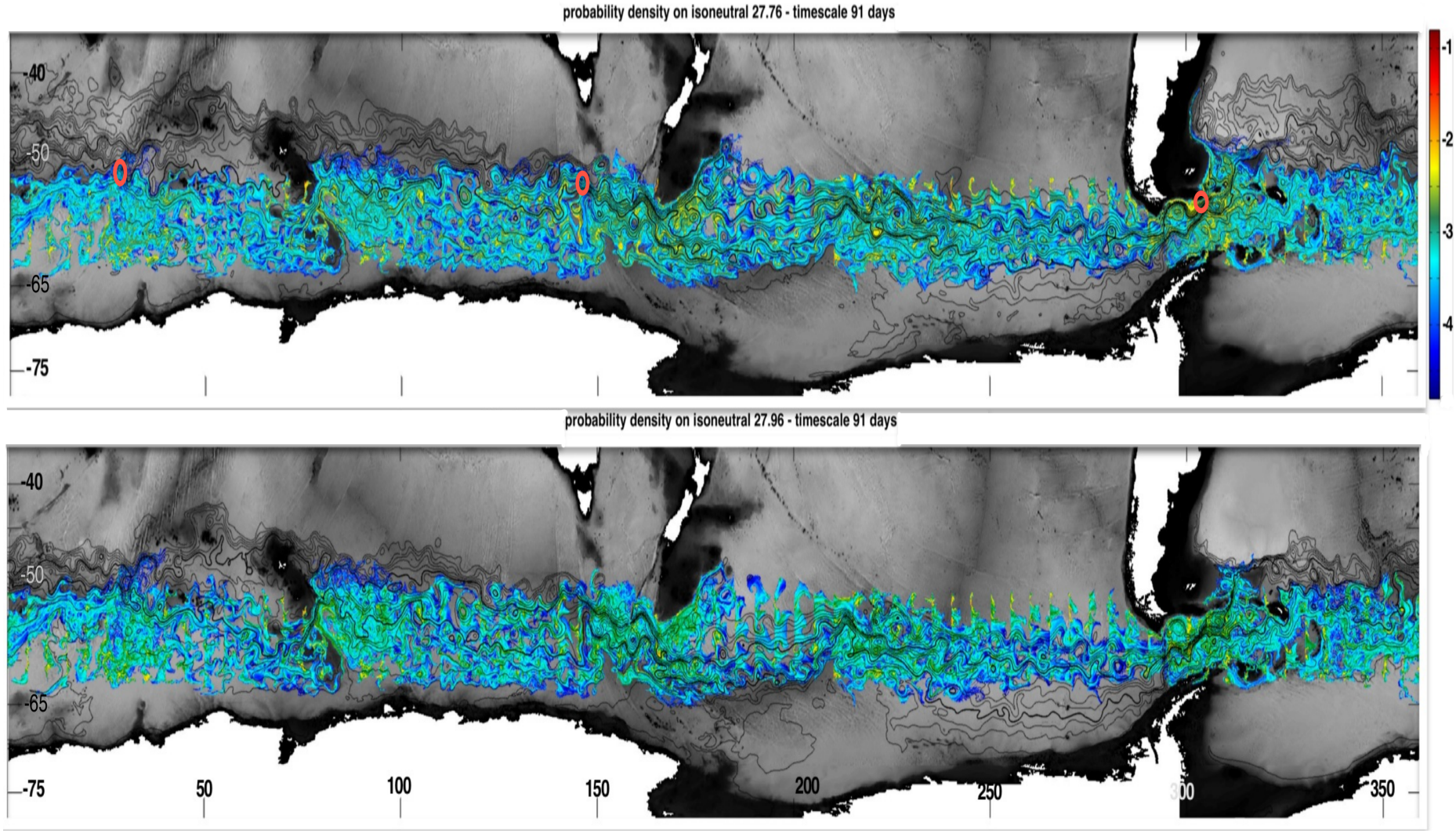

FIG. 3.4: Effective total pd (log_{10} scale) (see text for details) for occurrence events for all longitudinal releases, 5-359°, on isoneutral surfaces 27.76, 27.96, 28.06 and 28.16 (top to bottom) for a period of 91 days from initializing the particle releases. Red circles denote 'leaking' jets in the study of [*Naveira Garabato et al.*, 2011]. Black contour lines represent the mean geopotential anomaly (m^3 kg^{-1}) with respect to the surface for the aforementioned period. Contour spacing is 1unit, with bold lines denoting the 5 and 10 unit contours.

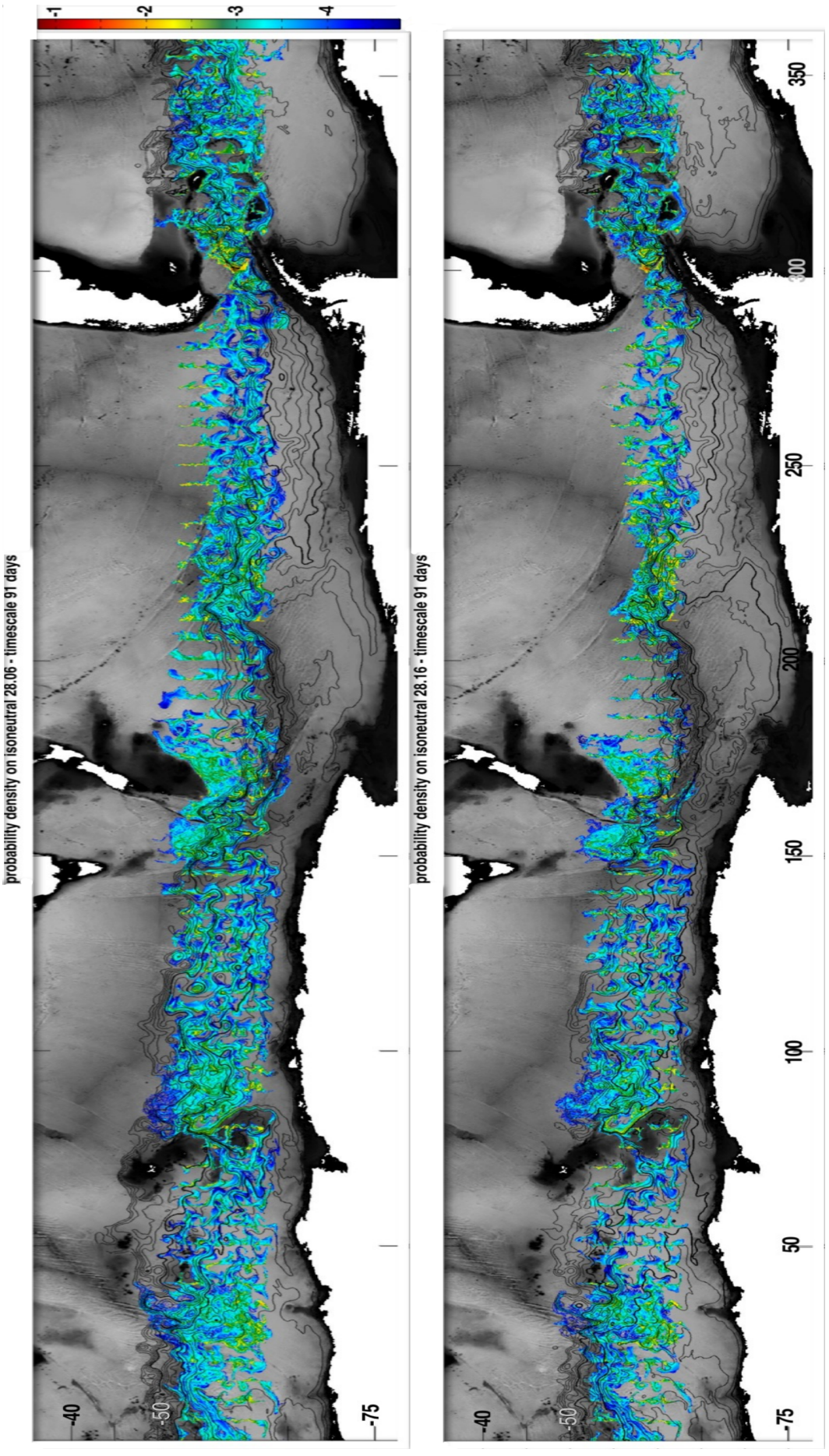

FIG. 3.5: Same as in figure 3.4 but for isoneutral surfaces 28.06 and 28.16.

particles are redistributed equivalently and randomly at all locations where the process of eddy stirring is effective. Cross-stream transport barriers, eddy-intensified regions and advection pathways all exhibit high probability indexes. Spatial homogeneity, though, is quite distinct. Floats in geophysical flows tend to drift up the gradient of eddy kinetic energy. Thus, the centre of mass of a cluster of particles is expected to migrate towards the more energetic regions [*LaCasce*, 2008]. On the other hand, intensified jets, because of kinetic energy spatial differentiation, tend to 'attract' particles and are delineated as filaments of higher index values. See, for example, 145°E poleward of Tasmania, along the meridional excursion of $\Delta\Phi$ contours and the ambient minima distribution just eastward (the transport barrier associated with this equatorward jet retains its effectiveness with a transition to denser isoneutrals).

Coherent vortices are delineated with circular and steady low to high values, depending on particle availability in the region for the period examined. These are ubiquitous in the ACC. They also correspond quite well with the closed contours of $\Delta\Phi$ (e.g see closed $\Delta\Phi$ contours at 120°E). Their vertical density coordinate mapping delineates a decrease in values and a more homogeneous distribution designating the weakening of the rotation-shear strain barrier and subsequent permeability increases. Regions that act as 'attractors' for particles have values (> -2.5 on the log_{10} scale). Empty centres (absence of particles during the release phase) or isolated circular patches of high values (presence of particles during the release phase) both signify impermeable vortices over the 91-day period.

Stagnation points in the flow are linked to slowly escaping and/or entering particles and thus are associated with advection 'stagnation' regions. Slowly escaping particle stagnation areas are illustrated by isolated patches of yellow and orange colours with minima-ambient values. Slowly entering particle stagnation areas are depicted by the minima. Space emptiness, when surrounded by records, is caused by the effect of transport barriers.

In theory, the probability index should be able to depict regions where the suppression of cross-stream transport ceases and jets become 'leaky' [*Naveira Garabato et al.*, 2011] (Figs. 3.4, red circles on the top panel) with increased ambient probability values in the respective areas; however, we were unable to replicate this tendency, perhaps because the 91-day period examined here is too small for the required spatial sampling of 'leaking' regions. Only in the area of the DP so we observe intensified jets in the vicinity of areas with high ambient index values, reduced ambient PV gradients (Fig. 8) and a noticeable pathway, just west of the main jets (diverging to the north) for the particles' escape route (exactly on the red circle in DP Figs. 3.4).

Nevertheless, the time persistency of the distributions cannot be assumed for time scales longer than those considered herein unless, we manage to justify the coherence of

the respective structures in a spatio-temporal framework in comparison to the variance of weak activity regions.

3.2.3 Structure persistency

Dynamical systems and mixing structures Are these finite-time Lagrangian structures, delineated by probability index mapping, the product of time-instant 'extreme' events or time-persistent distribution? *Haller* [2001] studied the role of Lagrangian coherent structures in mixing organization, when considering two-dimensional turbulence, recognising that such structures are special material lines[6], stable (repellers) and unstable (attractors) manifolds, that have a major influence on the kinematics of mixing over finite-time intervals. Apparently, in aperiodic flows such as geophysical dynamical systems, a material line is not expected to remain 'locked' in space but to exhibit a time-dependent movement [*Wiggins*, 1992; *Wiggins*, 2005]. According to *Haller and Yuan* [2000], local stretching in the flow appears to happen across coherent structural boundaries as a result of differentiated kinematic environments (local instabilities in the flow), while thinning and folding appear to happen along coherent structural boundaries. Both processes can be present at different flow instances, and each one can evolve into the other through flow progression (Fig. 16, Appendix B). In the probability index mappings herein, stretching is recorded by the spatial extensiveness of relatively high index values following filamented organisations of particles during the thinning and folding process and vice versa. Since these are instantaneous mappings, the only valid regions that we can deduce as the location of Lagrangian coherent structures are with regard to areas of relatively slowly varying velocity contours [*Haller and Yuan*, 2000], or in connection with persistent in-time structures (e.g PV gradients). The role of material lines in oceanic flows is that they constitute transport barriers and pathways. Thus they identify differentiated kinematic environments and are responsible for the development of the complex geometry accompanying an inhomogeneous mixing process through filamentation and stretching of tracer concentrations. Hence, the spatio-temporal distribution, density and evolution of these mixing regulators are important tools in the depiction of effective mixing regimes.

FSLE Visualising kinematic boundaries and pathways (hyperbolic trajectories) in oceanic flows takes advantage of how particles behave when approaching hyperbolic

[6] In dynamical systems theory, particles are organized along material lines in converging and stretching filaments (stable and unstable manifolds) constituting hyperbolic points at their intersection points [*Wiggins*, 2005]. The set of hyperbolic points in aperiodic flows is known as a hyperbolic trajectory, which is impermeable to particles and as such acts as a boundary to transport. A hyperbolic trajectory is a time-evolving structure in an infinite time series. Finite-time hyperbolic trajectories (or material curves) were approached with finite-scale -time formulations, i.e. the Lyapunov exponent and the 'leaking' method [*Aurell et al.*, 1997; *Haller*, 2001; *Schneider and Tél*, 2003].

trajectories with regard to their position along the corresponding stable and unstable manifolds. Particles in the vicinity of a stable manifold (repeller) are squeezed along this manifold until they are in close proximity to the hyperbolic trajectory (the set of points emerging from the intersection of stable and unstable manifolds) and transit to stretching along the unstable manifold (attractor). The close resemblance of the *Finite Scale Lyapunov Exponent* (FSLE) technique to a high density Lagrangian monitoring float experiment signifies it as a well-suited descriptor of oceanic flow characteristics [*d'Ovidio et al.*, 2004]. The FSLE, λ_δ, which is introduced as an alternative formulation for the study of dispersion processes, previously focused mainly on areas where the basin scale l_b was a restricting factor for asymptotic classical diffusion approximation [*Aurell et al.*, 1997; *Artale et al.*, 1997; *Boffetta et al.*, 2002]. Defined as the exponential rate of separation for a set of particles, with standard initial displacement δ_0 regulated by the dominant energetic scales it aims to decipher, it follows the relationship:

$$\lambda_\delta^n(\mathbf{x}, t_0, \delta_0|\tau, \delta_n) = \frac{1}{\tau} ln \frac{\delta_n}{\delta_{n-1}} \quad , \quad \lambda_\delta^n(t_0, \delta_0|T, \delta_n) = \frac{1}{\langle T \rangle} lnr \tag{3.3}$$

where $n = 1, 2, 3, ...$ and $\delta_n = r^n \cdot \delta_0$ with $r = ln\frac{\delta_n}{\delta_{n-1}}$. δ_0 and δ_n represent the initial and incremental separation distances of a particle's trajectory, from a trajectory initiating at position $\mathbf{x}$ at times t_0 and τ, respectively. T is the mean exit time for each separation distance, in terms of the respective time scale from one distance class to the next and $<>$ denote averages over all initializations. Values of r between > 1 and ~ 2 can be examined depending, in essence, on the spatio-temporal scales resolved for the flow dynamics' structures we aim to delineate [*Aurell et al.*, 1997]. Practically, the FSLE is computed over many realizations [*Boffetta et al.*, 2000], as an average or maxima, over pairs of trajectories' growth rates around a selected location $\mathbf{x}$ [*Koh and Legras*, 2002]. The forward and backward integration of particle displacements highlights stable and unstable manifolds for the respective periods.

FSLE is computed from monthly releases of particle advection time series (a period of 90 days is selected and considered adequate to resolve the spatio-temporal dimensions of the eddy field). The formulation of the release scheme aims to provide a qualitative insight in to full spatial scale representations. During initialization, particles form a cluster with grid point spacing δ_0 being $1/24°$, equal to $\delta_0 = 0.5 \times grid_{res}$ of OCCAM's $1/12°$ model. As such, regions of interest– eddy-intensified, weak and strong mean flow areas– are mapped within the uncertainties accompanying the initial separation and energetic scales [*Boffetta et al.*, 2001]. The final distance, δ_f, is selected at the equivalent length of 110 km (characteristic of general mesoscale variability but larger than the expected eddy length scale in the Southern Ocean [*Chelton et al.*, 2011]). A forward and backward in time advection scheme, aiming to depict the hyperbolic trajectories of the particles' travelling paths, is employed. Hence, repelling (stable manifolds of

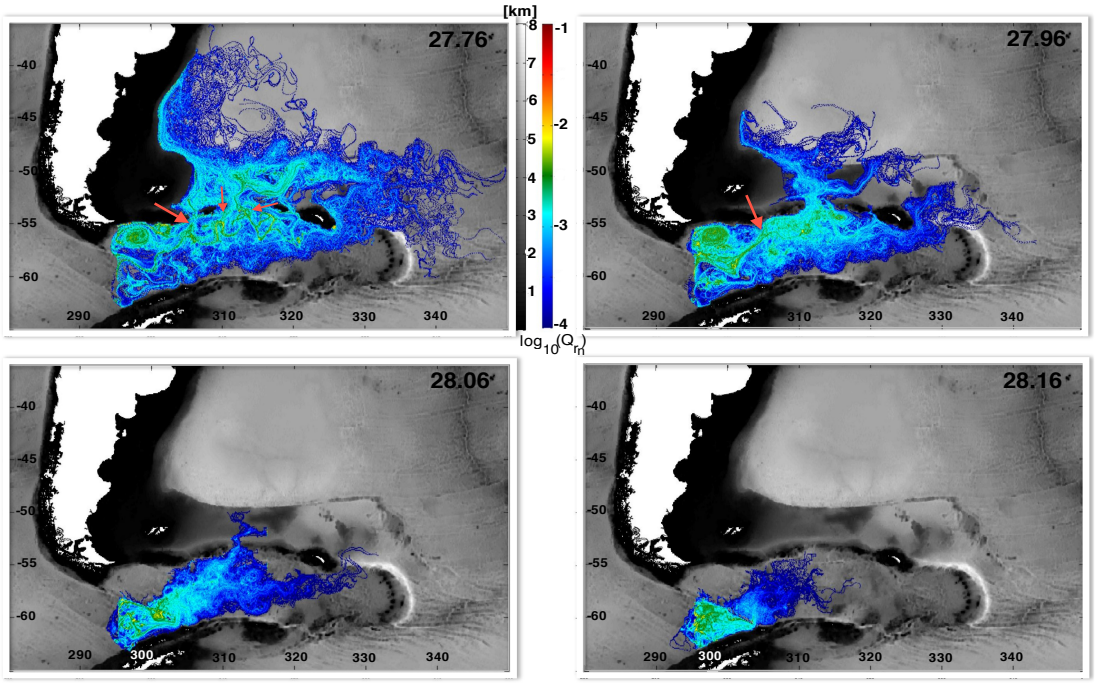

FIG. 3.6: Effective probability density (log_{10} colour scale, see text for units description) for occurrence events for a longitudinal release at 295°, on isoneutral surfaces 27.76, 27.96, 28.06 and 28.16 for a period of 365 days. Red arrows denote locations where we propose the depicted jet becomes 'leaky'.

hyperbolic particles' geometric space) and attracting (unstable manifolds of hyperbolic particles' geometric space) material lines are computed (with negative (positive) values denoting compressing (stretching) material lines) [*Joseph and Legras*, 2002; *Koh and Legras*, 2002; *Wiggins*, 2005]. Particle tracking follows the numerical scheme described in section 2.2, Chapter 2. Here, characterization of the largest separation rate is based on a measurement scheme similar to that found in *Joseph and Legras* [2002]. As a consequence, λ_δ is computed as the fastest growing distance for the temporal period of 90 days, reaching the separation scale δ_f (=110 km), among four anti-orthonormal particles around position $\mathbf{x}$. FSLE is mapped at location $\mathbf{x}$, at a distance the same as the initial displacement δ_0, from all four surrounding orthogonal directions. Both spatial and temporal scales under certain approximations are considered here as sufficient for the decorrelation of the examined particle trajectories.

FSLE and probability indexes FSLE computation provides us with a perspective on the 'mixing roadmap' in oceanic flows. Establishing a connection with the probability index of particles' distributions will allow us to decipher the intensity, structure's persistency and stirring[7] potential of local regimes. The scaled probability density Q_{r_n}

[7]We consider tracer mixing here as the ensuing stage of the stirring process acting for a sufficiently long time to produce finescale filamentation, thus leading to irreversible mixing.

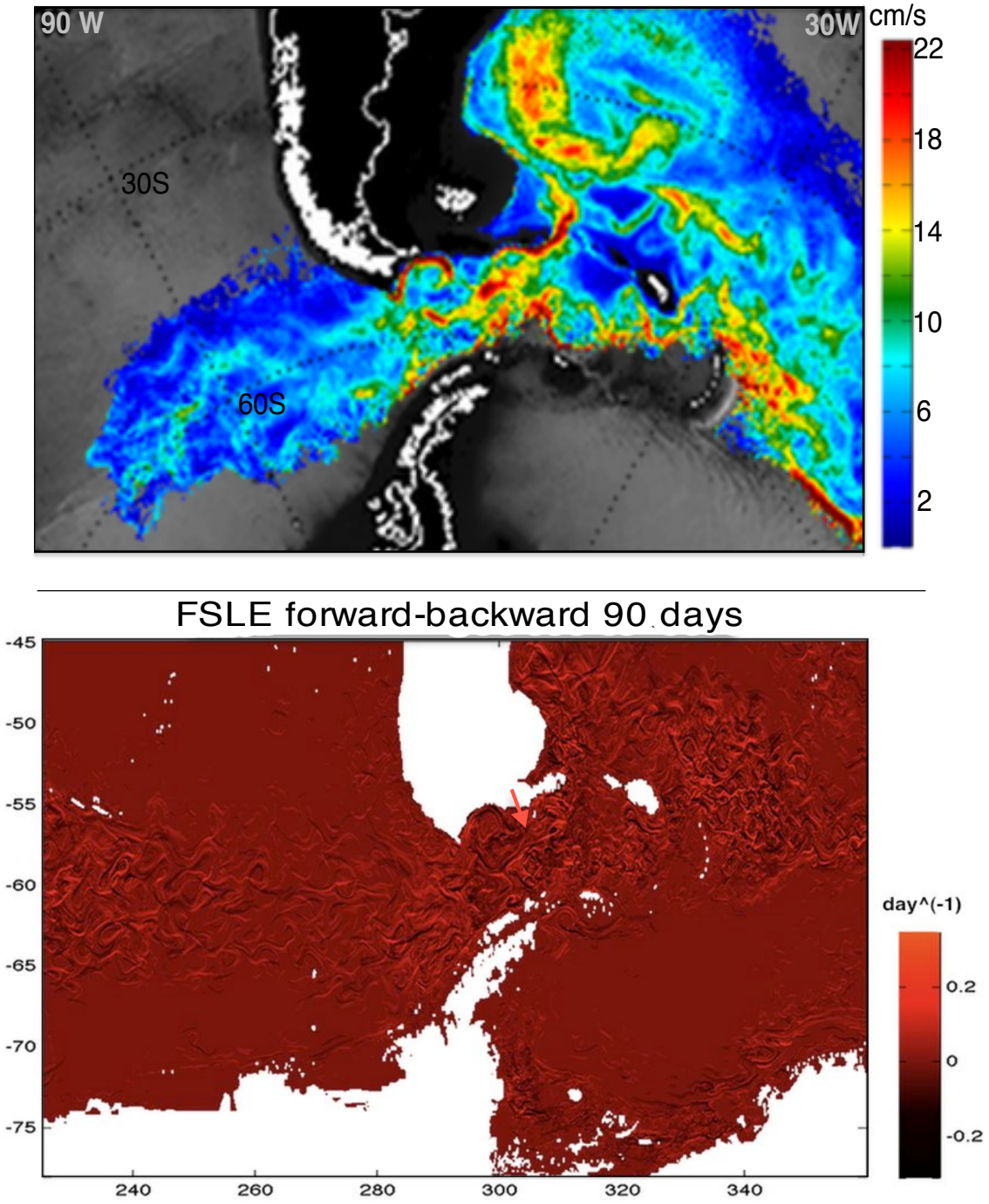

FIG. 3.7: (top panel) Lagrangian velocity (cm s^{-1}) and (bottom panel) FSLE (day^{-1}) with respect to the initial location of particles over the whole simulation period on isoneutral $\gamma^n = 27.96$. Stable (unstable) manifolds are accorded negative (positive) values, constituting kinematic boundaries over the period under examination and for the initial locations of the particles during their release.

for longitudinal release at 295° ($n = 55$) and for a period of 365 days from initialization (Fig. 3.6) is examined in comparison to the FSLE and Lagrangian velocity derived for all longitudinal releases in the area of interest (Fig. 3.7 - bottom and top panels, respectively). We choose Drake Passage as a case study of different 'mixing' regimes generated by the interaction of the following components: its complex bathymetry; its basin scale acting as a restricting factor for the application of classical diffusion theory; and flow intensity. Both the Q_{r_n} and FSLE distributions intelligibly delineate dynamic features of the flow. Advection is the factor responsible for the dispersion of the particles and, in effect, higher space capacity potential (SCP) (3.2) values for the different isoneutrals (Fig. 3.6). As such, SCP distribution also provides a measure of the general flow dispersion effectiveness scaled by release and time.

On isoneutral 27.76 (Fig. 3.6) the most prominent features illustrate the characteristic vortices system on the northern Drake Passage (a central dominant vortex, seen also on isoneutral 27.96, with two accompanying and significantly smaller size vortices, each at the west and east sides; green circular patterns) and an eastward meandering, jet-like structure that can be associated clearly with the pparticles' trajectory alignment with PV gradients (see also Figs. 9 and 12, Appendix A). These structures disappear during the transition to denser isoneutrals, where bottom topography controls the geometry of the density surfaces and consequently particle distributions and flow evolution. Characteristic features are: the topographical eddy-induced stirring delineation at 305° and 60°S on isoneutral 28.06 (green circular patch) transforming into an embedded topography flow on isoneutral 28.16; the reverse is seen at 300° where the spatial homogeneity of high probability index values (suggested here as the result of a topographical eddy over the rough seafloor) is depicted by filamented distributions with a transition from the 28.16 to the 28.06 isoneutral. This direct effect of topography is less obvious on lighter isoneutrals. The meandering structure on the 27.76 and 27.96 isoneutrals has a signal clearly corresponding to the FSLE record (only shown here for the 27.96 isopycnal). The geometric space of negative (positive) values denotes stable (unstable) manifolds (Fig. 3.7 - bottom panel). Particles concentrate and move along these kinematic boundaries. Homogenization is illustrated in connection with the increased complexity of manifolds, convoluted probability index strains and intensified advection (Fig. 3.7 - top panel). This can be seen clearly in the most energetic regions (for example east of Drake Passage at 310° of longitude). Westward of this area, a dipole (N-S direction) of low probability index values is actually controlled by frontal jet-induced transport barriers on the Lagrangian velocity representation (Fig. 3.7 - top panel). The geometric space evolution of attracting and repelling (FSLE material lines) points constitutes an indispensable system through the direct segmentation of space in dispersive and non- (or less) dispersive areas, as seen in the respective probability index illustration. Accordingly, the FSLE

indexes space with regard to this delineated mixing efficiency (see also Fig. 3.4).

Cross-stream complex mixing structures The delineated kinematic boundaries are not entirely effective as transport barriers throughout their course. On isoneutral 27.76 (Fig. 3.6), at 305°E (westward of the Shag Rocks Passage) and at around 315°E (Shag Rocks Passage), the depicted filamented structure (green colour) becomes 'leaky' (red arrows) and creates a pathway for particles in the Malvinas Chasm (see figure 3.3 for detailed bottom topography) while continue to propagate downstream. The equatorward 'loops' of the meandering large-scale filaments create deviating branches which provide escape corridors and homogeneous distributions of probability indexes indicative of local mixing 'pools' (see also Fig. 3.4). Chaotic mixing regimes, previously associated with chaotic advection with corresponding exponential separation rates of particles [*Pierrehumbert*, 1991; *Pierrehumbert and Yang*, 1993], emerge here in relation to the local absence of transport barriers [*Uleysky et al.*, 2012].

Why does the jet become 'leaky' in this location? *Wiggins* [2005] in his review study provides a number of references to explain the kinematic mechanism leading to cross-jet transport. The author mentions that induced persistent cross-jet flows are linked to primary disturbances having phase speeds close to the jet speed. *Naveira Garabato et al.* [2011] suggested that ACC jets become leaky where eddy stirring inhibition is non-effective in regions of large mean flow strain and where jets are narrow and twisted. They associate the breakdown of mixing suppression with the presence of stationary, short barotropic Rossby waves in the ACC's path, resulting in a topographic localization of eddy stirring [*Rhines*, 2007]. The non-parallel flow approximation is definitely valid here, based solely on the geometry of the meandering jet and in comparison with a favourably reduced ambient PV gradient distribution in the homogenized areas (Fig. 8, Appendix A). In the context of this study we did not examine the stagnation of westward propagating, short Rossby waves through the mean flow as a possible explanation for the dynamics behind the twisting and breaking down of mixing suppression in transport barriers. Nevertheless, we were able to identify topographic steering of the jet as a major factor in the emergence of deviating branches at the 'loops' of the meander.

We propose as a mechanism for the observed 'leakiness' in DP a combination of azimuth jet 'loops' due to bottom topography, as they have significant wave amplitudes, as seen in figure 3.6 (top left panel), with either a concurrent direct topographic slowing down of their phase speed or through the presence of stagnant coherent vortices over lower ambient bottom roughness regions (see also Fig. 3.3, left panel and Fig. 9, Appendix A). In this way the non-parallel twisted jets create 'stagnation' points at their 'loops' where the transport barrier effect is destroyed. The meandering of the jet is analogous with the advection speed of the jet (Fig. 2.22) and in effect the PV

gradients' spatial alignment (Fig. 8, Appendix A). We do not suggest that this kinematic mechanism actually exists in all regions where non-parallel flows are observed or expected to be the dominant expression of local flow dynamics. We do think that the structure of eddy stirring efficiency (if we accept that homogenized values of Q_{R_n} are indicators of this mixing capacity) is depicted more clearly by the distributions on isoneutral 27.96 at 310° of longitude. The convoluted strains of particles are associated with a multi-filamented spatial arrangement of kinematic boundaries correlated with strain and vortical elements (Fig. 9, Appendix A) which favour 'chaotic' mixing in the area through the non-parallel organization of the flow. The difference between the two isoneutrals is that the jet on the denser one is not 'strong' enough to 'overcome' the effect of the 'chaotic' organization of vortical and strain elements in its pathway. According to *Ferrari and Nikurashin* [2010], we can deduce that the structure inhibiting large-scale jet coherence is generated by the inability of the jet to further advect eddies downstream. This has as a corollary that mixing inhibition is not the result of mean flow shear. Nonetheless, the Q_{r_n}, Lagrangian velocity and FSLE records indicate the existence of a kinematic boundary acting as a transport barrier. We thus need to establish the existence of a factor that slows down the jet in a similar pattern to supercritical flows ending in stagnant water bodies. This mechanism leads to the generation of eddies and shear-strain pathways that constitute a further factor for jet segmentation and the emergence of multi-filamented structures. At the specific region and with the Lagrangian dataset approach we can only propose as our favourite candidate the role of bottom topography. Its effect on the flow is greater on the denser isoneutral through the generation of topographical eddies creating the 'stagnation' factor required. We will discuss this approach to mixing efficiency further in the chapters to follow.

3.3 Cloud dispersion. A real time experiment simulation.

Deciphering flow properties requires the statistical interpretation of cloud dispersion evolution. Examining the probability density distributions of particle occurrences (section 3.2.1) provides a means of visualizing oceanic transport capacity for the periods examined. Here, a cross-examination of the DIMES experiment (see B.6, Appendix B) in isoneutral and isobaric contexts is presented. While the scope of this thesis is not to reproduce or quantify a real-time experiment, it is interesting for two reasons to present tracer dispersion (a comparison with a tracer release simulation in OCCAM is provided in Appendix B) from the perspective of Lagrangian particles. First, as a validation approximation of OCCAM 1/12° model dynamics (even though this is better suited to future work, since data were not available from the field experiment, with regard to the evolution of the tracer, when writing this thesis). Second, as a descriptor of dispersion evolution from 'cloud' probability density values. The average effective

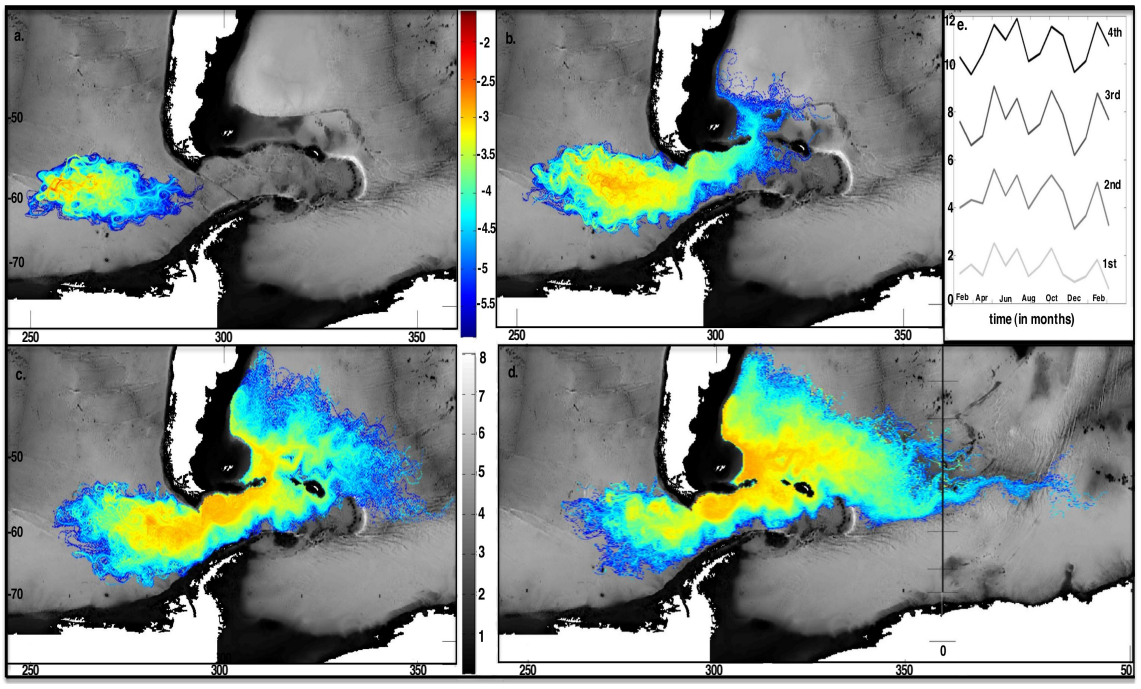

FIG. 3.8: Average effective probability density of the dispersion evolution of a cluster of particles (DIMES experiment-release at 255.5°) on neutral density $\gamma^n = 27.9$ surface for selected times of 1(a.), 2 (b.), 3 (c.) and 4 (d.) years. On panel e., the intra-annual variability of cluster sizes for monthly releases between 3315 and 3705 model days, and a travel time period up to model day 5500, are presented for cloud dispersion at the aforementioned yearly distributions (units in 10^4 1/12° grid box area –average 1/12° grid box area is ~ 45.36 km^2 with regard to the latitudinal extent of the distributions). Colour values are in the log_{10} scale.

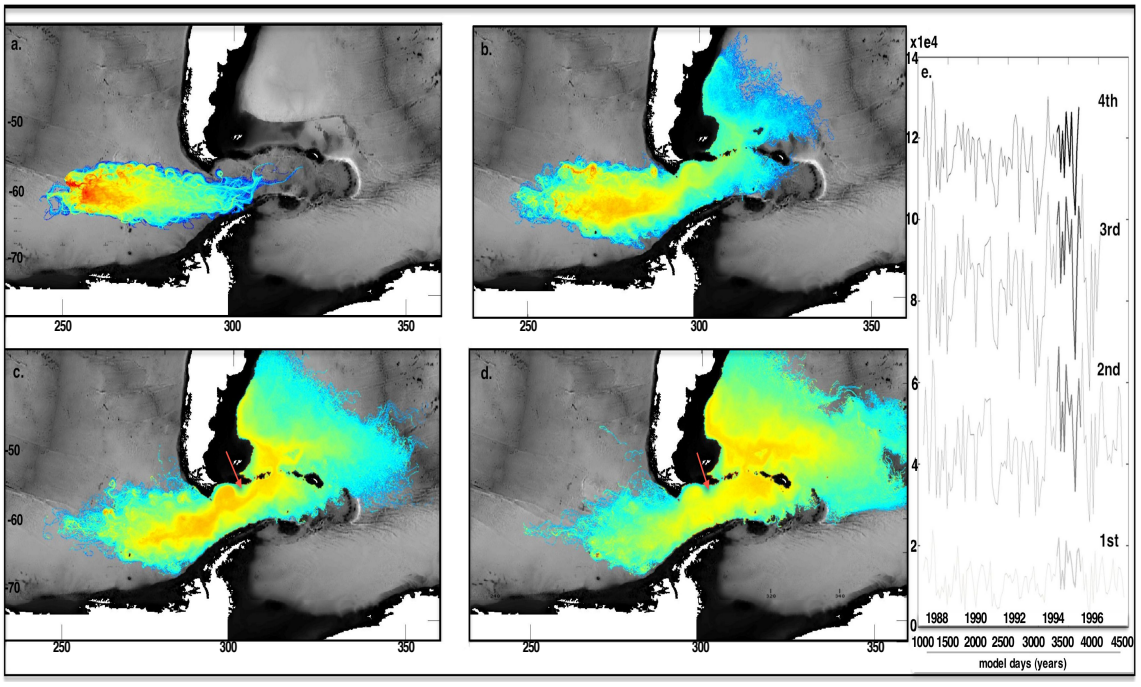

FIG. 3.9: Same as in figure 3.8 but for isobaric level 38 ($\sim$ 1252 m). On panel e., overlapping periods with the isoneutral releases are denoted by thicker segments, with calendar years (along with model days) seen on the abscissa. Compared with the isoneutral distributions in figure 3.8 (see text for details). Colour scale same as in 3.8.

probability density (see section 3.2.1) is computed as yearly time averages of spatial ensembles $\langle PD_{\mathcal{A}} \rangle$ ($\mathcal{A} = 1$ grid box size of OCCAM $1/12^{\circ}$ model) over all available monthly initializations. Since isobaric releases span a longer period (a cluster of particles in the DIMES context is released every month from model day 1095 to 4425), the existence of a potential statistically significant discrepancy needs to be examined. In accordance with the differentiation of advection dynamics and flow characteristics among isobaric and isoneutral velocity field representations, deciphering the statistical significance of results is based purely on variability signals derived from the isobaric distributions over equal duration periods and then compared with the respective time periods of the isoneutral realizations.

In figures 3.8 and 3.9, the computed averaged annual effective probability density is illustrated. Isobaric simulations exhibit greater spatial extent during the first two years of travel time. This is indicative of higher velocity values on the isobaric level. Averaged Lagrangian velocities on level 38 ($\sim$ 1252 m) are approximately higher by 5 to 10 cm s^{-1}. The difference between the two computed Lagrangian velocities minimizes and at points reverses on entry into the Scotia Sea (not shown here). As such, distributions during the $3rd$ year and on, scale almost identically on horizontal space. The space extent time series, though, shown in panels e. in 3.8 and 3.9, reveal that even for the $3rd$ year, when distributions seem in agreement, a mean difference of roughly 0.5×10^4 grid boxes (or $\simeq 2.27 \times 10^5$ km^2) exists. This is an area of approximately 1/3 of the Scotia Sea (7×10^5 km^2). One of the main reasons for this situation, apart from differences in advection dynamics, is that the isoneutral distributions appear to comply better with dominant flow features, i.e. the ACC's jet structure and their spatial variability or coherent vortices (see, for example, the spatial extent of the two schemes into the Scotia Sea). Consequently, local areas where dispersion is inhibited or suppressed have a higher census on the isoneutral representation. This is partially true because balanced natural flow is expected to be isopycnal, regardless of their barotropic or baroclinic nature, with preferential alignment along frontal jets [*Hofmann*, 1985].

Examining the $1st$ year probability density distributions closer, fine structures are depicted by both realizations, especially in regions with low density values. One additional reason for the more locally dispersive (homogenized) illustration of densities in space through isobaric initializations can be attributed to longer averaging initialization periods. This point is valid, especially if the time series have low autocorrelation values. Indeed, the analysis of the time series of the space extent have a maximum autocorrelation of < 0.2 for time lags different to zero. This implies that the illustrated discrepancies in distribution, shown in figures 3.8 and 3.9, are prone to the overall variability of isobaric time series based averages (high autocovariance of the time series at temporal scales longer to the ones regraded here are not excluded). On the contrary,

cross-correlations of the isobaric time series are 0.82 (zero lag), 0.36 (210-day time lag) and 0.66 (zero lag) for pairs of the $1st$ with the $2nd$, $3rd$ and $4th$ years, respectively. Higher cross-correlation values are computed for both isobaric and isoneutral distributions when examined for the same period (yearly averages for model days 3315 to 3705 monthly releases). It is interesting that the intra-annual signal is retained, in general, among the different annual distributions. This is probably indicative of the fact that, when examining the spatial extent for the time periods covered here, climatology during the initialization of the releases is fundamental for their evolution , which is in agreement with *Davis*'s [1991] assertion about the importance of initial conditions in particle trajectory evolution. Nonetheless, the rate of spatial expansion is not implied to be monotonic for a specific release.

In conclusion, 'clouds' of higher values seem to disperse analogously in the spatio-temporal context herein. One of their main differences is that the maxima in isobaric releases appear to shift poleward on the $2nd$ and $3rd$ year distributions in the Drake Passage area. The isobaric surface is in essence a horizontal section of various isoneutrals due to poleward and upward isopycnal tilting (Figs. 2.22 and 2, 3). Hence, isobaric 'cloud' dispersion represents denser isopycnals in the poleward direction. In our case particles appear to be shifted poleward at DP with transition to a denser isoneutral, which is mainly due to an equatorward constraint caused by isoneutral surface geometry (Fig. 3.4 and 3.5). In general, isoneutral releases conform well with the average geometry of the neutral density surface and mean positions of the dynamic height with respect to the surface, with no pronounced extrusions from local transport barriers. This also has some implications in observational oceanography experiments designs aiming to decipher mixing, since isopycnal floats will, based on the distributions presented here, provide a more robust sampling of transport barriers. Regardless of all the exhibited discrepancies, isobaric and isoneutral representations are in good agreement when considering time averages. Diffusivity estimates, though, are expected to be overestimated in an isobaric context, especially in intensified advective environments characterized by vigorous shear dispersion and baroclinicity [*Davis*, 1991].

3.4 Concluding remarks

In this chapter we deciphered flow characteristics associated with kinematic boundaries and advection pathways in the ACC. We illustrated how flow structures, linked to dynamical systems theory, and their temporal variation can lead to 'favourable' local mixing regimes. Particle occurrence distributions depict an ACC acting as a constraint for particles released outside or inside of its main path in order to infiltrate its major frontal jet structure. Localization of mixing is delineated as a process emerging from a

complicated spatial structure alignment of kinematic boundaries acting as repellers and attractors of particles, thus inducing the squeezing and stretching of tracer filaments (particle patches) in the respective directions.

Overall, the distribution of probability density values delineates the persistence of flow structures over a substantial period in specific regions. This pattern is common to all isoneutrals. We think that the persistence of the structures depicted by the Q_{r_n} record, at the temporal scales of 91 and 365 days, is remarkable and fundamental for the spatial arrangement of particles. In theory, thesubstantial time evolution of particle dispositions would exhibit a 'chaotic' distribution, with the particles exhibiting anisotropic dispositions, mainly affected by the instant local regime of velocity partition distribution, which will tend to smear out as the shear-strain vortex system interaction rearranges the flow through time evolution.

In order to depict particle rearrangement we employed and illustrated the usefulness of Lagrangian representations. Within the 91-day mappings period we connected regions exhibiting homogenized large-scale distributions with eddy-intensified areas, 'chaotic' (non-parallel) filamentation of PV gradients and bounded by topography or azimuthal meandering of geopotential anomaly contours associated here with geostrophic streamlines. On a different time series involving the 365-day mapping of a probability index in the Drake Passage region (Fig. 3.6), there is a clear indication that the flow becomes more dispersive, or at least on the 27.96 neutral density surface. We attribute this finding to the weakening of large-scale jet structure coherence. The same argument is not valid for the denser surfaces, though, since their geometry (merely as to their spatial extent) is substantially different at the region of interest. The effective probability index visualizes the jet-vortex system described as being in apparent conformity. Collocation of the delineated structures with PV gradients was also identified. This flow and local regime mixing potential segmentation, as shown with the FSLE and Q_{r_n} indices, is an important factor that should be considered in eddy diffusivity parameterizations, as it presents a more detailed and subtle view of the responsible underlying mechanism. In this thesis's context, the time persistency of flow structures is of primary importance when deciphering representative (or absolute) diffusivity distribution with respect to the dynamics of the flow.

The depicted flow characteristics and the probability index mappings in relation to the FSLE gave us an insight into a possible mechanism for the observed 'leakiness' of jets in DP. There the jet structure becomes 'leaky' as a result of a combination of large wave amplitude meanders slowed down by stagnant coherent vortices or topographic obstacles. Within the same context we proposed that the structure of eddy stirring efficiency, accepting that homogenized values of Q_{R_n} are indicators of this mixing capacity, is associated with convoluted strains of particles in a multi-filamented, non-parallel spatial

arrangement of kinematic boundaries correlated with strain and vortical elements. A fundamental requirement for this mechanism is 'stagnation' areas downstream of intensified coherent jets. We believe that these could be created by a network of topographical coherent vortices or an eddy field generated downstream of intensified jets from the dissipation of their kinetic energy and PV conservation (analogous to supercritical jets entering stagnant water bodies). The most important factor delimiting and conserving these 'stagnation' areas is to be bounded by topography itself or topography steered kinematic boundaries. Several examples of this potential mechanism in effect exist, for example at 30°, 90° and 150°E, all residing within the main ACC path. We need further justification for this mechanism by computatiin the diffusion and mapping of the mixing structure. At this point, and with the probability index mappings, we are not certain as to what degree we could assert that mixing suppression in the ACC is not due to eddy propagation speed with the mean flow [*Ferrari and Nikurashin*, 2010] but instead is due to mean flow shear, as we propose to be the case in DP.

Even though the probability index is a useful tool to illustrate the complex structure of geophysical flows and their characteristics, it remains a qualitative assessment of mixing capacity and structure persistency. While the effectiveness of the illustrated kinematic boundaries and advection pathways was addressed during the early stages of particle advection, we believe that these relatively small time scales are fundamental for depicting the mechanism described. However, we aim to establish a connection between the dynamical features depicted by the probability index and a measure of the homogenization rate for the respective environments by computating absolute diffusivity and relative dispersion over extended periods in Chapters 4 and 5.

Chapter 4

Diffusion in the ACC

4.1 Introduction

4.1.1 Deciphering Mixing

As a critical component of global ocean circulation, the ACC provides a pathway for tracers and water mass exchange between the Pacific, the Atlantic and the Indian oceans. Its significance as one of the primary global climate regulatory factors has been recognized in numerous studies. The relevance of the ACC to the global heat budget (and eventually climate) depends on the absolute strength of the current and on the fluxes that mix water from the subtropics into and across the ACC [*Gille et al.*, 2001].

Deciphering the way the various components of Earth's climate interact and improve our capacity to delineate future climate projections requires an intrinsic understanding of the major controlling factors of dynamical systems evolution. One of the most important regulatory components, in both oceanic and atmospheric dynamics, is turbulent mixing. Turbulent mixing by geostrophic eddies is closely related to circulation patterns and water mass formation, stratification maintenance and mixed layer homogenization in the Southern Ocean. With theoretical and observational studies still presenting results that vary greatly, a representative parameterization of turbulent mixing is of the utmost importance in our effort to determine and predict the ramifications of climate change.

Various key parameters in relation to eddy mixing (EKE, mean flow and topography interaction) in the ACC were discussed in the introductory chapter and Chapter 3 of this thesis. While many studies have proposed different theories to demonstrate a connection between them [e.g *Killworth*, 1997; *Zhurbas*, 2003; *Waugh and Abraham*, 2008; *Shuckburgh et al.*, 2009a; *Smith and Marshall*, 2009; *Ferrari and Nikurashin*, 2010; *Griesel et al.*, 2010; *Naveira Garabato et al.*, 2011; *Lu and Speer*, 2011], general agreement has yet to be established.

The spatial distribution of eddy stirring in the Southern Ocean, as in other areas, is still an ongoing argument with regard to its role as an indicator of eddy diffusivity variability. Estimates differ with regard to the suppression of mixing by frontal jets and mean-flow intensity, enhancement with depth on steering levels below the ACC jets' cores and whether an analogous scale to eddy kinetic energy (EKE) exists. There are two fundamental hypotheses regarding eddy stirring: the first one embraces a high EKE analogy to an invigoration of eddy diffusivity [*Holloway*, 1986; *Visbeck et al.*, 1997; *Waugh and Abraham*, 2008; *Sallée et al.*, 2008b], in line with homogeneous turbulence theory and mixing intensity scaled as the product of $\sqrt{EKE}$ and an eddy mixing length $\mathcal{L}_e$ derived from classical diffusion theory [*Taylor*, 1921; *Davis*, 1991]; the second hypothesis promotes the idea of the existence of a Rossby wave critical layer where eddy diffusivity is enhanced [*Killworth*, 1997; *Smith and Marshall*, 2009; *Abernathey et al.*, 2010]. A third emerging perspective, introducing the factor of mean flow intensity when considering eddy diffusivities, was posited by *Shuckburgh et al.* [2009a]. Mean versus eddy flow interactions [*Stammer*, 1998; *Hughes and Ash*, 2001] scale down to the delineation of depicted non-coherent, locally reorganised barriers in the flow [*Sokolov*, 2002]. The generation, effectiveness and persistence of regional frontal jets was evaluated by *Thompson et al.* [2010] by examining isentropic potential vorticity (IPV) gradients. The role of topography in the ACC's jet structure was also indicated in this study.

This part of the present study explores the dynamical processes related to the isopycnal mixing of the ACC below the mixed layer on four density surfaces computed from a mesoscale eddy-resolving GCM. We aim to illustrate the spatial distribution of eddy stirring in connection with mean flow intensity, EKE, topography and the role of potential vorticity gradients.

4.1.2 Chapter outline

Hereinafter, Lagrangian statistics in the context of classical diffusion theory are presented. Lagrangian time integral and characteristic eddy length scales are estimated for single particle statistics. Absolute diffusivity is presented in the context of classical diffusion theory and caveats in the different approximations are discussed.

Relative dispersion and diffusion from pairs of particles are calculated and analysed with respect to prevailing mixing theories. A comparison to relative dispersion variability at selected regions is examined. The ability to detect transport 'barriers' and the role of potential vorticity gradients in diffusivity evolution is also considered. The efficiency of eddy stirring is examined in comparison to the dispersion of numerically integrated particles' trajectories and vortex field mapping by computating the Okubo-Weïss parameter. The interaction of vortices with jets is examined in the context of 'coherent' and persistent structures, and their role as an eddy-stirring mechanism is evaluated.

Emphasis is given to local averaging factors, thus indicating their prominence in the time evolution of dispersion and highlighting the importance of local dynamics in deciphering eddy mixing. Our results are accompanied by an evaluation of the Okubo-Weïss parameter and the mixing suppression factor [*Shuckburgh et al.*, 2009b; *Nikurashin and Ferrari*, 2010; *Naveira Garabato et al.*, 2011] for selected regions. Effectiveness in detecting barriers in the flow is ventured through computation of the aforementioned parameters in two distinct Lagrangian experiment formalizations; the previously described SOL experiment (see section 2.3.4); and releases on selected regions with a spatial density of one numerical particle at each node on a $1/24^\circ$ grid resolution for all isoneutral surfaces and for a period of 90 days. A mechanism is proposed in order to justify the depicted distributions.

4.2 Absolute - relative dispersion - Eddy diffusivity

4.2.1 Diffusivity context. Single and multiple particle statistics.

Single particle Formulating diffusivity κ_{Taylor} [*Taylor*, 1921; *Davis*, 1991] from a time-varying velocity field requires deriving the unresolved motions component from the velocity time series. In a Lagrangian framework and from a *single particle's* perspective, diffusivity κ for a particle arriving at position $\mathbf{x}$ at time t_0 is described in equation (4.1),

$$\kappa_{ij}(\mathbf{x},t) = \int_{-t}^{0} \langle u_i'(t_0|\mathbf{x},t_0) u_j'(t_0+\tau|\mathbf{x},t_0)\rangle \, d\tau \tag{4.1}$$

where τ is the autocorrelation time lag and u' the residual velocity in equation (2.12). The integral is computed backwards in time, denoting that the current displacement of a particle at position $\mathbf{x}$ and time t_0 is the integration of all previously experienced velocities. The lower integral limit $-t$ is regulated by the assumption of homogeneous displacement behaviour exhibited by the particle in line with specific spatial scaling [*LaCasce*, 2008]. In a preceding transformation with a Lagrangian notation, based on the moments of a probability density function $Q(X|t)$ for a homogeneous flow (at least at the spatial extent constructed), dispersion is expressed by the second central moment [*Sallée et al.*, 2008b] as $\overline{D_0^2}(t) = \overline{(X(t) - \overline{X}_0)^2}$, where the overbar denotes the mean over all available particles. $\overline{D_0^2}$ is the absolute dispersion and describes average displacement with regard to the particles' initial positions $\overline{X}_0$. Diffusivity $\kappa(t)$ is then derived by computing the time derivative of $\overline{D_0^2}$ as

$$\kappa(t) \equiv \frac{1}{2}\frac{d}{dt}\overline{\mathcal{D}^2}(t) \tag{4.2}$$

An analogous scaling of diffusivity time dependence is employed for characterizing of diffusion evolution regimes. The characteristic temporal dispersion scale is represented by the introduction of the integral time T_{L-E}, where the subscripts L or E denote a Lagrangian or Eulerian framework. The integral time denotes the time frame over which a particle's or an Eulerian point's velocity remains highly correlated with itself, and thus it is basically a quantity measuring the time scale over which a particle or point in the velocity field retains a memory of its previous kinematic state. T_{L-E} is computed from the integral of the velocity autocorrelation function $R(\tau)$ in Eq. (4.3).

$$T = \int_0^\infty R(\tau)\, d\tau \tag{4.3}$$

Assuming a stationary mean flow, and considering the spatio-temporal scaling approximations required in order to adopt a valid decomposition of the flow motions, only the turbulent component will contribute to the particle's varying motion (see Chapter 3 2.4.1). The normalized velocity autocorrelation function, $R(\tau|\mathbf{x})$, at location $\mathbf{x}$ is defined in equation (4.4).

$$R(\tau|\mathbf{x}) \quad = \quad \lim_{t_z \to \infty} \frac{1}{\sigma_{u_t}^2 t_z} \int_0^{t_z} u'(t|\mathbf{x}) u'(t+\tau|\mathbf{x})\, d\tau \tag{4.4}$$

where σ_{u_t} the standard deviation of the velocity component equal to the *rms* residual eddy velocity component $\mathcal{U}'_{rms}$. In a Lagrangian framework, $R(\tau)$ is calculated for a particle trajectory, in which case the notation $\mathbf{x}$ becomes redundant. Thus, the dispersion of a *single particle* in a Lagrangian framework can be rewritten as (4.5)

$$\overline{D_i^2}(t) = 2\sigma_{u_{i,t}}^2 \int_0^t (t-\tau) R_i(\tau)\, d\tau \tag{4.5}$$

where the overbar denotes the average over the designated time. The t subscript in the $\sigma_{u_{i,t}}$ indicates the time scaling of the velocity decomposition and refers to the transient character of this component, while the i subscript denotes the specific trajectory under analysis.

Diffusivity κ_∞, then, in the classical diffusion theory context, is commonly computed as the product of $\overline{EKE}$ with the derived integral time T_{L-E}.

Taking into consideration that a particle experiences a variety of dynamic regimes, as recorded in a trajectory's evolution, $R(\tau)$ will vary for different particle paths. Even for a single particle, depending on the lengths of its trajectory over which autocorrelation is computed, the distribution of $R(\tau)$ will exhibit variations. *Pasquero et al.* [2001] examined the relationship of Lagrangian integral times with particle trajectory lengths,

by considering a single particle dispersion parameterization in a two-dimensional turbulence framework. In the same context of a particle's trajectory length scaling of $R(\tau)$, *Veneziani et al.* [2004] analysed the variability of the autocorrelation function with respect to particles' positions in vortices. A common practice solution, aiming to provide a statistically significant result, is to account for an ensemble of a high number of trajectories with uniform spatial distribution and sufficient travel time [*Davis*, 1991]. In the real ocean, though, such an ensemble is in most cases non-existent.

Multiple particles In the case of *multiple particles* analysis, the squared separation distance for a set of particle pairs is equivalent to relative dispersion, which is notated as

$$\overline{\mathcal{D}^2}(t) = \langle (X_i - X_j)^2(t) \rangle \tag{4.6}$$

where $\langle \cdot \rangle$ denotes the average computed over all possible pair combinations in the designated set of particles and subscripts i, j denote the particles in a pair. Deriving relative dispersion follows a joint probability function measuring the prospect of a position's occupation x by a particle i at time $t_0 + \tau$ with respect to a particle's j position, $y|t_0 + \tau$, and with regard to initial positions x_0 and y_0 at time t_0. If $\mathbf{x}, \mathbf{x}_0$, the particles' positions and $\mathbf{d}, \mathbf{d}_0$ the separation distances among paired particles at times $t_0 + \tau$ and t_0, respectively, their PDF, following the notation devised by *LaCasce* [2008], is

$$Q(\mathbf{d}, t_0 + \tau) = \int P(\mathbf{x}, \mathbf{d}, t_0 + \tau | \mathbf{x}_0, \mathbf{d}_0, t_0) d\mathbf{x}_0 \tag{4.7}$$

and relative diffusion κ_r formulates as the second central moment of the above distribution, or equivalently as the time derivative of relative dispersion, analogous to (4.2) and by substituting (4.6)

$$\kappa_\tau = \overline{\mathbf{X}_{ij} \mathbf{u}_{ij}} \tag{4.8}$$

where $\overline{\mathbf{u}_{ij}}$ is the separation velocity of all possible pairs of particles.

We will present both single and multiple particle statistics in order to delineate the scaling of diffusivity in the ACC with respect to jets, EKE and bottom topography. Computation is performed along- and cross-stream by the local mean Eulerian velocity vector. At each particle's position the mean Eulerian velocity is linearly interpolated and subtracted from instantaneous velocity. The computed residual velocity is then projected along and across the mean velocity vector, thus ensuring that cross-stream diffusivity by the mean flow is zero.

4.2.2 Diffusivity regimes

In the simplest cases of flow (i.e. absence of coherent structures), and for temporal scales significantly shorter than the integral time, $\tau \ll T_{L-E} \rightarrow R(\tau) \approx 1$ (since memory of previous motion is correspondingly high when time approaches the zero time lag). In such a regime, the flow field can be considered as stationary at the spatial extent examined. Dispersion will scale proportionally to the squared velocity $\overline{D_0^2}(\tau) = \overline{u(\tau)^2}\tau^2 = 2\overline{KE}(\tau)\tau^2$, so particles will undergo a quadratically growing law (ballistic regime).

Examining the case where $\tau \gg T_{L-E}$ and the velocity autocorrelation integral converges to a constant value (accordingly, in this asymptote limit $\lim_{t\to\infty} \int_0^t R(\tau)\, d\tau$ converges to a constant value), dispersion as formulated in equation (4.5) should increase linearly. Thus, diffusivity, as defined in (4.2), is constant. Diffusivity in the asymptote limit is scaled as $\kappa_\infty = \mathcal{U}'^2_{rms} T_{L-E}$ and is characterized as absolute diffusion [*Davis*, 1982], hence suggesting the representation of advection as a diffusive process [*LaCasce*, 2008]. In this regime, particles are infused with a random or Brownian movement walk [*Rupolo*, 2007]. This distinguishes the *standard diffusion* process regime [*Artale et al.*, 1997] in which dispersion is computed over scales notably greater than the typical scale of the velocity field.

One should point out that the convergence of the velocity autocorrelation functions is addressed in a statistical context, meaning that the approach is based on the examination of an ensemble of Lagrangian trajectories for the spatially specified dynamically homogeneous regions. Thus, we expect great variability for individual events but a statistically robust diffusive spreading for a large ensemble of such events [*LaCasce*, 2008].

How does relative diffusion behave with respect to the cross-correlation of particles' velocities at different separation scales? An immediate physical parallel can be inferred for small and large separation distances. In a dynamic homogeneous regime, at scales comparable to the characteristic velocity scale l_u, particles' responses to the imposed advective-diffusive transformations are similar. Large pair distances place particles in 'disparate' local dynamic regions and consequently their velocities are uncorrelated. Analogously to a *single particle* dispersion analysis of growth variability with respect to integral time, κ_τ encounters quadratic growth for $t \ll T_L$ (*ballistic* regime) and asymptotes, theoretically, at a steady state κ_∞ which is equal to twice the absolute diffusion at times $t \gg T_L$. *Veneziani et al.* [2004] and *Rupolo* [2007] (see also the review paper of *LaCasce* [2008]) give a detailed analysis of the relative diffusion relationship on intermediate time scales, $\tau \approx T_{L-E}$, where velocities are correlated and consequently dispersion is dependent on the relative scale. They analyse the evolution of diffusion with respect to a logarithmic power spectra slope α. A sub-diffusive regime is identified with dispersion $\overline{\mathcal{D}^2} \propto t^\alpha$ and $\alpha < 1$, where the dispersion's growth rate is smaller in

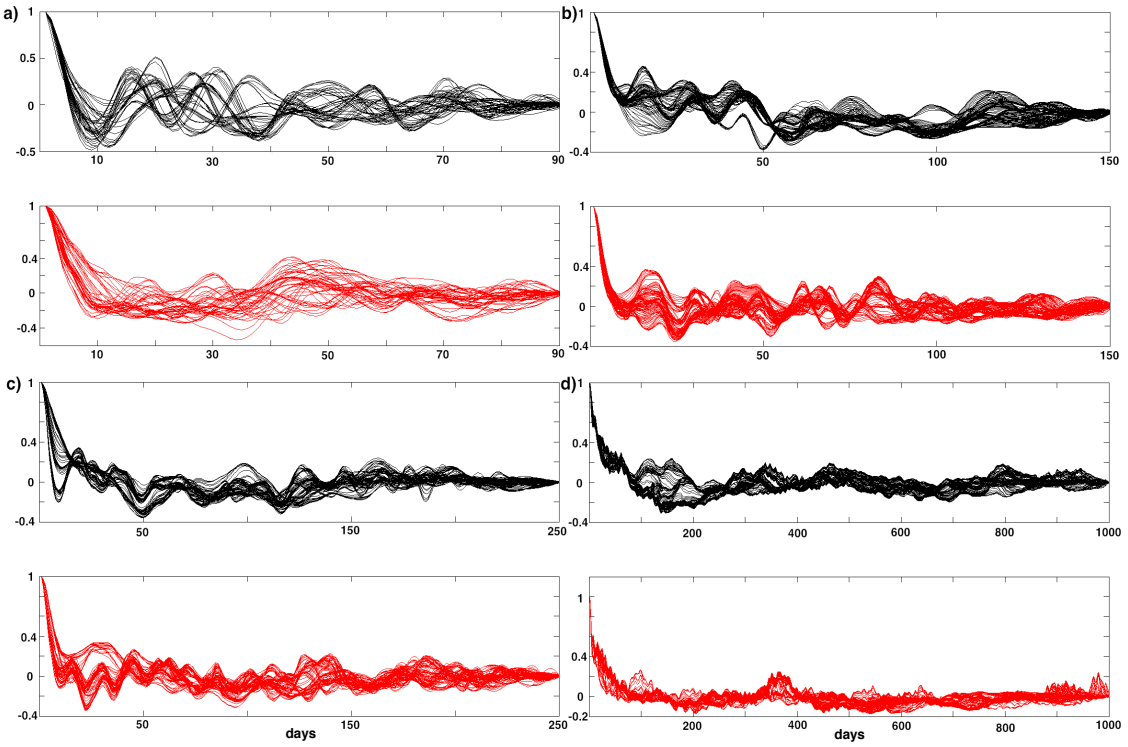

FIG. 4.1: Plots of autocovariance function R_τ (along-stream (black), upper panels - cross-stream (red), lower panels) for randomly selected spatial points on specific regions representative of ACC dynamics. Each function represents a fixed point in space. a)-d) Different time series 90-150-250 and 1000 days, respectively. The oscillatory character of individual events, with pronounced negative and positive lobes denoting late time lag correlations, can be seen in even the longest time series.

comparison with typical diffusive regimes that share the same parameters; a super-diffusive regime where dispersion scales proportionally to t^α and $\alpha > 1$. Exponential growth is expected for steep spectra ($\alpha \gg 3$), which signifies a *Lagrangian chaos* regime (see also Chapter 2, page 31).

The finite scale of available velocity data time series does inflict an upper time limit on the auto- and cross-correlation formulations considered in the theoretical context of integral time estimation, assuming convergence of the autocorrelation integrals at an infinite time. Since the integration is performed in practice on a finite defined domain, uncertainty emerges regarding the relative scale of dependence of the integration domain on the 'physically' representative domain. An autocorrelation function presents various forms of spatial dependence and minima that do not necessarily decrease with time. A usually rapid decrease until the first zero-crossing time lag is followed by oscillations which are either negatively or positively correlative in character (Fig. 4.1). The corresponding correlation is not constrained to small amplitudes, and thus, oscillations at large time lags may contain essential information about the underlying dynamic relations of energetics.

Anomalous diffusion [*Artale et al.*, 1997; *Berloff et al.*, 2002; *Reynolds*, 2002; *Ferrari*, 2007] (in the sub- or super- diffusive regime) claims an important place in the formalization of dispersion characteristics and the evolution of particles' trajectories in oceanic flows. Anomalous dispersion regimes are dynamic environments where dispersion does not grow linearly with time for $t \gg T_L$, as *Taylor's* classical theory of particle displacement evolution states. *Ferrari* [2007] provides a detailed description in extending the approach to portraying anomalous diffusion in the presence of coherent structures beyond the classicalrelative dispersion $\overline{\mathcal{D}^2}$ approach. In general, as a first approximation to characterizing the dispersion regimes the scaling of dispersion with time, $\overline{D^2}(t) \propto t^{\gamma}$, is suggested to distinguish between normal ($\gamma = 1$) and anomalous ($\gamma \neq 1$) diffusion.

We further examine and present our results in connection with the respective diffusivity regime characterization at different stages of dispersion evolution, for constrained or unconstrained flows, and with respect to local dynamics in the following sections.

4.2.3 Absolute diffusion

4.2.3.1 Stationary and homogeneous dynamics scales

Classical diffusion theory conformation *Taylor* [1921] conceptually devised classical diffusion theory for single particle trajectory analysis on two fundamental assumptions. Stationarity and homogeneity of the temporal and spatial scales of the eddy transport component, over which Lagrangian statistics are computed, in order for velocity autocorrelation functions to converge (see 4.2.1). Non-stationarity leads to persistent, large time lag, correlations in the autocovariance function (Fig. 4.1), and thus to the potential non-convergence of the $\lim_{\tau \to \infty} \kappa(\tau)$ even with adequate sampling. Homogeneity guarantees that the computed diffusivity is an accurate representation of the particular spatial region's diffusion [*Bauer et al.*, 2002].

Deciphering flow dynamics with Lagrangian data, in order to secure stationarity, requires particles to travel for a period that is long enough to account for low frequency variability. With an extensive advection time scale of $\sim$ 17 years in this study, particles adequately experience fundamental oceanic lower frequencies. Thus, estimating the velocity autocovariance function for time lags longer than a finite upper limit of decorrelation time is sufficient from a time perspective. What could render this approach problematic, though, is the presence of anomalous large time lag correlations. Nevertheless, in the absence of anomalous diffusion (see p.91) adequate statistical sampling (Fig. 4.2, c) should diminish the effect of pronounced negative and positive lobes in the autocovariance functions [*Veneziani et al.*, 2005].

Additionally, apart from the time constraints on stationarity, a local criterion is imposed by the homogeneity of dynamics on the spatio-temporal scales examined. The

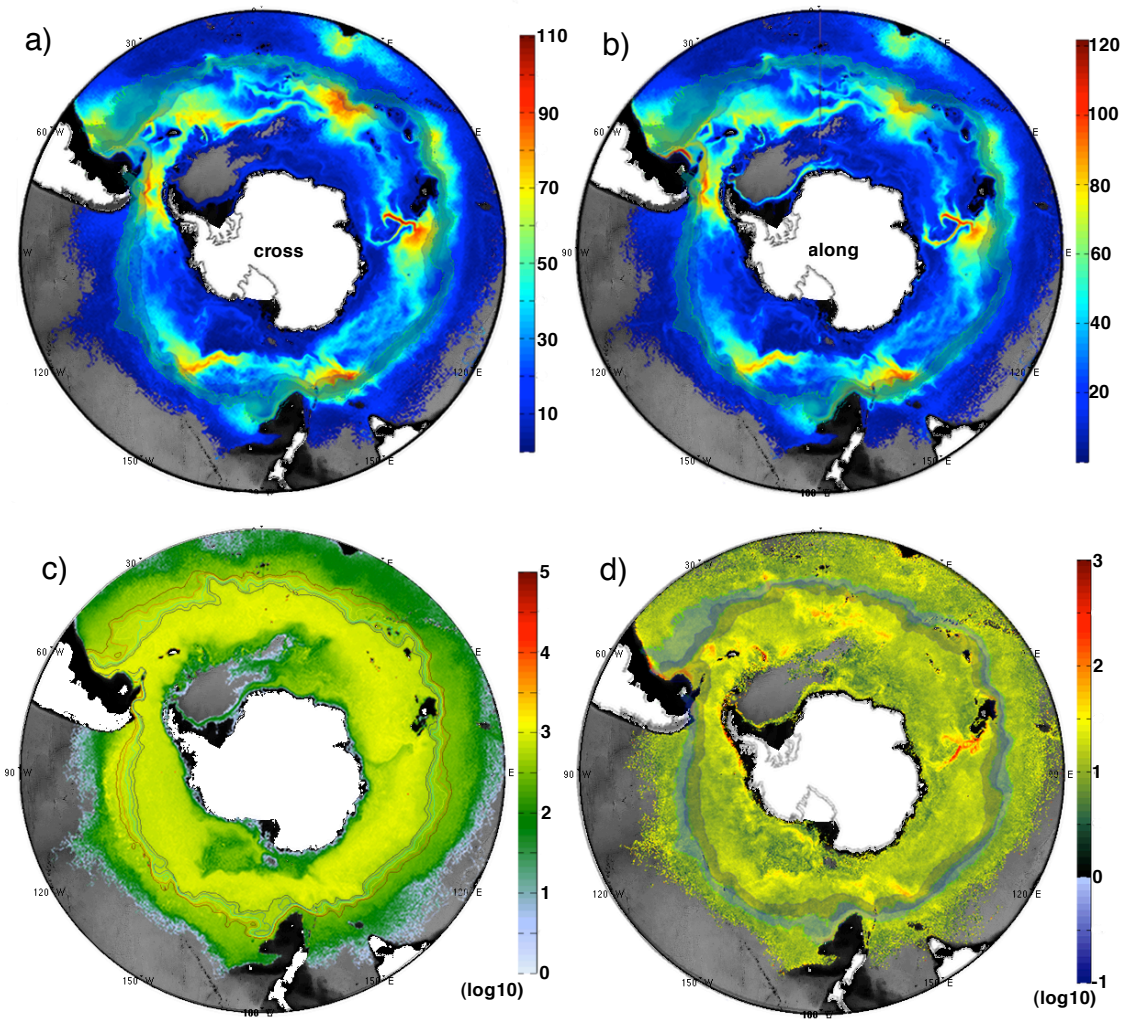

FIG. 4.2: Cross- (a) and along-stream (b) typical trajectory length in diffusion estimation (80 days time scale) scaled by OCCAM 1/12° model grid resolution. The similarity in recorded values suggests that the method employed for the flow decomposition, in time-mean and eddy components, successfully removes much of the shear in the along-stream direction by the mean flow. c) Number of sampled individual events per grid cell. More than 500 individual autocorrelation functions are averaged in order to produce the integral time T_L estimation, in order to diminish negative and positive correlations that persist even at longer time lags as a result of coherent structures presence in the flow. d) Ratio of advective time scale (grid resolution to cross- or along-stream residual velocity) to integral T_L time for isoneutral surface $\gamma^n = 27.76$ as a criterion of stationarity. The integral time used here is the maximum integral computed from the autocorrelation functions up to the time lag, where integration is at its maximum (see text for details). Negative values denote non-stationarity. Superimposed in a), b) and d) diagrams are ensembles (semi-transparent regions) of positions for the SAFN and PF from *Sallée et al.* [2008a] for the period 1992-2004. In diagram c) superimposed are contours of average geopotential anomalies with respect to the surface, for the same period, ranging from 9 (south) to 14 (north) with 1-unit spacing, signifying the same fronts in *Sallée et al.* [2008a].

exceeding localized constraint factor is examined by the ratio of advective time scale to the computed decorrelation time T_L (Fig. 4.2, d). Advective time scales are computed as the ratio of grid cell resolution to the averaged relative particle residual velocity (cross- or along-stream) from an ensemble of all particles going through the respective grid box during the entire simulation period. The main path of the ACC is well characterized as stationary (Fig. 4.2, d) independent from which the density coordinate is examined (not shown here). Stationarity exceedance events are present but statistically insignificant. A delineated correlation, in the regions of the Malvinas (Falkland) Current, Agulhas Current and jets north and south of the Kerguelen Island, of high values of the stationarity index with small values of cross-stream typical trajectory length is apparent, thus also suggesting the suppression of cross-stream mixing in the cores of those jets.

In computing absolute diffusivity, the assumption is made that an apparent representative diffusion quantity exists for the particular location. The over - or under - estimation of decorrelation times is predominantly a consequence of the method employed in this case. The notion adopted here is that an apparent variable is always understood in the context of some statistical mean. Therefore, if a spatial reference area registers a statistically significant sample, absolute diffusivity should be robust on these terms. The occurrence density per grid cell of particles' positions throughout their travel time indicates specific location preferences in the spatial distributions (Fig.4.2, c) but a significant number of records characterize most of the study area. Considering the ACC flow as predominantly zonal [*Munk and Palmén*, 1951; *Orsi et al.*, 1995; *Rintoul et al.*, 2001] with observed intensified jet structures acting as transport barriers, particles' trajectories in general exhibit a constrained spatial extent when examined in relatively small time scales with respect to the general planetary scale of oceanic circulation (see also in Chapter 3 the depiction of ACC dynamics through the spatial distribution of particles' positions).

4.2.3.2 Absolute - relative diffusion computation

Absolute diffusion In the generic *modus operandi* of *normal* (or *apparent* or absolute) diffusion [*Taylor*, 1921], time series formalization of Lagrangian trajectories statistical analysis is achieved with the following method. Lagrangian integral times are calculated for each particle's daily position from the cross- and along-stream residual velocity by the local time-mean flow. High frequency variability ($n \geq 1/5$ day^{-1}), i.e. tidal and inertial oscillations, is by definition filtered out, since the velocity field employed in this study has a fundamental 5-day time interval. Lagrangian velocity time series, derived from the daily absolute displacement for two sequential positions, were constructed with a range of 180 days. Following *Bauer et al.* [2002], due to the incomplete separation of the flow in mean and eddy components (see section 2.4.1 p. 51),

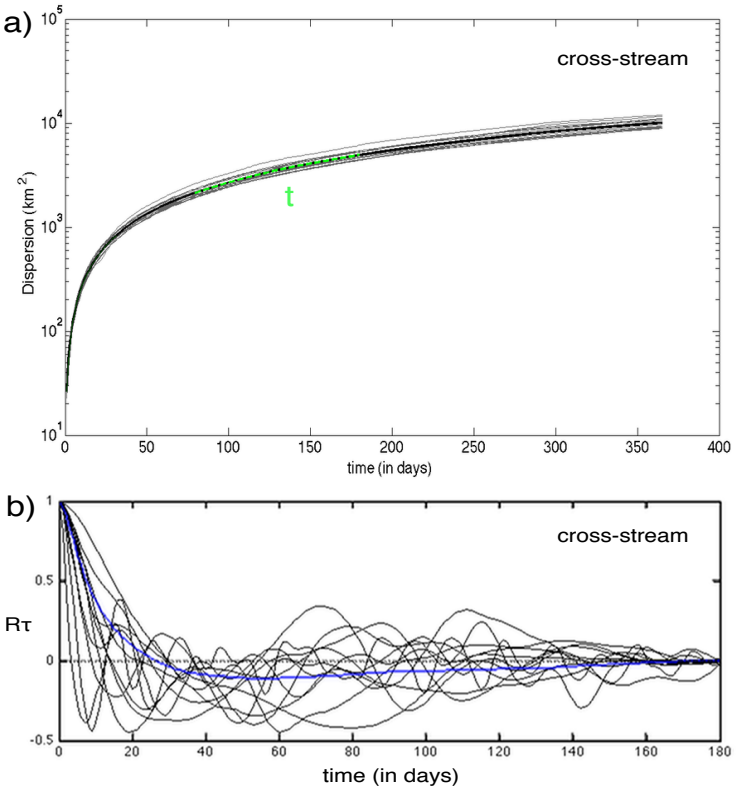

FIG. 4.3: a) Annual cross-stream dispersion (grey) scaling with time for all releases on isoneutral 27.76 for consecutive periods of 365 days and average dispersion (black) for the entire simulation period 1988-2004. Dispersion evolves linearly with time for the time lag (80 days) used in the integral time T_L computation. Linear scaling with time can be found for even smaller time lags in the range of time lags of the first zero-crossing calculation, but it is intermittent. b) A sample of an ensemble of Lagrangian cross-stream residual velocity autocorrelation functions (black lines) and the averaging result (blue line) for the whole extent (180 days) of the velocity time series in the analysis. Negative correlations produce a significant counteracting average effect which reduces the integral and thus decorrelation times, even below zero in many areas, thus rendering classical diffusion problematic for the specific time scales. Convergence of the integral R_τ to a constant value is therefore not secured. We end up with an 80-day time lag based on dispersion evolution with time as shown in a) and a comparative calculation of the maximum integral (see text for details).

the residual field inherits mean shear characteristics with the potential to alter or even dominate diffusion through shear dispersion. Deduced from the instantaneous flow, a Eulerian mean, stationary but spatially variant, is bilinearly interpolated on particles' daily positions. A period of 17 years, from model days 1095 to 7300, inferred as the most valid proxy for the decomposition of the temporal scales of the flow, is selected. The cross- and along-stream derived velocities (Fig. 4.2, a, b) are similar (within the order of a maximum of 10 grid cells/80 days or ≈ 1.4 cm s^{-1}) suggesting that most of the mean shear characteristics in the along-stream direction are removed by the method followed on the subtracted mean flow. The derived integral times are mapped on OCCAM's 1/12° model grid and then averaged on the respective spatial scales based on the

satisfaction of homogeneity and stationarity criteria (see p. 92). Thus, an ensemble is constructed over the entire simulation period and scaled with a spatial factor denoting the particle number of incidents or density of occurrence per grid box[1]. The results are used to produce maps illustrating the spatial distribution of diffusivity based on single particle statistics. We compute three different diffusivity estimations, with the aim of presenting different perspectives on diffusion spatio-temporal scales.

Initially, the classical diffusion approximation is employed with computation of the residual velocity autocovariance functions. These are calculated backwards in time (see section 4.2.1 p. 87) up to a time lag of 80 days, which is considered adequate to resolve the spatio-temporal scales of mesoscale eddies in the flow and for R_τ, and thus for diffusivity to converge to a constant value (dispersion scales linearly with time) (Fig. 4.3, a). We find that the estimation of diffusivity with the velocity autocovariance function is extremely sensitive to the time lag used. Even with a slightly longer time lag, of 90 days for example, in many regions the integration of the ensembles leads to negative values. This suggests an abrupt reduction of the velocity autocorrelation function up to the first zero-crossing as well as pronounced negative correlations that have not diminished completely through the averaging process (Fig. 4.3, b). Regardless of the fact that diffusion seems to converge for even smaller time lags, when considering the whole dataset these events still bias our calculations. Our interest in this computation of diffusivity focuses first on its use as a comparison quantity for our main estimation, due to its direct analogy to EKE, and second on examining the physical meaning, if any, of the derived eddy length scales.

As our main calculation of absolute diffusivity, due to the uncertainty in the velocity autocorrelations functions approach, we use the time derivative of particles' mean dispersion $\overline{D^2}$, backwards in time, on a spatial ensemble controlled by average trajectory length (Fig. 4.2, a, b) and individual events density per grid cell (Fig. 4.2, c). No less than 500 individual events on average per grid cell account for each representation of diffusion.

A third approach is based solely on the effect of persistent correlations caused by remnant low frequency variability. The idea is built on the theoretical context of unsuccessful flow decomposition, suggesting that low-frequency components are still present in the time series of the residual velocity component, thus rendering the observations as

[1]The ensembles for integral time computation are constructed from a uniform, randomly selected, and statistically significant set of trajectories. I.e. from the whole set of particles per longitudinal release, a subset is constructed at 1/4 size of the initial, for computation efficiency. The subset contains pseudo-random integer values drawn from the discrete uniform distribution of the initial particles' positions. A second sub-sampling, with a resulting size of 1204, is formulated with the same procedure on the time evolution of particles' coordinates with regard to the length of the time series in the autocorrelation function. The result is a matrix of 1204×500 elements instead of a 6204×2000. There is no effect on the overall spatio-temporal extent of the simulation. Sensitivity tests justify the selection of size reduction without a statistically significant effect on spatial averaging during the mapping of results on OCCAM's $1/12^\circ$ model geolocated grid.

not statistically independent [*Emery and Thomson*, 2001]. As a result, the convergence of the integral R_τ to a constant value is not secured (Fig. 4.3, b). As an alternative, integral time is computed as the maximum value of the integration, which is performed depending on the position of the upper limit time lag with respect to the lag range. Considering the case the upper limit time lag is in the last 1/10th section, T_L is estimated up to first zero-crossing. The longer the length of the time series examined, the higher the chance of the R_τ diverging.

Previous studies have also addressed diffusion decorrelation time up to the first zero-crossing of the normalized autocorrelation function for positive time lags [*Poulain and Niiler*, 1989; *Figueroa and Donald*, 1994; *Li et al.*, 1996; *Lumpkin et al.*, 2002; *Veneziani et al.*, 2005; *Rupolo*, 2007]. Several drawbacks are potentially in effect in this approach [*Figueroa and Donald*, 1994; *Griesel et al.*, 2010]. Especially when spatially dense eddy distribution in the flow requires a sufficient number of float trajectories in order to cancel out the rotational components effect, and in the presence of anomalous diffusion where high correlation events at large time lags are expected. *Rupolo* [2007] specifically mentions that the application of the first zero-crossing technique may lead to an overestimation of time scales.

Different approaches do exist. Their results are mainly regulated by the datasets employed. *Stammer* [1998] applied a scaling factor based on Richardson number Ri[2] distribution, computed from an average over the top 1000 m of the *Levitus et al.* [1994] climatology, in order to derive a baroclinic time scale T_{bc}, which he then compared with the integral time scale derived from the autocorrelation function from TOPEX/POSEIDON observations. *Sallée et al.* [2008b] implemented a more intricate method by following *Garraffo et al.* [2001] and using a Monte-Carlo error estimation for integral times. We therefore expect that our third approach – computing the maximum of the integral time– will actually be a representation of maximum diffusivities for the respective period.

Further analysis of the residual flow component's contribution fraction shows that is of interest to interpret the dissemination scales of the dynamics of oceans' kinetic energy from an absolute diffusivity perspective. Lagrangian integral times are founded on time series analysis and therefore are computed in a transient eddy time scale framework. Conversely, in the absolute diffusivity context a valid EKE component can only be chosen in the stationary spatio-temporal framework. As such, intrinsic to the classic diffusion theory approximated by Lagrangian trajectories analysis, as deciphered here, is the average of transient turbulence ephemerality, with both space and time foundations, and an *rms* residual velocity product, although over a 'holistic period' for oceanic

[2]The Richardson number, *Ri*, is the dimensionless number that expresses the relative importance of mechanical to density effects $Ri = \frac{N^2}{u_z^2}$ where N is the Brunt-Väisälä frequency and u_z the velocity shear.

dynamic lifetime scale. Focusing on the lifetimes of vortices, the assessment is made on the degree of randomness of the transient turbulent field, i.e. we determine whether or not the separation of organized large-scale turbulence is appended to standing eddies. Following *Hallberg and Gnanadesikan* [2001], transient eddies can only be seen as part of a general mechanism of momentum transfer, in addition to standing eddies and diapycnal fluxes. According to their numerical experimental results, a relationship between transient eddies and a partial homogenization of potential vorticity gradients can be established, especially at the deeper layers. The localized trail of transient eddies in the presence of a restraining dispersion factor should tend to diminish when temporally averaged. Additionally, the decorrelation time should minimize in the presence of a dispersion boundary.

Relative diffusion *Richardson* [1926] expanded *Taylor*'s [1921] work on single particle diffusion derivation by examining the progression of a pair of particles relative displacement when considering atmospheric isotropic turbulent regimes. Multiple particles' statistics are considered here by examining the second-order moments of the *joint probability functions* of particle positions in an ensemble of constructed pairs in order to define dispersion, as shown in Eq. (4.6). The aim is to elucidate relative dispersion $\overline{\mathcal{D}^2}$ and the rate of separation behaviour with respect to the cross-correlation of Lagrangian velocities in a time-evolving framework and to use $\overline{\mathcal{D}^2}$ as a tool to delineate barriers in the flow.

Summary In essence, both approaches monitor the instantaneous flow at spatial points visited in a particle's travel history. Obviously, the normalized velocity autocorrelation function for each particle, regardless of proximity, depends on the momentum subjoined to it at each timestep by the advection algorithm employed. The expectation is that in high-frequency environments where decorrelation times are shorter, some similarity should exist. However, maintaining uniformity does not hold in turbulent environments, since fundamental fluid dynamics suggest a 'chaotic' displacement of initial differences in particles' positions (notion of chaos [*Wiggins*, 2005] and in connection with non-parallel flows). Taking advantage of the degrees of freedom provided by this conjecture, the statistical average robustness of the velocity autocovariance functions, at a specific point, is delineated as a measure of the randomness of the particles' position distribution during their travel history. Accordingly, the longer the model time series examined, the higher the probability the sampling pattern will be spatially homogeneous.

4.2.4 Integral times and absolute diffusivity

In figures 4.4-4.5, integral time T_L in the asymptote limit and maximum integral time $T_{L_{max}}$, derived from the cross-stream Lagrangian residual velocities time series for the entire simulation period are illustrated for the isoneutral surface $\gamma^n = 27.76$. Absolute diffusivity κ_∞, derived following the formulation in the section 4.2.1, and $\overline{EKE}$ are also presented.

Examining the spatial distributions of T_L and $T_{L_{max}}$ (Fig. 4.4, b and Fig. 4.5, b) with respect to the spatial variations of mean EKE (Fig. 4.5, a) a general agreement between $T_{L_{max}}$ and $\overline{EKE}$ is illustrated. Regions with $\overline{EKE}$ values > 40 (cm s^{-1})^2 correlate with $T_{L_{max}} < 5$ day. Early decorrelation times in T_L mapping are also scaled analogously to high $\overline{EKE}$ values. In both cases, though, especially in the T_L distribution, the signal is somewhat unclear. The relationship with $\overline{EKE}$ is not direct, meaning that the highest $\overline{EKE}$ values are not associated with the lowest decorrelation times. Noticeable examples are almost the majority of the regions with $\overline{EKE} > 200$ (cm s^{-1})^2, as is the Brazil-Malvinas Current (50°W), upstream of Crozet Island (at 30°E, at the south boundary of PF front), downstream of Crozet Island (45°E, at the northern boundary of the SAFN front), downstream of the Kerguelen Plateau (85°E, at the south boundary of the PF front), at Macquarie Island (165°E, at the south boundary of the PF front), the Udintsev Fracture Zone (145°W, between the PF and SACCF fronts) and certain patches in the Drake Passage (see Fig. 2.3 for exact locations and bottom topography). All of these regions are characterized by integral times T_L around 0.5 days, which is about three times larger than the smallest T_L values associated with the other depicted high EKE regions. A possible mechanism behind this discrepancy could be the result of the high spatial density of stagnant coherent vortices and ensuing strain pathways in the flow. We further analyse the mechanism later in this chapter, but as a brief introduction, the presence of the impermeable coherent vortices would tend to redistribute the particles through a stirring process leading to homogeneous mixing regimes at longer temporal scales. Homogeneity intrinsically permits decorrelations at large time lags. Absolute diffusivity κ_∞ (Fig. 4.4, a) is also highest in the areas mentioned above, with values exceeding 1000 m^2 s^{-1}. In general, in both computations, higher decorrelation times characterize the less energetic regions, since the velocity field approximates stationarity in smaller time scales. This has already been noted by *Rupolo* [2007] in his study of surface drifters and subsurface floats.

Small integral times do not associate exclusively with high EKE values, though. Coherent structures in the flow can lead to persistent correlations in the R_τ functions. During the averaging process of particle ensembles, these do not necessarily cancel out in order to remove the effect of coherent structures but rather diminish the integral sum to zero or even a negative value. In view of a vanishing integral time, dispersion

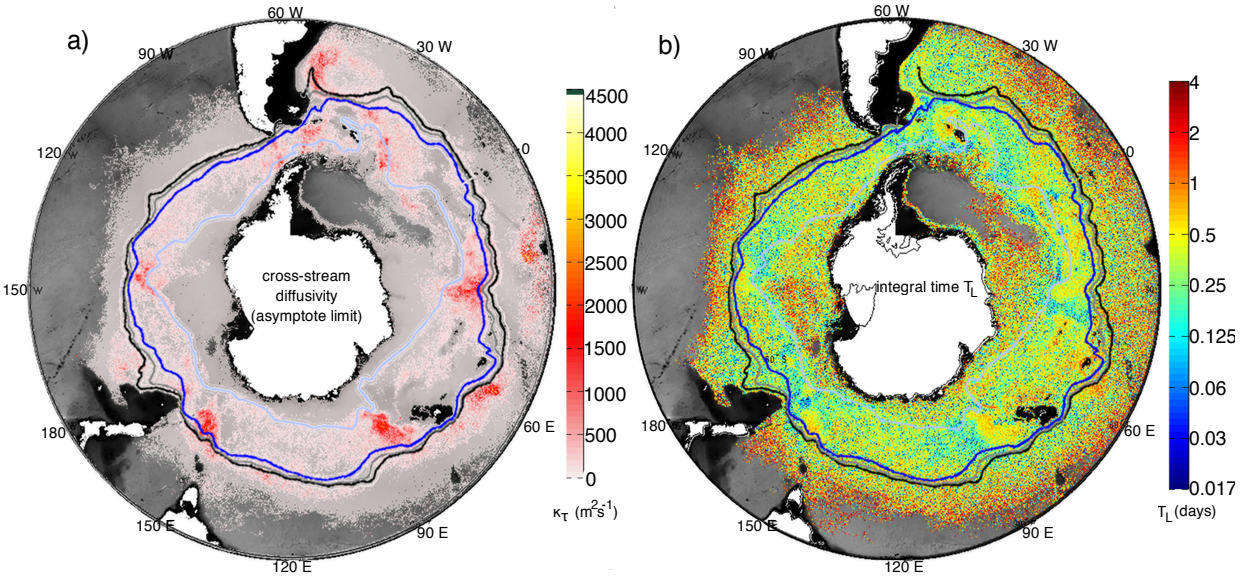

FIG. 4.4: Absolute cross-stream diffusivity (m^2 s^{-1}) for isoneutral $\gamma^n = 27.76$ for the entire simulation period 1988-2004. Cross-stream diffusivity is the product of the cross-stream $\mathcal{U}'_{\perp rms}$ with the respective $\perp$ component of the Lagrangian integral time T_L b) derived estimating velocity autocorrelation functions up to the asymptote limit where diffusivity is assumed to reach a constant value (dispersion evolves linearly with time) (Fig. 4.3, a) (see also 4.2.3.2). SAFN (black), SAFS (grey) and PF (blue) fronts from *Sallée et al.* [2008a] for the same period 1992-2004 while the SACCF (cyan) from *Orsi et al.* [1995].

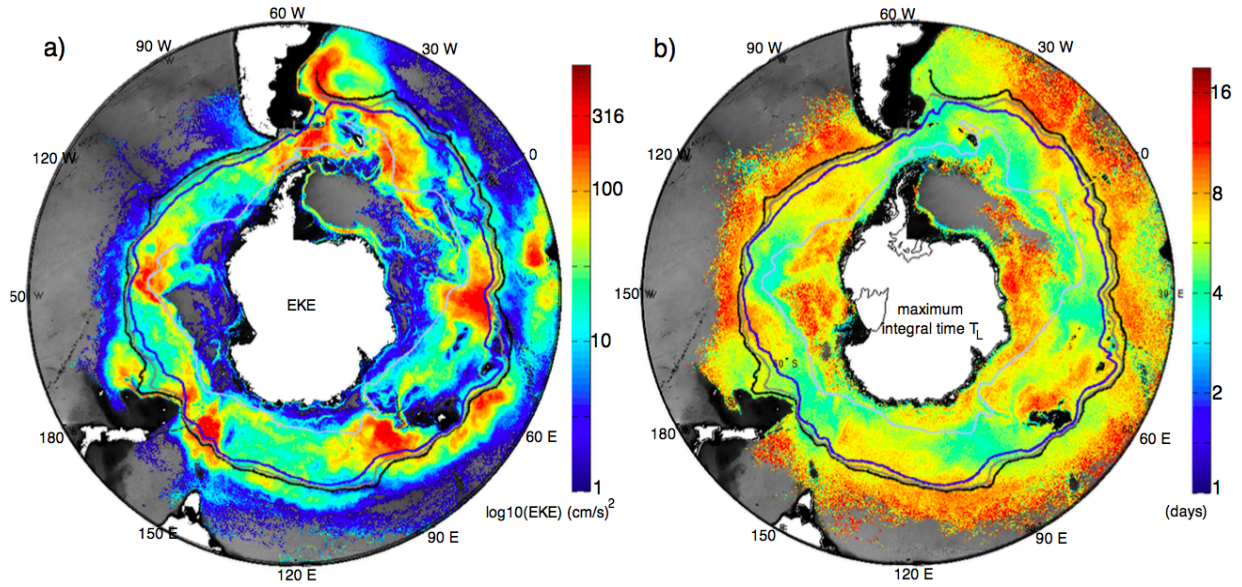

FIG. 4.5: a) Mean EKE (cm^2 s^{-2}) derived from the whole dataset of Lagrangian trajectories and b) maximum cross-stream integral time T_L (in days) for isoneutral $\gamma^n = 27.76$ for the entire simulation period 1988-2004. Integral time is computed up to the time lag where the integral of the velocity autocorrelation functions is at its maximum (see text for details). Both colour maps are in a logarithmic scale.

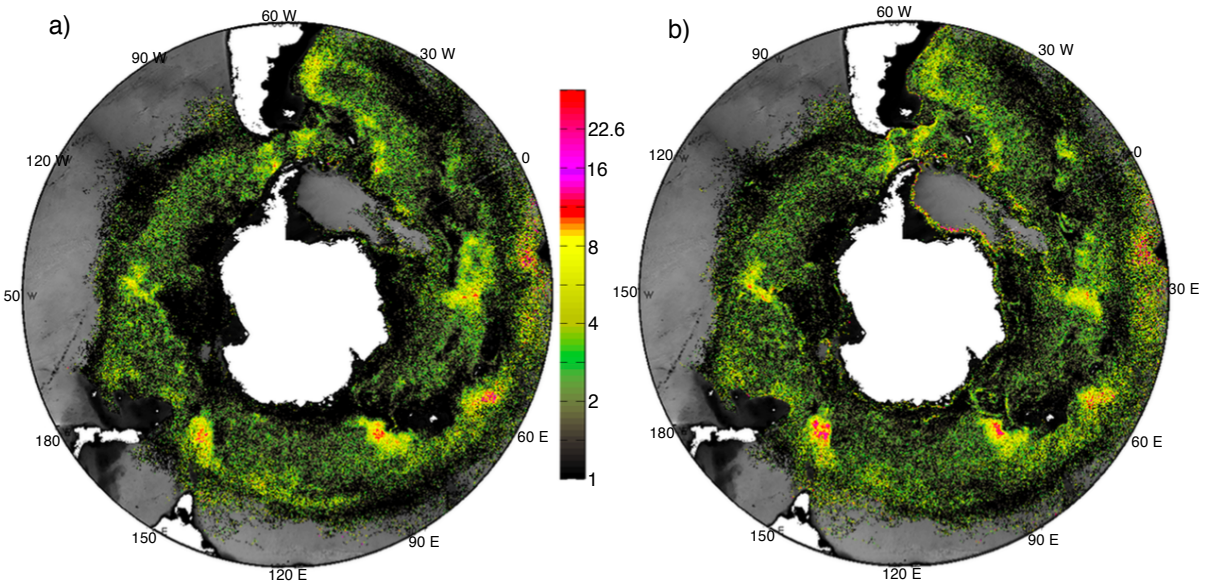

FIG. 4.6: a) Cross- and b) along-stream eddy length scales (in km) for isoneutral $\gamma^n = 27.76$ computed as $\mathcal{U}'_{rms} \cdot T_L$, using the $\perp$ or $\parallel$ component of the residual velocity field, respectively. The derived values are within the range of the first baroclinic Rossby radius of deformation for the ACC [*Chelton et al.*, 1998], although with significant spatial variability. Therefore, it is suggested that employing a constant mixing length scale for the whole ACC regime in order to parameterise diffusivity would be inappropriate and incomplete.

on the respective time scale is bounded [*Tennekes and Lumley*, 1972; *Ristorcelli and Poje*, 2000]. This means that an upper limit length scale exists which is fundamental for the dispersion constraint. As such, absolute diffusivity at these areas verges on the $\lim_{t \to t_f} \kappa_{t_f} \simeq 0$, where t_f is the upper time limit of the integral computation. Of course, based on the absolute diffusivity definition, the scaling of $\kappa_\infty = \mathcal{U}'_{rms}\mathcal{L}_e$, with $\mathcal{L}_e$ denoting the eddy length scale and being $\propto \sqrt{EKE} \cdot T_L$, is an expected result (Fig. 4.4, a, b). But the point is first, if indeed our computation of T_L up to a certain time lag, which is derived from a non-local average of dispersion time evolution (Fig. 4.3, a), is valid; and second, whether the subdiffusive behaviour in those areas can be connected with the existence of barriers in the flow for the respective time scales.

Computation of the cross- and along-stream eddy length scales as $\mathcal{U}'_{rms} \cdot T_L$ ($\perp$ *or* $\parallel$ respectively) is shown in figure 4.6. Both estimations are below the upper limit of values for the first baroclinic Rossby radius of deformation $\mathcal{L}_d$ in the Southern Ocean [*Chelton et al.*, 1998][3]. The $\mathcal{L}_d$ was used in previous studies of isopycnal diffusivities in the ACC [*Sallée et al.*, 2008b] as an alternative approximation for the mixing length scale. It is also considered as the input scale of energy into the ocean through baroclinic instability

[3] `http://www-po.coas.oregonstate.edu/research/po/research/rossby_radius/index.html`

[*Fu et al.*, 2010]. In our computation, though, as expected, the $\mathcal{L}_e$ exhibits substantial spatial variability, as it records the counteractive relationship of T_L and $\mathcal{U}'_{rms}$.

As a validation tool for the $\mathcal{L}_e$ estimation we also examined the spatial distribution of a representative vortex radius based on the Okubo-Weïss $\mathcal{OW}$ parameter[4] [*Okubo*, 1970; *Weiss*, 1991], computed as the radius of an equivalent area circle with respect to the area of depicted vortices. The value of -2 ($\times 10^{-11}$), derived from the Eulerian velocity field for the entire simulation period, in order to reduce data noise, was chosen identifying the vortices. We find that our computation of eddy length scale $\mathcal{L}_e$ is of the same order with the eddy radius based on the $\mathcal{OW}$ parameter, but it appears somewhat decreased (by 4-6 km) in the regions of the largest $\mathcal{L}_e$ values exhibited. Hence, our approach possibly underestimates $\mathcal{L}_e$.

On the other hand, the cross-stream $T_{L_{max}}$, evaluated with the maximum integral method of the autocorrelation function R_τ, is > 10 times larger than the $T_{L_\perp}$. If the integral time $T_{L_{max}}$ is to be retained, absolute diffusivity ($\kappa_{\perp\infty} = \mathcal{U}'_{\perp rms}\mathcal{L}_e$) would be of $\mathcal{O}(10^4)$ (m^2 s^{-1}) (Fig. 4.7, b) in the respective eddy intensified regions (Fig. 4.5, a). The result would be spuriously high compared with diffusivity values derived for the same isoneutral density range from other studies [*Griesel et al.*, 2010; *Abernathey et al.*, 2010]. In addition, the maximum diffusivity is inappropriate in a physical context when taking into consideration the mean depth of isoneutral $\gamma^n = 27.76$ (Fig. 2.14).

The spatial distribution of $T_{L_{max}}$ in $\overline{EKE}$ regions within the low limit value of 20 (cm s^{-1})^2 indicates that Lagrangian particles retain memory of their previous kinematic state for more than 5-6 days and in the low $\overline{EKE}$ regions in the order of > 10 days. This is in agreement with decorrelation time scales derived by *Griesel et al.* [2010], applying the first zero crossing method on their Lagrangian cross-stream velocity autocovariance, though, in contrast to the T_L estimation in this study. They also suggested overestimating diffusivity when employing the first zero-crossing method in R_τ estimation.

Eddy length scales $\mathcal{L}_e$ for maximum integral computation will accordingly increase at a range of 25 km, for the low EKE ACC, to 35 and even >80 km, for the highest EKE regions. The larger scales of the eddies with respect to $\mathcal{L}_d$ are consistent with surface eddy radii derived from satellite altimetry [*Chelton et al.*, 2011] and are in agreement with surface quasi-geostrophic (QG) turbulence theory, where an energy cascade from smaller to larger scales is expected [*Fu et al.*, 2010]. However, a vortex is expected not to retain its surface spatial horizontal extent[5] with a depth increase. *Lumpkin et al.* [2002], in their study of actual and simulated Lagrangian floats in the North Atlantic, agree with an eddy length scale reduction with a depth increase, though they found that

[4]The Okubo-Weïss $\mathcal{OW}$ parameter is computed as the algebraic sum of squared strain σ rate components (normal $\sigma_n = \partial_x u - \partial_y v$ and shear $\sigma_s = \partial_x v + \partial_y u$) and relative vorticity, $\zeta = \partial_x v - \partial_y u$ as $\mathcal{OW} = \sigma_n^2 + \sigma_s^2 - \zeta^2$.

[5]This is a direct effect of vortex stretching in order for a forward energy transfer to smaller scales to be complete, concordant with three-dimensional turbulence [*Vallis*, 2006b].

the relationship does not hold in the first few hundred metres, mainly due to reduced sampling resolution. A vortex retaining its area is in accordance with incompressible two-dimensional turbulence [*Vallis*, 2006b] whereby an 'inverse cascade' of energy is expected, as discussed, and diffusion follows a 4/3 power law dependency (see A.5, Appendix A) on displacement up to the decorrelation time scale. For scales up to at least 30 km we find that diffusion evolves accordingly to the 4/3 power law with respect to displacement (derived from both the relative and absolute diffusivity estimates, Fig. 5.2, Appendix A). We find that by employing the $\mathcal{OW}$ parameter, a small reduction in eddy radius during transition to denser isoneutral surfaces will occur. Nonetheless, our eddy length scales computed from T_L are smaller than the reduction expected from the surface scales. On the contrary, our $\mathcal{L}_{e\perp}$ are in good agreement with the cross-stream eddy scales at the same depth, as derived by *Griesel et al.* [2010].

Summary What is suggested, from the association of T_L, $\overline{EKE}$ and κ_∞, is that diffusivity parameterizations that depend solely on EKE are prone to oversimplifications in the representation of mixing potential in the ACC. Under certain approximations, the T_L computation is valid, though. *Griesel et al.* [2010] also suggested that the high correlation of $T_{L_{max}}$ on EKE can lead to the misleading argument of a homogeneous $\mathcal{L}_e$ and thus to an incomplete dependence of diffusivity on EKE.

Both of our computations, based on integrating velocity autocorrelation functions, produce results that are accompanied by a number of inconsistencies regarding their physical meaning and robustness. Integration up to a constant lag is prone to result in unreasonably small decorrelation times [*Sallée et al.*, 2008b], even though the derived diffusivity is in agreement with previously derived values in OCCAM 1/12° [*Lee et al.*, 2007, 2009]. On the contrary, the first zero-crossing method overestimates integral times [*Sallée et al.*, 2008b; *Griesel et al.*, 2010]. The same problem rests also with the maximum integral computation, employed in order to mitigate the effect of persistent correlations due to the presence of low frequency variability [*Emery and Thomson*, 2001]. Regardless of small decorrelation time scales, our time lag is considered long enough to resolve the dominant spatial scales and still be able to record diffusivity in the asymptote limit (as seen by the dispersion evolution with time in figure 4.3).

We believe that the problem resides with the sampling of the flow by Lagrangian particles in the presence of coherent structures. *Berloff et al.* [2002], *Veneziani et al.* [2005, 2004] and *Griesel et al.* [2010] among others discussed oscillatory patterns emerging in autocorrelation functions due to meandering and eddy rotational motions. They argue that at time lags longer than the meander or circling time scale, diffusivity should not be affected. We also showed that spatial ensembles of a large number of particle trajectories do have the potential to cancel out oscillatory patterns in velocity autocorrelation

functions. The problem arises, though, when coherent structures have lifetimes which are significantly larger or at least comparable with the time series under examination. Diffusion in this case does not evolve linearly with time; consequently, classical diffusion theory is not applicable because an asymptote limit is not reached. This is the case of anomalous diffusion [*Artale et al.*, 1997; *Berloff et al.*, 2002; *Reynolds*, 2002; *Ferrari*, 2007], which is only qualitatively assessed in the context of this study.

In order to overcome the uncertainty of integral times we compute diffusivity according to the derivative of dispersion (as described in 4.2.3.2), backwards in time (starting from the ending particle position in our simulation period), with the assumption that the asymptote limit has been reached during the first year of travel. The derived cross-stream diffusivity $\kappa_{\perp\tau}$ for isoneutral $\gamma^n = 27.76$ is illustrated in figure 4.7 (a). The method captures the spatial distribution of $\mathcal{L}_{\perp e}$ (Fig. 4.6, a) in great detail. It is also in good agreement with the high diffusivity regions computed from integrating velocity autocorrelation functions (Fig. 4.4, a). Nonetheless, regions of relatively increased diffusion are also depicted, and values of $\kappa_{\perp\tau}$ appear intensified by 80% downstream of the most enhanced mixing areas where the T_L record is reduced (see, for example, the regions at 30°E at the Atlantic-Indian Ridge, just upstream of the South-west Indian Ridge and at 90°E downstream of the Kerguelen plateau (Fig. 2.3)).

In conclusion, the along-stream diffusivity $\kappa_{\parallel\tau}$ scales analogously with $\kappa_{\perp\tau}$ in accordance with the typical trajectory length (Fig. 4.2, a-b) suggesting that most of mean flow shear dispersion is successfully removed by subtracting the 17-year local mean velocity component from the instantaneous one. In comparison with the maximum diffusivity $\kappa_{\perp max}$ (Fig. 4.7, b) in the high mixing regions $\kappa_{\perp\tau}$ is significantly smaller.

4.3 Diffusion in the ACC

4.3.1 Depicting patterns

In the context of classic diffusion theory, diffusivity in the asymptote limit κ_∞, if it does indeed exist, is regulated in direct analogy to the EKE derivation and computation of integral times T_L. Disregarding the ambivalent theoretical formalization of kinetic energy power spectrum separation in oceanic turbulent flows, a factor of uncertainty remains in relation to the adopted computation methodology of decorrelation times. In contrast, computation of diffusion backwards in time, based on the derivative of dispersion for a similar length time series, as in the integral time calculation, is more straightforward. The main assumption requires that the diffusivity limit has been reached during the first year of travel. Both stationarity and homogeneity criteria are already met by constructing the ensemble average and time series length.

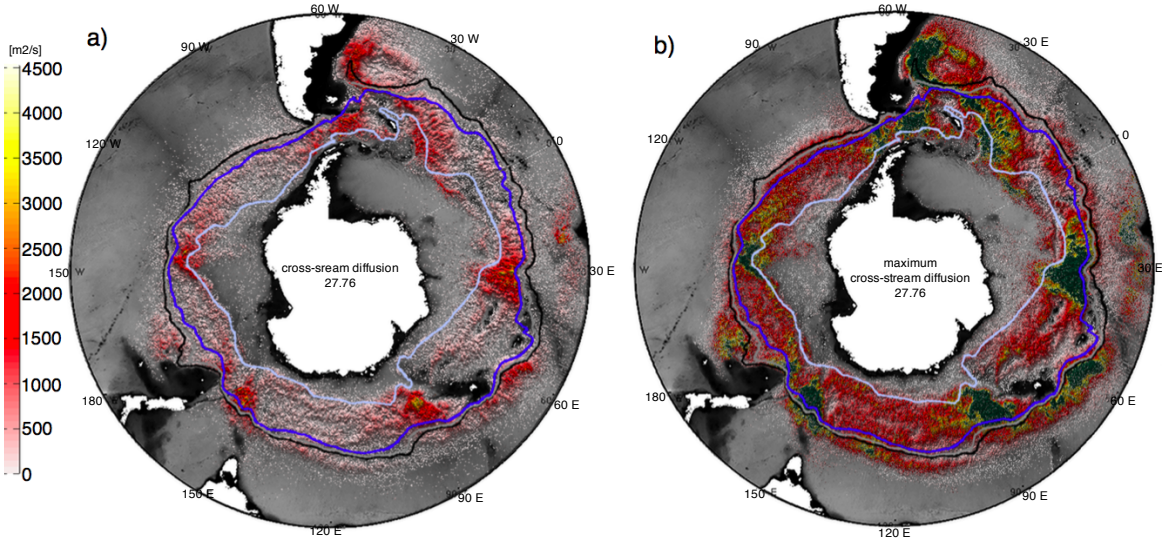

FIG. 4.7: Absolute a) versus maximum b) cross-stream diffusivity (in $m^2\ s^{-1}$) for isoneutral $\gamma^n = 27.76$ for the entire simulation period 1988-2004. Maximum values (green areas) are of $\mathcal{O}(10^4)$ so they are substantially elevated with respect to the absolute diffusivity result in a). Cross-stream diffusivity in a) is computed through the derivative of particle displacement due to the effect of cross-stream residual velocity. Maximum diffusivity in b) is the product of the cross-stream $\mathcal{U}'_{\perp rms}$ with the respective $\perp$ component of the Lagrangian integral time T_L (Fig. 4.5, b) derived estimating velocity autocorrelation functions up to the time lag where the integral is at its maximum (see section 4.2.3.2).

Cross- and along-stream absolute eddy diffusivities ($> 100\ m^2\ s^{-1}$) for all isoneutral surfaces in the context of the SOL experiment are presented in figures 4.8 and 4.9. For all isoneutral surfaces small differences are exhibited between the $\kappa_\perp$ and $\kappa_\parallel$ components. As we can also see in figure 4.10 (c, d), dispersion evolution over time is quite similar for the two components. The subtracted 'local' mean velocity component was proposed as being responsible for the analogy, reducing remnant mean shear dispersion in the along-stream direction which characterizes results in all similar Lagrangian studies so far. Diffusivity is reduced by transitioning to denser isoneutrals, which is in agreement with the decline of available TKE with depth. The spatial distribution of intensive mixing ($> 1000\ m^2\ s^{-1}$), as depicted by κ_τ, appears to be the same on all isoneutrals, with differences mainly emerging due to the constraints imposed by the geometry of the respective density surface against the spatial extent of the Lagrangian trajectories (Fig. 3.1 and Fig. 3.3 for a detailed bathymetry schematic representation). One of the characteristics absent from the isoneutral 27.76 cross-stream mapping is located at the section 60°W-30°E and southern of 60°S. This is a region of observed reduced KE, encompassing the Weddell Sea area, and delineated to the north by an intensified eastward ACC flow and to the south by a westward jet flow, the Antarctic Coastal Current (ACoC), which is impeded by the Antarctic Peninsula [*Fahrbach et al.*, 1992].

The southernmost coherent jet structure of the ACoC is depicted by a dominant along-stream flow, with the continental shelf of the Antarctic Peninsula responsible for the northward stirring of the ACoC. Following *Tchernia and Jeannin* [1980], the relocation of the flow further offshore and to the east realigns the *Coriolis* force to the north. The flow becomes unstable, and in the absence of a restrained jet structure the potential of detached vortices to form is increased and thus, mixing to ensue.

We find mixing intensified regions collocate with the highest $\overline{EKE}$ values over smooth slope areas (Fig. 6, Appendix A). Spatial homogeneity of the slope could serve as a bottom roughness index, being in agreement with the roughness mapping of global bottom topography in *Gille et al.* [2000a]. They also provided evidence of high EKE correlation with low roughness. We expect an analogy between EKE and diffusivity, but we should also consider a number of accompanying factors that shape this relationship (see introductory Chapter 1 and section 1.2, p.10). We attempt an explanation for the mechanism behind those distributions in the following sections.

The main ACC path is characterized by the highest κ_τ values, although with certain exceptions. The Brazil-Malvinas Confluence Zone (50° W) and Argentina Basin, the Agulhas Retroflection Current (30° E), Crozet Island (60° E) and the Chatham Rise (190° E). All of these regions reside in the equatorward flank of the ACC at the northern extent of the SAFN. The main ACC fronts delimit the spatial extent of diffusivity distribution as well. *Gille* [2003] proposed that the ACC could act as a barrier to horizontal mixing due to the intensity of its frontal jet structure.

4.3.2 Depth dependence and the general effect of ACC's main fronts in absolute diffusion

In figure 4.10 the effect of the ACC's frontal jet structure in our diffusivity estimate as a function of depth and longitude is presented. We construct averages of κ_τ along-streamlines, selected as the best representations of the main ACC fronts, for each isoneutral in the context of the SOL simulation. Streamlines are based on values of mean geopotential anomaly (Fig. 4, Appendix A), for the entire simulation period 1988-2004, focusing on the main ACC path and excluding its equatorward flanks. A value of 400 $m^2\ s^{-1}$ is representative of the main core of the ACC as an average over all records. Diffusivity as a function of depth south of the PF (purple) (between 3 - 8.8 $m^2\ s^{-2}\ \Delta\Phi$) scales up to 2500 $m^2\ s^{-1}$. Depth varies between 500-1900 m as a direct expression of the upward tilting of the isopycnals as we move south. Along-stream diffusion appears to increase by $\sim$ 500 $m^2\ s^{-1}$ with respect to the cross-stream extending to a depth of 1200 m versus 1900 m for the $\kappa_\perp$ record. This signifies a gradual dominance of $\kappa_\perp$ on $\kappa_\parallel$ in line with depth, although at depths greater than 1400 m $\kappa_\perp$ is reduced well below 500 $m^2\ s^{-1}$. It is also the only continuously decreasing signal as a function of depth, delineating

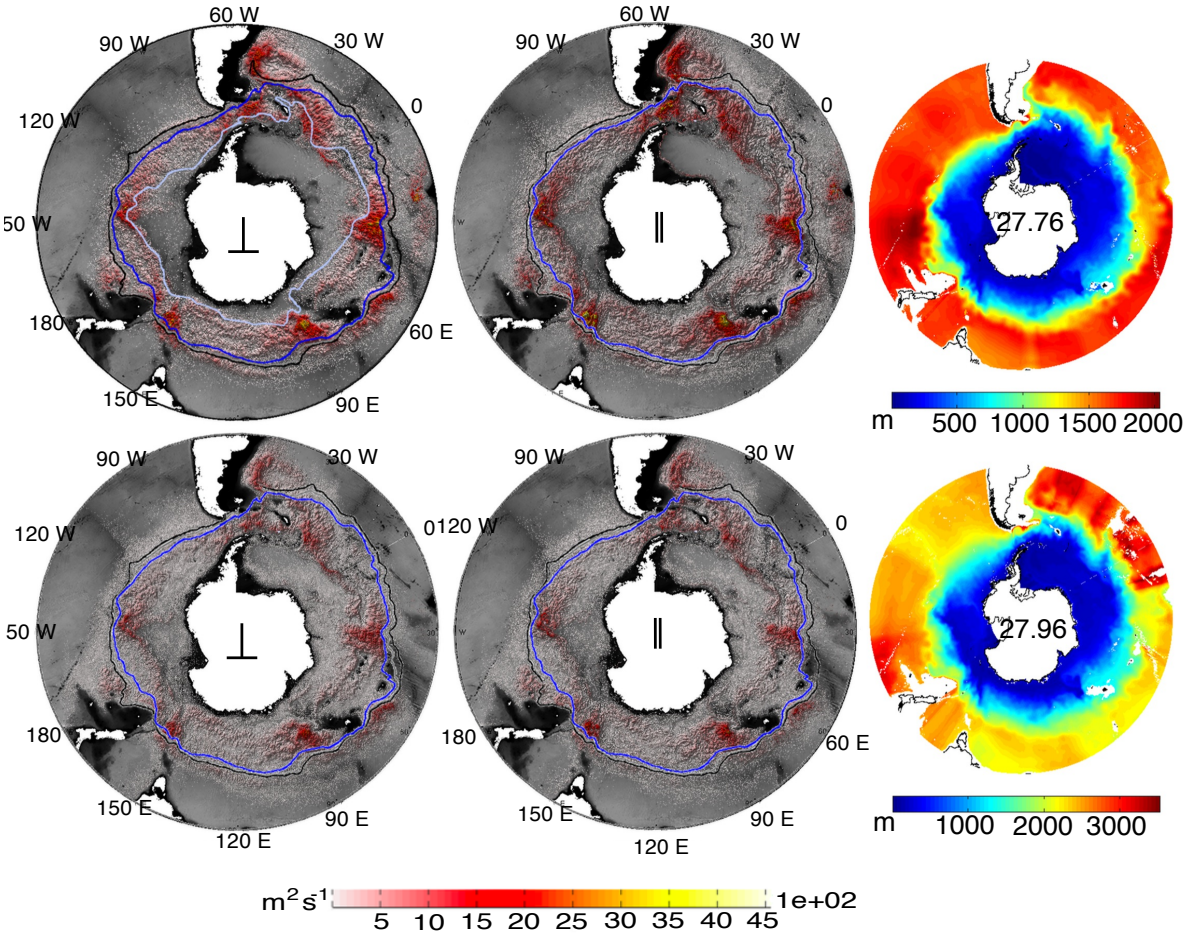

FIG. 4.8: (left panels) Cross- and (middle panels) along-stream diffusivity ($m^2\ s^{-1}$) for isoneutrals (top to bottom) 27.76 and 27.96. Also shown is (right panels) the average depth of respective isoneutral surfaces. ACC fronts from *Sallée et al.* [2008a]. Values of diffusivity <100 $m^2\ s^{-1}$ are not shown.

a correlation with a decrease in EKE. Conversely, both the PF (green) and PF-SAF (red) averages are intermittent, with a great deal of variation associated with specific depth values reducing through transition to greater depths. The along-streamline average around the PF exhibits high variability at 1000, 1300 and 1500-1600 m. The cross-stream component presents an extra spike at a depth of 2000 m. The spikes are related to the respective depths of maxima in diffusivity for each isoneutral. The same pattern characterizes the average between the PF-SAF. The intermittent pattern indicates that the ACC fronts act as barriers to mixing and that, depending on jet spacing, mixing is also suppressed in the jet cores, excluding the maxima presented here.

Below 2000 m $\kappa_\perp$ exhibits greater variability than $\kappa_\parallel$. This is not an exclusive event. On density coordinates there are several regions where cross-stream diffusivity dominates the along-stream component (Fig. 4.11). Mapping of along-streamline averaged isopycnal diffusivity using depth coordinates is prone to mask local regimes indicated by

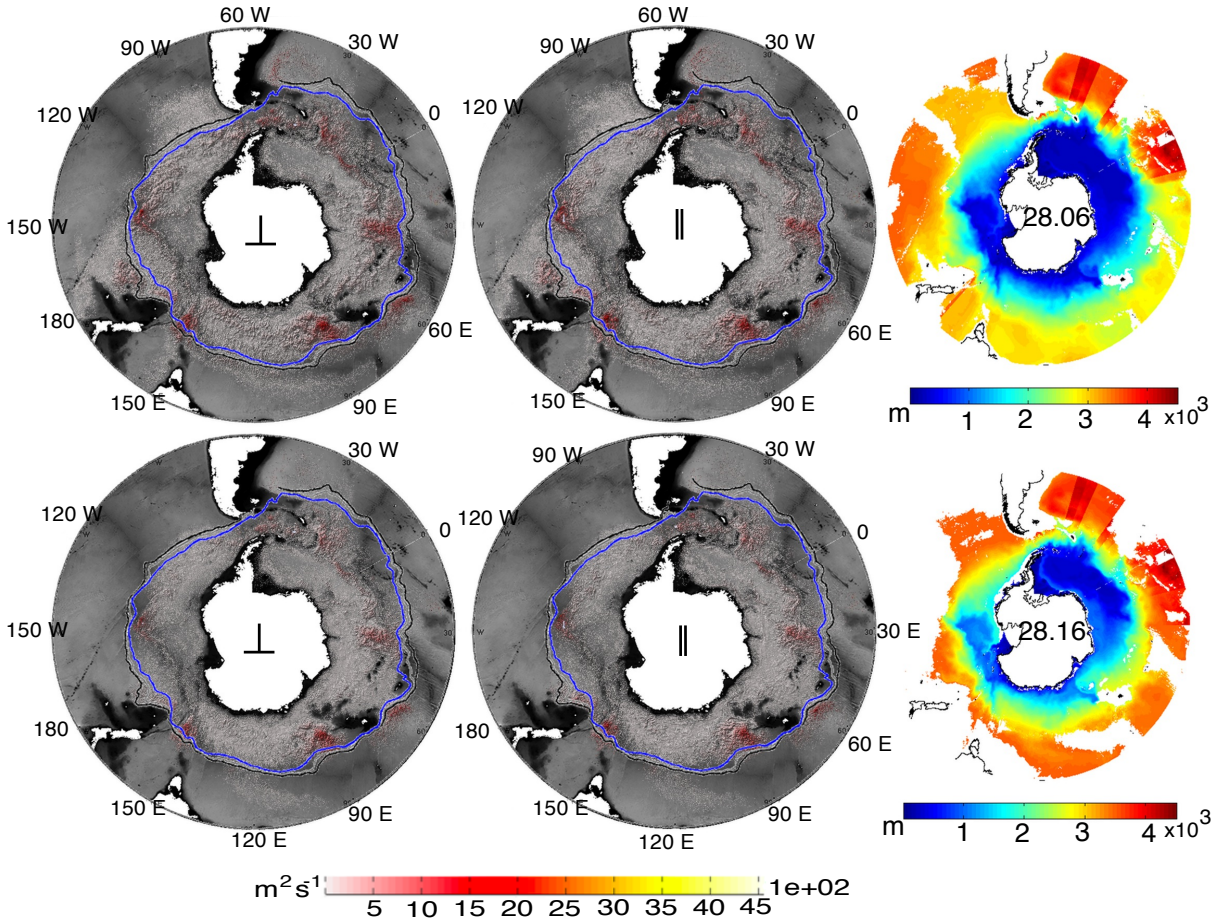

FIG. 4.9: Same as in figure 4.8 but for isoneutrals (top to bottom) 28.06 and 28.16 instead.

the patchy pattern of the cross- and along-stream diffusivity relationship (Fig. 4.11).

As far as depth dependence is concerned, $\kappa_{\parallel}$ seems to be more sensitive to it, although, the depicted maxima make the relationship problematic. *Griesel et al.* [2010] found a more pronounced depth dependence for the along-stream component, which they associated with an EKE reduction. They binned diffusivities over larger regions, and more importantly their along-stream diffusivity is 2-3 times larger than ours. On the contrary, cross-stream diffusivities are in good agreement with *Griesel et al.* [2010], but their result exhibits less variance. Their averaging technique on mean depth intervals reduces the resolution of the maxima that we aim to depict. We record a small increase of both $\kappa_{\perp}$ and $\kappa_{\parallel}$ at a depth of $\sim$1 km, mainly regulated by the high variant signal of the PF and PF-SAF averages and consistent with the steering level of critical layer theory [*Killworth*, 1997; *Smith and Marshall*, 2009; *Abernathey et al.*, 2010]. Irrespective of the depicted increase, the result cannot be thought as a confirmation of critical layer theory. What we actually record is an increase in average diffusivity computed along-stream the PF and the respective area between the PF and SAF. However, both

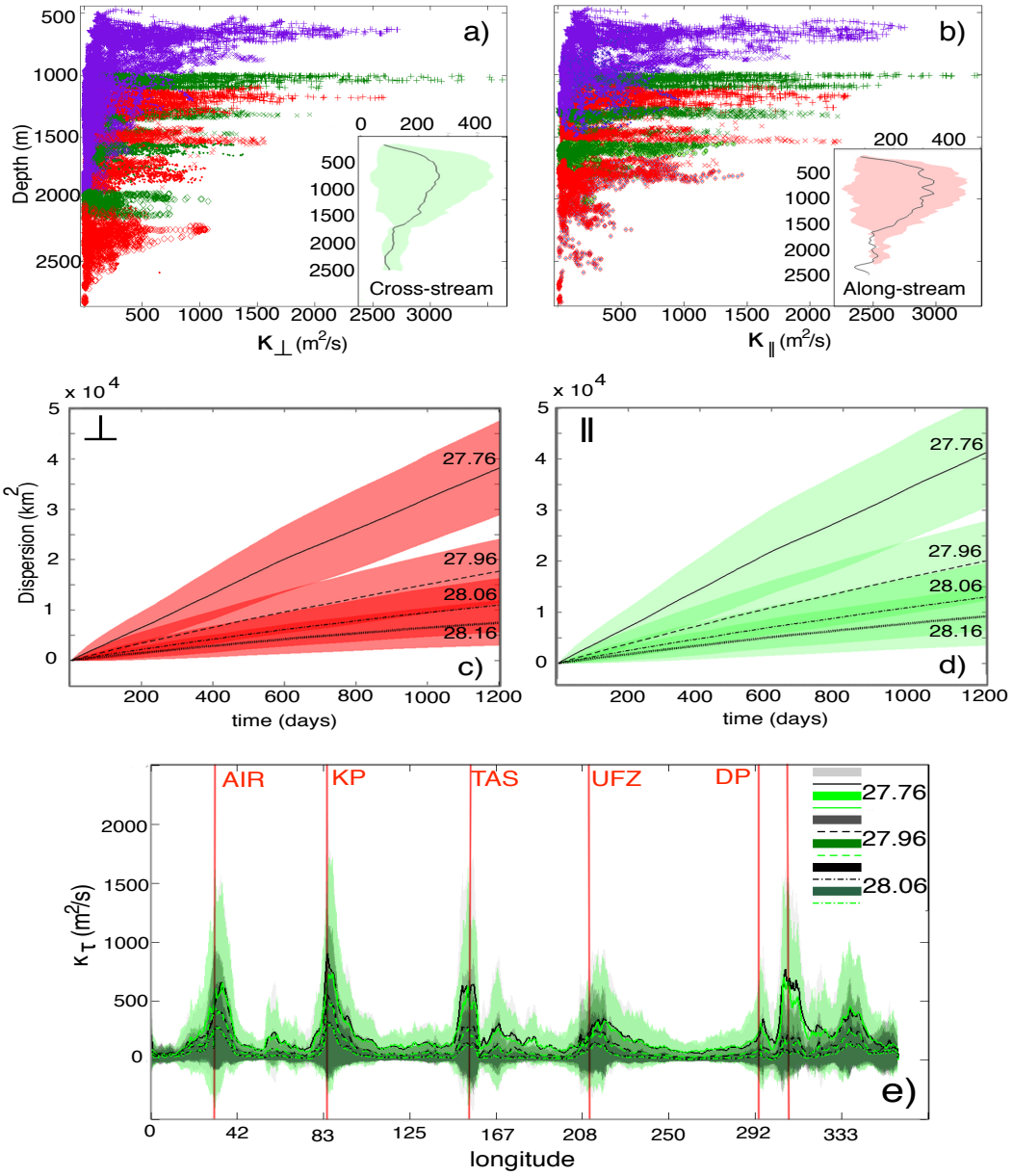

FIG. 4.10: a) Cross- and b) along-stream diffusivity as a function of depth averaged along-streamlines depicting the regions between SAF-PF (red), around PF (green) and south of PF (purple) for isoneutrals 27.76 (+), 27.96 (×), 28.06 (·) and 28.16 (◇). Boundaries are selected from mean geopotential anomaly values (m s^{-1})^2 (Fig. 4, Appendix A), computed with respect to surface, over the entire simulation period 1988-2004. Values of 9.2-12.4 (SAF-PF), 8.8-9.2 (around PF) and 3-8.8 (south of PF) are selected in agreement with ACC fronts from *Sallée et al.* [2008a] and dispersion of particles during the first year of travel (Fig. 5, Appendix A). Insert diagrams are means and $\pm\sigma$ (shaded areas) over all observations (the horizontal scale is exaggerated). c) Cross- and d) along-stream dispersion $\overline{\mathcal{D}^2}$ (in km^2) as a function of time for all longitudinal releases in the SOL experiment for isoneutral surfaces 27.76, 27.96, 28.06 and 28.16. e) Cross- (green colours) and along-seam (grey colours) diffusion (m^2 s^{-1}) computed as an average over all particle releases in the main ACC (geopotential anomaly <14 m^2 s^{-2}) as a function of longitude. Maxima are concentrated in the Atlantic-Indian Ridge and the South-west Indian Ridge conjunction (AIR); downstream of the Kerguelen Plateau (KP); Tasmania (TAS) and the Campbell Plateau; the Udintsev Fracture Zone (UFZ); Drake Passage (DP) and South Georgia. Means are constructed over all particles. Shaded areas denote $\pm\sigma$ range.

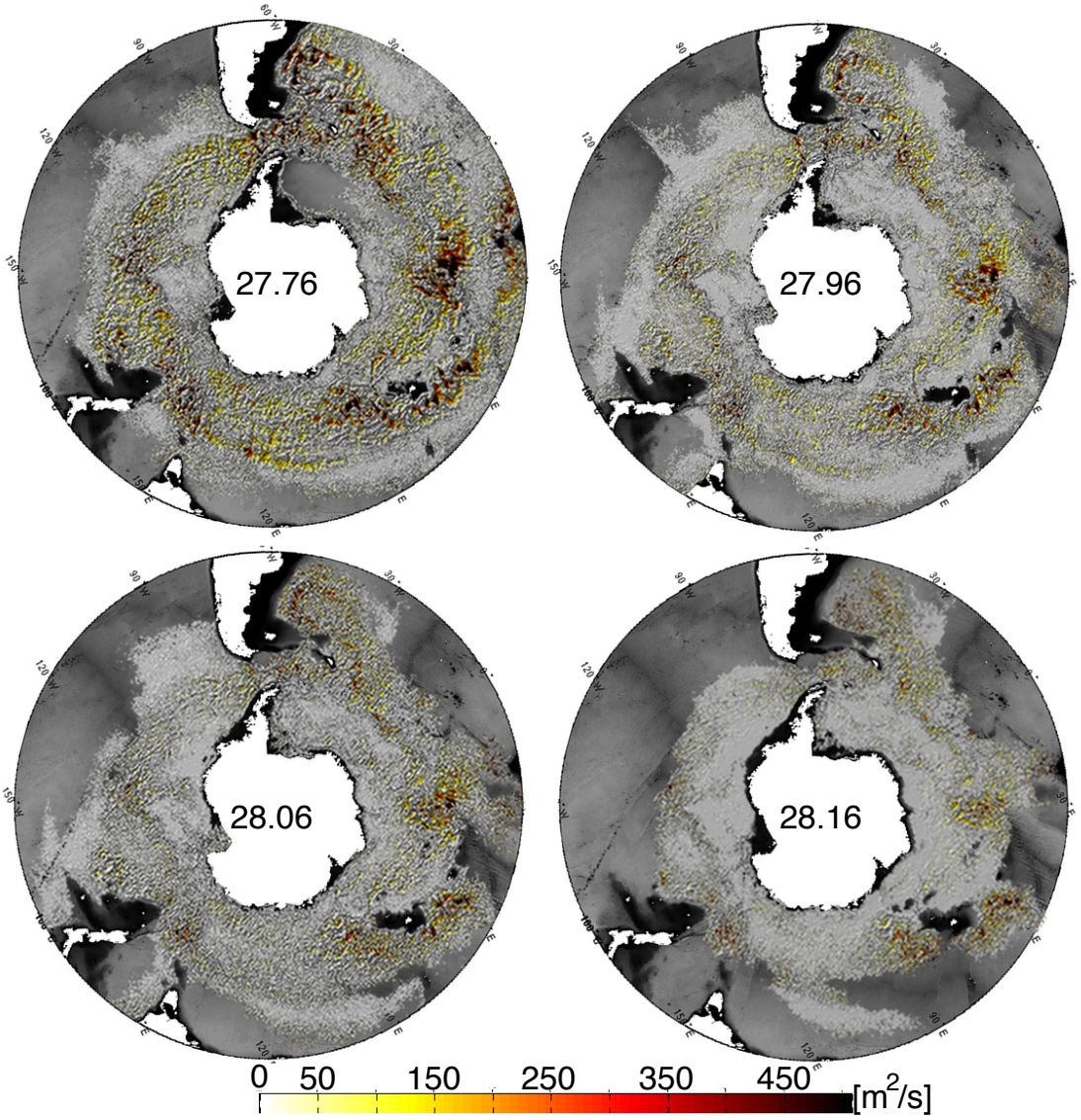

FIG. 4.11: Differences between $\kappa_\perp$ and $\kappa_\parallel$ for all isoneutrals in the SOL experiment. Only values of $\kappa_\perp$ greater than $\kappa_\parallel$ are shown.

fronts on the respective isoneutrals are located in depths deeper than 800 m in general, and thus shallower depths are not sampled. The increase is mainly due to the observed maxima of the specific along-streamline averages.

Examining diffusivity as a function of longitude for all records in the main ACC path (Fig. 4.10, e) we can identify the intensified mixing events mentioned in the previous paragraph and clearly depicted in figures 4.8 and 4.9. Regardless of the density surface under consideration, the suppression of mixing in the respective longitudes is not effective. Diffusivity increases 3-4 times compared to the background values where the Atlantic Indian Ridge meets the South-west Indian Ridge at 30°E, downstream (eastward) of the Kerguelen Plateau, Tasmania and downstream of Drake Passage.

4.4 Concluding remarks

The Lagrangian estimate of absolute diffusivity stated herein is consistent with previous numerical model studies with moderately derived values [*Treguier et al.*, 2007; *Lee et al.*, 2009; *Abernathey et al.*, 2010; *Griesel et al.*, 2010]. Nonetheless, the underlying proposed mechanisms and spatial distribution of values are not fully in accordance, as we explain later on.

Our estimate is characterized by a mean value in agreement with the diffusivity value used by *Danabasoglu and Marshall* [2007] ($\simeq$ 400 m^2 s^{-1} at a depth of 2 km) in their adjusted Parallel Ocean Program (POP) version model. With the employed vertical variation of the diffusivity scheme they found a better comparison of POP's model output with observational data.

Values in general, excluding the vigorous mixing regimes (>1500 m^2 s^{-1}), seem to be in agreement with those derived by *Griesel et al.* [2010] for the same depth. Our spatial resolution, though, is significantly higher, so the detailed spatial arrangement here is not expected to depict the same level of detail. The discrepancy in diffusivity values for the respective depths is mainly due to the fact that their derivation of isopycnal diffusivities is performed in a depth release coordinate system. They record a potential density variance of floats, during their lifetime, which equals our isoneutral surface density resolution. In contrast, our numerical scheme through construction does not allow the migration of floats in different isoneutrals during their travel time. As such, they compute an average diffusivity for a range of potential density values which in our case would be equivalent to a mean κ_τ between two consecutive isoneutrals.

The regions and spatial distribution of our maxima are consistent with the respective intensified local mixing regimes depicted by *Lu and Speer* [2011], with the application of relative dispersion and the Finite Scale Lyapunov Exponent (FSLE) as their mixing indices. In this context, OCCAM 1/12° model performs similarly to the Southern Ocean State Estimate (SOSE) used in their study to depict mixing regimes. They also find that both relative dispersion and FSLE are positively correlated with $\sqrt{EKE}$, but there are potential limitations in their ability to depict the role of jets as barriers to mixing. Our diffusivity estimation is consistent with the spatial distribution of high EKE, but it does not scale analogously to EKE everywhere in the ACC. Furthermore, we show in the sections to follow that both relative dispersion and separation rates (an analogous index to FSLE) are very useful tools in depicting local jet barriers to mixing. We suggest that the discrepancy is mainly due to the ability provided by the increased spatial resolution of the Lagrangian scheme employed here.

In agreement with *Griesel et al.* [2010] we argue that parameterizations of diffusivity with a constant eddy length $\mathcal{L}_e$ and time scales T_L is not valid. Nonetheless, they

found high variation in derived Lagrangian diffusivities with respect to EKE. In all our computations, we find great spatial variability of $\mathcal{L}_e$, which is consistent with high EKE at specific regions. In a backward calculation using a constant mixing length, as for example the $\mathcal{L}_d$ [*Stammer*, 1998; *Sallée et al.*, 2008b], in order to compute an equivalent diffusivity as $\kappa = \alpha\sqrt{\overline{EKE}}\mathcal{L}_d$, we derive a scaling parameter α of $\mathcal{O}(10)$ smaller than that produced by *Sallée et al.* [2008b]. Our result presents a substantial spatial discrepancy and closely follows the high mixing areas (Fig.4.8). Although *Sallée et al.* [2008b] computed diffusivity in the surface mixed layer, our EKE presents an analogous spatial distribution on the various isoneutrals; therefore, we expect the same spatial pattern on OCCAM's mixed layer (Figs. 2.21 - 2.22).

Additionally, as far as the high variability of κ_τ with EKE in the study of *Griesel et al.* [2010] is concerned, the focus should be on the different time series involved in the Lagrangian trajectories simulation. They advect particles for a period of 3 years and subtract a 2 year Eulerian local mean from the instantaneous velocity field. We determined (Chapter 2 2.4.1 p.51) that any Eulerian mean constructed from a time series smaller than 5 years (we use 17 years) does not lead to a robust decomposition of the flow, and the EKE result still carries characteristics of the intensified time-invariant component. As such, Lagrangian diffusivities cannot be clearly associated with the EKE. In addition, regardless of using a spatially-varying Eulerian mean, for the velocity decomposition in time invariant and variant components, the short time series in their study does not, effectively, remove shear dispersion by way of the mean. This affects their along-stream diffusivity with a computed $\kappa_\parallel$ substantially greater than $\kappa_\perp$. We find this discrepancy with our derived result to hold in all reviewed Lagrangian statistics studies herein.

The mixing intensified regions, mentioned previously in this section, are related to high EKE values, low bottom roughness and high probability index values (see Chapter 3 section 3.3). These regions are also characterized with non-parallel small scale PV gradients (Fig. 8, Appendix A) and a spatially dense arrangement of coherent vortices (Fig. 9, Appendix A). In the sections to follow we examine each one of these factors in supporting our proposed mechanism for the observed diffusivity structure.

Based on the scaling of diffusion here, OCCAM 1/12° model certainly does not underestimate eddy diffusivity in comparison with results derived from OGCM and altimetric observations in previous studies. In contrast with a previous suggestion regarding OCCAM's inadequacy for a complete representation of eddy transport processes and KE [*Scott et al.*, 2010], we believe that OCCAM's performance does not undermine the results presented here. Any discrepancies are more attributed to the methodologies and datasets employed than to flow dynamics representation. This is an assessment based on derived diffusivity and EKE values, since our main focus is to decipher the dominant

eddy stirring mechanism in a similar dynamical context with other studies, rather than a model evaluation in comparison with other GCM or hydrographic datasets.

Chapter 5

The fundamental structure of mixing

Introduction Stirring and mixing pathways and mixing suppression are by no means restricted to specific spatial scales. On the contrary, theories and conceptual experiments, spread through the whole range of small to large scale dynamics, seem to denote the resemblance of structures when considering turbulence. In general, considering a tracer release in a turbulent flow, the exhibited dispersion is the combined result of: *stirring*, due to velocity shear, and *mixing*, due to micro-scale molecular diffusion. Stirring as an adiabatic process leads to stretching of the tracer contours and the subsequent sharpening of concentration gradients. Ensuing molecular diffusion induces irreversible mixing and diminishes the gradients' contrast [*Lee et al.*, 2009].

Large scale ocean dynamics are dominated by large mesoscale eddies of $\mathcal{O}(100)$, being the dominant energy-containing oceanic feature, and gyre circulations. The importance of local regimes, though, where the smaller scales act to control deep water formation, 'erosion' of stratification, mixed layer stabilization and to create pathways for climate signals communication into the ocean's interior, has previously been documented in a variety of ocean basin scales and latitudes, for example the North Atlantic, the Mediterranean basin and the Southern Ocean [*Artale et al.*, 1997; *Thomas et al.*, 2008; *Sallée et al.*, 2008a, 2010; *Thompson et al.*, 2010]. Relative dispersion, as we shall show, is quite sensitive in depicting underlying dynamics and thus provides a useful insight into their parameterization in circulation models.

5.1 Relative dispersion, PV gradients and separation rates as diagnostic tools for mixing dynamics

In order to provide a context for a description of underlying flow dynamics, it is of interest to establish a relationship between the semantics of particles' dispersion values and the transitory mixing capability of respective environments.

Particle trajectories are examined at discrete intervals of time, designated by sequential points in space rather than viewing a particle trajectory as a curve in space. Intuitively, the following generalized approximations can be argued. Based on the initial separation distance d_0 and its proximity to release time t_0, as the time interval $[t_0, t_0 + \tau]$ where diffusion κ_{τ_∞} has not yet reached the asymptote limit, rapid increases of $\overline{\mathcal{D}^2}$ delineate the movement of the two respective particles under consideration in quite differentiated kinematic environments. The opposite is signified by small recorded values. What is of interest is the way in which the two environments correlate with the mixing potential of specific areas.

The dynamical systems theory perspective Mixing progression is conveyed by spatio-temporal mappings' evolution of particles' positions. The organization of particles' future positions in converging and stretching filaments (in dynamical systems theory this terminology is referred to as stable and unstable manifolds) can infer mixing processes [*Schneider and Tél*, 2003]. In geophysical flows the approach of identifying and assessing stable and unstable material lines (manifolds) as hyperbolic trajectories is well documented (see *Haller and Yuan* [2000]; *Haller* [2001, 2002] and *Wiggins* [1992]; *Wiggins* [2005] for detailed discussions). Both stable and unstable material lines are impermeable to particles by definition. Because particles follow material lines, in a fluid dynamics perspective mixing can be portrayed by the gradual divergence of material lines. Crossing points of stable and unstable manifolds emerge in space and hold both diverging and converging material lines. Material lines around a barrier in mixing, and thus impervious to particles, would tend to be parallel where mixing is inhibited and dispersive at each side of the barrier. The mapping hence delineates their 'behavioural' characteristics of repeller (finite-time stable manifolds) or attractor (finite-time unstable manifolds) structures, respectively [*Haller and Yuan*, 2000].

Consistent with dynamic systems theory representations, the presence (absence) of barriers in transport, and in effect mixing suppression (expression), can thus be mapped with regard to values of relative dispersion on one (arbitrarily selected) particle's trajectory in an evaluation pair. *Gildor et al.* [2009], in their study on sub-mesoscale processes, demonstrate the partitioning of different mixing regimes (different growth law dependencies) separated by a contour of high relative dispersion also depicting the transport

barrier effect. A caveat exists for particles initially displaced at distances insufficiently small to resolve the spatial signature of such regimes. Initial separation controls the resolution of the computed dispersion growth rates (Fig. 11, Appendix A).

The aim, in this part of the present study, is to exhibit the importance of particles' dispersion evolution to the typical scales of energy provision to the system with respect to a pseudo-anisotropic organization of the flow at small time lags. In this way we can propose a mechanism for the regions where mixing ceases to be suppressed. Additionally, relative dispersion, apart from the depiction of local jets and barriers to particle movement, has one fundamental difference from diffusivity approximations based on single particle statistics. It does not require decomposinghe flow into mean and time variant components. On the other hand, it is influenced by background shear dispersion [*LaCasce*, 2008].

Of importance is the definition of typical length scales after which particles' relative displacements are considered uncorrelated and diffusion derivation is not representative of local dynamics. Defining diffusion regimes and the fundamental time scales associated with their stages of evolution, we rely on the separation rates of pairs' of particle trajectories as a diagnostic tool. Transport barriers can be delineated by the mappings of these separation rates.

Potential vorticity and particle trajectory evolution PV gradients' inhomogeneous distribution affect particle pairs' dispersion evolution based on the PV regime at the time of release. PV is computed on the selected isoneutral density surfaces in this study following (5.1)[1],

$$PV_n = \frac{(f + \zeta) \cdot N^2}{g} \tag{5.1}$$

where f is the *Coriolis* parameter (s^{-1}), ζ is relative vorticity (m^{-1} s^{-1}) and N^2 is the squared Brunt -Väisälä frequency (s^{-2}).

Dependence on initial position is a controlling factor in relative dispersion evolution, since it characterizes the kinematic environment at the time of release. As such, it involves an intrinsic deficiency in constructing averages in space and time, especially considering the inhomogeneity of the environments visited by a particle at the respective time scales. Furthermore, dispersion regimes can be classified as isotropic (non-dispersive) and anisotropic (dispersive). In the dynamical context of an intensified

[1]In the calculation of q, relative vorticity ζ and the squared Brunt -Väisälä frequency

$$N^2 = \frac{g}{\gamma^n} \frac{\partial \gamma^n}{\partial z}$$

are computed from isoneutral velocity and neutral density γ^n for each of the 5-day mean files (see section 2.3.1.1).

multiple filamented jet structure, characteristic of the ACC, isotropic regimes can be associated with a weak strain factor (hyperbolic regions in the flow based on the $\mathcal{OW}$ parameter with the elliptic ones associated with the vortices, see figure 9, Appendix A).

Following *Marshall et al.* [2006]; *Abernathey et al.* [2010] and *Dritschel and McIntyre* [2008] on PV gradients' role in effective diffusivity K_{eff} distribution and the resilient eddy transport barrier effect, we show that the spatial alignment of PV gradients in non-parallel structures is essential for the proliferation of mixing environments. As such, the relative initial position with respect to background PV allocation plays an important role in κ_τ distribution. We also discuss the energy cascade scales associated with the evolution stages of relative dispersion, in order to examine whether OCCAM 1/12° model is consistent with a physical context of ACC dynamics.

5.1.1 Relative diffusion and energy cascade scales

In order to assess OCCAM and our results in a physical context of ACC dynamics, we examine relative diffusivity in relation to energy cascade scales for both isopycnal and isobaric surface levels.

Relative diffusion κ_τ, as a function of distance among particles for all available pairs, is computed for all isoneutral surfaces in the SOL experiment (Fig. 5.1) and for isobaric level 2 (8 m) in the DIMES experiment context (Fig. 5.2) (see section B.6, Appendix B). We also present diffusivity for the zonal and meridional components, as opposed to the cross- and along-stream components in the section 4.3, in order to decipher the scales of separation in a geographical context with respect to OCCAM model grid resolution.

In agreement with 2D 'incompressible' turbulence theory (see *Vallis* [2006b], Chapter 8), κ_τ in the ACC depicts a forward enstrophy $\mathcal{E}$ cascade towards smaller scales for distances <3-4 km and an inverse energy cascade from smaller to larger scales at intermediate separations of >3-4 km and up to 10-20 km (in fact, the inverse energy cascade continues for larger scales but the correlation coefficient of the statistical fit is reduced). Relative diffusivity for level 2 depicts a Richardson scaling between 10-200 km (inverse energy cascade). In theory, the upper limit of the energy injection scale is considered to be equal to the first baroclinic Rossby radius of deformation $\mathcal{L}_d$ [*Salmon*, 1980], which for the Southern Ocean is 10-20 km [*Chelton et al.*, 1998]. Above that scale and up to the eddy mesoscale of $\mathcal{O}$(100 km) ($\sim$ *Rhines* scale), energy is transferred from smaller to larger scales (for an introduction to growth law dependencies and energy cascades see p.176, Appendix A). Our computation of eddy length scales $\mathcal{L}_e$ (section 4.2.4) agree with the first limit of forward $\mathcal{E}$ cascade and are close to $\mathcal{L}_d$. Smaller than the $\mathcal{L}_d$[2] energy

[2] A dependence on latitude has previously been discussed by *Arbic and Scott* [2007] for the surface ratio $\mathcal{L}_e/\mathcal{L}_d \in [0.5 \quad 2]$ versus quadratic and linear bottom drag, for a 'low' (10-30°) to 'high' (50° - poleward) latitudes respective variation.

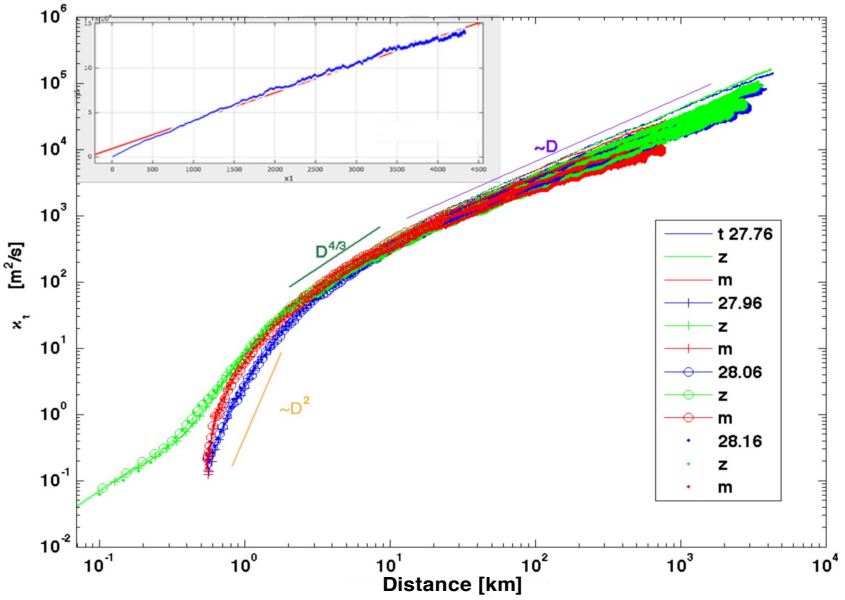

FIG. 5.1: Relative diffusion κ_τ ($m^2\ s^{-1}$) versus displacement for all isoneutral surfaces over all available pairs and longitudinal releases. A linear dependency on dispersion is depicted for early time distances (forward enstrophy $\mathcal{E}$ cascade towards smaller scales), with a transition to a 4/3 *Richardson's* power law at intermediate separations ('local dispersion'), characteristic of an inverse energy cascade from smaller to larger scales. Later on, and for distances larger than 10-20 km ($\sim \mathcal{L}_d$) the relationship becomes linear with respect to displacement (insert diagram) (see section A.5, Appendix A). The meridional component of diffusivity is bounded but applies to much larger separation scales at $\sim$ 900 km ($\simeq 40°$ on the meridional direction). Is this a large scale flow restriction effect? This value is well fitted to the ACC meridional extent, as depicted by the particles' PDFs in section 3.2.

injection scales have previously been suggested in the presence of baroclinic instability [*Scott and Wang*, 2005; *Scott and Arbic*, 2007]. Nonetheless, the proximity of our $\mathcal{L}_e$ and $\mathcal{L}_d$ means that the necessary energy for eddy formation is of the same order as the injection scale [*Stammer*, 1997; *Shuckburgh et al.*, 2009b]. Absolute diffusivity (Fig. 10, Appendix A) also follows *Richardson's* 4/3 power law for scales up to 100 km, which is a common result of many Lagrangian studies of ocean dynamics [*LaCasce*, 2008]. Richardson scaling is indicative of 'local dispersion' or 'shear dispersion', depending on the characteristic decorrelation length scale. A representative decorrelation length scale for isoneutral 27.76 would be $\sim$ 45 km, based on absolute dispersion scaling with respect to time (Fig. 4.3).Thus, with regard to the isoneutral simulations, Richardson's law indicates 'local dispersion' (Fig. 5.1). The same is true for isobaric level 2 (8m) even though decorrelation length scales are greater by $\mathcal{O}(8-10)$ (Fig. 5.2, b).

Relative diffusion does not enter the diffusive limit in the context of classical diffusion theory. Non-convergence to the theoretical value of $2\kappa_\infty$ (κ_∞, absolute diffusivity), has already been referenced in a Lagrangian study of surface drifters in the Gulf of Mexico [*LaCasce and Ohlmann*, 2003] and particle dispersion studies in modelled free-surface

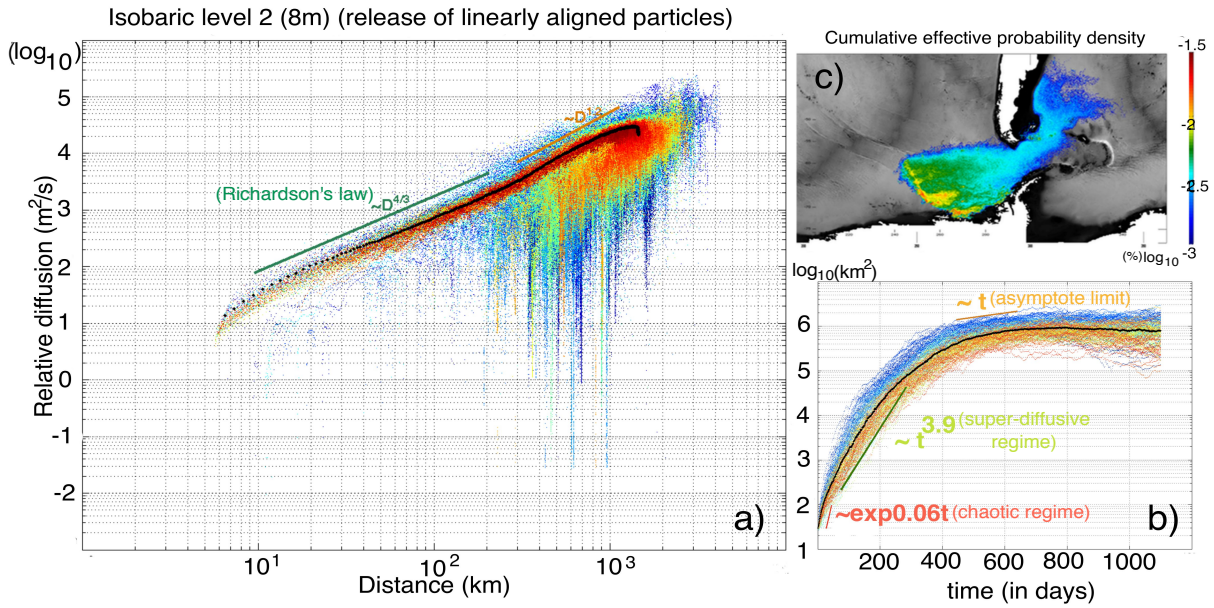

FIG. 5.2: (a) Relative diffusion ($m^2\ s^{-1}$) versus separation distance (km) for monthly releases on OCCAM's 1/12° model isobaric level 2 in the vicinity of DIMES release. Colours denote the monthly releases (blue-first; dark red-last) initiated on model day 1095 and concluding on model day 6765. (b) Relative dispersion $\overline{\mathcal{D}^2}$ versus time for the aforementioned dataset. The discrepancy in the power law for intermediate times ($\sim t^{3.9}$-super-diffusive regimes, see section 4.2.2 p.90) for the dispersion plot is because of filtering out of outliers. The statistical median then denotes non-local dispersion for the respective times, which is converse to *Richardson's* law (denoting 'local dispersion' or shear dispersion, depending on the characteristic decorrelation length scale). The asymptote limit is reached at time lags >500 days, thus suggesting late time lag correlations and the existence of coherent structures in the flow (see Fig. 8, Appendix A). (c) Cumulative effective probability density (see Chapter 3) for all monthly releases and a travel time of 1 year on isobaric level 2, presented here in order to delineate the dynamics of the specific release.

flows [*Schumacher and Eckhardt*, 2002]. In theory, whether or not κ_τ converges depends on Lagrangian velocity time series behaviour. Where the Lagrangian velocity covariance does not approach zero faster than $1/t$ as $t \to \infty$, indicating that memory of past time lags is retained, as in the case of coherent structures in the flow, κ_τ is not admitted to a diffusive stage [*Davis*, 1991]. Accordingly, diffusivity grows without an upper bound limit at distances even of $\gg 100$ km.

Both relative and absolute diffusion methods are quite consistent and within certain approximations are consistent with the interpretation of physically realistic dynamics of the ACC by OCCAM. Diffusivity at the surface layer appears reduced in comparison with that on the density surfaces for respective displacements. Since we have not examined absolute diffusion on any isobaric level, we are unable to argue with an increase of diffusivity at greater depth in line with the existence of a steering level at depth in the context of critical layer theory.

Following *Thomas et al.* [2008], it is possible that mesoscale dynamics in the ocean interact with sub-mesoscale mechanisms producing complex sub-mesoscale structures within the same mesoscale field. Borrowing a scaling argument from the authors, sub-mesoscale characteristic lengths for the main path of the ACC would be around 1.5 km in OCCAM. Eddies below the mesoscale range of $\mathcal{O}$(10-100 km) tend to have high Rossby numbers, which are scaled as ζ/f and $\zeta = \mathcal{O}(f) = 10^{-4}$ s^{-1}, where ζ and f represent relative and planetary vorticity, respectively. In OCCAM 1/12° model, though, Rossby numbers are half of the expected value, and thus sub-mesoscale lengths of $\mathcal{O}$(1km) are inadequately delineated by QG dynamics [*Thomas et al.*, 2008] and are not resolved herein.

5.2 Delineating mixing barriers and pathways

5.2.1 Dispersion, flow differentiation and the role of PV gradients in local-regimes

Relative dispersion has been considered so far in a non-local approximation. However, local regimes are more complex (see section A.5.2, Appendix A). The growth law dependencies described above are not characteristic for all groups of pairs of particles but are nonetheless spatial means (dependent on dominant flow patterns and directions) can be constructed in order to define a general potential trend and the distribution of $\overline{\mathcal{D}^2}$.

5.2.1.1 Dispersion and flow differentiation

In figure 5.3 time evolution of dispersion $\overline{\mathcal{D}^2}$ is presented for releases between 0-180° on isoneutral density surface 27.76 for a period of 18 days. The time scale is selected in order to minimize overlapping for each of the longitudinal releases. In agreement with the stretching and folding of coherent barriers [*Haller and Yuan*, 2000], relative dispersion mapping shows an analogous spatial alignment with contours of mean velocity $\mathcal{U}_m$, depicted here with isotachs of 10 cm s^{-1}. Following *Wiggins* [1992], in the context of dynamical systems, the trajectory of any particle starting on a material curve (stable or unstable manifolds) is invariant as to its displacement relative to the evolution of the geometric space of the curve. Since particles follow specific material curves, dispersion minima and maxima are associated with isotropic (parallel) and anisotropic (diverging or converging) material line arrangement. As the dispersion resolution is regulated by the initial small separation of particles (Fig. 11, Appendix A), for scales comparable to the jet cross-stream extent, pairs residing within it should exhibit small values. The distribution of minima also indicates isotropic particle displacements.

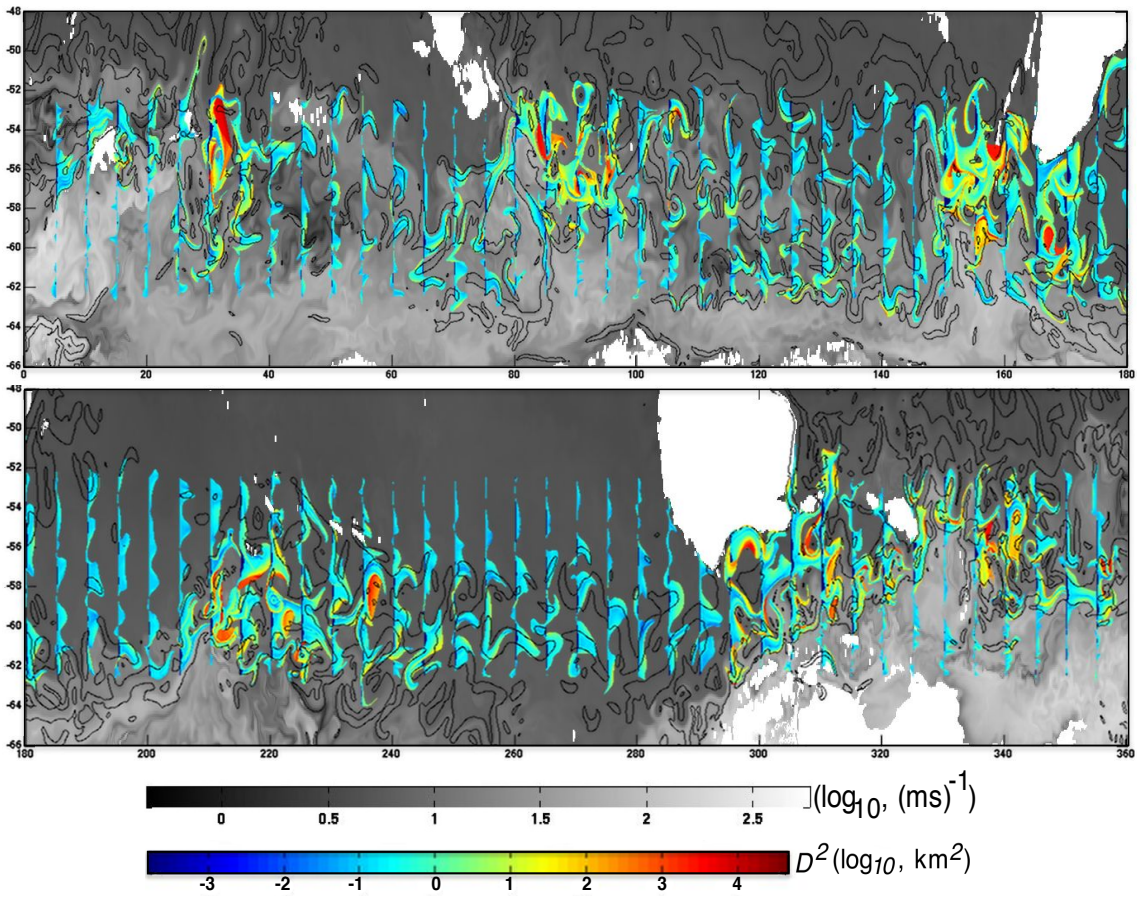

FIG. 5.3: Relative dispersion $\overline{\mathcal{D}^2}$ (log_{10}, km^2) evolution for a time length of 18 days from experiment initialization, superimposed on mean PV ($log_{10}(|PV| \times 10^{11})$ (m s)$^{-1}$) (grey-scale) for longitudinal releases 0-180° (top panel) and 180-360° (bottom panel) in the SOL experiment for isoneutral surface 27.76. Also shown are isotachs (black contours; 10 cm s^{-1}) of isopycnal computed mean horizontal velocity $\mathcal{U}_m$. Minima in dispersion denote coherent shear strain regions which, where they are aligned with locally strong PV gradients (see also figure 5.4), depict the jet structure, as seen also from the latitudinal gradient of the dispersion mapping, where intensified shear strain rate co-alignment is obvious. The relevance of mixing barriers with high relative dispersion values is discussed in the text. Dispersion is mapped on one of the particles' trajectories constituting the respective pair examined.

Collocation with resilient barriers, depicted by locally intensified gradients of PV (Fig. 5.4) and induced by shear strain, is depicted. The potential of PV gradients to act as transport barriers is attributable to difference $\Delta q_{barrier}$ with regard to $\Delta q_{particle}$. When large, fluid particles are unable to change their vorticity enough so as to cross the barrier [*Provenzale*, 1999]. In figure 5.5, illustrating an example release from the Kerguelen Plateau area, relative dispersion, as a diagnostic tool of barriers in the flow, successfully reproduces the role of PV gradients. Dispersion inhibition is also recorded (see pairs around 900ID and 1500ID), where particles travel in homogeneous PV regions (jet cores) defined by strong PV gradients (Fig. 5.4, 80°E).

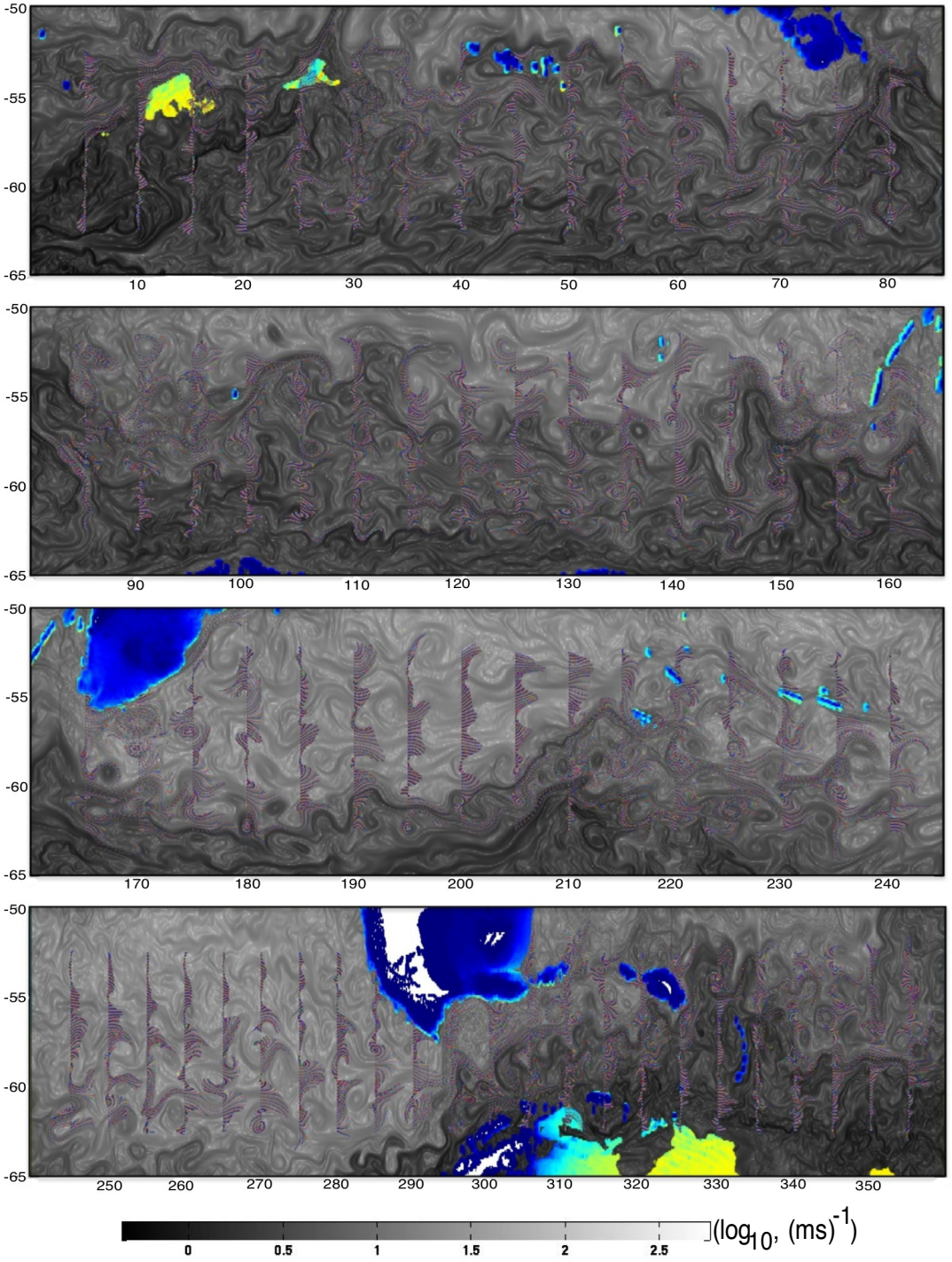

FIG. 5.4: Particles' (individually colour-coded) positions for a 20-day evolution period superimposed on the PV gradient ($log10(\times 10^{16})$ (m s)$^{-1}$ km^{-1}) averaged over a period of 20 days on isoneutral surface 27.76. The period covered equals that of 20 days from the initialization of the SOL experiment (model day 1095). The role of PV gradients as drive-guides of relative dispersion contour evolution can be seen clearly. PV gradients in grey-scale. Bathymetry depicted by a different colour scale.

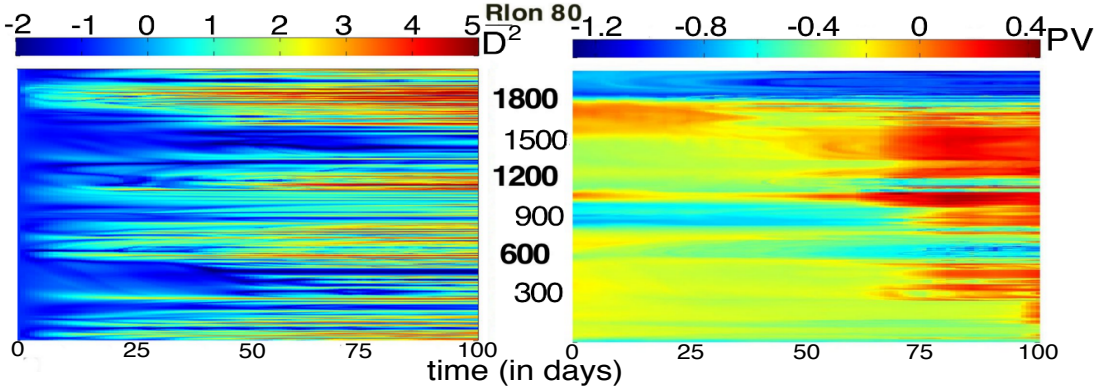

FIG. 5.5: Hovmöller diagrams of: (left panel) relative displacement, $\mathcal{D}^2 - \mathcal{D}_0^2$ (log_{10}, km^2) for all pairs of particles, time evolution for the first 100 days for releases at 80°E in the SOL experiment context and for isoneutral surface 27.76. Y axis denotes particles pairs' IDs at respective release latitudes (N-S; up-down); standard latitudinal extent at the location of release, -62.5° to -52.5°; (right panels) PV ($log_{10}(|PV| \times 10^{-9})$, in (m s)$^{-1}$). Colour scale for PV denotes a south (hot colours) to north (cold colours) alignment (colour scale differs for each release). Initial separation distance is $\mathcal{D}_0 = 550$ m.

In both mappings (Fig. 5.3 and 5.5), on both sides of these minima, values of $\overline{\mathcal{D}^2}$ delineate flow differentiation as a function of distance from the jet core. Maxima then also signify the existence of a barrier residing between the respective particles in a pair. A continuous signal (Fig. 5.3) of minima in dispersion with time demonstrates a resilient jet structure. Multiple parallel jets, diverging or converging, can also be seen, with their relative progression being the direct result of jet enhancement or destruction.

5.2.1.2 PV gradients and eddy stirring

A closer look at figure 5.4 reveals an essential characteristic of PV gradients' spatial distribution and intensity in regions where $\overline{\mathcal{D}^2}$ is high. The PV gradient is characterized by a non-parallel structure of reduced scale, in comparison with the strong PV gradients engulfing them to the south. In agreement with *Thompson* [2010], which highlights mixing suppression by jets in the presence of non-parallel and small scale structure PV gradients as non effective, all regions of relative dispersion maxima (Fig. 5.3) and high mixing areas of absolute diffusivity (Fig. 4.8) are associated with regions of PV with a non-parallel small-scale structure. See, for example, in figure 5.4, the South-west Indian Ridge between 30-40°E and 50-55°S, downstream of the Kerguelen Plateau between 85-100°E and 50-60°S, the region upstream (westward) of the Macquarie Ridge at 150°E and east of the Campbell Plateau at 165-180°E and 50-60°S, the Udintsev Fracture Zone at 220°E, the Drake Passage and the Scotia Sea and downstream of 330°E. Nevertheless, the non-parallel alignment of the PV gradients is not exclusive to these areas.

These PV regions, downstream of a meridional jet excursion, do not necessarily coincide with regions of intensified mixing. The fundamental nature of stirring, and the subsequent mixing of a tracer, is established on the existence of a spatially and temporally differentiated kinematic environment. In figure 5.6 two different mixing regimes are illustrated as being characteristic of the mixing potentials associated with PV gradients' non-parallel alignment (left vs. right) for a period of 121 days. A 'chaotic' PV spatial distribution at 215.5°, opposed to an apparently more organized structure for the DIMES location (signifying the existence of strong gradients for the release further west, as seen by the values range) can be seen. Previously, enhanced diffusivity κ has been associated with strong PV gradients [*Morel and McWilliams*, 2001], especially in 'leaking' areas [*Naveira Garabato et al.*, 2011]. Accepting a chaotic advection regime at small time lags, potential vorticity should exhibit a transition to an arrangement of filaments progressively becoming finer in scale and with a gradual increase in space occupancy [*Pierrehumbert*, 1991].

In both figures 5.5 and 5.6 PV is not exactly conserved for particles. In a QG turbulence context, forcing and dissipation can cause fluid particles to overcome PV gradients [*Provenzale*, 1999]. The ability for a fluid particle to cross a vorticity isoline and change its own PV is controlled by the intensity of the exerted forcing (dissipation). This explains why strong PV gradients act as transport barriers [*McIntyre*, 2003].

Through jet realization, local PV gradients and KE exhibit maxima in the jet-cores, thus defining explicitly the inhibition of mass exchange. Differentiation of a kinematic environment is provided as a nonlinear, shear-straining mechanism result, with the subsequent formation and maintenance of transport barriers and vortices, from the interaction between eddies, generated by baroclinic or Kelvin-Helmholtz instabilities and the mean flow [*Thompson*, 2010]. Consequently, the mixing capacity of such an environment is likely related to the spatial density of those interacting vortices and jets, being a direct ramification of the underlying shear-straining mechanism.

5.3 The role of EKE and mean flow in controlling mixing

Addressing eddy stirring as the spatial distortion of particles through the combined processes of stretching and eddying [*Davis*, 1991], the mapping of κ_τ per release (Fig. 13, Appendix A) should be able to depict eddy-intensified stirring regimes. Additionally, for small time scales and travel times of particles, relative dispersion is able to delineate the jets' boundaries (Fig. 5.3). The spatial extent of dispersion mapping (Fig. 5.3, see also Fig. 13, Appendix A) for each longitudinal release and the specific time scales considered are also used in the assessment of transport inhibition and the existence of constraints in dispersion evolution at the respective spatio-temporal scales.

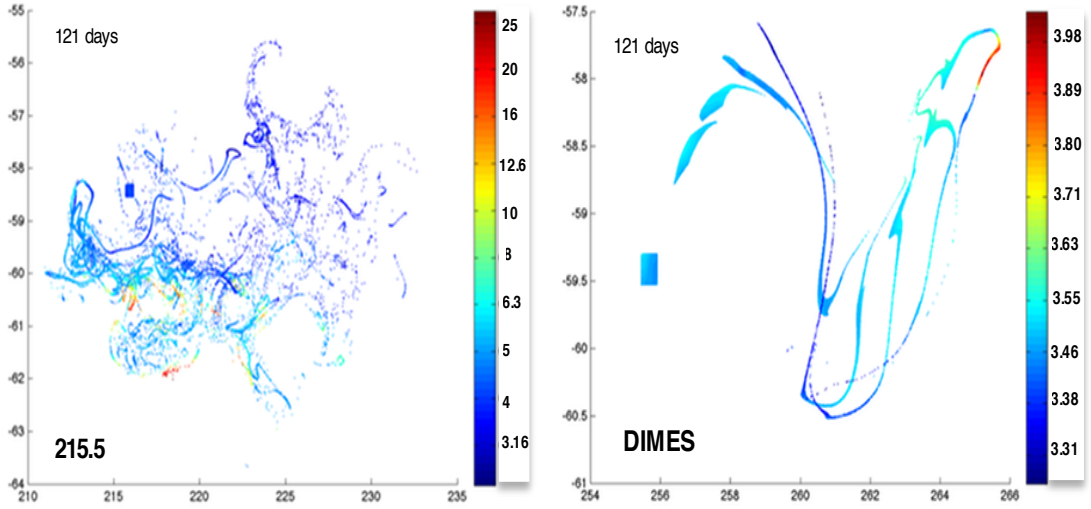

FIG. 5.6: Particles' PV evolution for a period of 1221 days are depicted for releases at 215°E (left) and at 255.5°E (DIMES) (right) (see section B.6, Appendix B). Particles' positional progression are colour-coded with PV $((|PV| \times 10^1 1))$ (m s)$^{-1}$. Obvious points of note are high concentration particle streaks characteristic of the stirring and stretching processes acting on particles' trajectories. Releases are initialized in clusters of 2500 particles.

Eddy stirring suppression in the cores of intensified jets has been suggested [*Ferrari and Nikurashin*, 2010; *Naveira Garabato et al.*, 2011] where mean flow $\mathcal{U}_m$ is much greater than eddy propagation velocity c. If mixing potential is solely a function of the residual and mean flow ratio, then the suppression mixing factor $\mathcal{S}_\kappa$ [*Naveira Garabato et al.*, 2011; *Nikurashin and Ferrari*, 2010; *Shuckburgh et al.*, 2009b], as

$$\mathcal{S}_\kappa = (1 + 4\mathcal{U}_m^2 \cdot \overline{EKE}^{-1})^{-1} \quad \text{with } \mathcal{U}_m \text{ denoting the mean flow,}$$

depicted in figure 5.7, should reveal this mixing capacity. Values ~ 0.5 denote that the mean flow is balanced by EKE, and values towards 1 depict that EKE is dominating. Suppression of mixing is associated with values smaller than 0.5 and decreasing towards 0. In order to delineate the stirring mechanism by showing the proliferation of vortices and the accompanying strain regimes, where eddy stirring suppression ceases, we also illustrate coherent vortices' spatial distribution employing the Okubo-Weïss parameter $\mathcal{OW}$ (see p.102). Overlaid are isotachs of 5 and 10 cm s^{-1} of total velocity $\mathcal{U}$ and particles' positions for the respective time scales.

5.3.1 The role of coherent vortical elements

The time evolution of particle displacement in figure 5.4, compared with figure 5.7, indicate that eddy stirring of particles commences at regions of non-parallel PV gradients

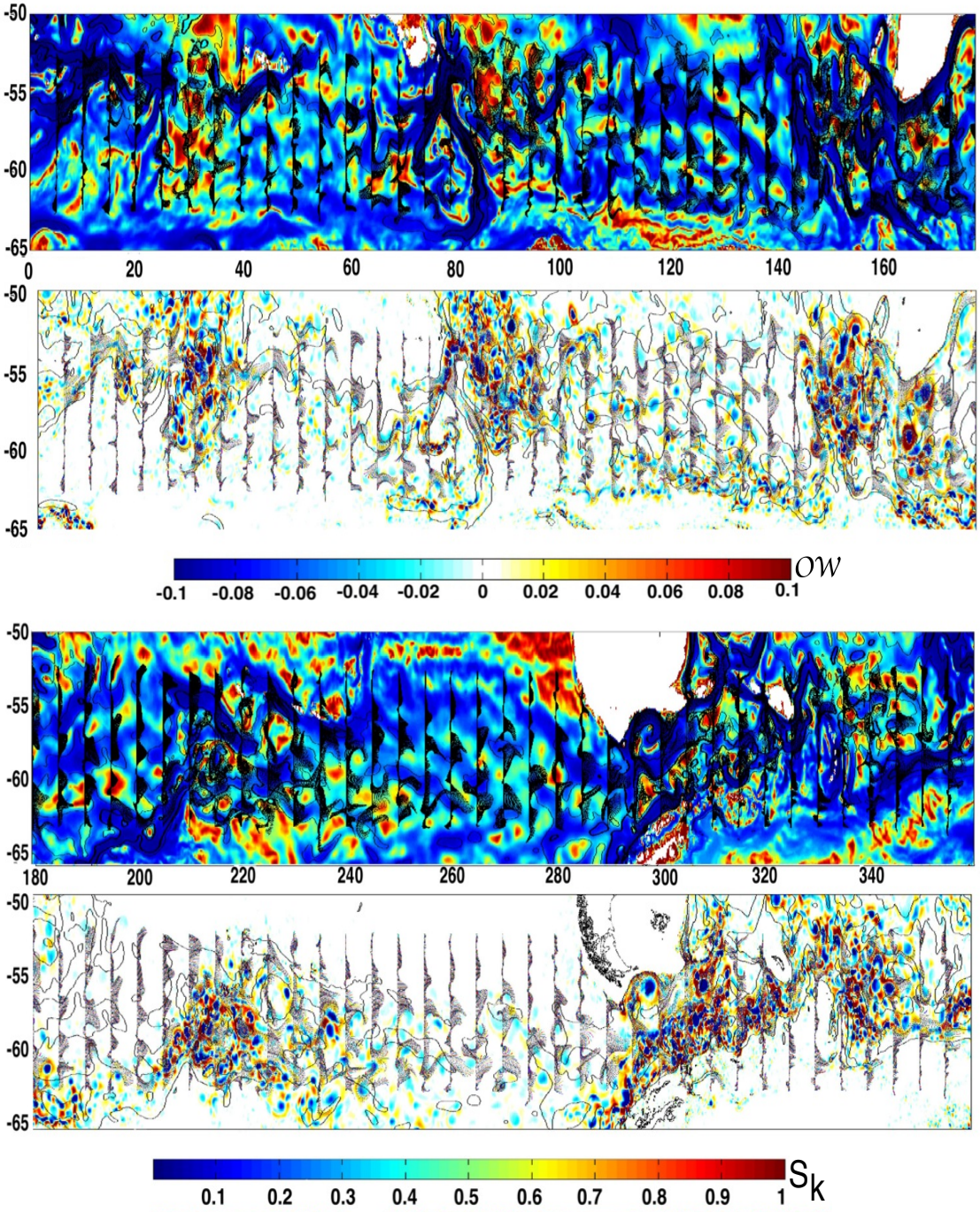

FIG. 5.7: Particle trajectory evolution with respect to suppression factor $\mathcal{S}_\kappa$, $(1 + 4U_m^2 \overline{EKE}^{-1})^{-1}$ and $\mathcal{OW}$ parameter (10^{-9} s^{-2}) for longitudinal releases, 0-180° (the two top panels) and 180-360° (the two bottom panels) for isoneutral surface 27.76 and for a period of 20 days. Negative values depict vortices, while positive values delineate shear strain regions usually engulfing the stirring-enhanced region of a vortex and occupying the interspace of vortex pairs. Also shown are isotachs (black contours; 5 (light) and 10 (bold; only on mixing coefficient images) (in cm s^{-1}) of isopycnal computed horizontal velocity $\mathcal{U}$. Isotachs are illustrated in order to delineate the spatial extent of the potential jet structure formation. Recall that eddy energy utilized in the suppression factor computation is mean EKE over the entire period of simulation.

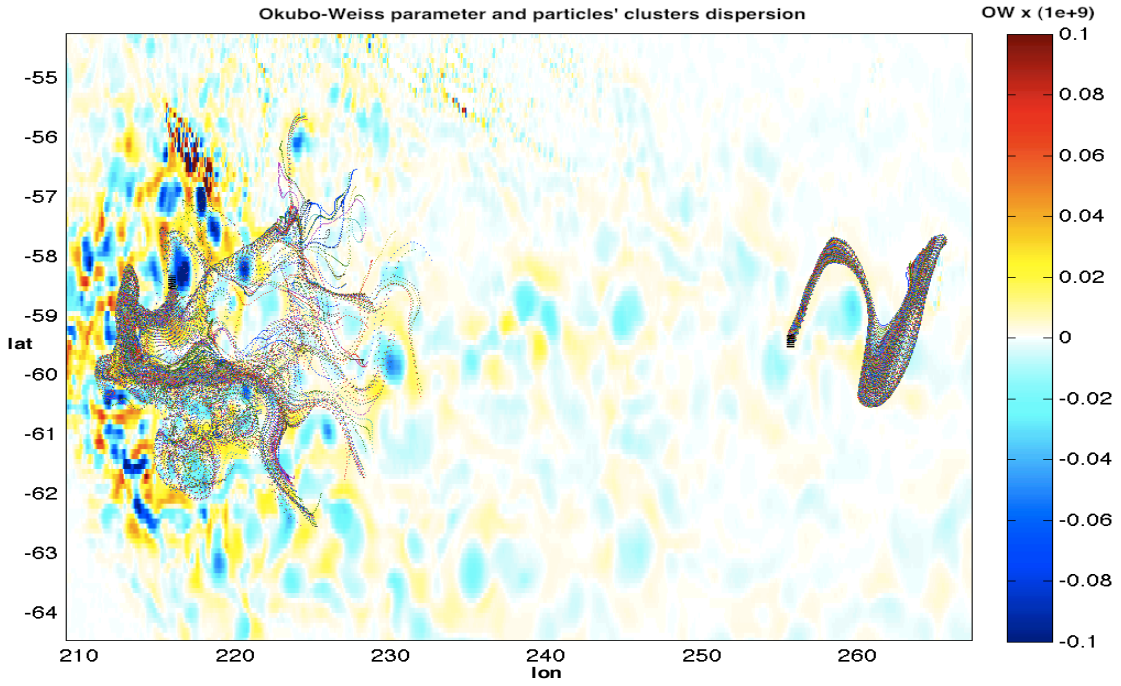

FIG. 5.8: Averaged Okubo-Weïss parameter, $\mathcal{OW}$ (10^{-9} s^{-2}), and particle dispositions for a period of 121 days from initialization at release locations 215.5°E and DIMES (255.5°E). The periods averaged out are 3275 to 3395 model days. Particle dispersion evolution, in the two releases, is regulated analogously by the 'census' of vortices present. The spatial distribution of vortical elements, which control the stirring of the hypothesized 'tracer' (particle trajectories) at their impervious boundaries, gives rise to a convoluted and interchangeable shear pathway cell (in the 215.5° release) which is responsible for the stretching of the trajectories. A simpler shear-strain structure results in an equivalently simple, coherent (spatially), stirred and stretched organization of the subsequent trajectories (DIMES release).

(vorticity mixing) and in the presence of a high spatial density arrangement of coherent vortices. Eddy stirring efficiency is therefore positively correlated with the number of vortices present in the suppression-'free' area, which consequently is a function of vortex size.

Long-lived vortices (a lifetime greater than that of the local turbulence time), known as coherent vortices, can be associated in general with the presence of an inverse energy cascade from smaller to larger scales [*Provenzale*, 1999]; nonetheless, a clear mechanism for their generation is yet to be agreed upon. One the most important aspects of these locally 'concentrated' vorticity traps is that the velocity field associated with their action is non-local (the range of their effect connected with their degree of baroclinicity --greater for barotropic vortices) [*Provenzale et al.*, 2008].

Regions of high relative dispersion values coincide with a reduction in eddy suppression in the $\mathcal{S}_\kappa$ index. Spatial distributions of both the $\mathcal{S}_\kappa$ and coherent vortex proliferation areas are in general agreement with the regions (see p.124), which is related to

homogeneous bottom slope following the steering of the flow by topographic features.

A comparison of the two distributions shows that the vortices' high 'census' does not necessarily coincide with regions where $\mathcal{S}_\kappa$ is $\geq$0.5 (0.5 signifying that mean flow and eddy contributions are equal, and then 1 indicating that EKE is much greater than mean advection, $4U_m^2/\overline{EKE} \ll 1$). If indeed the $\mathcal{OW}$ correctly depicts the vortex field, then, as seen here, the main regulator for the $\mathcal{S}_k$ factor is the mean advection velocity and not $\overline{EKE}$. This is in agreement with the results presented by *Naveira Garabato et al.* [2011], dictating the mixing suppression of eddies due to a counteracting enhanced mean flow. High values of $\mathcal{S}_\kappa$ not associated with vortices distribution are mainly located at the equatorward flanks of the ACC, where mixing has previously been shown to be high [*Sallée et al.*, 2008b; *Shuckburgh et al.*, 2009b; *Griesel et al.*, 2010]. We believe the discrepancy is due to the temporal resolution between the two mappings.

At the temporal scale at which this paradigm is examined, dispersion evolution seems to be a function of structure complexity caused by the relative alignment of vortices and induced by shear-strain interspace areas (Fig. 5.8, see also Fig. 16, Appendix A for a comparison between particle dispersion evolution in two distinct kinematic environments). As such, this is a function of non-parallel PV gradients. What also needs to be clarified is that, dependent on the scales examined, unconstrained movement of particles does not imply mixing ($\mathcal{OW}$=0). This is clearly the case for parallel material lines. Conversely, a high 'census' of vortices creates converging and diverging points in space, so mixing indeed does occur, since particles are forced to relocate randomly through eddy stirring (Fig. 5.6).

5.4 Zooming in

Coherent structures in the flow, either in the form of jets or vortices, are ubiquitous. It is important to reproduce their interaction, through Lagrangian representations of flow dynamics in a local-regime framework, in order to establish a connection between eddy stirring and coherent structures as a plausible mechanism for eddy diffusivity evaluation.

Following the spatial distribution of the $\mathcal{OW}$ parameter (Fig. 5.7) and the along-streamlines mixing distribution (Fig. 4.10, e) we set up releases of particles with an increased spatial resolution of 1/24° grid spacing initiating on selected areas of high diffusivity. Our aim is to determine that eddy stirring, in the high mixing areas (Fig. 4.8), is built upon a system of densely aligned shear-strain and coherent vortical elements arrested at those locations. As a prerequisite, eddy stirring is believed to be associated with the emergence of baroclinic instability through the interaction of intensified mean flow with bottom topography and proliferate just downstream of those topographic obstacles.

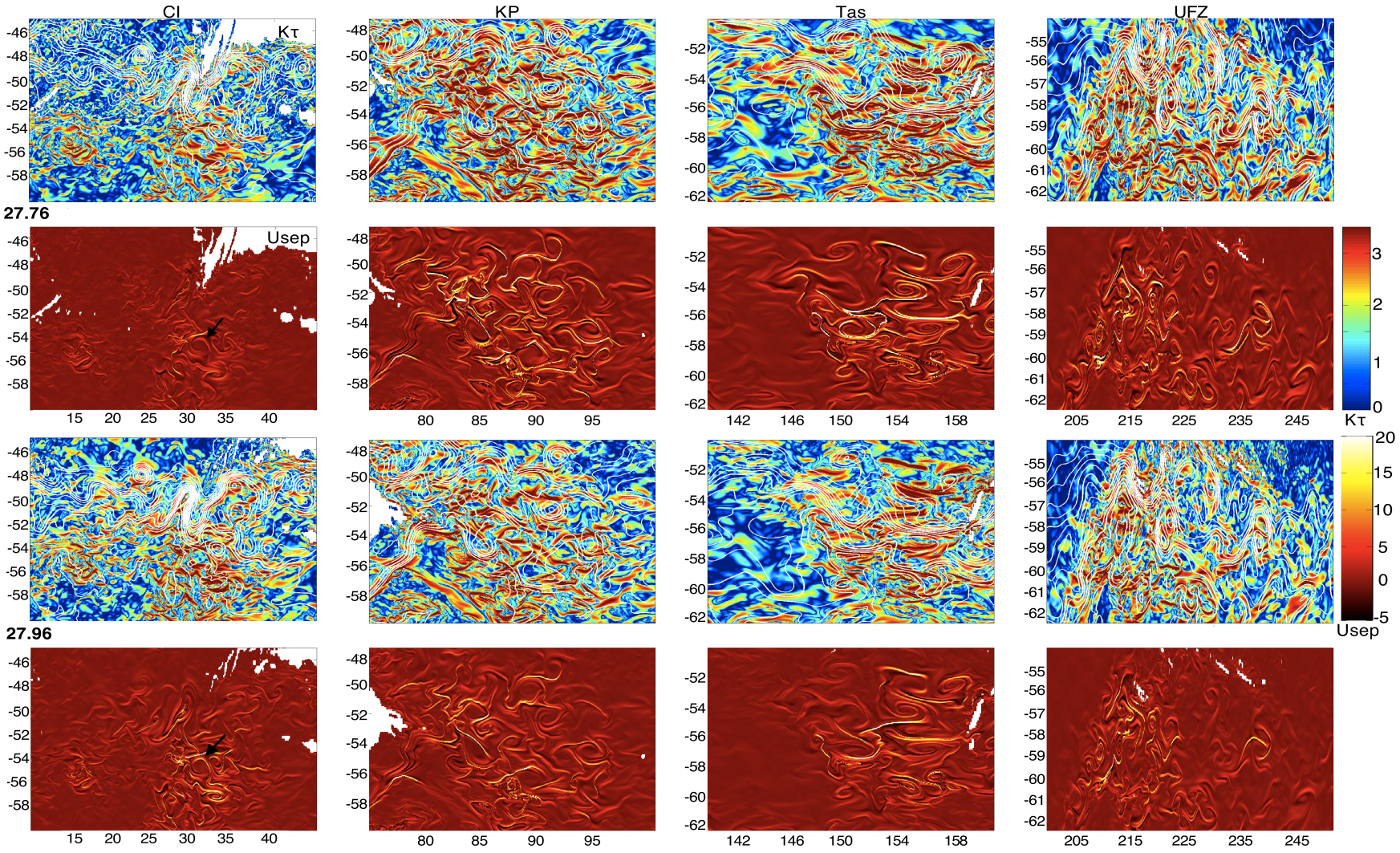

FIG. 5.9: Snapshots of relative diffusion κ_τ ($m^2\ s^{-1}$) and rate of separation (km day^{-1}) at day 15 from initialization, for releases of particles with 1/24° resolution. The Lagrangian experiment commences at the selected locations of the eastward Atlantic Indian Ridge (CI), the Kerguelen Plateau (KP), Tasmania (Tas) and the Udintsev Fracture Zone (UFZ) (left to right panels) on isoneutral surfaces 27.76 and 27.96 (top to bottom panels). White contour lines are mean geopotential anomaly ($m^3\ kg^{-1}$) with respect to the surface for a period of 15 days (model days 1095 to 1115). Contour spacing is represented by 1-unit, with bold lines denoting the 5 and 10 contours. Mapping is done on initial locations of particles during the release phase. White areas denote the isoneutral surfaces' boundary limits.

Relative diffusion and particle separation rates $\mathcal{U}_{sep}$ are computed at time $t_0+\tau$, with t_0 indicating the initialization of the release, as

$$\mathcal{U}_{sep}(t_0+\tau) = \overline{(X_i - X_j)^2(t_0+\tau)}/\tau$$

with i, j denoting anti-orthonormal positions in relation to the release location and the average constructed on both cartesian directions[3] for particle mappings up to 15 days from initialization (Fig. 5.9). Growth law dependency (Fig. 5.10) is also evaluated for the selected regions of the eastward Atlantic Indian Ridge, the Kerguelen Plateau (KP), Tasmania (Tas) and the Udintsev Fracture Zone (UFZ). Even though the result is not statistically robust, since computed diffusion is performed only on three-monthly repetitive means, it should be qualitatively indicative of the relationship between separation rate representations, relative diffusion and the existence of mixing barriers.

At first glance, material lines are quite well represented from the $\mathcal{U}_{sep}$ distribution, with dark and light colours, respectively, signifying small and high rates. The material curves are associated with 'saddle' regions of the flow (regions with strong expansion in one direction and compression in another)[4]. In a dynamical systems context, a material boundary, if formed by two 'parallel' material curves, designating the expansion and compression direction, respectively, is known as a hyperbolic trajectory[5].

Anticyclonic (counter-clockwise) and cyclonic (clockwise) vortical elements are also illustrated in comparison with closed lines of geopotential anomalies. Vortices' diameters conform with the first baroclinic Rossby radius of deformation $\mathcal{L}_d$ ∼10 km[6] for the Southern Ocean [*Chelton et al.*, 1998].

A scaling argument needs to be made at this point, in order to decipher how vortical and shear elements interact. Assume a set of particles entering the area in figure 5.9 (top panels, CI section, black arrow - an equivalent kinematic background exists at the Tas section, 53-55°S 150-155°E with a southward direction, though). Let us envision a scenario that involves a group of particles diverging either left or right, with a subsequent trapping in the flanks of the ensuing vortex pair (seen more clearly on isoneutral 27.96 in the same region) as the combined response to a multiple transport barrier - two vortex

[3]This follows a scheme employed by *Koh and Legras* [2002] for the computation of FSLE as a method to decipher hyperbolic lines in the stratospheric vortex.

[4]A reference is made here to *Kuznetsov et al.* [2002] who also approached the jet and vortex interactions in the Gulf Stream, and their transport characteristics , in the context of dynamical systems theory.

[5]Clarifying the characterization of hyperbolic and elliptic trajectories in dynamical systems theory (as manifolds of hyperbolic (exponential growth) and elliptic (linear growth) of pair separations in time), in general acceptance, a hyperbolic or 'saddle' trajectory is characterized by stable (repellers) and unstable (attractors) manifolds, which themselves are material curves and are therefore impervious to particles crossing [*Wiggins*, 1992]. Additionally, the stable (unstable) material curves correspond to unstable (stable) Poincare maps in periodic dependent flows [*Haller and Yuan*, 2000].

[6]Transient eddies' diameters vary substantially from this value ranging from a few tens to hundreds of km [*Olbers et al.*, 2004; *Döös et al.*, 2008].

system. Depending on the lifetime and transient character of the two vortices, if spatially stationary, then particles will be confined to their conjugate space extent[7]. Therefore, regardless of their relative kinematic potential[8], the exhibited relative dispersion will be bounded at a scale $\sim \sum \mathcal{L}_e$, where $\mathcal{L}_e$ are the respective eddy lengths of the vortices. Additionally, PV gradients for a pair of particles that are compensated with an equivalent dispersion 'blow up' depict a front existence with differentiated kinematic environments on either side and are impermeable to a vortex pair. Intuitively, the minima of $\mathcal{U}_{sep}$ refer to the homogeneity of the flow. Based on the assumption that a nonlinear shear-straining mechanism could serve as a descriptor for the structures observed in this Lagrangian set-up, the spatial homogeneity of dynamics is controlled by the relationship between the respective PVs Δq_{vortex} to $\Delta q_{barrier}$. Perturbations around a threshold value, measuring the penetration aptness of vortices, materialize in undulations in the jet's position, with vortex lobes trying to penetrate the barrier. Exceeding this threshold value leads to vortex merging, the destruction of the jet-barrier and the mixing of the respective vortex cores [*Dritschel and McIntyre*, 2008].

As expected, diffusion has an analogous distribution to $\mathcal{U}_{sep}$, but it is less sensitive to a fine-structure representation. Multiple filamented jets are depicted as interchangeable low and comparatively higher values of $\mathcal{U}_{sep}$ (see 54° to 58°S and 75° to 80°E, KP). Equally, the separation, merging and collision of barriers accompanied by shear-stain-induced vortex pair interaction, is characteristic (e.g see 54° to 56°S and 30° to 35°E, CI; 52° to 56°S and 152° to 158°E, Tas). Vortex cores and regions characterized by low separation rates are depicted as sub-diffusive. This also illustrates coherency of the vortical element from the perspective of impermeability to fluid particles.

5.4.1 Growth law dependencies

The growth law dependencies for the separation rates of particle pairs (Fig. 5.10) depict exponential dependence (the relationship is exponential for the dispersion also, not shown here) at small time lags (chaotic regime [*Artale et al.*, 1997]) progressing to a linear relationship for time lags larger than 60 days, and quadratic scaling for dispersion indicative of a ballistic regime (see section 4.2.2, p.90). A plausible mechanism for the dispersion dependence observed herein was proposed by *Schumacher and Eckhardt* [2002] in their study of particle dispersion in free-surface flows. Apart from a chaotic velocity field supporting exponential growth, dispersion characteristics were appended

[7]This is basically the 'law of the wall', as referred to by *Tennekes and Lumley* [1972].

[8]Obviously, in the set-up described, the anticyclonic vortex to the left has a smaller kinematic potential than the cyclonic to the right. A counteraction with the eastward transport barrier to the north of the pair will reduce relative vorticity ζ and as such the thickness of the isoneutral at the respective location. Cyclonic (anti-cyclonic) rotation can also be inferred from the geopotential anomaly $\Delta\Phi$ contours. Recall that $\Delta\Phi$ is calculated with respect to the surface and as such increasing values denote damping of the isosurface z-level.

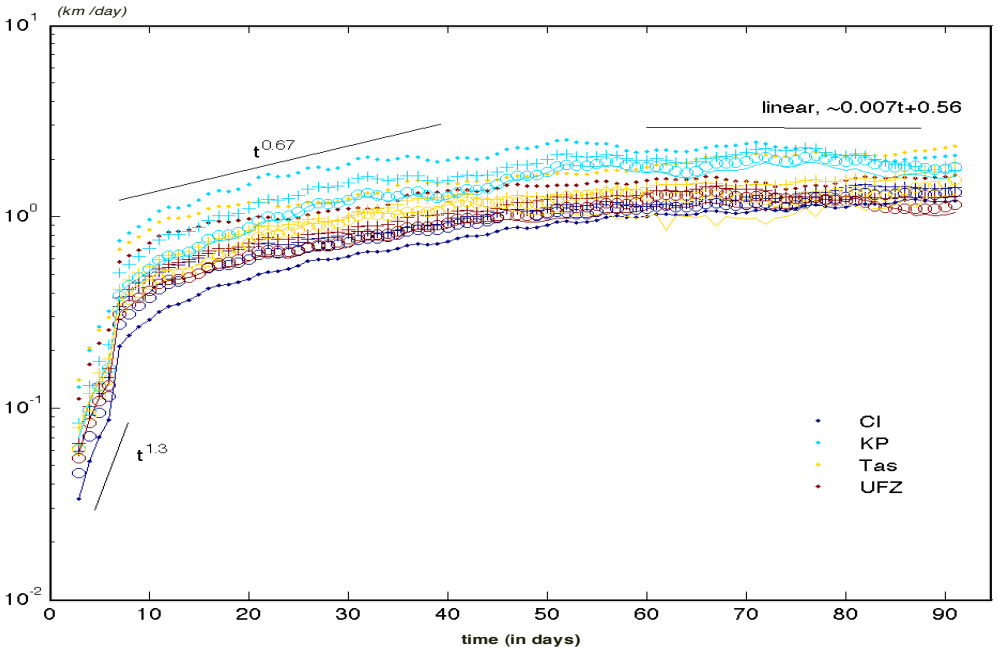

FIG. 5.10: Separation velocity growth law dependence for all available pairs of particles on isoneutral surfaces 27.76 (filled circles), 27.96 (crosses), 28.06 (open circles) and 28.16 (line) for the selected regions discussed in figure 5.9. Decreasing power law dependence can be seen at early time lags progressing to a linear relationship and ballistic regime (dispersion scales quadratically over time). Elliptic and hyperbolic points in the flow (or alternatively 'saddle' points in dynamical systems nomenclature) exhibit a typical linear and exponential growth in time of pair separations rates, respectively. Here, exponential growth can also be proposed as an alternative to the largest exponent power law dependency but with a smallest correlation factor 0.96 vs 0.99 (indicative of non-parallel flows, see text for details). Recall the description provided in 5.9 for the computation of quantities at each location.

to rapidly emerging divergence patterns in the flow. The $\sim$ 60-day time lag coincides with that expected for absolute diffusivity to reach the asymptote limit, as discussed in 4.2.3.2. In practice, though, as seen from the relative diffusion κ_τ distribution in figure 5.9, absolute diffusivity values are reached earlier, of $\mathcal{O}$(15 days) or even sooner, for regions characterized by high rates of separation. Previous Lagrangian studies [*Weiss et al.*, 1998] suggest that the exponential growth of dispersion on time at small time lags is characteristic of non-parallel flows (see for example Fig. 5.6), in contrast to parallel flows where linear scaling is more appropriate. Exponential growth and tracer filamentation during the early stages of a tracer release have also been documented [*Sundermeyer and Price*, 1998]. In a dynamical systems approach, elliptic and hyperbolic points in the flow exhibit, respectively, a characteristic linear and exponential growth in time of pair separation rates. Consequently, the growth law dependency presented herein suggests a strain and deformation mechanism controlling the stirring of particles at small time lags. It also indicates that vortical elements in the flow dominate stirring of particle

trajectories at later times. This is not necessarily in contrast with what is expected for large scale circulation, where the eddy stirring role is maximized in small time lags of particles' travel time (Fig. 5.2, b). On the contrary, it signifies the importance of vortical elements in a high spatial density arrangement accompanied by a multi-filamented, non-parallel jet structure. Nonetheless, the two-component spatial decomposition in vortical and shear-strain areas of the kinematic environment should be considered as simultaneous expressions of mesoscale turbulence acting together, rather than separate stirring mechanisms.

Distributions of increased relative diffusivity values, in an equivalent $\mathcal{OW}$ representation, would coincide with the interspace (hyperbolic areas - shear-strain) between vortices (elliptical areas - vortical elements). The mixing evolution of this structure arrangement is the result of non-linear interactions between jets and vortices where strong local PV gradients (Fig. 5.4 and 8) reorganize jets in a chaotic, stretched, multi-filamented manner creating pathways for the spatial redistribution of particles. This deterministic chaotic regime approach rests on the notion of chaos, where trajectories are expected to be redistributed near every point in a bounded chaotic region during their time evolution [*Wiggins*, 2005], and where trajectory evolution is dependent of the initial position [*Davis*, 1991]. This mechanism, we believe, is representative of all high mixing regimes and indicative that sub-mesoscale processes are responsible for even finer structures that regulate eddy stirring efficiency. We are not able to resolve mixing at those scales of $\mathcal{O}(\sim 1$ km) with the current spatial resolution of OCCAM; nonetheless, we argue that it might be worth approaching eddy stirring – and thus mixing – in the sub-mesoscale range in light of the structures emerging from increasing the resolution of fluid dynamics representations [*Thomas et al.*, 2008].

5.5 Geographical identification of the high mixing regions

The influence of topography in the mixing capacity and circulation patterns of the ACC has been addressed in numerous studies [*Hughes and Killworth*, 1995; *LaCasce*, 2000; *Shuckburgh et al.*, 2009a; *Thompson*, 2009; *Naveira Garabato et al.*, 2011; *Lu and Speer*, 2011; *Sallée et al.*, 2011]. In this thesis, regions, characterized by intensified isopycnal mixing, are almost exclusively located downstream of meridional excursions of PV 'tongues' (Fig. 8) [*McIntyre*, 2008; *Dritschel and McIntyre*, 2008; *Thompson et al.*, 2010] and associated with the topographic steering of the mean flow crossing closed contours of f/H (Fig. 7), followed by relatively smoother and homogeneous bottom slope areas downstream (Fig. 6). Why is baroclinic instability, generated over topographic obstacles, arrested at those regions, with the ramifications of of eddy stirring enhancement?

Witter and Chelton [1998] proposed that unstable mode growth rates are greatest where topographic steering forces the jet into regions of reduced ambient potential vorticity gradients, therefore increasing eddy energy (upper part of the water column) downstream of topography features (zonally uniform topography). *Gille et al.* [2000a] also provided evidence of a connection between high EKE (surface layer) and low bottom roughness. According to *Witter and Chelton* [1998], mixed baroclinic-barotropic instability and strong downward transfers of eddy energy occur in cases with zonal modulations in topography. While this generally seems to capture the fundamentals of the distributions recorded herein, it lacks a further description of the characteristics of the PV gradient field (as non-parallel flows of inhomogeneous PV mixing generated by the interaction of jets and vortices) which, as we propose (section 5.2.1), is essential for eddy stirring evolution.

The mixing of PV and the subsequent formation of jets have previously been discussed within the concept of PV inversion [*McIntyre*, 2008; *Dritschel and McIntyre*, 2008] and by establishing a connection with the frontal structure of the Southern Ocean [*Thompson et al.*, 2010]. *Dritschel and McIntyre* [2008] suggested that in an environment of spatially inhomogeneous PV, the flow evolves through the interaction of jets with vortex pairs. *Thompson* [2009, 2010] commented on the contribution of topography in unsteady jet behaviour through the modification of local PV. In such a case, the presence of well-mixed PV regions can be time-persistent, but not necessarily homogeneous if we take into consideration the presence of coherent vortical elements (high vorticity 'pools') (Fig. 5.6). In a generic approximation, the presence of coherent boundaries, signified by strong PV gradients, is topographically steered, thus exhibiting substantial meridional excursions (Fig. 5.4). Baroclinic instability expressed through vortex formation accompanied by the interaction of the flow with obstructing topographic areas, results in oscillations in jet structure. These periodic oscillations, according to *Thompson* [2010], tend to exhibit a characteristic structure varying between a zonal and a steered-by-topography one. As a consequence, mixing should also exhibit an analogous variation associated with the transition between the two regimes (Figs. 4.8 and 4.9).

In fact, high diffusivity values occur just downstream of this topographic steering of the mean flow with an accompanied crossing of closed f/H contours (Fig. 7, black circles). The case is true for all high mixing regions apart from the Drake Passage, which constitutes a more complicated kinematic environment, since the PF subdivides the area into low (N) and high (S) mixing locations at the entrance point (Fig. 4.8). Diffusivity appears more segmented downstream, following closely the bathymetry geometry (see Fig. 3.3), steering the accelerated mean flow (see Fig. 2.22) and in agreement with strong PV gradients. We find mixing to be more detailed and controlled by PV gradients' small scale meridional excursions (Fig. 5.4, bottom panel). The signal is also in good

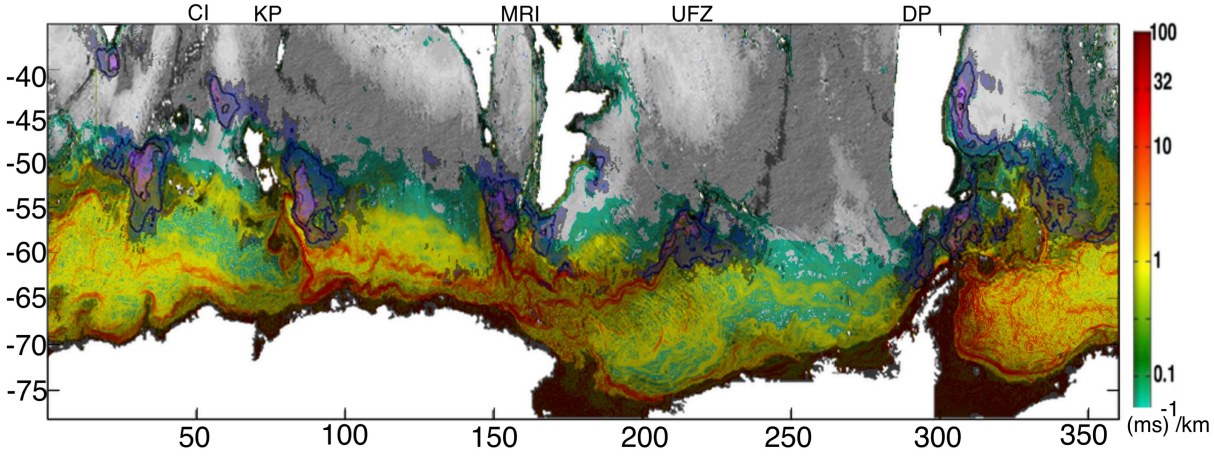

FIG. 5.11: Average PV gradient ($(log_{10}, |PV| \times 10^{13})$, (m s)$^{-1}$ km^{-1}) (colour-scale with a degree of transparency) overlaid on f/H map (grey colours) for isoneutral 27.76. H is height of isoneutral above bottom topography. Black contours are $\overline{EKE}$ above 100 (cm^2 s^{-2}) with 100-unit spacing. Blue and purple shaded areas denote cross-stream diffusivity of 500 and 1500 m^2 s^{-1} respectively.

agreement with the suppression mixing factor $\mathcal{S}_\kappa$ of *Naveira Garabato et al.* [2011] (Fig. 5.7, bottom panel).

Our mixing-intensified regions are consistent with the spatial distribution of $\mathcal{S}_\kappa$, therefore indicating that the intensity of the mean flow with respect to EKE is indeed a controlling factor in mixing inhibition. However, the relationship breaks down in specific regions where emerging structures, based on the $\mathcal{OW}$ parameter and separation rate mappings (Fig. 5.9), suggest the existence of a more complex, non-parallel flow framework consisting of multiple interacting jets and vortices (see, for example, the region at the Macquarie Islands Ridge 140-160°E, Fig. 5.7, top panels).

What we propose is that these high diffusivity regions could fit into a combination of *Witter and Chelton* [1998] and *Thompson*'s [2010] proposed frameworks with additional details of PV mixing in the wake of topography borrowed from *Rhines* [2007] and an enhancement of the role of coherent vortices and jets in redistributing particles in a chaotic way. As such, mixed baroclinic-barotropic instability, generated through the interaction of the mean flow with bottom topography (Fig. 7), results in eddy- intensified regions in the wake of the obstacle and which are arrested downstream (Fig. 5.11, black contours) where the mixing of PV [*Rhines*, 2007] and the subsequent formation of jets [*Thompson et al.*, 2010] and vortices in a non-parallel flow approximation (Fig. 5.7) takes place. The mixing regimes, illustrated in figures 4.8, 4.9 and 5.11, are delimited by meridional excursions of strong PV gradients to the west and east. These engulf the baroclinically generated eddy-intensified regions with similar equatorward PV 'tongues' (following closely the f/H distribution) and create characteristic PV mixing 'pools' of

relatively reduced and homogenized ambient PV gradients. See regions at 50-57°S 90°E - downstream of KP; 60°S 300°E - DP; 50-60°S 30°E, 55°S 155°E - Macquarie Ridge; 55-60°S 215-220°E - UFZ; 55°S 330°E. In the theoretical study of *Rhines* [2007], PV stirring in the wake of topography creates almost stagnated areas of particle advection. Here, though, the steering of the mean flow results in inhomogeneous PV mixing and the mechanism for the ensuing jet and vortices, where particles are dispersed in the chaotic notion described in section 5.4.

The controlling factor for the EKE stagnation, we believe, is the delimitation of the flow by the equatorward PV gradients (Fig. 5.11), which closely follow planetary vorticity contours. Their role is actually delineated as the action of topography on an upstream intensified mean flow, and its partial destruction, on non-parallel flow downstream through the creation of multiple jets and vortical elements [*Thompson et al.*, 2010] . When adopting a 1D-layer hydraulics analogue for supercritical flows (the ACC flow is indeed supercritical with respect to baroclinic Rossby waves [*Hughes et al.*, 1998]), high phase speed flows 'enter' a water body of reduced ambient velocity, with the simultaneous action of topographic slow down, which will result in the generation of eddies, turbulent heat exchanges and the extension of the water column height downstream of the obstacle (and a counteracting relative vorticity increase in order for PV to be conserved). *Naveira Garabato et al.* [2011], following the work of *Rhines* [2007], suggested that the clustering of stagnant Rossby waves around topographic obstacles, generated by the interaction of the ACC flow with those obstacles, displays a similar structure to atmospheric 'lee' waves. In a hydraulics equivalent, non-parallel flows can be produced by the dissipation of TKE due to topographic obstruction and steering, consequently generating coherent vortices downstream in regions of reduced ambient PV (where the atmospheric 'lee' waves are observed and dissipation takes place). These are delimited by closed planetary vorticity contours. The generated coherent vortices and jet structure could further act with positive feedback to slow down the eastward flow. However, we did not examine whether standing waves, through the interaction of the mean flow with westward propagating Rossby waves [*Hughes*, 2005; *Rhines*, 2007; *Naveira Garabato et al.*, 2011], are responsible for the EKE energy arrest downstream of these topographic obstacles[9].

The proposed framework by *Witter and Chelton* [1998]; *Thompson* [2010] ably fits the localization of eddy stirring downstream of topographic obstacles as suggested by our analysis. We find that both the arrest of mixed baroclinic-barotropic instability-generated eddies [*Witter and Chelton*, 1998] over smooth roughness regions, as depicted by the $\mathcal{OW}$ parameter (Fig. 5.7), and meridional excursions of PV gradients (Fig.

[9]Barotropic Rossby waves have significantly greater phase speeds in comparison to the mean flow at this depth. Baroclinic Rossby waves are advected with a 1.4-2.0 m s^{-1} westward velocity [*Chelton et al.*, 1998; *Hughes et al.*, 1998].

5.4) (steering of PV gradients in the wake of topographic obstacles) are satisfied. The adopted mechanism justifies the structures observed, as a result of non-linear interactions between jets and vortices, where strong local PV gradients reorganize jets and vortices in a chaotic way, which duly explains the exponential growth law dependency of dispersion on time associated with non-parallel flows.

5.6 Concluding remarks

An improved Lagrangian scheme, relative to similar studies approaches', with high density spatial coverage was employed in order to resolve the spatio-temporal scales associated with eddy stirring and the underlying dynamics of the ACC.

We demonstrated the role of topographic obstacles in PV gradient steering in relation to f/H spatial distribution and set up an efficient eddy stirring mechanism. We found that coherent structures in time regulate tracer distribution and proposed a framework, satisfying the results of our work, in which a spatial correlation with high EKE regions exists where mixing suppression by the mean flow ceases and whereby the interaction of vortical elements and multi-filamented jets in non-parallel flows result in enhanced diffusivity. Suppression of mixing in regions where the flow is characterized by intensified and coherent – both in space and time – jets (strong PV gradients), therefore signifying the separation of the flow in differentiated kinematic environments, was illustrated in connection with high relative dispersion values.

In agreement with *Shuckburgh et al.* [2009a]; *Thompson et al.* [2010]; *Ferrari and Nikurashin* [2010]; *Naveira Garabato et al.* [2011]; *Lu and Speer* [2011], the importance of local mixing regimes was delineated through the employment of relative diffusivity and separation rates in an analogue borrowed from dynamical systems theory.

We believe that twisted narrow jets in the wake of topography, ensuing PV mixing [*Rhines*, 2007] and the delimiting distribution of strong PV gradients (Figs. 5.3 and 5.11) controlled by the non-zonal orientation of topographic obstacles are providing the necessary conditions for the downstream arrest of eddies and intensified eddy stirring in a non-parallel structure [*Thompson*, 2010]. The mechanism proposed in this study as an eddy stirring efficiency measure focuses on the role of coherent vortices and jets in redistributing particles in a chaotic manner. Particles' dispersion evolution is controlled by the stretching and folding of their trajectories (equivalent of tracer filaments). Hence, their growth rate defines the local intensity of mixing and provides some insight into the responsible mechanism. Our derived exponential growth of dispersion on time at small time lags is characteristic of non-parallel flows [*Weiss et al.*, 1998]. As suggested in section 5.4, a sub-mesoscale approach in eddy stirring has the potential to portray the

role of coherent structures in diffusivity in greater detail and to reveal the underlying mechanism proposed herein.

Chapter 6

Conclusions

6.1 Summary

Deciphering the effects of eddies in the ACC requires an understanding of their mixing capacity and underlying dynamics. This thesis is primarily concerned with simulations of Lagrangian particle trajectories on selected isoneutral surfaces and isobaric levels. This is to quantify and delineate mixing, circulation patterns and to propose a mechanism explaining where and how eddy stirring is effective in the ACC. We utilized an improved Lagrangian scheme relative to similar studies approaches', with a high density spatial coverage, in connection with output from an eddy-resolving OGCM to resolve the spatio-temporal scales associated with eddy stirring and kinematic boundaries in the ACC. A numerical algorithm with no explicit diffusion parameterization was further developed for the tracking of 576,000 passive particles for a period of 17 years. In this thesis's writer knowledge, no previous work attempting such a large scale and density of simulated particle analysis exists in this conceptual framework. Diffusivity κ_{Taylor} (or κ_{∞}) estimates, based on classical diffusion theory, relative dispersion $\overline{\mathcal{D}^2}$ and the delineation of the relationship with local distributions and potential vorticity gradients were analysed. Stirring and eddy diffusivity were discussed within the context of previous studies and by computation of a space effective probability index. Whether eddy mixing follows the complex spatial distribution of eddy variability described by eddy kinetic energy was confronted. Various local simulation experiments were performed in order to give a better insight into the evolution of particle dispersion and the respective kinematic regimes. In the following paragraphs an effort to encapsulate the results, remarks and possible indications for future work and refinement of employed methods is attempted.

Output from the *run401* of GCM OCCAM 1/12°, covering the period 1988-2004, was employed for the advection of particles and computation of isoneutral density surface geometry. No slip was allowed at the boundaries and particles remain on the same isoneutral surface (by construction of the isopycnal velocity fields). The main release

scheme comprises of a 5° longitudinal spacing linear alignment of particles (single in time releases). Cluster releases were also performed in the context of the DIMES experiment and with 1/24° grid spacing for specific regions in order to delineate kinematic boundaries in the context of dynamical systems theory (multiple in time releases).

One the differences with previous relevant Lagrangian studies involving a flow separation, in time-variant and invariant constituents, was that our cross- and along-stream components are of the same magnitude (Fig. 4.8 and 4.9). We attributed this to the subtraction of a local mean, derived from an extended time series of 17 years (all other studies employed much shorter time series), from every particle position reducing shear by the mean flow which would affect the along-stream component (by construction cross-stream dispersion by the mean is zero). We also showed that $\overline{EKE}$ derivations from velocity time series shorter than 5 years are inadequate to represent a valid flow separation approximation.

We presented cross- and along-stream diffusivity variation, approached in the context of classical diffusion theory, in comparison with the mixing hypotheses in the Southern Ocean (see 1.2). Caveats of integral time computations in the presence of persistent structures were presented. As such, integration of velocity autocorrelation functions up to a constant lag (where diffusion reaches the asymptotic limit), maximum integral and first-zero-crossing are all prone to uncertainties (see section 4.2.4). Additionally, and in contrast with absolute dispersion, relative diffusivity does not enter a diffusive limit in the time-scales considered here (see 5.1.1). We only record a diffusive limit for the isobaric level 2 (8m) and this for time-scales 4-5 times larger than for absolute diffusion. This indicates the existence of persistent structures in the flow that render the computation of diffusion from the integration of the velocity autocorrelation functions incomplete. Previous studies [*Veneziani et al.*, 2004, 2005; *Griesel et al.*, 2010] suggested that an ensemble of Lagrangian velocity autocorrelation functions is adequate to mitigate the effect of coherent vortices in the sampling trajectories. We showed that persistent structures exist for periods at least up to 365 days. This would render classical diffusion theory computations, based on integral times, problematic regardless of the size of the Lagrangian spatial ensembles. We believe that anomalous diffusion approximations [*Ferrari*, 2007] should also be considered in future works of ACC mixing in a Lagrangian context.

Our results show that parameterizations of diffusivity with a constant eddy length $\mathcal{L}_e$ and time scales T_L are not valid. The computed $\mathcal{L}_e$ exhibits great spatial variability consistent with high EKE in specific regions (Fig. 5.11). Examining the constant mixing length hypotheses [*Stammer*, 1998; *Sallée et al.*, 2008b] our result is of $\mathcal{O}(10)$ smaller than that of *Sallée et al.* [2008b], and also exhibits a substantial spatial discrepancy. Its spatial distribution is consonant with $\mathcal{L}_e$ (Fig. 4.6) delineating its correlation with the

underlying eddy stirring mechanism. As such, and regardless of the fact that diffusivity follows high EKE spatial distribution, we disagree that κ_∞ scales with EKE in contrast to the studies of *Holloway* [1986]; *Visbeck et al.* [1997]; *Sallée et al.* [2008b]. As mentioned by *Shuckburgh et al.* [2009b], since eddy diffusivity is linked to the intensity of the overturning circulation and to the associated baroclinic transport in the ACC, within the context of the residual-mean framework of *Marshall and Radko* [2003], variations in the EKE cannot be directly connected to variations in the strength of these dynamical quantities.

Even though our diffusivity estimation is consonant with the spatial distribution of high EKE it does not scale analogously to EKE in the ACC. Instead, we agree that a connection of eddy stirring with high EKE exists [*Waugh and Abraham*, 2008]. A similar distribution of maxima in relative dispersion and FSLE, positively correlated with the residual root mean square velocity $\mathcal{U}'_{rms}$, is also consistent with the intensified local mixing regimes depicted by *Lu and Speer* [2011]. They attributed the increase in diffusivity to merging of multiple jets in the main path of the ACC over topography to locally enhanced baroclinicity and instability within the wake, which itself is partly due to the convergence of eddies in merging branches of the ACC. Unsurprisingly, high eddy diffusivity regions here are found downstream of the ACC's frontal jets convergence areas. While we do not reject the mechanism proposed by *Lu and Speer* [2011] we have not examined whether the convergence of eddies and stagnation observed here is associated with eddy propagation from opposite directions.

A scaled diffusivity as $\kappa = \kappa_{Taylor} \times S_\kappa$, consistent with that of *Ferrari and Nikurashin* [2010], was also computed in order to examine if we are overestimating diffusion with regard to the role of mean currents in mixing suppression [*Naveira Garabato et al.*, 2011]. The resulting distribution has smaller values than both our estimates (integral time and derivative of dispersion). Nonetheless, our derived κ_{Taylor} at the top isoneutral 27.76 is in agreement, both spatially and in magnitude (within approximations of a depth reduction in the less energetic areas of the ACC), with their diffusion estimate based on altimetric observations and including the effect of mean currents. This means that our scheme, with the computed cross-stream time-variant velocity component, has already accounted for the suppression of mixing due to the mean flow.

Regarding absolute diffusivity values, the Lagrangian estimate here is consistent with previous numerical model studies with moderate derived values [*Treguier*, 1999; *Abernathey et al.*, 2010; *Griesel et al.*, 2010]. However, the underlying proposed mechanisms and the spatial distribution of diffusivity are not fully in agreement. Typical values of cross-stream diffusion in the ACC are between 1000-2500 $m^2\ s^{-1}$ in the high mixing regions. A value $\simeq$500 $m^2\ s^{-1}$ is characteristic of less energetic regions in the ACC.

The circumpolar average diffusivity is of the same order as the value used by *Danabasoglu and Marshall* [2007] ($\simeq$ 400 m^2 s^{-1} at a depth of 2 km) in their adjusted Parallel Ocean Program (POP) version model. The values of cross-stream diffusivity in general, excluding the vigorous mixing regimes (>1500 m^2 s^{-1}), seem to be in agreement with those derived by *Griesel et al.* [2010] for the same depth but our spatial resolution is significantly higher so the detailed spatial arrangement here is not expected to coincide. Their computation though, is in fact an average diffusivity for a range of potential density values that in our case would be equivalent to a mean κ_∞ between two consecutive isoneutrals and as such, smaller.

We find inhibition of mixing within the main ACC fronts (especially the SAF and PF) which also act as barriers to particle dispersion equatorward (PF-SAF) and poleward (SACCF). Their effectiveness as transport barriers breaks down at the specified high diffusivity regions where the role of kinematic boundaries is far more complex as depicted by the FSLE and probability index records. *Ferrari and Nikurashin* [2010] have shown that suppression of mixing is associated with the propagation of eddies along mean currents because they follow PV gradients associated with the mean currents. We demonstrated that PV gradients are clearly associated with transport barriers but we did not calculate eddy propagation rates in the mean currents. Still, absolute diffusion (Fig. 4.8), relative dispersion (Fig. 5.3) and $\mathcal{OW}$ parameter mappings (Fig. 5.7) reproduce the *Ferrari and Nikurashin* [2010] results. The existence of eddies in intensified mean currents are not an efficient stirring mechanism as can be seen by low relative dispersion (absolute diffusion) values regardless of the existence of vortical elements in intensified mean currents. The main ACC seems to act also as a transport barrier for the equatorward displacement of particles with reduced effectiveness at denser isoneutrals coincident with a decrease in the advective mean flow.

We do not find mid-depth mixing enhancement below ACC jet cores as critical layer theory suggests [*Marshall et al.*, 2006; *Abernathey et al.*, 2010]. Both the along-streamline averages and mappings on a geographical coordinate system do not imply any notable increase below ACC jet cores. Of course, we have only considered mappings on isoneutral surfaces, which have a minimum density of γ^n=27.76. Hence, a comparison with surface diffusivities has not taken place here and our vertical sampling resolution is low, i.e. the PF and SAF positions are on a depth of 1000 m on isoneutral 27.76 while on our next density surface, γ^n=27.96, they reside at a depth of 1500-1800m (Fig. 4.8).

Studying Lagrangian particle distributions allowed us to depict flow characteristics both in space and time in great detail. The probability index mappings in relation to the FSLE gave us insight to a possible mechanism for the observed 'leakiness' of jets in Drake Passage. It was suggested that large wave amplitude meanders slowed down by 'stagnant' coherent vortices, as topographical eddies or 'trapped' vortices by

f/H contours, result to a 'leaky' jet structure. We showed that the structure of eddy stirring efficiency (based on relative homogenized values of the probability index and its fine structure) is associated with convoluted strains of particles in a multi-filamented non-parallel spatial arrangement of kinematic boundaries.

6.2 Mixing structure

This work has resulted in new contributions to our understanding of the role of coherent vortices in the mixing dynamics of the ACC and eddy stirring efficiency. Consideration of the characteristic features of the ACC being its multi filamented jets and vortex interaction was of focal interest in defining the structure of mixing. The spatial arrangement of coherent vortices and subsequent emerging circulation patterns as weak non-parallel flows were found to be a fundamental mechanism controlling stirring of particles at the smallest resolved scales in OCCAM 1/12°. The depiction of these transport-mixing barriers, from the perspective of numerically integrated particle trajectories, were proved to be more than kinematic boundaries and advection pathways. These transport-mixing barriers play a major role in defining mixing efficiency. This is a new result for the full longitudinal extent of the ACC. Even though we find a spatial agreement between high values of absolute diffusivity and inadequate mixing suppression by the mean flow (by computation of the mixing suppression factor $\mathcal{S}_k$) and vice versa, the distributions of relative dispersion, the FSLE, the $\mathcal{OW}$, the PV gradient field and the exponential growth of particles' displacements at small time lags signify a chaotic advection regime and non-parallel flow structure.

Localization of diffusion regimes throughout this study was exhibited with a close connection to bottom topography obstruction and steering of the flow, and the downstream spatial distribution of high EKE over smooth slope bathymetry defined by closed *f/H* contours. We think that the role of topography is much more important than asserted in the previous studies regarding mixing in the ACC, as it regulates the flow conditions of eddy 'stagnation' areas allowing for proliferation of efficient eddy stirring. The importance of local mixing regimes was determined with the employment of relative diffusivity and separation rates in an analog borrowed from dynamical systems theory. By spatially mapping the flow dynamics of the ACC, through the computation of particles' spatial occurrences in a 17 year period, we illustrated that coherent structures in time control the distribution of tracers. In line with the findings of our work we proposed a framework that combines a high spatial density of vortical elements and PV gradient field evolution in relation to the spatial distribution of *f/H* contours.

We believe that a fundamental requirement for the eddy stirring efficiency mechanism, as depicted by our results, are 'stagnation' areas downstream of intensified coherent jets.

We think that these could be created by a network of topographical coherent vortices (i.e. eddies generated above topographic obstacles, in the case of Drake Passage) or an eddy field generated downstream of intensified jets from the dissipation of their kinetic energy and PV conservation (in an analogy to supercritical jets entering stagnant water bodies) over regions with smooth topographic slopes. These vortex dense spatial concentrations are further sustaining the slow down, due to topographic steering and obstruction, and rearrange the upstream intensified jets in small scale kinematic boundaries of secondary weak flow. These 'stagnation' areas are found to be bounded by large topography (closed f/H contours) or topographically steered kinematic boundaries (strong PV gradients). Several examples of this potential mechanism exist, for example at 30°, 90° and 150°E all within the main ACC path.

Our proposed mechanism is that the high diffusivity regions here are the result of a chaotic advection regime. This is performed with an enhancement of the role of coherent vortices and kinematic boundaries. As such, mixed baroclinic-barotropic instability, generated through the interaction of the mean flow with bottom topography results in eddy intensified regions in the wake of large bottom topography and arrested downstream where mixing of PV and the subsequent formation of jets and vortices in a non-parallel flow approximation takes place. The mixing regimes are delimited by meridional excursions of strong PV gradients to the west and east, which engulf the eddy intensified regions with similar equatorward PV tongues (following closely the f/H distribution) creating characteristic PV mixing pools of relatively reduced and homogenized ambient PV gradients. In the theoretical study of Rhines [2007] PV stirring in the wake of topography creates nearly stagnant areas of particle advection. Here though, we found inhomogeneous PV mixing, generated from a topographically steered mean flow, to support the formation of small scale multiple jets and vortical elements, responsible for the dispersion of particles in a chaotic manner.. We need further justification for this mechanism by mapping of the mixing structure in the submesoscale range, defining the exact eddy length scales[1] over the high diffusivity areas (these are found over smooth topography), eddy propagation speeds[2] on the isoneutrals here, EKE arrest and clarifying what is the exact process for the coherent vortex concentration.

Our focus in this study was on determining the structure of mixing processes in the ACC from a Lagrangian perspective and not a direct model evaluation (even though an attempt to present a parallel simulation of DIMES experiment was attempted). Nonetheless, values of derived diffusivity here indicate that OCCAM 1/12° performs

[1] Even though we believe that the velocity autocorrelation based method underestimates eddy length scales, the computed values are in agreement with maximum growth scales in the ACC derived from *Smith* [2007] studying local linear baroclinic instabilities.

[2] While we could assert that mixing suppression in the ACC, as depicted by the $\mathcal{S}_k$ factor [*Naveira Garabato et al.*, 2011] is due to eddies propagation speed with the mean flow [*Ferrari and Nikurashin*, 2010], we also found that mean flow shear acts as a transport barrier in Drake Passage.

well in expressing ACC's dynamics in comparison with results derived from OGCM [*Lu and Speer*, 2011; *Griesel et al.*, 2010] and altimetric observations in previous studies [*Ferrari and Nikurashin*, 2010]. It is left for future work to cross-examine OCCAM's results here with field derived datasets focused on isopycnal diffusivity in the ACC.

Deciphering mixing distribution and flow features from a Lagrangian perspective In the introductory sections and throughout this thesis the ability of a Lagrangian approximation to simulate fluid particles was noted. The numerically integrated particles' trajectories were to a significant degree able to depict prominent circulation patterns in the Southern Ocean and especially at the latitudinal extent of the ACC. Lagrangian studies have the ability through both time and space sampling of being a useful tool for the depiction of local regime characteristics in contrast to, for example the effective diffusivity method (even though regional approximations by *Shuckburgh et al.* [2009a] have been attempted). With adequate spatial resolution (high density releases) advection pathways and kinematic boundaries can be mapped. Here, our Lagrangian representation of the flow dynamics , the quantification of the particle spatial occurrence progression, both in space and time, are useful in revealing flow structures and prominent features. It is obvious that evolution of particle dispersion in oceanic, and in general in geophysical flows (even when considering time-dependent periodic perturbations) presents a chaotic (homogenized) image with time progression as a consequence of dispersion itself. In this mixing perspective[3] the patterns depicted from a Lagrangian approach provide a connection between dispersion, transport barriers, stagnation and 'end-point' organization.

6.3 Concluding remark

As a concluding remark, I would like most of all to point out the immense capabilities to decipher flow characteristics in a Lagrangian framework. Especially when the datasets we are now able to produce are large enoug to derive significant statistical results and increase our resolution of depictinglow's kinematic segmentation. Integration of the particles trajectories here was performed in an offline simulation exploiting the advantages of parallel computation. The datasets produced have the potential of still providing some additional insightful perspectives on flow characteristics (e.g different formalizations consonant with existing natural experiments), which could be presented in a future publication. The main focus of this thesis was examined and presented on the basis of knowledge acquired and matured during the duration of a research studentship.

[3]Mixing is considered a consequence to jet-filament formation and the spatial distribution of vortex density in a holistic perturbed dynamic system.

Caveats accompanying this study are mainly associated with the inadequacy of the release scheme employed to capture the full vertical and horizontal distribution of eddy diffusivity and the temporal variation of flow characteristics. Surface diffusivity was not computed while eddy propagation phase speeds or even computation of vortex trajectories , based solely on Lagrangian data, require different tracking schemes. These would be helpful in deciphering and even confronting more robustly mechanisms proposed from other studies. Even though, the scheme employed here has adequate spatial sampling, it is computationally inefficient to study relative dispersion of particle pairs after some period of time due to the chaotic rearrangement of particle positions. Multiple releases in time covering shorter simulation periods have the possibility of illustrating persistency in time and flow characteristics evolution through a statistically significant relative dispersion calculation.

Bibliography

Abernathey, R., J. Marshall, M. Mazloff, and E. F. Shuckburgh (2010), Enhancement of Mesoscale Eddy Stirring at Steering Levels in the Southern Ocean, *J. Phys. Oceanogr.*, *40*(1), 170–184, doi:10.1175/2009JPO4201.1.

Aksenov, Y. (2002), The sea ice-ocean global coupled model, ARCICE Project report Part I: dynamical-thermodynamical sea ice model., *Southampton Oceanography Centre Research and Consultancy Report 103, 83 pp.*

Aksenov, Y., S. Bacon, and A. C. Coward (2007), The North Atlantic Inflow into the Arctic Ocean: High-resolution Model Study, *National Oceanography Centre, Southampton.*

Antonov, J., S. Levitus, T. P. Boyer, T. Conkright, M nad O' Brien, and C. Stephens (1998), World Ocean Atlas 1998 Vol. 1: Temperature of the Atlantic Ocean., *NOAA Atlas NESDIS 27. U.S. Gov. Printing Office, Wash., D.C.*, *1*, 166.

Arbic, B., and R. Scott (2007), On quadratic bottom drag, geostrophic turbulence, and oceanic mesoscale eddies, *J. Phys. Oceanogr.*, *38*, 84–103.

Arhan, M., A. C. Naveira Garabato, K. J. Heywood, and D. P. Stevens (2002), The Antarctic Circumpolar Current between the Falkland Islands and South Georgia, *J. Phys. Oceanogr.*, *32*, 1914–1931.

Artale, V., G. Boffetta, A. Celani, M. Cencini, and A. Vulpiani (1997), Dispersion of passive tracers in closed basins: Beyond the diffusion coefficient, *Phys. Fluids*, *9*(11), 3162–3171.

Aurell, E., G. Boffetta, A. Crisanti, G. Paladin, and A. Vulpiani (1997), Predictability in the large: an extension of the concept of Lyapunov exponent, *J. Physics A-Mathematical and General*, *30*, 1–26.

Bauer, S., M. S. Swenson, and A. Griffa (2002), Eddy mean flow decomposition and eddy diffusivity estimates in the tropical Pacific Ocean: 2. Results, *J. Geophys. Res.: Oceans*, *107*(C10), 3154–3161.

Berloff, P. S., J. C. McWilliams, and A. Bracco (2002), Material transport in oceanic gyres. Part I: Phenomenology, *J. Phys. Oceanogr.*, *32*, 764–796.

Bishop, J. K. B., and W. B. Rossow (1991), Spatial and temporal variability of global surface solar irradiance, *J. Geophys. Res.*, *96*, 839–858.

Boffetta, G., A. Celani, M. Cencini, G. Lacorata, and A. Vulpiani (2000), Nonasymptotic properties of transport and mixing, *Chaos: An Interdisciplinary Journal of Nonlinear Science*, *10*, 50.

Boffetta, G., G. Lacorata, G. Redaelli, and A. Vulpiani (2001), Detecting barriers to transport: a review of different techniques, *Physica D: Nonlinear Phenomena*, *159*, 58–70.

Boffetta, G., M. Cencini, M. Falcioni, and A. Vulpiani (2002), Predictability: a way to characterize complexity, *Phys. Rep.*, *356*, 367–474.

Boyer, T. (1998), World Ocean Atlas 1998 Vol. 4: Salinity of the Atlantic Ocean., *NOAA Atlas NESDIS 30. U.S. Gov. Printing Office, Wash., D.C.*, *4*, 166.

Bryan, K. (1969), A Numerical Method for the Study of the Circulation of the World Ocean, *J. Comp. Phys.*, *135*, 154–169.

Carmona, R. A., and B. Rozovskii (1999), *Stohastic Partial Differential Equations: Six Perspectives*, *Mathematical Surveys and Monoghraphs*, vol. 64, chap. 4. TRANSPORT SIMULATIONS, p. 156, American Mathematical Society.

Charney, J. (1971), Geostrophic turbulence, *J. Atmos. Sci.*, *28*(6), 1087–1095.

Chelton, D. B., M. Schlax, K. E. Naggar, and N. Siwertz (1998), Geographical variability of the first baroclinic Rossby radius of deformation, *J. Phys. Oceanogr.*, *28*, 433–460.

Chelton, D. B., M. Schlax, and R. Samelson (2007), Global observations of large oceanic eddies, *Geophys. Res. Lett*, *34*, L15,606.

Chelton, D. B., M. Schlax, and R. Samelson (2011), Global observations of nonlinear mesoscale eddies, *Prog. Oceanogr.*, *91*(2), 167–216, doi:10.1016/j.pocean.2011.01.002.

Courant, R., K. Friedrichs, and H. Lewy (1928), Über die partiellen Differenzengleichungen der mathematischen Physik, *Mathematische Annalen*, *100*(1), 32–74.

Courant, R., K. Friedrichs, and H. Lewy (1967), On the partial difference equations of mathematical physics, *IBM Journal, English translation of the 1928 German original*, pp. 215–234.

Coward, A. C., and B. A. De Cuevas (2005), The OCCAM 66 Level Model: physics, initial conditions and external forcing -run202, *Southampton Oceanography Center, Internal Report No. 99*, pp. 1–58.

Cox, M. D. (1984), A primitive equation 3-dimensional model of the ocean, *Tech. Rep. 1*, Geophysical Fluid Dynamics Laboratory/NOAA, Princeton University, Princeton, N.J. 08542.

Cunningham, S., S. Alderson, B. A. King, and M. A. Brandon (2003), Transport and variability of the Antarctic Circumpolar Current in Drake Passage, *J. Geophys. Res.*, *108*(C5), 8084, doi:10.1029/2001JC001147.

Danabasoglu, G., and J. Marshall (2007), Effects of vertical variations of thickness diffusivity in an ocean general circulation model, *Ocean Model.*, *18*, 122–141.

Davis, R. E. (1982), On relating Eulerian and Lagrangian velocity statistics: single particles in homogeneous flows, *J. Fluid Mech.*, *114*, 1–26, doi:10.1017/S0022112082000019.

Davis, R. E. (1991), Lagrangian ocean studies, *Annu. Rev. Fluid Mech.*, *23*, 43–64.

Dong, S., J. Sprintall, S. T. Gille, and L. Talley (2008), Southern Ocean mixed-layer depth from Argo float profiles, *J. Geophys. Res.*, *113*(C06013).

Döös, K. (2008), *Numerical Methods in Meteorology and Oceanography*, Department of Meteorology, Stockholm University.

Döös, K., and D. J. Webb (1994), The Deacon cell and the other meridional cells of the Southern Ocean, *J. Phys. Oceanogr.*, *24*, 429–429.

Döös, K., J. Nycander, and A. C. Coward (2008), Lagrangian decomposition of the Deacon Cell, *J. Geophys. Res.*, *113*(C07028), 13, doi:10.1029/2007JC004351.

d'Ovidio, F., V. Fernández, E. Hernández-García, and C. López (2004), Mixing structures in the Mediterranean Sea from Finite-Size Lyapunov Exponents, *Geophys. Res. Lett.*, *31*(L17203), 4, doi:10.1029/2004GL020328.

Drijfhout, S., P. D. Vries, K. Döös, and A. C. Coward (2003), Impact of eddy-induced transport on the Lagrangian structure of the upper branch of the thermohaline circulation, *J. Phys. Oceanogr.*, *33*(10), 2141–2155.

Dritschel, D. G., and M. McIntyre (2008), Multiple jets as PV staircases: The Phillips effect and the resilience of eddy-transport barriers, *J. Atmos. Sci.*, *65*(3), 855–874.

Düing, W. (1978), Spatial and temporal variability of major ocean currents and mesoscale eddies, *Bound.-Lay. Meteorol.*, *13*, 7–22, 10.1007/BF00913859.

Eden, C., and J. Willebrand's (1999), Neutral density revisited, *Deep-Sea Res. II*, *46*(1), 33–54.

Einstein, A. (1955), *The world as I see it*, John Lane.

Emery, W. J., and R. E. Thomson (2001), *Data Analysis Methods in Physical Oceanography*, 2nd ed., Elsevier Science Inc.

Euler, L. (1756/7), Principia motus fluidorum, *Novi Commentarii Acad. Sci. Petropolitanae*, *6*, 271–311.

Evans, P. L., and B. J. Noye (1995), A model for fast oil spill trajectory prediction in shallow gulfs., *In: Bellwood, O., Choat, H., Saxena, N. (Eds.), PACON '94 Proceedings: Recent Advances in Marine Science and Technology PACON International and James Cook University of Northern Queensland, Australia*, pp. 119–130.

Fahrbach, E., G. Rohardt, and G. Krause (1992), The Antarctic Coastal Current in the southeastern Weddell Sea, *Polar Biol.*, *12*(2), 171–182.

Ferrari, R. (2007), Statistics of dispersion in flows with coherent structures, *Extreme Events: Proc. 15th 'Aha Huliko' a Hawaiian Winter Workshop, Honolulu, HI, US. Office of Naval Research, the School of Ocean and Earth Science and Technology and the Department of Oceanography, University of Hawaii at Manoa*, pp. 99–108.

Ferrari, R., and M. Nikurashin (2010), Suppression of eddy diffusivity across jets in the southern ocean, *J. Phys. Oceanogr.*, *40*(7), 1501–1519.

Ferrari, R., and C. Wunsch (2009), Ocean Circulation Kinetic Energy: Reservoirs, Sources, and Sinks, *Annu. Rev. Fluid Mech.*, *41*(1), 253–282, doi:10.1146/annurev.fluid.40.111406.102139.

Ferrari, R., and C. Wunsch (2010), The distribution of eddy kinetic and potential energies in the global ocean, *Tellus A*, *62*(2), 92–108.

Figueroa, H. A., and B. O. Donald (1994), Eddy resolution versus eddy diffusion in a double gyre GCM. Part I: The Lagrangian and Eulerian description, *J. Phys. Oceanogr.*, *24*, 371–386.

Fu, L.-L., D. B. Chelton, P.-Y. L. Traon, and R. A. Morrow (2010), Eddy dynamics from satellite altimetry, *Oceanography*, pp. 1–12.

Garraffo, Z., A. J. Mariano, A. Griffa, C. Veneziani, and E. P. Chassignet (2001), Lagrangian data in a high-resolution numerical simulation of the North Atlantic: I. Comparison with in situ drifter data, *J. Mar. Res.*, *29*, 157—176.

Garrett, C. (2006), Turbulent dispersion in the ocean, *Prog. Oceanogr.*, *70*(2-4), 113–125.

Gent, P., and J. C. McWilliams (1990), Isopycnal mixing in ocean circulation models, *J. Phys. Oceanogr*, *20*(1), 150–155.

George, W. (2006), Lectures in Turbulence for the 21st Century, Chalmers University of Technology.

Gildor, H., E. Fredj, J. Steinbuck, and S. Monismith (2009), Evidence for submesoscale barriers to horizontal mixing in the ocean from current measurements and aerial photographs, *J. Phys. Oceanogr.*, *39*(8), 1975–1983.

Gill, A., J. Green, and A. Simmons (1974), Energy partition in the large-scale ocean circulation and the production of mid-ocean eddies, *Deep-Sea Research*, *21*(7), 499–508.

Gill, A. E. (1982), *Atmosphere-Ocean Dynamics*, *International Geophysics Series*, vol. 30, Academic Press.

Gille, S., M. Yale, and D. Sandwell (2000a), Global correlation of mesoscale ocean variability with seafloor roughness from satellite altimetry, *Geophys. Res. Lett*, *27*(9), 1251–1254.

Gille, S. T. (1999), Evaluating Southern Ocean response to wind forcing, *Phys. Chem. Earth*, *24*(4), 423–428.

Gille, S. T. (2003), Float observations of the Southern Ocean. Part II: Eddy fluxes, *J. Phys. Oceanogr.*, *33*, 1182–1196.

Gille, S. T., and L. Romero (2003), Statistical behavior of ALACE floats at the surface of the Southern Ocean, *J. Atmos. Ocean. Tech.*, *20*, 1,633–1,640.

Gille, S. T., M. M. Yale, and D. T. Sandwell (2000b), Global correlation of mesoscale ocean variability with seafloor roughness from satellite altimetry, *Geophys. Res. Lett*, *27*(9), 1251–1254.

Gille, S. T., D. P. Stevens, R. Tokmakian, and K. J. Heywood (2001), Antarctic Circumpolar Current response to zonally averaged winds, *J. Geophys. Res.*, *106*(c2), 2743.

Gille, S. T., E. J. Metzger, and R. Tokmakian (2004), Seafloor topography and ocean circulation, *Oceanography*, *17*(1).

Goodwin, P., R. Williams, A. Ridgwell, and M. Follows (2009), Climate sensitivity to the carbon cycle modulated by past and future changes in ocean chemistry, *Nature Geosci*, *2*(2), 145–150.

Gouretski, V. (1996), A new hydrographic data set for the South Pacific: Synthesis of WOCE and historical data., *WHP SAC Technical Report 2, WOCE Report No 143/96*.

Gouretski, V., and K. Koltermann (2004), WOCE global hydrographic climatology, *Berichte des BSH*, *35*, 1–52.

Griesel, A., S. T. Gille, J. Sprintall, J. McClean, J. H. LaCasce, and M. Maltrud (2010), Isopycnal diffusivities in the Antarctic Circumpolar Current inferred from Lagrangian floats in an eddying model, *J. Geophys. Res.*, *115*(C06006), 18, doi: 10.1029/2009JC005821.

Griffies, S., A. Gnanadesikan, and R. C. Pacanowski (1998), Isoneutral diffusion in a z-coordinate ocean model, *J. Phys. Oceanogr.*, *28*(5), 805–830.

Gwilliam, C. S. (1995), The OCCAM Global Ocean Model, *Tech. rep.*, NOC.

Hallberg, R., and A. Gnanadesikan (2001), An exploration of the role of transient eddies in determining the transport of a zonally reentrant current, *J. Phys. Oceanogr.*, *31*(11), 3312–3330.

Haller, G. (2001), Lagrangian structures and the rate of strain in a partition of two-dimensional turbulence, *Phys. Fluids*, *13*, 3365.

Haller, G. (2002), Lagrangian coherent structures from approximate velocity data, *Phys. Fluids*, *14*, 1851.

Haller, G., and G. Yuan (2000), Lagrangian coherent structures and mixing in two-dimensional turbulence, *Physica D: Nonlinear Phenomena*, *147*, 352–370.

Heath, M. T. (2002), *Scientific Computing, An Introductory Survey*, chap. 11.2, 2nd ed., McGraw-Hill.

Heywood, K. J., A. C. Naveira Garabato, and D. P. Stevens (2002), High mixing rates in the abyssal Southern Ocean, *Nature*, *415*, 4.

Hodell, D. A., M. Brenner, J. H. Curtis, and T. Guilderson (2001), Solar forcing of drought frequency in the Maya lowlands, *Science*, *292*(5520), 1367–1370, doi:10.1126/science.1057759.

Hofmann, E. (1985), The large-scale horizontal structure of the Antarctic Circumpolar Current from FGGE drifters, *J. Geophys. Res.*, *90*(C4), 7087–7097.

Holloway, G. (1986), Estimation of oceanic eddy transports from satellite altimetry, *Nature*, *323*, 243–244.

Holton, J. R. (2004), *An Introduction to Dynamic Meteorology*, *International Geophysics Series*, vol. 88, Fourth ed., Elsevier Academic Press.

Huang, R. (2004), Ocean, energy flows in, *Encyclopedia of Energy*.

Huang, R. (2010), Is the neutral surface really neutral? A close examination of energetics of along isopycnal mixing, *Tech. rep.*, Department of Physical Oceanography, WHOI.

Huang, R., and W. Wang (2003), Gravitational potential energy sinks in the oceans, *Near-Boundary Processes and Their Parameterization, Proceedings,'Aha Huliko'a Hawaii Winter Workshop, University of Hawaii at Manoa, January 21–24, 2003*, pp. 239–247.

Hughes, C. W. (2005), Nonlinear vorticity balance of the Antarctic Circumpolar Current, *J. Geophys. Res.*, *110*, 11.

Hughes, C. W., and E. R. Ash (2001), Eddy forcing of the mean flow in the Southern Ocean, *J. Geophys. Res.*, *106*(C2), 2713–2722.

Hughes, C. W., and P. D. Killworth (1995), Effects of bottom topography in the large-scale circulation of the Southern Ocean, *J. Phys. Oceanogr.*, *25*(11), 2485–2497.

Hughes, C. W., M. Jones, and S. Carnochan (1998), Use of transient features to identify eastward currents in the Southern Ocean, *J. Geophys. Res.*, *103*(C2), 2929–2943.

Hunke, E., and J. Dukowicz (1997), An elastic–viscous–plastic model for sea ice dynamics, *J. Phys. Oceanogr.*, *27*, 1849–1867.

Iudicone, D., G. Madec, and T. J. McDougall (2008), Water-mass transformations in a neutral density framework and the key role of light penetration, *J. Phys. Oceanogr.*, *38*, 1357—1376, doi:10.1175/2007JPO3464.1.

Jackett, D. R., and T. J. McDougall (1997), A neutral density variable for the World's Oceans, *J. Phys. Oceanogr.*, *27*, 237–263.

Jakobsson, M., N. Cherkis, and J. Woodward (2000), New grid of Arctic bathymetry aids scientists and mapmakers, *adsabs.harvard.edu*.

Joseph, B., and B. Legras (2002), Relation between kinematic boundaries, stirring, and barriers for the Antarctic polar vortex, *J. Atmos. Sci.*, *59*(7), 1198–1212.

Kalnay, E., M. Kanamitsu, R. Kistler, and W. Collins (1996), The NCEP/NCAR 40-year reanalysis project, *Bull. Am. Meteorol. Soc.*, *77*, 437–471, doi:10.1175/1520-0477(1996)077⟨0437:TNYRP⟩2.0.CO;2.

Killworth, P. D. (1997), On the parameterization of eddy transfer Part I. Theory, *J. Mar. Res.*, *55*, 1171–1197.

Killworth, P. D., D. Stainforth, D. J. Webb, and S. M. Paterson (1991), The development of a free-surface Bryan-Cox-Semtner ocean model, *J. Phys. Oceanogr.*, *21*, 1333–1348.

Koh, T., and B. Legras (2002), Hyperbolic lines and the stratospheric polar vortex, *Chaos: An Interdisciplinary Journal of Nonlinear Science*, *12*, 382.

Kolmogorov, A. (1991), The local structure of turbulence in incompressible viscous fluid for very large Reynolds numbers, *Proc. R. Soc. Lond. A (reprint from Dokl. Akad. Nauk SSSR (1941))*, *437*(1890), 9–13.

Kraichnan, R. (1961), The closure problem of turbulence theory, *Proc. Symp. Applied Math. AMS*, *13*, 56.

Kraichnan, R. (1967), Inertial ranges in two-dimensional turbulence, *Phys. Fluids*, *10*(7), 7, doi:10.1063/1.1762301.

Kraichnan, R. (1971), Inertial-range transfer in two-and three-dimensional turbulence, *J. Fluid Mech.*, *47*, 525–535.

Kuznetsov, L., M. Toner, J. Kirwan, C. Jones, L. Kantha, and J. Choi (2002), The loop current and adjacent rings delineated by Lagrangian analysis of the near-surface flow, *J. Mar. Res.*, *60*, 405–429.

LaCasce, J. H. (2000), Floats and f/H, *J. Mar. Res.*, *58*(1), 61–95.

LaCasce, J. H. (2008), Statistics from Lagrangian observations, *Prog. Oceanogr.*, *77*, 1–29.

LaCasce, J. H., and C. Ohlmann (2003), Relative dispersion at the surface of the Gulf of Mexico, *J. Mar. Res.*, *61*(3), 285–312, notes quadratic law of relative dispersion.

Lacorata, G., E. Aurell, and A. Vulpiani (2001), Chaotic Dynamics Title: Drifters dispersion in the Adriatic Sea: Lagrangian data and chaotic model, *Ann. Geophys.*, *19*, 121–129.

Lankhorst, M., and W. Zenk (2006), Lagrangian observations of the middepth and deep velocity fields of the northeastern Atlantic Ocean, *J. Phys. Oceanogr.*, *36*(1), 43–63.

Large, W. G., and A. G. Nurser (2001), *Ocean surface water mass transformation*, *In: Sielder, Gerold and et al. Eds, Ocean circulation and climate: observing and modelling the global ocean., International Geophysics Series*, vol. 77, pp. 317–336, Academic Press.

Large, W. G., and S. Pond (1982), Sensible and latent heat flux measurements over the ocean, *J. Phys. Oceanogr.*, *12*(5), 464–482.

Large, W. G., J. C. McWilliams, and S. C. Doney (1994), Oceanic Vertical Mixing: A review and a model with a nonlocal boundary layer parameterization, *Rev. Geophys.*, *32*(4), 363–403.

Large, W. G., G. Danabasoglu, S. C. Doney, and J. C. McWilliams (1997), Sensitivity to surface forcing and boundary layer mixing in a global ocean model-annual-mean climatology, *J. Phys. Oceanogr.*, *27*, 1–30.

Le Quéré, C., M. R. Raupach, J. G. Canadell, G. Marland, and L. Bopp (2009), Trends in the sources and sinks of carbon dioxide, *Nature Geosci.*, pp. 1–6, doi:10.1038/ngeo689.

Ledwell, J., A. Watson, and C. Law (1993), Evidence for slow mixing across the pycnocline from an open-ocean tracer-release experiment, *Nature*, *364*(6439), 701–703.

Ledwell, J. R. (2009), DIMES: First US cruise preliminary summary, *Tech. rep.*, WHOI.

Ledwell, J. R., E. T. Montgomery, K. L. Polzin, L. Laurent St., R. W. Schmitt, and J. M. Toole (1999), Evidence for enhanced mixing over rough topography in the abyssal ocean, *Nature*, *403*, 4.

Ledwell, J. R., J. M. Toole, L. Laurent St., and J. Girton (2010), Diapycnal Mixing in the Antarctic Circumpolar Current, *J. Phys. Oceanogr.*, *41*, 241—246.

Lee, M.-M., and A. C. Coward (2003), Eddy mass transport for the Southern Ocean in an eddy-permitting global ocean model, *Ocean Model.*, *5*, 249–266.

Lee, M.-M., and R. Williams (2000), The role of eddies in the isopycnic transfer of nutrients and their impact on biological production, *J. Mar. Res.*, *58*(6), 895–917.

Lee, M.-M., A. C. Coward, and A. G. Nurser (2002), Spurious diapycnal mixing of the deep waters in an eddy-resolving global ocean model, *J. Phys. Oceanogr*, *32*, 1522–1535.

Lee, M.-M., A. G. Nurser, A. C. Coward, and B. A. D. Cuevas (2007), Eddy advective and diffusive transports of heat and salt in the Southern Ocean, *J. Phys. Oceanogr.*, *37*, 1376–1393.

Lee, M.-M., A. G. Nurser, A. C. Coward, and B. A. D. Cuevas (2009), Effective eddy diffusivities inferred from a point release tracer in an eddy-resolving ocean model, *J. Phys. Oceanogr*, *39*, 894–914.

Lenton, T. M., and J. Lovelock (2000), Daisyworld is Darwinian: constraints on adaptation are important for planetary self-regulation, *J. Theoretical Biol.*, *206*, 109–123.

Levitus, S., R. Burgett, and T. P. Boyer (1994), *World Ocean Atlas 1994 Volume 3: Salinity, Vol. 4:Temperature*, p. 99, NOAA Atlas NESDIS 3, 4, U. S. Department of Commerce, Washington, D. C.

Li, Y., J. Worth D. Nowlin, and R. O. Reid (1996), Spatial-scale analysis of hydrographic data over the Texas-Louisiana continental shelf, *J. Geophys. Res.*, *101*(C9), 20,595–20,606.

Lorenz, E. (1963), Deterministic Nonperiodic Flow, *J. Atmos. Sci.*, *20*, 130–141.

Lovelock, J. (1991), *Gaia: The practical science of planetary medicine*, Gaia Books Ltd; 2nd Revised edition edition (27 Oct 2000).

Lovelock, J. (2008), A geophysiologist's thoughts on geoengineering, *Philos. Trans. R. Soc. Lond. A: Mathematical, Physical and Engineering Sciences*, *366*(1882), 3883.

Lu, J., and K. Speer (2011), Topography, jets, and eddy mixing in the Southern Ocean, *J. Mar. Res., In Press.*

Lumpkin, R., and K. Speer (2007), Global ocean meridional overturning, *J. Phys. Oceanogr.*, *37*, 2550—2562.

Lumpkin, R., A. Treguier, and K. Speer (2002), Lagrangian eddy scales in the northern Atlantic Ocean, *J. Phys. Oceanogr.*, *32*(9), 2425–2440.

Marsaglia, G., and A. Zaman (1991), A new class of random number generators., *Ann. Appl. Probab.*, *1*(3), 462–480.

Marshall, D. P. (2000), Vertical fluxes of potential vorticity and the structure of the thermocline, *J. Phys. Oceanogr*, *30*(12), 3102–3112.

Marshall, D. P., and A. C. N. Garabato (2008), A conjecture on the role of bottom-enhanced diapycnal mixing in the parameterization of geostrophic eddies, *J. Phys. Oceanogr.*, *38*(7), 1607–1613.

Marshall, J., and T. Radko (2003), Residual-mean solutions for the Antarctic Circumpolar Current and its associated overturning circulation, *J. Phys. Oceanogr.*, *33*, 1–14.

Marshall, J., H. Jones, R. Karsten, and R. Wardle (2002), Can eddies set ocean stratification?, *J. Phys. Oceanogr*, *32*(1), 26–38.

Marshall, J., E. F. Shuckburgh, H. Jones, and C. Hill (2006), Estimates and implications of surface eddy diffusivity in the Southern Ocean derived from tracer transport, *J. Phys. Oceanogr.*, *36*, 1806—1821.

Marshunova, M. (1966), Principal characteristics of the radiation balance of the underlying surface and of the atmosphere in the Arctic., *Trans. Arctic Antarctic Research Institute*, *229*(RM-500 3-PR, translated from Russian by the Rand Corporation, Santa-Monica, CA.).

Maximenko, N., and P. P. Niiler (2005), Hybrid decade-mean global sea level with mesoscale resolution, *Recent Advances in Marine Science and Technology*.

Maximenko, N., P. Niiler, L. Centurioni, M. Rio, O. Melnichenko, D. Chambers, V. Zlotnicki, and B. Galperin (2009), Mean dynamic topography of the ocean derived from satellite and drifting buoy data using three different techniques*, *J. Atmos. Ocean. Tech.*, *26*(9), 1910–1919.

McDougall, T. (1987), Neutral surfaces, *J. Phys. Oceanogr.*, *17*, 1950–1964.

McIntyre, M. (2003), Potential vorticity, in *Encyclopedia of Atmospheric Sciences*, vol. 2, edited by J. R. Holton, J. A. Pyle, and J. A. Curry, chap. 15, pp. 434–450, London: Academic/Elsevier.

McIntyre, M. (2008), Potential-vorticity inversion and the wave-turbulence jigsaw: Some recent clarifications, *Adv. Geosci.*, *15*, 47–56.

McWilliams, J. C. (2006), *Fundamentals of Geophysical Fluid Dynamics*, 283 pp., Cambridge University Press.

Meredith, M. P., and A. Hogg (2006), Circumpolar response of Southern Ocean eddy activity to a change in the Southern Annular Mode, *Geophys. Res. Lett.*, *33*, L16,608.

Meredith, M. P., A. C. N. Garabato, A. Hogg, and R. Farneti (2011a), Sensitivity of the overturning circulation in the Southern Ocean to decadal changes in wind forcing, *J. Climate, Accepted for publication*.

Meredith, M. P., P. L. Woodworth, T. Chereskin, D. P. Marshall, L. C. Allison, G. R. Bigg, K. Donohue, K. J. Heywood, C. W. Hughes, A. Hibbert, A. M. Hogg, H. L. Johnson, L. Jullion, B. A. King, H. Leach, Y.-D. Lenn, M. A. M. Maqueda, D. R. Munday, A. C. N. Garabato, C. Provost, J.-B. Sallée, and J. Sprintall (2011b), Sustained monitoring of the Southern Ocean at Drake Passage: past achievements and future priorities, *Rev. Geophys., In Press*.

Morel, Y., and J. C. McWilliams (2001), Effects of isopycnal and diapycnal mixing on the stability of oceanic currents, *J. Phys. Oceanogr.*, *31*, 2280—2296.

Munk, W. (1950), On the wind-driven ocean circulation, *J. Meteorol.*, *7*(2), 80–93.

Munk, W. (1966), Abyssal recipes, *Deep-Sea Research*, *13*(4), 707–730.

Munk, W., and E. Palmén (1951), Note on the Dynamics of the Antarctic Circumpolar Current, *Tellus*, *3*(1), 53–55.

Munk, W., and C. Wunsch (1998), Abyssal recipes II: Energetics of tidal and wind mixing, *Deep-Sea Res. I*, *45*, 1997–2010.

Naveira Garabato, A. C. (2010), *Energetics of Ocean Mixing. In, Encyclopedia of Ocean Sciences, Steele, J.H., Turekian, K.K. and Thorpe, S.A. (eds.), San Diego, US*, pp. 261–270, 2nd ed., Academic Press.

Naveira Garabato, A. C., D. P. Stevens, and K. J. Heywood (2003), Water mass conversion, fluxes, and mixing in the Scotia Sea diagnosed by an inverse model, *J. Phys. Oceanogr.*, *33*, 2565–2587.

Naveira Garabato, A. C., K. L. Polzin, B. A. King, K. J. Heywood, and M. Visbeck (2004), Widespread intense turbulent mixing in the Southern Ocean, *Science*, *303*, 210–213.

Naveira Garabato, A. C., D. P. Stevens, A. J. Watson, and W. Roether (2007), Short-circuiting of the overturning circulation in the Antarctic Circumpolar Current, *Nature*, *447*, 194–197.

Naveira Garabato, A. C., R. Ferrari, and K. L. Polzin (2011), Eddy stirring in the Southern Ocean, *J. Geophys. Res.*, *116*(C09019), 29, doi:10.1029/2010JC006818.

Nikurashin, M., and R. Ferrari (2010), Radiation and dissipation of internal waves generated by geostrophic motions impinging on small-scale topography: Theory., *J. Phys. Oceanogr.*, *40*, 2025–2042.

Nycander, J. (2011), Energy conversion, mixing energy and neutral surfaces with a nonlinear equation of state, *J. Phys. Oceanogr.*, *41*, 28–41.

O'Brien, J. J. (Ed.) (1986), *Advanced Physical Oceanographic Numerical Modelling*, *NATO ASI Series C: Mathematical and Physical Sciences*, vol. 186, chap. 6, pp. 177–181, D. Reidel Publishing Company.

Okubo, A. (1970), Horizontal dispersion of floatable particles in the vicinity of velocity singularities such as convergences, *Deep-Sea Research*, *17*, 445–454.

Olbers, D., and M. Wenzel (1989), Determining diffusivities from hydrographic data by inverse methods with applications to the Circumpolar Current., *Oceanic circulation models: Combining data and dynamics*, pp. 95–139.

Olbers, D., D. Borowski, C. Völker, and J.-O. Wölff (2004), The dynamical balance, transport and circulation of the Antarctic Circumpolar Current, *Antarctic Science*, *16*(4), 439–470.

Olbers, D., K. Lettman, and R. Timmermann (2007), Six circumpolar currents—on the forcing of the Antarctic Circumpolar Current by wind and mixing, *Ocean Dynamics*, *57*, 12—31, doi:10.1007/s10236-006-0087-9.

Orsi, A. H., T. Whitworth III, and W. D. Nowlin Jr. (1995), On the meridional extent and fronts of the Antarctic Circumpolar Current, *Deep-Sea Res. I*, *42*(5), 641–673.

Pacanowski, R. C. (1995), MOM 2 documentation, user's guide and reference manual., *Tech. Rep. 3*, Geophysical Fluid Dynamics Laboratory/NOAA Ocean Group.

Pacanowski, R. C., and A. Gnanadesikan (1998), Transient response in a z-level ocean model that resolves topography with partial cells, *Mon. Weather Rev.*, *126*(12), 3248–3270.

Pahnke, K., and R. Zahn (2005), Southern hemisphere water mass conversion linked with North Atlantic climate variability, *Science*, *307*, 1741—1746.

Pasquero, C., A. Provenzale, and A. Babiano (2001), Parameterization of dispersion in two-dimensional turbulence, *J. Fluid Mech.*, *439*, 279–303.

Paulson, C., and J. Simpson (1977), Irradiance measurements in the upper ocean, *J. Phys. Oceanogr.*, *7*(6), 952–956.

Pierrehumbert, R. T. (1991), Chaotic mixing of tracer and vorticity by modulated traveling rossby waves, *Geophys. Astro. Fluid*, *58*, 285–320.

Pierrehumbert, R. T., and H. Yang (1993), Global chaotic mixing on isentropic surfaces, *J. Atmos. Sci.*, *50*(15), 2462–2480.

Pollard, R. T., H. Venables, J. F. Read, and J. T. Allen (2007), Large-scale circulation around the Crozet Plateau controls an annual phytoplankton bloom in the Crozet Basin, *Deep-Sea Res. II*, *54*, 1915–1929.

Polzin, K. L., J. M. Toole, and J. R. Ledwell (1997), Spatial variability of turbulent mixing in the abyssal ocean, *Science*, *276*, 93.

Poulain, P., and P. P. Niiler (1989), Statistical analysis of the surface circulation in the California Current System using satellite-tracked drifters, *J. Phys. Oceanogr.*, *19*(10), 1588–1603.

Price, J. F. (2006), Lagrangian and Eulerian representations of fluid flow: Kinematics and the equations of motion, *Tech. rep.*, WHOI.

Provenzale, A. (1999), Transport by coherent barotropic vortices, *Annu. Rev. Fluid Mech.*, *31*(1), 55–93.

Provenzale, A., A. Babiano, A. Bracco, C. Pasquero, and J. Weiss (2008), Coherent vortices and tracer transport, *Transport and Mixing in Geophysical Flows*, pp. 101–118.

Regier, L., and H. Stommel (1979), Float trajectories in simple kinematic flows, *Proc. Natl. Acad. Sci. USA*, *76*(10), 4760–4764.

Renner, A. H. H., K. J. Heywood, and S. E. Thorpe (2009), Validation of three global ocean models in the Weddell Sea, *Ocean Model.*, *30*, 1–41, doi:10.1016/j.ocemod.2009.05.007.

Reynolds, A. M. (2002), Lagrangian stochastic modeling of anomalous diffusion in two-dimensional turbulence, *Phys. Fluids*, *14*, 1442—1450.

Rhines, P. (2007), Jets and orography: Idealized experiments with tip jets and lighthill blocking, *J. Atmos. Sci.*, *64*(10), 3627–3639.

Richardson, L. (1926), Atmospheric diffusion shown on a distance-neighbour graph, *Proc. Roy. Soc. Lond. A Mat.*, *110*(756), 709.

Rintoul, S. R., C. W. Hughes, and D. Olbers (2001), The Antarctic Circumpolar Current system, in *Ocean Circulation and Climate: Observing and Modelling the Global Ocean*, *International Geophysics Series*, vol. 77, chap. 4.6, pp. 271–314, Academic Press.

Ristorcelli, J., and A. Poje (2000), Lagrangian covariance analysis of β-plane turbulence, *Theoretical and Computational Fluid Dynamics*, *14*(1), 1–20.

Romanov, I. (1995), Atlas of ice and snow of the Arctic Basin and Siberian Shelf Seas., *A. Tunik (Ed.), Backbone Publishing Company.*, p. 277.

Rossow, W. B., and R. A. Schiffer (1991), ISCCP cloud data products, *Bull. Am. Meteorol. Soc.*, *72*(1), 2–20.

Rupolo, V. (2007), A lagrangian-based approach for determining trajectories taxonomy and turbulence regimes, *J. Phys. Oceanogr*, *37*(6), 1584–1609.

Salazar, J., and L. Collins (2009), Two-particle dispersion in isotropic turbulent flows, *Annu. Rev. Fluid Mech.*, *41*, 405–432.

Sallée, J., K. Speer, and S. Rintoul (2011), Mean-flow and topographic control on surface eddy-mixing in the southern ocean, *J. Mar. Res.*, *69*(4-6), 4–6.

Sallée, J.-B., K. Speer, and R. A. Morrow (2008a), Response of the Antarctic Circumpolar Current to atmospheric variability, *J. Climate*, *21*(12), 3020–3039.

Sallée, J.-B., K. Speer, R. A. Morrow, and R. Lumpkin (2008b), An estimate of Lagrangian eddy statistics and diffusion in the mixed layer of the Southern Ocean, *J. Mar. Res.*, *66*, 441–463.

Sallée, J.-B., K. Speer, S. R. Rintoul, and S. Wijffels (2010), Southern Ocean thermocline ventilation, *J. Phys. Oceanogr.*, *40*(3), 509–529.

Salmon, R. (1980), Baroclinic instability and geostrophic turbulence, *Geophys. Astro. Fluid*, *15*(3-4), 167–211.

Sanford, T., J. Dunlap, J. Carlson, J. Girton, and D. Webb (2005), Autonomous velocity and density profiler: EM-APEX, in *Current Measurement Technology, 2005, Proceedings of the IEEE/OES Eighth Working Conference on*, pp. 152—156, doi: 10.1109/CCM.2005.1506361.

Schmitz, W. (1996), On the world ocean circulation. Volume II, the Pacific and Indian Oceans/a global update, *darchive.mblwhoilibrary.org*.

Schneider, J., and T. Tél (2003), Extracting flow structures from tracer data, *Ocean Dynamics*, *53*, 64–72.

Schumacher, J., and B. Eckhardt (2002), Clustering dynamics of lagrangian tracers in free-surface flows, *arXiv*, *nlin.CD*, doi:10.1103/PhysRevE.66.017303.

Scott, R. B., and B. K. Arbic (2007), Spectral energy fluxes in geostrophic turbulence: Implications for ocean energetics, *J. Phys. Oceanogr.*, *37*(3), 673–688.

Scott, R. B., and F. Wang (2005), Direct evidence of an oceanic inverse kinetic energy cascade from satellite altimetry, *J. Phys. Oceanogr.*, *35*, 1650–1666.

Scott, R. B., B. K. Arbic, E. P. Chassignet, A. C. Coward, M. Maltrud, W. Merryfield, A. Srinivasan, and A. Varghese (2010), Total kinetic energy in four global eddying ocean circulation models and over 5000 current meter records, *Ocean Model.*, *32*(3-4), 157–169.

Screen, J. A., N. P. Gillett, D. P. Stevens, G. J. Marshall, and H. K. Roscoe (2008), The role of eddies in the Southern Ocean temperature response to the Southern Annular Mode, *J. Climate*, *22*(3), 806–818, doi:10.1175/2008JCLI2416.1.

Semtner, A. J. (1974), A general circulation model for the World Ocean, *Tech. Rep. 9*, Deparment of Meteorology, University of California, Los Angeles.

Semtner, A. J. (1976), A model for the thermodynamic growth of sea ice in numerical investigations of climate, *J. Phys. Oceanogr.*, *6*, 379–389.

Shuckburgh, E. F., H. Jones, J. Marshall, and C. Hill (2009a), Understanding the Regional Variability of Eddy Diffusivity in the Pacific Sector of the SO, *J. Phys. Oceanogr.*, *39*, 2011–2023.

Shuckburgh, E. F., H. Jones, J. Marshall, and C. Hill (2009b), Robustness of an effective diffusivity diagnostic in oceanic flows, *J. Phys. Oceanogr.*, *39*, 1993–2009.

Smith, K. S. (2007), The geography of linear baroclinic instability in Earth's Oceans, *J. Mar. Res.*, *65*, 655–687.

Smith, K. S., and R. Ferrari (2009), The production and dissipation of compensated thermohaline variance by mesoscale stirring, *J. Phys. Oceanogr*, *39*, 2477—2501, doi: 10.1175/2009JPO4103.1.

Smith, K. S., and J. Marshall (2009), Evidence for enhanced eddy mixing at middepth in the Southern Ocean, *J. Phys. Oceanogr.*, *39*(1), 50–69, doi:10.1175/2008JPO3880.1.

Smith, W. H. F., and D. T. Sandwell (1997), Global sea floor topography from satellite altimetry and ship depth soundings, *Science*, *277*(5334), 1956–1962.

Sokolov, S. (2002), Structure of Southern Ocean fronts at 140 E, *J. Mar. Syst.*, *37*, 151–184.

Sokolov, S., and S. R. Rintoul (2009a), Circumpolar structure and distribution of the Antarctic Circumpolar Current fronts: 1. Mean circumpolar paths, *J. Geophys. Res.*, *114*(C11), C11,018.

Sokolov, S., and S. R. Rintoul (2009b), Circumpolar structure and distribution of the Antarctic Circumpolar Current fronts: 2. Variability and relationship to sea surface height, *J. Geophys. Res.*, *114*(C11), C11,019.

Solomon, S., D. Qin, M. Manning, Z. Chen, M. Marquis, k B Averyt, M. tignor, and H. L. Miller (2007), Climate Change 2007: The Physical Science Basis, *IPCC Assessment Report*, *4*.

Speich, S., B. Blanke, P. D. Vries, S. Drijfhout, K. Döös, A. Ganachaud, and R. Marsh (2002), Tasman leakage: A new route in the global ocean conveyor belt, *Geophys. Res. Lett*, *29*(10), 1416–1420.

Spencer, R. W. (1993), Global oceanic precipitation from the MSU during 1979-91 and comparisons to other climatologies, *J. Climate*, *6*, 1301–1326.

Stammer, D. (1997), Global characteristics of ocean variability estimated from regional TOPEX/POSEIDON altimeter measurements, *J. Phys. Oceanogr.*, *27*, 1743–1769.

Stammer, D. (1998), On eddy characteristics, eddy transports, and mean flow properties, *J. Phys. Oceanogr.*, *28*, 727–739, doi:10.1175/1520-0485(1998)028⟨0727:OECETA⟩2.0.CO;2.

Stark, J. D., and J. Marotzke (2003), *Scientific visualization of ocean model data*.

Steele, M., R. Morley, and W. Ermold (2001), Phc: A global ocean hydrography with a high-quality Arctic Ocean, *J. Climate*, *14*(9), 2079–2087.

Sundermeyer, M. A., and J. F. Price (1998), Lateral mixing and the North Atlantic Tracer Release Experiment: Observations and numerical simulations of Lagrangian particles and passive tracer, *J. Geophys. Res.*, *103*(C10), 21,481–21,497.

Swallow, J., and L. V. Worthington (1961), An observation of a deep countercurrent in the western North Atlantic, *Deep-Sea Res. II*, *8*, 1–19.

Taylor, G. I. (1921), Diffusion by continuous movements, *Proc. Lond. Math. Soc.*, *20*, 196–211.

Taylor, J. R., and R. Ferrari (2009), On the equilibration of a symmetrically unstable front via a secondary shear instability, *J. Fluid Mech.*, *622*(1), 103–113.

Taylor, J. R., and R. Ferrari (2010), Buoyancy and wind-driven convection at mixed layer density fronts, *J. Phys. Oceanogr*, *40*(6), 1222–1242, doi:10.1175/2010JPO4365.1.

Tchernia, P., and P. F. Jeannin (1980), Observations on the Antarctic East Wind Drift using tabular icebergs tracked by satellite Nimbus F (1975-1977), *Deep-Sea Research*, *27A*, 467–474.

Tennekes, H., and J. L. Lumley (1972), A first course in turbulence, *The MIT Press*, p. 300.

Thomas, L., A. Tandon, and A. Mahadevan (2008), Submesoscale processes and dynamics, *Geophysical Monograph*, *177*, 17–38, doi:10.1029.

Thompson, A. F. (2009), The atmospheric ocean- eddies and jets in the Antarctic Circumpolar Current, *Philos. Trans. R. Soc. Lond. A: Mathematical, Physical and Engineering Sciences*, *366*(1885), 4529.

Thompson, A. F. (2010), Jet formation and evolution in baroclinic turbulence with simple topography, *J. Phys. Oceanogr.*, *40*, 257—278, doi:10.1175/2009JPO4218.1.

Thompson, A. F., P. H. Haynes, C. Wilson, and K. J. Richards (2010), Rapid southern ocean front transitions in an eddy-resolving ocean gcm, *Geophys. Res. Lett*, *37*(L23602), 5, doi:10.1029/2010GL045386.

Thompson, S. R. (1995), Sills of the global ocean: a compilation, *Ocean Model.*, *109*, 7–9.

Thorpe, S. E. (2001), Variability of the southern Antarctic Circumpolar Current in the Scotia Sea and its implications for transport to South Georgia., Ph.D. thesis, University of East Anglia, Norwich, UK.

Thorpe, S. E., K. J. Heywood, M. A. Brandon, and D. P. Stevens (2002), Variability of the southern Antarctic Circumpolar Current front north of South Georgia, *J. Mar. Syst.*, *37*, 87–105.

Thorpe, S. E., K. J. Heywood, D. P. Stevens, and M. A. Brandon (2004), Tracking passive drifters in a high resolution ocean model: implications for interannual variability of larval krill transport to south georgia, *Deep-Sea Res. I*, *51*, 909–920, doi: 10.1016/j.dsr.2004.02.008.

Thorpe, S. E., E. J. Murphy, and J. L. Watkins (2007), Circumpolar connections between Antarctic krill (Euphausia superba Dana) populations: Investigating the roles of ocean and sea ice transport, *Deep-Sea Res. I*, *54*, 792–810.

Tilburg, C., H. Hurlburt, J. O'Brien, and J. Shriver (2002), Remote topographic forcing of a baroclinic western boundary current: An explanation for the Southland Current and the pathway of the Subtropical Front east of New Zealand, *J. Phys. Oceanogr.*, *32*(11), 3216–3232.

Treguier, A. (1999), Evaluating eddy mixing coefficients from eddy-resolving ocean models: A case study, *J. Mar. Res.*, *57*, 89–108.

Treguier, A., and J. C. McWilliams (1990), Topographic influences on wind-driven, stratified flow in a -plane channel: An idealized model for the Antarctic Circumpolar Current, *J. Phys. Oceanogr.*, *20*(3), 321–343.

Treguier, A., M. H. England, S. R. Rintoul, G. Madec, J. L. Sommer, and J. Molines (2007), Southern Ocean overturning across streamlines in an eddying simulation of the Antarctic Circumpolar Current, *Ocean Sci. Discuss.*, *4*(4), 653–698.

Uleysky, M. Y., M. V. Budyansky, and S. V. Prants (2012), Mechanism of destruction of transport barriers in geophysical jets with rossby waves, *arXiv*, *nlin.CD*, doi:10.1103/PhysRevE.81.017202.

Vallis, G. K. (2006a), *Time Derivatives for Fluids, In, Atmospheric and Oceanic Fluid Dynamics, Fundamentals and Large Scale Circulation*, chap. 1. Equations of motion, p. 3, Cambridge University Press.

Vallis, G. K. (2006b), *Viscosity and difussion, In, Atmospheric and Oceanic Fluid Dynamics, Fundamentals and Large Scale Circulation*, chap. 1. Equations of motion, p. 13, Cambridge University Press.

Venaille, A., G. K. Vallis, and K. S. Smith (2011), Baroclinic turbulence in the ocean: Analysis with primitive equation and quasigeostrophic simulations, *J. Phys. Oceanogr.*, *41*, 1605–1623.

Veneziani, M., A. Griffa, A. M. Reynolds, and A. J. Mariano (2004), Oceanic turbulence and stochastic models from subsurface Lagrangian data for the northwest Atlantic Ocean, *J. Phys. Oceanogr.*, *34*, 1884–1906.

Veneziani, M., A. Griffa, A. M. Reynolds, Z. Garraffo, and E. P. Chassignet (2005), Parameterizations of Lagrangian spin statistics and particle dispersion in presence of coherent vortices, *J. Mar. Res.*, *63*(6), 1057–1083.

Visbeck, M., J. Marshall, T. W. N. Haine, and M. Spall (1997), Specification of eddy transfer coefficients in coarse-resolution ocean circulation models*, *J. Phys. Oceanogr.*, *27*, 381–402.

Watson, A. J. (2004), Gaia and observer self-selection, *Scientists Debate Gaia: The Next Century*, pp. 201–210.

Watson, A. J., and J. R. Ledwell (2000), Oceanographic tracer release experiments using sulphur hexafluoride, *J. Geophys. Res.*, *105*(C6), 14,325–14,337.

Watson, A. J., and A. C. Naveira Garabato (2006), The role of Southern Ocean mixing and upwelling in glacialinterglacial atmospheric CO^2 change, *Tellus B*, *58*, 73–87, doi:10.1111/j.1600-0889.2005.00167.

Waugh, D., and E. Abraham (2008), Stirring in the global surface ocean, *Geophys. Res. Lett*, *35*(20), 1–5, doi:10.1029/2008GL035526.

Webb, D. J., and B. A. D. Cuevas (2007), On the fast response of the Southern Ocean to changes in the zonal wind, *Ocean Sci.*, *3*, 417–427.

Webb, D. J., B. A. D. Cuevas, and A. C. Coward (1998), The first main run of the OCCAM global ocean model, *Southampton Oceanography Centre, Internal Document No. 34*, pp. 1–43.

Weiss, J. (1991), The dynamics of enstrophy transfer in two-dimensional hydrodynamics, *Physica D: Nonlinear Phenomena*, *48*, 273—294.

Weiss, J., A. Provenzale, and J. C. McWilliams (1998), Lagrangian dynamics in high-dimensional point-vortex systems, *Phys. Fluids*, *10*, 1929—1941.

White, A. A. (2003), The primitive equations, in *Encyclopedia of Atmospheric Science*, edited by J. Holton and J. Pyle, J & Curry, pp. 694–702, Academic Press.

Whitehead, J. (2005), Effect of potential vorticity on flow rate through a gap, *J. Geophys. Res.*, *110*, C07,007 (1–4), doi:10.1029/2004JC002720.

Wiggins, S. (1992), Chaotic transport in dynamical systems, *NASA STI/Recon Technical Report A*, *92*.

Wiggins, S. (2005), The dynamical systems approach to Lagrangian transport in oceanic flows, *Annu. Rev. Fluid Mech.*, *37*, 295–328.

Willebrand, J., and D. Haidvogel (2001), Numerical Ocean Circulation Modelling: present status and future directions, in *Ocean Circulation and Climate - Observing and Modelling the Global Ocean*, *International Geophysics*, vol. 77, edited by J. C. Gerold Siedler and J. Gould, chap. 7.2, pp. 547 – 556, Academic Press, doi: 10.1016/S0074-6142(01)80138-8.

Williams, R., and M. Follows (2003), Physical transport of nutrients and the maintenance of biological production, *Ocean Biogeochemistry: The Role of the Ocean Carbon Cycle in Global Change*, pp. 19–51.

Witter, D., and D. Chelton (1998), Eddy-mean flow interaction in zonal oceanic jet flow along zonal ridge topography, *J. Phys. Oceanogr.*, *28*(10), 2019–2039.

Wunsch, C. (1997), The vertical partition of oceanic horizontal kinetic energy, *J. Phys. Oceanogr.*, *27*(8), 1770–1794.

Wunsch, C., and R. Ferrari (2004), Vertical mixing, energy, and the general circulation of the oceans, *Annu. Rev. Fluid Mech.*, *36*, 281–314.

Xie, P., and P. Arkin (1996), Analyses of global monthly precipitation using gauge observations, satellite estimates, and numerical model predictions, *J. Climate*, *9*(4), 840–858.

Zang, X., and C. Wunsch (2001), Spectral description of low-frequency oceanic variability, *J. Phys. Oceanogr.*, *31*, 3073–3095.

Zhurbas, V. (2003), Lateral diffusivity and Lagrangian scales in the Pacific Ocean as derived from drifter data, *J. Geophys. Res.*, *108*, 3141—3148, doi:10.1029/2002JC001596.

Appendix A

A.1 Diabatic processes and relative position of isoneutrals

An additional benchmark needed to be satisfied regarding the relative position of the first isoneutral surface with respect to the depth of the direct effect of diabatic processes. The mixed surface layer owes its main characteristic to diabatic forcing convection. In order to retain the 'adiabatic' character of the isoneutral surface it has to reside below the mixed layer depth. In a study of ARGO floats datasets in the vicinity of the Southern Ocean, *Dong et al.* [2008] computed mixed layer depths (MLD), using temperature and density criteria, that exceed 400 m, during the austral winter, in specified regions of Antarctic Intermediate Water (AAIW) and Subantarctic Mode Water (SAMW) formation. Maximum surface density for their MLD is 27.04 kg m^{-3}. Comparing the latitudinal extent of the mixed layer excessive depths, as illustrated in figure 3 of *Dong et al.* [2008], with isoneutral surface 27.76 depths in this study, the following conclusions were drawn. Minimum depth ($\leq$ 1200 m) of γ^n=27.76, as evaluated from OCCAM 1/12° model output, for the whole simulation period can be seen in figure 1. The monthly mean sea surface height (SSH) contours of -0.4 m and -1.15 m are overlaid (*Dong et al.* [2008] use -0.4 m and -1.2 m). Minimum depth north of the -0.4 m contour is in excess of 1200 m, in contrast to the intensified computed signals of MLD in their paper. Maximum MLD depth in this region is 400-500 m. In the designated region between the selected SSH contours, though, a match for the isoneutral surface depth and their MLD is potentially valid at two or more areas however, at longitudes between 0 and 220 degrees. At what amount, if any, the 'adiabatic' character of the isoneutral surface notion is biased and possibly breaks down at these areas is left to be seen in the main chapters the present where particle trajectories are analysed.

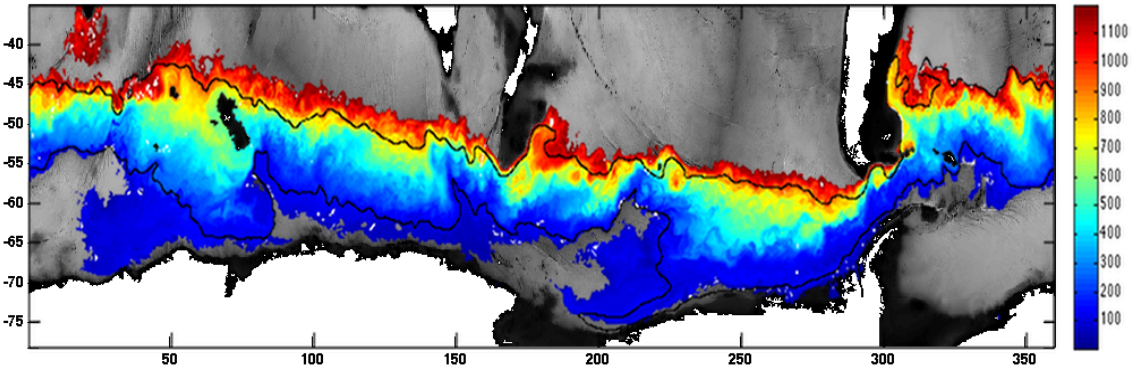

FIG. 1: Minimum depth ($\leq$ 1200 m) of isoneutral surface with density $\gamma^n = 27.76$ estimated for a period of 17 years covering model days 1095 to 7300. Black solid lines denote monthly mean sea surface height of -0.4 m and -1.15 m to the north and south respectively. Colorbar denotes depth in meters.

A.2 Selection of isoneutral surfaces

A.2.1 EKE from sea surface height

In order to derive EKE from sea surface height (ssh) for the whole period from model days 1095 to 7300, computation of residual geostrophic velocity from sea level anomaly, η', is required. Fundamental in the calculation is the definition of the time scale of the mean. As discussed in chapter 2, mean sea surface height is computed for 17 years (model days 1095 to 7300) and extracted from absolute dynamic topography (ssh) allowing the computation of geostrophic eddy velocities, in spherical polar coordinates, following the relationship

$$u'_g = -\frac{g}{f\alpha} \cdot \frac{\partial \eta'}{\partial \vartheta} \tag{1}$$

$$v'_g = \frac{g}{f\alpha \cos\vartheta} \cdot \frac{\partial \eta'}{\partial \varphi} \tag{2}$$

where g is the Earth's gravitational acceleration and f the *Coriolis* parameter as a function of latitude ϑ. Sea level anomaly is defined as $\eta' = ssh - \langle ssh \rangle$ where the average $\langle \cdot \rangle$ is calculated over the whole simulation period. As a consequence, $\overline{EKE}$ is computed as the average of EKE for each file in the calculation,

$$\overline{EKE} = 1/N \sum_{1}^{N} EKE \tag{3}$$

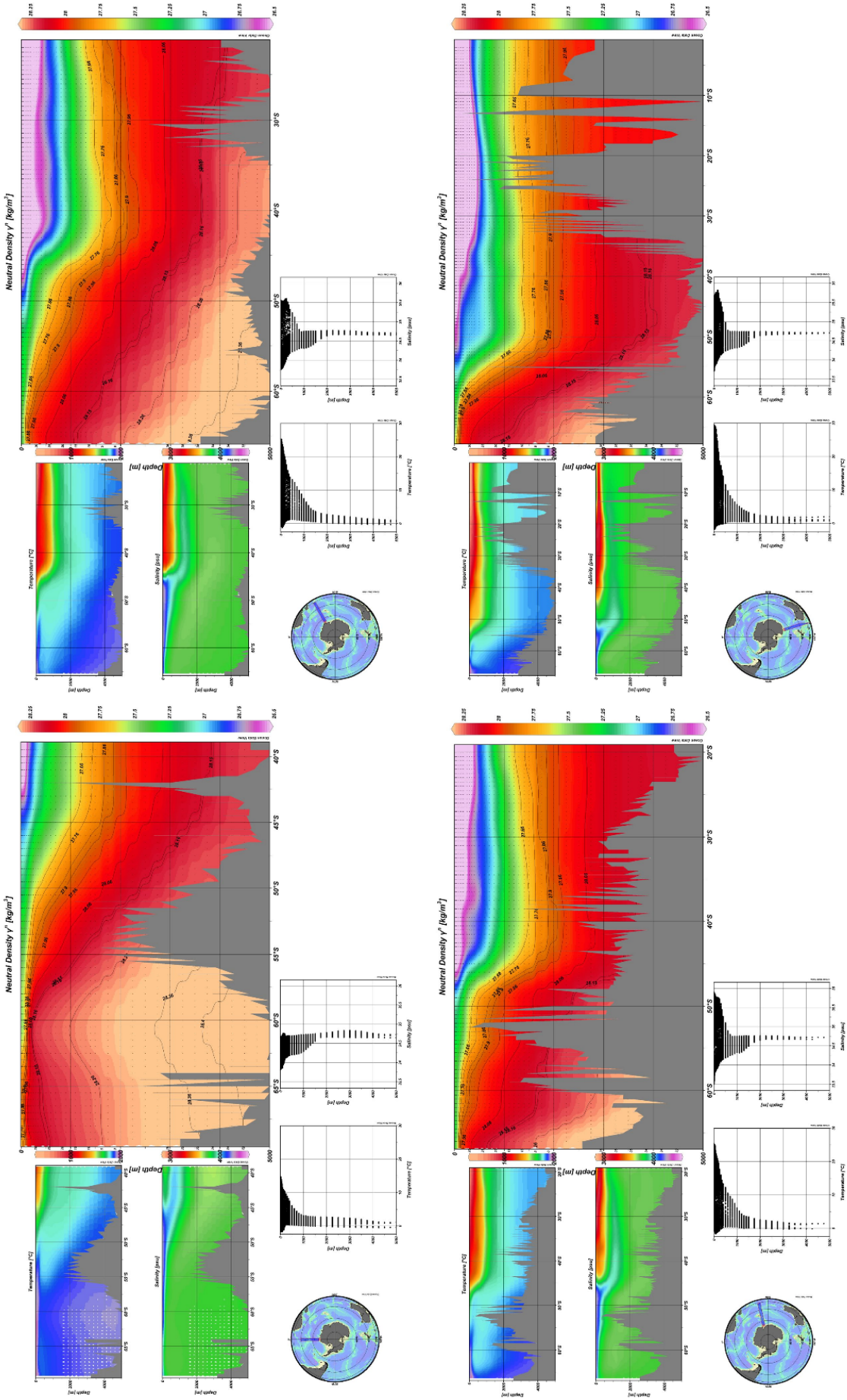

FIG. 2: Vertical meridional sections of WOCE climatology after *Gouretski and Koltermann* [2004] for selected regions in the Southern Ocean. Illustrated are temperature, salinity and neutral density γ_n as also depth-T and depth-S diagrams for the southern most station.

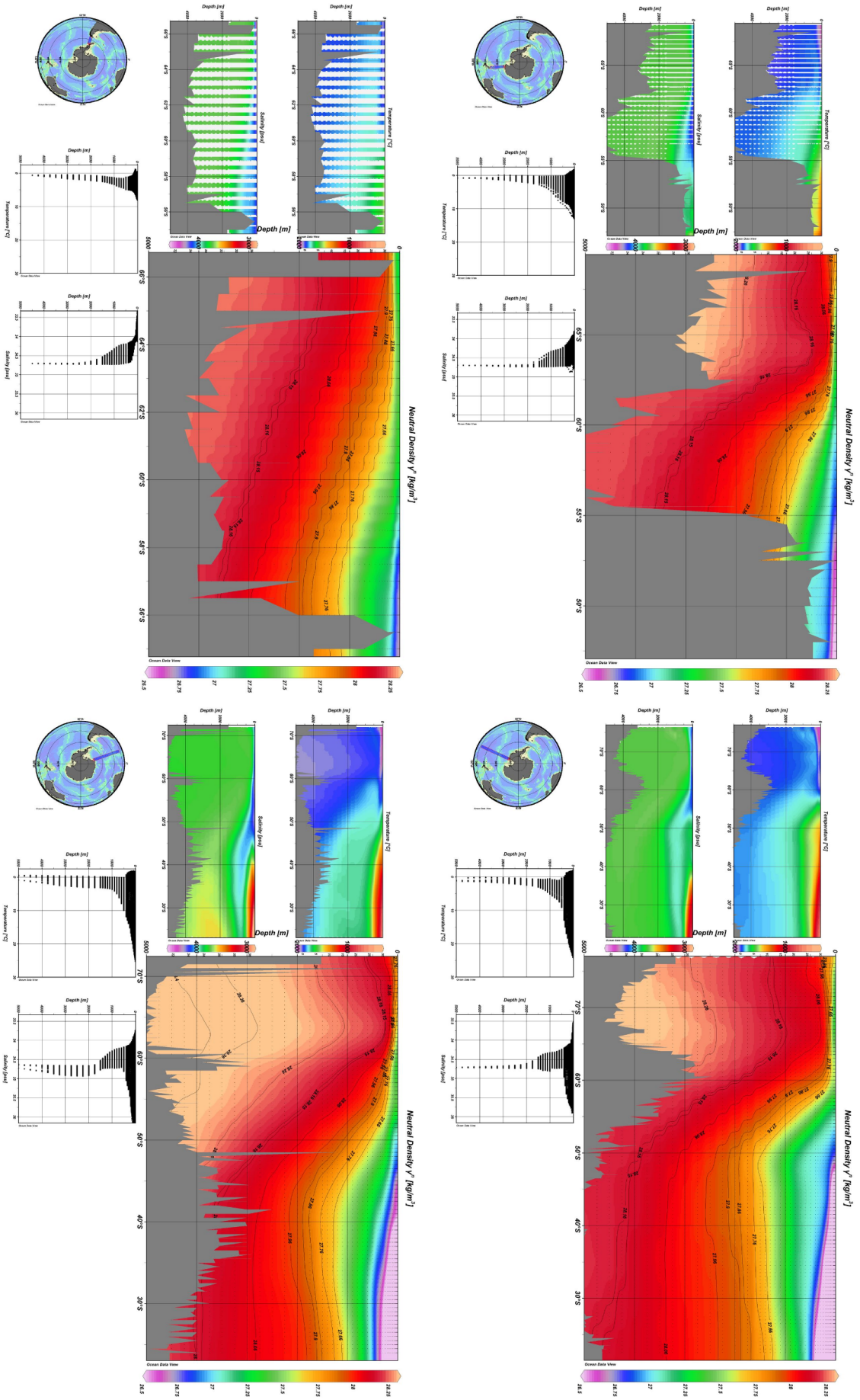

FIG. 3: Same as in figure 2.

A.3 Isopycnal mappings of geopotential anomaly, potential vorticity, slope and planetary vorticity

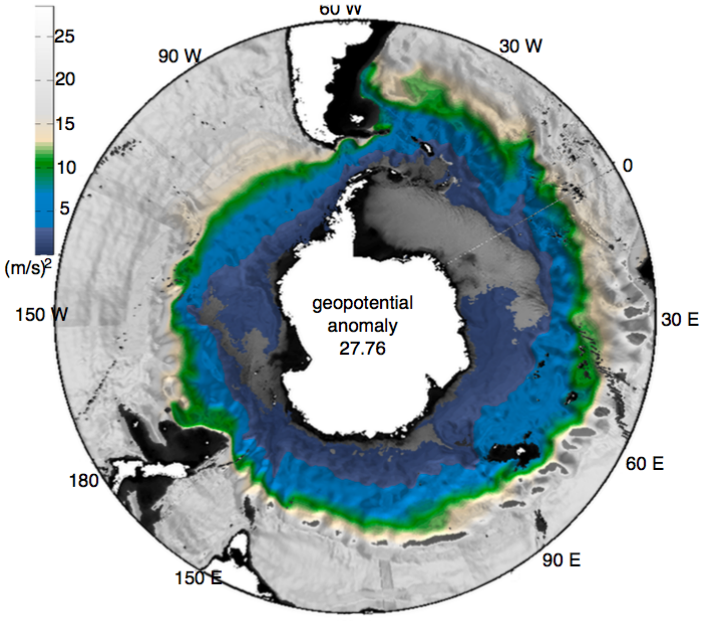

FIG. 4: Mean geopotential anomaly (m s^{-1})^2 with respect to surface for isoneutral surface 27.76 and depiction values for areas between ACC jets; SAF-PF (9.2-12.4), around PF (8.8-9.2) and south of PF (3-8.8).

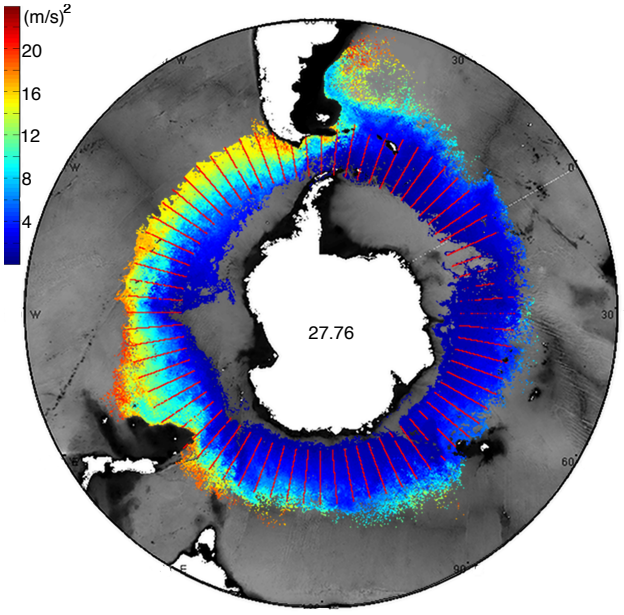

FIG. 5: Average monthly geopotential anomaly (m s^{-1})^2 with respect to surface interpolated on particles' positions during their 1st year of travel on isoneutral 27.76.

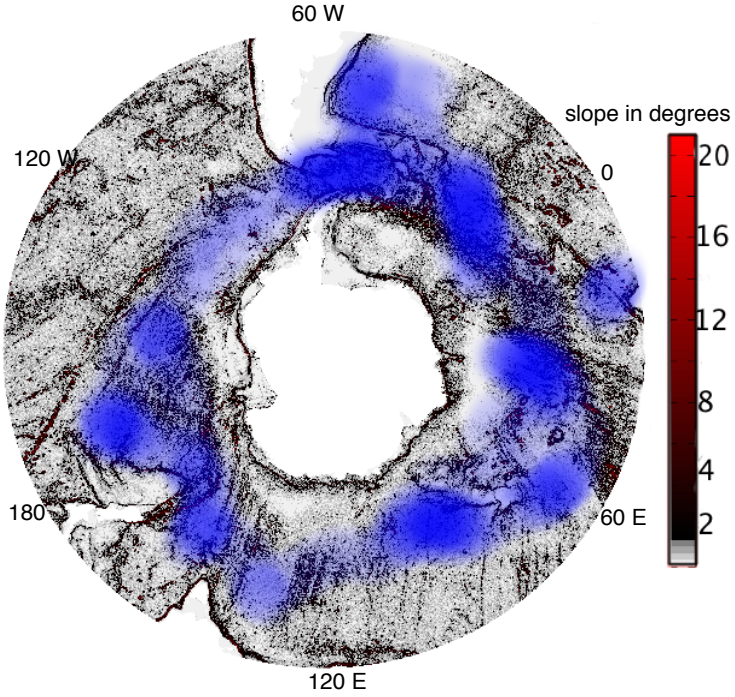

FIG. 6: Slope (in degrees) of OCCAM 1/12° model bottom topography. Blue areas illustrate schematically diffusivity intensity for comparison reasons.

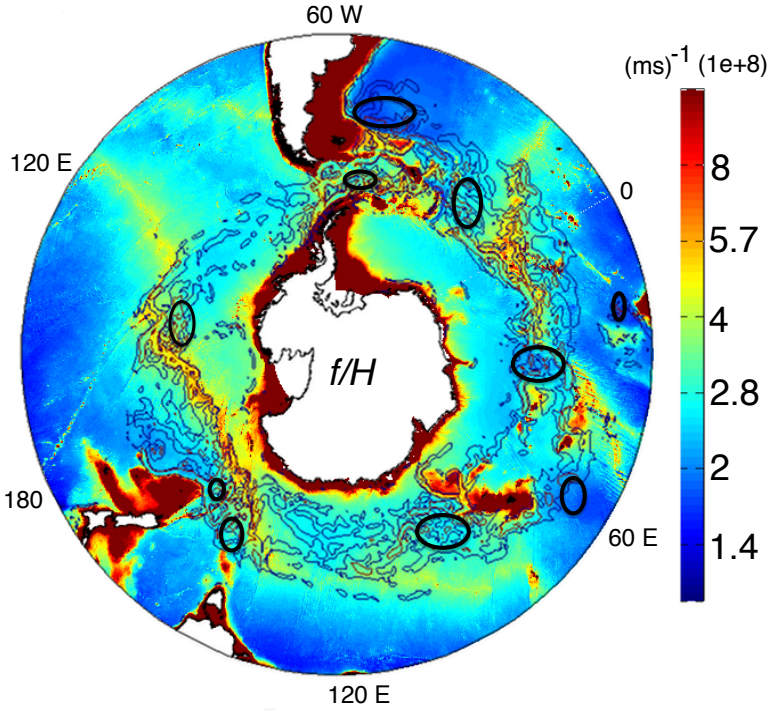

FIG. 7: f/H (10^8 (m s)$^{-1}$) for the Southern Ocean. Superimposed are contours of $\mathcal{U}_m$ (cm s^{-1}) (5-blue, 10-red) for isoneutral surface 27.76. Black circles denote regions of intensified isopycnal mixing.

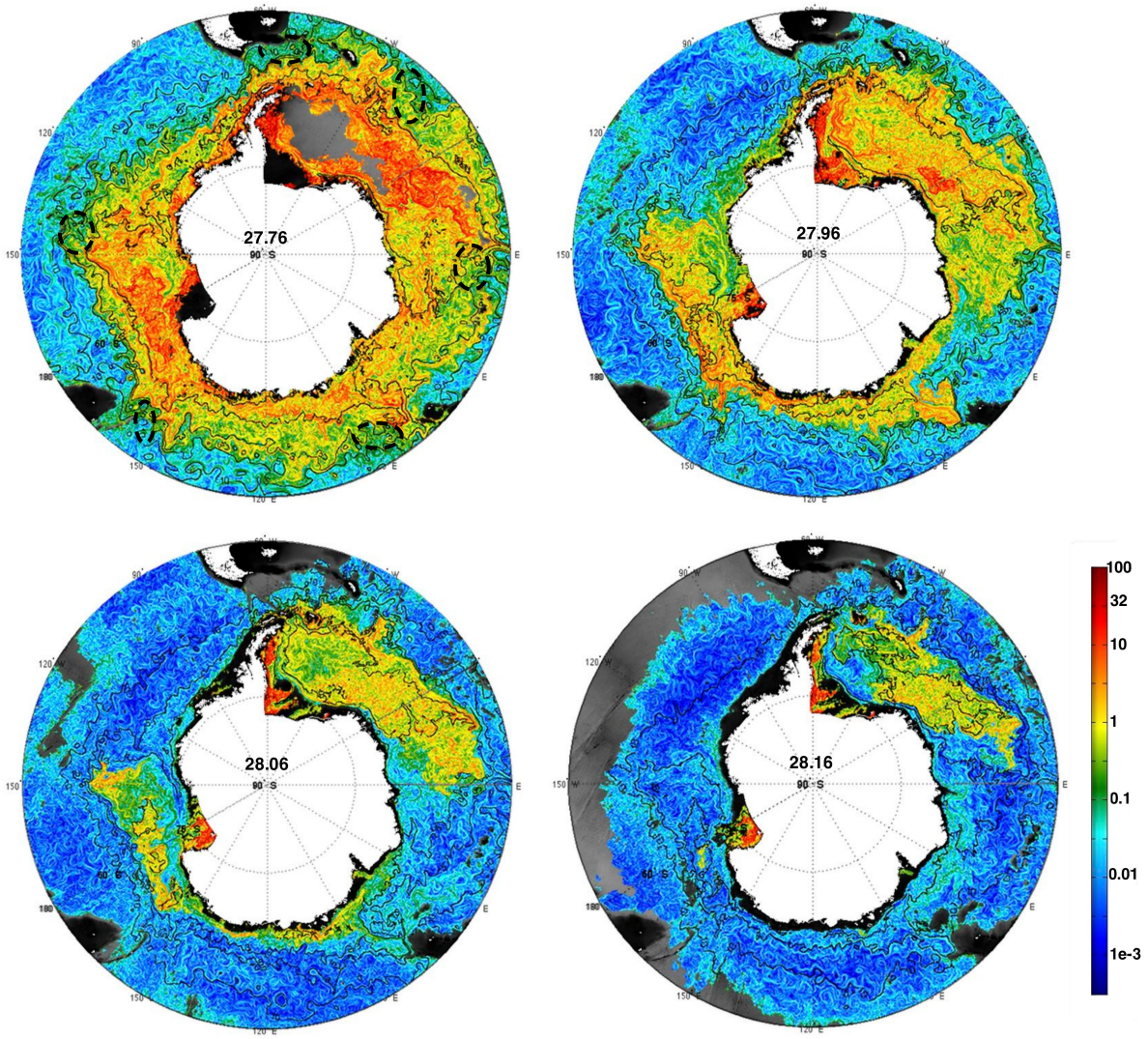

FIG. 8: Potential vorticity gradients ($10^{13}\times$(m s)$^{-1}$ km^{-1}) for all isoneutral surfaces for a period of 20 days. Overlaid are geopotential anomaly contours of 1, 3, 5 and 10 (m s^{-1})^2.

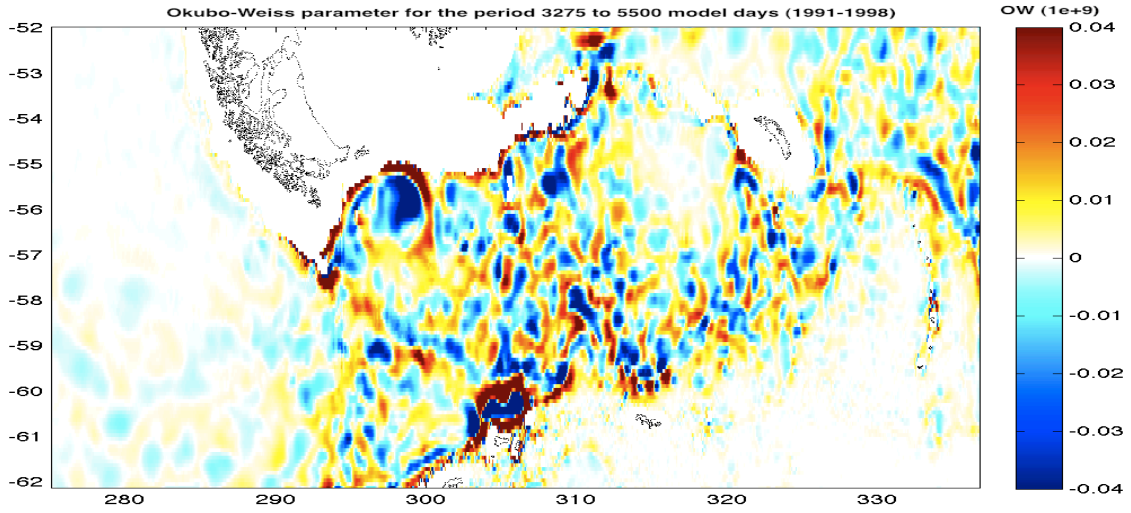

FIG. 9: Averaged Okubo-Weïss parameter (1e+9) for the period 1991-1998 in the region of Drake Passage on neutral density surface $\gamma^n = 27.9$. This spatial alignment of strain (positive values) and vortical elements (negative values) is considered here as a favourable mechanism for mixing efficiency in a bounded region. Persistent small scale vortices are spread throughout the whole domain, indicating the potential weakness of the large scale flow field to homogenise potential vorticity.

A.4 Diffusion, dispersion and geopotential anomaly in the ACC

Examining cross-stream diffusion for selected ensembles of particles, based on latitude of release, with respect to single particle displacement for all longitudinal releases (Fig. 10) we find that diffusion exhibits an upper limit for a range of displacement values when considered in a non-local framework. Different colours denote different longitudinal releases. A variety of diffusion events are recorded with scales above 20-40 km exhibiting the highest diffusivity values.

A.5 An introduction to relative dispersion dependance on inertial range cascades, temporal and spatial scales

When examining relative dispersion $\overline{\mathcal{D}^2}$ of particle pairs ensembles provision of energy transfer scaling arguments, at the respective environments, are also considered (see also section 4.2.1). In this study, with regard to the approximations of ocean dynamics simulation by OCCAM 1/12° model, reference only to 'incompressible' 2D turbulence is made (see *Vallis* [2006b], chapter 8 for a detailed discussion). Turbulence in the ocean interior can be approximated as two-dimensional if someone considers the scaling ratios

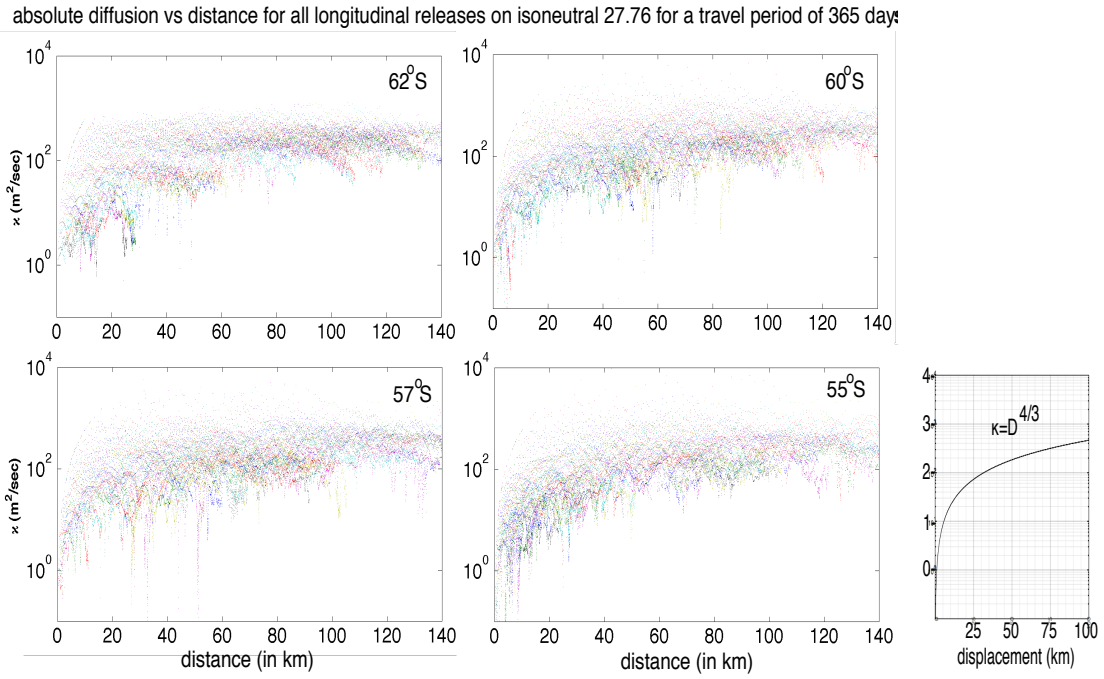

FIG. 10: Cross-stream diffusivity for all longitudinal releases versus distance for ensembles of particles at latitudes 62, 60, 57 and 55°S for isoneutral 27.76 and during the 1st year of travel. Different colours denote different longitudinal releases (see section 2.3.4 p.49 and Fig. 2.15). Absolute diffusion seems to be upper bounded but for different spatial scales with respect to the release location. Releases between 5 and 45° E, for example, occupy the lower left portion of the diagram regardless of latitudinal ensemble. The aim is to delineate that local dynamics influence diffusion approximations differently and thus computation of global averages are not representative of dispersion (Fig. 4.3,a). Nevertheless, classical diffusion theory computes a non-local estimate, since the computation is based on time series of particle positions, in a non-Markovian approximation of the flow. Also shown is the 4/3 power law dependence of diffusion on displacement for time scales up to the decorrelation time.

of density's vertical distribution (stratification) and rotation to vertical displacement rate[4].

In the inertial range, three dimensional turbulence energy cascade expression [*Kolmogorov*, 1991], emerged with an equivalent reverse nature for the two-dimensional turbulence [*Kraichnan*, 1967, 1971] also. An inverse energy E cascade towards larger than smaller scales is performed across wavenumbers k that follows a constant rate with a $E(k) \propto \epsilon^{2/3} k^{-5/3}$ dependency, where ϵ is a scale-independent energy dissipation rate[5]. As such, relative dispersion $\overline{\mathcal{D}^2}$ and diffusion κ_τ will exhibit an ϵt^3 time dependence and

[4]Considering the ratio of horizontal to vertical displacement rates (Fig. 2.19 and 2.18) and the horizontal velocity vertical variation, then a quasi two-dimensional approximation for turbulence is probably also valid for the OCCAM representation. Following *Ferrari and Wunsch* [2009] in this case, energy cascade direction is sensitive due to the $\mathcal{U}$ vertical variations.

[5]Energy ϵ and enstrophy η dissipation rates have straight forward units of $1/\mathcal{T}^3$ and $\mathcal{L}^2/\mathcal{T}^3$, with $\mathcal{L}$ and $\mathcal{T}$ defining the length and time scales respectively (notation after *Vallis* [2006b]).

a 4/3 power law dependence on displacement[6] respectively.

A second inertial range exists where forward enstrophy $\mathcal{E}$ cascade is towards smaller scales with a k^{-3} dependence on the spectrum [*Kraichnan*, 1967; *Charney*, 1971; *Salazar and Collins*, 2009]. In the enstrophy inertial cascade range, following *Vallis* [2006b], relative dispersion $\overline{\mathcal{D}^2}(t)$ would grow exponentially in time since $\overline{\mathcal{D}^2} \sim exp(B\eta^{1/3}t)$, with B being a non-dimensional constant, and $\kappa_\tau \propto \frac{d}{dt}\overline{\mathcal{D}^2(t)} \sim \eta^{1/3}\overline{\mathcal{D}^2}$.

Conceptually, in 2D turbulence the computed relative dispersion would vary in relation to the respective inertial range cascade environment. The capacity for a pair of particles to resolve the scales of cascade in the inertial range is actually a function of the initial separation distance d_0. A scaling argument, thus, with respect to the scale $\mathcal{L}_E$ at which energy is provided to the system by stirring (usually taken equal to the first baroclinic Rossby radius of deformation $\mathcal{L}_d$), is also required for the initial displacement d_0 of the examined pairs of particles. As such, relative dispersion $\overline{\mathcal{D}^2}$, for an ensemble of particle pairs with initial separation distance $d_0 \ll \mathcal{L}_E$[7], will exhibit exponential growth in time until the energy provision scale $\mathcal{L}_E$, when in the second inertial range of forward enstrophy cascade, and a cubic dependance on time until the larger scales (in a baroclinic unstable environment that would be equal to the size of the dominant large eddies present).

A.5.1 Multiple particles pairs separation analysis statistics

Initial separation distance of particle pairs Sensitivity to various initial separation distances d_0 is examined. Both time based evolution of separation and separation distance based criteria are analysed. Local factors corollaries are approached with examination of PV gradients for the respective time scale of relative dispersion.

The interpretation of relative dispersion $\overline{\mathcal{D}^2}$ results is somewhat problematic due to the fact of the diminishing of local factors' importance in constructing global averaging representations. Growth law examination can also reveal potential deficiencies of latitudinal (longitudinal) constructed averages in examining various initial separation distances. In figure 11 only separations significantly smaller than the grid size resolutions demonstrate exponential growth law at early time lags. At travel periods larger than 250 days, meridional dispersion scales close to a constant value. An analogous signal is depicted by diffusivity estimates (with all accompanying uncertainties due to

[6] *Richardson* [1926] (see their Fig. 8) had already demonstrated the 4/3 power law dependence of diffusivity on relative displacement $\mathcal{D}$ in what it was later to be referred as *Richardson's 4/3 law.*

[7] [*Scott and Wang*, 2005; *Scott and Arbic*, 2007], through their analysis of satellite observational data (2005) and reconfirmed by modelling studies (2007) derived a source of KE, through PE transformation to EKE, comparable or smaller to the Rossby deformation radius $\mathcal{L}_d$, ($\mathcal{L}_d = \frac{NH}{f_0}$ where N the Brunt -Väisälä frequency, H the scale depth and f_0 the *Coriolis* parameter at the reference latitude), in the presence of baroclinic instability. *Salmon* [1980], suggested that the first mode of baroclinic radius is the energy injection scale.

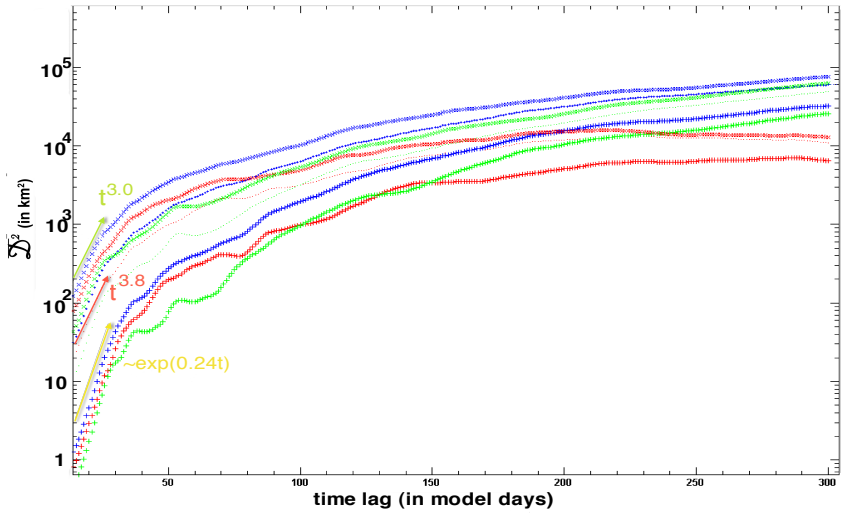

FIG. 11: Relative dispersion $\overline{\mathcal{D}^2}$ (in km^2) for various initial separation distances versus time for longitudinal release at 100°E in the SOL experiment for isoneutral surface 27.76. Means are constructed over all available pairs. Total dispersion (blue), meridional (red) and zonal (green) components are computed for initial particle pairs' displacements of $\sim$ 550 m (cross), $\sim$2.5 km (dot) and $\sim$5.5 km (x-cross). Growth law dependency for time lags up to 25 days from initialization reveals that only the smallest separation distance can depict exponential growth for relative dispersion (exponential growth functions can also be fitted for the displacements of 2.5 and 5.5 km, however, with a smaller correlation coefficient R-squared, 0.98 instead of 0.99 for a power law dependency). It is unclear how statistically significant is that discrepancy in growth law rates and if a substantial conclusion can be drawn in order to fit the distribution to a theoretical one. Meridional dispersion is 'upper' bounded at $\sim$ 20 km (550 m initial separation) and $\sim$ 100 km (2.5-5.5 km initial separation). The two distance scales are equivalent to the *Rossby* radius of deformation $\mathcal{L}_d$ for the Southern Ocean and the characteristic meso-scale for oceanic flows, respectively. On the contrary, total dispersion, as also the zonal component, exhibit a power law dependence even at larger time lags without though being considered as isotropic.

the global averaging). Computed values of κ_τ for separation scales between 10-100 km are in agreement with previous studies' results referenced in the main thesis text.

A.5.2 Dispersion, growth law dependency, flow differentiation and the role of PV gradients in local-regimes. An example from Drake Passage.

In figure 12, the release at 295° of longitude, exactly at Drake Passage is examined, in order to illustrate the connection between relative dispersion, mixing barriers and PV gradients in a local-regime context. Four different groups of 30-50 pairs of particles and growth laws for selected travel time periods are illustrated (bottom panels). Additionally, relative dispersion and diffusion as also PV[8], bilinearly interpolated on

[8]Revisiting the concept of a material invariant quantity, this translates to constant PV for a fluid particle [*McIntyre*, 2003]. As such, the distribution of the interpolated PV on particles' positions (Fig.

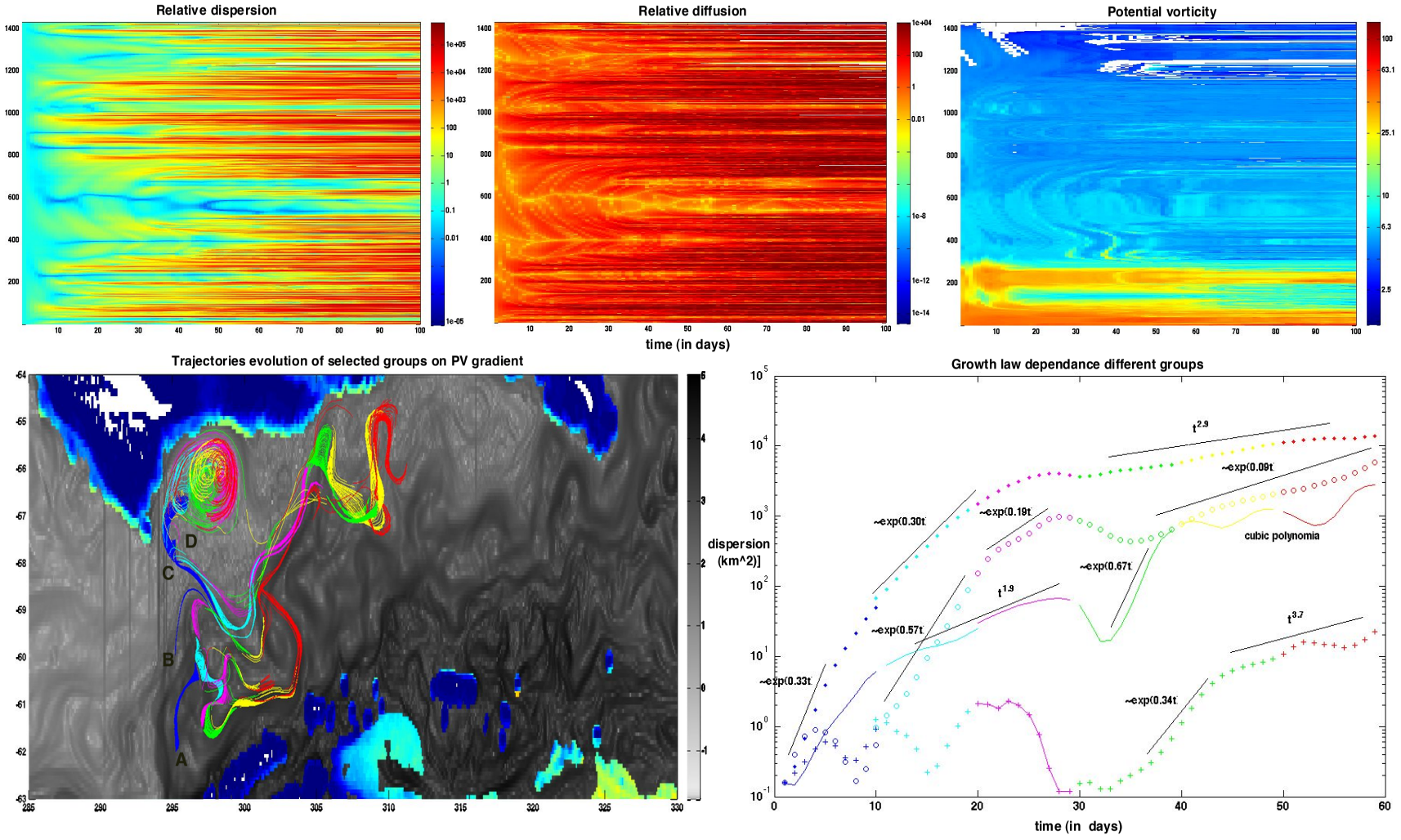

FIG. 12: Time evolution of relative dispersion $\overline{\mathcal{D}^2 - \mathcal{D}_0^2}$ (in km^2), relative diffusion κ_τ and PV interpolated on particles' trajectories for selected release at 295° in SOL experiment for isoneutral surface 27.76 for a period of 100 days (top panels). Illustration of particle trajectory evolution for groups of particles A (100-150; open circles), B (510-540; cross), C (910-950; line) and D (960-1000; closed diamonds) and $\overline{\mathcal{D}^2}$ growth laws for selected travel time periods are illustrated (bottom panels). Colours denote time travel periods of 1-10 (blue), 11-20 (cyan), 21-30 (magenta), 31-40 (green), 41-50 (yellow) and 51-60 days (red) respectively.

each sequential particle position, for the 100-day period ($\simeq$ to the length of the time-series considered for the absolute diffusivity convergence) are presented. An interesting delineated feature is the relative dispersion minima characterizing a group of particle pairs from 500-600 release pair ID (particle ID is shown on the vertical scale at the top diagrams) (equivalent to $\sim$ 60°S initial location). The minima temporal distribution of dispersion (and equivalently diffusion) reveals that particles in their travel time can transverse from regions that impose constrains in their relative displacement to more diffusive regimes, as expected. The 'true' nature of particles' separation, can, depending on the time scales examined, be evocative of an oscillating trend in the growth law dependencies referenced in section 5.1.1 p.118.

The particles' pair groups A (100-150), B (510-540) and C (910-950) (Fig. 12 bottom panel right) are indicative of the above small time lags 'oscillation', with group D (960-1000) being the only exemption. Group B represents a group of minima dispersion up to a period of ∼35 days following the strong PV gradient at south and resting in an isotropic (non-dispersive) homogenized PV area. On the contrary, group A exhibits exponential growth (forward enstrophy cascade) for most of the period under examination and is associated with an anisotropic (dispersive) inhomogeneous PV with a multi filamented spatial distribution of PV gradients denoting multiple jets (the PV gradients are consistent with the maximum mean velocity jets in the region). Group B exhibits a continuous growth trend initiating at approximately 35 days after release time in agreement with the flow separation at that timelag. Exponential growth and a power law dependence of 3.7 (recall that Richardson's law denote a t^3 power law dependence of $\overline{\mathcal{D}^2}$, inverse energy cascade) characterize larger time lags. Group C exhibits, similarly, an exponential growth dependence at small time lags transgressing to an approximate quadratic power law dependence (ballistic regime) at mid times. At large time lags, $\overline{\mathcal{D}^2}$ is reduced and exponential growth is characteristic for time lags between 30-40 days. Group D, which is the one reproducing in greater detail the theoretical approximations discussed, also engulfs the most prominent vortex feature at the north eastward exit of Drake Passage. Simultaneous entrance ($\sim$ 40th day) of particles into the vortex area of effect can be assumed based on the polarization and spatial distribution of colour coded time trajectory increments. Relative dispersion demonstrates a $t^{2.9}$ dependency (inverse energy cascade).

Further examining the evolution of the branch of group C, especially those particle pairs centered at 900 ID (minima of $\overline{\mathcal{D}^2}$ up to the $30th$ day, relative dispersion panel - same figure) after 30 days of travel time (the green colour represents the ensuing period from ∼40-50 days). In the same area in the relative diffusion diagram, the variation, depicted through colour alteration at time lags $>$ 30 days, signifies the mixing

12) is somewhat puzzling. For PV conservation following a fluid particle, no dissipation or rotational external forcing should be exerted [*Provenzale et al.*, 2008].

'bursts' mentioned by *Thompson* [2010]. Those rapid mixing events, associated with an accompanying PV mixing, correspond with the meridional northward jet tip and relate to the oscillations of growth law dependency.

Dispersion of most of the groups follow an exponential growth law dependence (forward $\mathcal{E}$ cascade from larger to smaller scales) with apparent, at the same time, pairs with minima dispersion related with particles sharing a similar kinematic environment. That is either initially in close proximity to a strong PV gradient (for example the flanks of a vortex or a jet) (strain dominates - positive Okubo-Weïss parameter values) or afterwards in the vortex core (rotation dominates - negative Okubo-Weïss parameter values) (Fig. 8). Not every particle pair experiences the same mixing regime. High values of relative dispersion do actually signify differentiated kinematic environments for each of the constituents in a pair in agreement with previous studies [*Gildor et al.*, 2009].

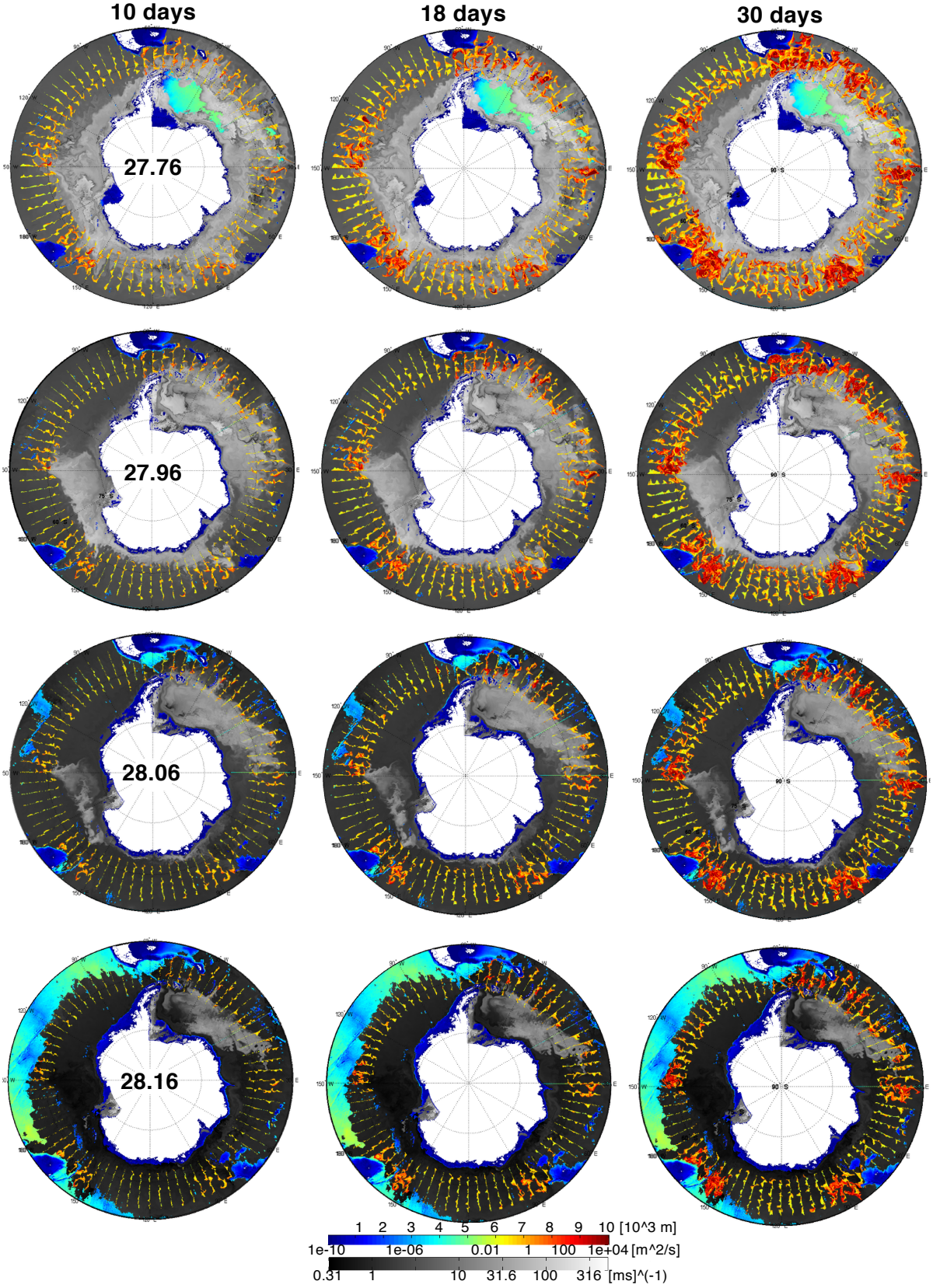

FIG. 13: Relative diffusion κ_τ (m^2 s^{-1}) (in logarithmic colour scale) for all longitudinal releases in the SOL experiment for isoneutral surfaces 27.76 (top row), 27.96 (second row), 28.06 (third row) and 28.16 (bottom row) for a period of 10 (left), 18 (middle) and 30 (right) days. Underlying is PV ($log10(|PV| \times 10^{11})$ (m s)$^{-1}$) (grey scale) and bathymetry after Smith & Sandwell (v6.2, 1997) (colour scale).

Appendix B

B.6 DIMES experiment

In order to demonstrate the underlying connection with stratification, the overturning circulation and recognition of the asymmetric regulatory character of the Southern Ocean in the global climate system, a robust dataset is required to justify debated mixing theories in the scientific community. In light of the diapycnal diffusivity estimates reported so far, and an isopycnal mixing dynamics interpretation and establishment, the Diapycnal Isopycnal Mixing Experiment in the Southern Ocean (DIMES) was conceived as a multi-perspective approach offering a connection among 'differentiated' energetic regimes. The experimental constituents of the DIMES project are: a non-natural chemical tracer patch ($\sim 25 \times 25$ km) release of CF_3SF_5 at a nominal depth of 1500 m (approximately centred on neutral density surface $\gamma^n = 27.9$, the deployment of a set (150) of isopycnal RAFOS floats, microstructure measurements of turbulence, 8 shearmeter floats, 15 EM-APEX floats [*Sanford et al.*, 2005], a mooring array in Drake Passage, hydrographic observations from research vessels (XBTs, CTDs), high resolution numerical modelling of effective diffusivities and Lagrangian studies in general (HYCOM, MITgcm, OCCAM, POP, SOSE), inverse modelling and analysis of satellite altimetry observations. In figure 14, the schematic time schedule for the DIMES project and proposed fieldworks are illustrated (left panel). The right panel, in the same figure, represents the sea surface height field close to the day of release based on AVISO satellite altimetry data.

B.6.1 The DIMES experiment simulation formulation

Sections of this thesis were formulated among the so-called 'friends of DIMES' group context, with complementary simulations, both in an isoneutral and isobaric framework,

considering exclusively Lagrangian trajectories (not a passive tracer[9]) conducted in accordance to the proposed project set-up[10]. Diapycnal diffusivity is not part of this study and further references were only presented in a bibliographic context.

Simulations performed with monthly releases, covering a travel time period of approximately 5-6 years, on an pressure depth of 1258 m and on a neutral density surface $\gamma^n = 27.9$. Each release is constituted by a cluster of 2500 particles, with a homogeneous spatial distribution of ~ 500 m initial separation distance. The location and initialization of the numerical simulations were based on the climatology on site immediately following the injection date, between $2nd - 5th$ of February 2009, see figures 14 and 15, in accordance to the DIMES project formalization. Martin Wadley (pers.comm), examined sea surface height and velocity on the isoneutral 27.9, at 255.5° of longitude and -59.416° of latitude. Analysis of model's climatology was found to resemble the initial conditions and velocity regime of the actual tracer release at model day 3315[11]. Monthly releases of patches of particles conclude on model day 3705.

B.6.2 Tracer release and Lagrangian particles

But how should a tracer release, with initializations formulated in the same context and flow dynamics interpretation, evolve in comparison with a particle advection scheme? Since a Lagrangian approach to transport is naturally constructed on the passive particles resemblance of kinematics we expect particles to act as proxies for molecules [*Davis*, 1991]. Reference was made in the previous paragraphs to simulation efforts in the DIMES project theoretical studies setting, to present the early stages of a passive tracer evolution. Even though, no access to a complete analysis was available at the time of the completion of this section, average snapshots of tracer concentration were kindly provided [Dr. Martin Wadley, 14 July 2009, pers. comm] to serve as a comparison background with the Lagrangian realizations.

In figure 18 (see also figure 17 in Appendix A for a 4-year time series of selected tracer realizations), numerically estimated tracer distributions[12] from full tracer equations utilization and for travel time of 1 (left panel) and 2 (right panel) years respectively, are illustrated. In general, the tracer cloud has a consonant representation among the two

[9]The distinction is based on the introduction of a parameter to simulate the effect of diffusion in the advection scheme employed. It is anticipated, though, that passive tracers have the same lateral diffusivities as fluid particles [*Davis*, 1991].

[10]For comparison reasons, the early stages of a passive tracer simulation evolution [Dr. Martin Wadley, 14 July 2009, pers. comm], formulated in the same context and performed on the same numerical model, are presented later on.

[11]It is significant to point out that common initial conditions in a general circulation model and reality do not at any aspect secure future resemblance. So, interest is mainly focused on statistical coherence and/or an assessment of model performance on a basis of correct dynamics representation and not reproduction of the exact spatio-temporal geographic coordinates but delineation of a subtle relative space and time relationship.

[12]Tracer distributions are combined over all realizations, different patches of the initial release grid.

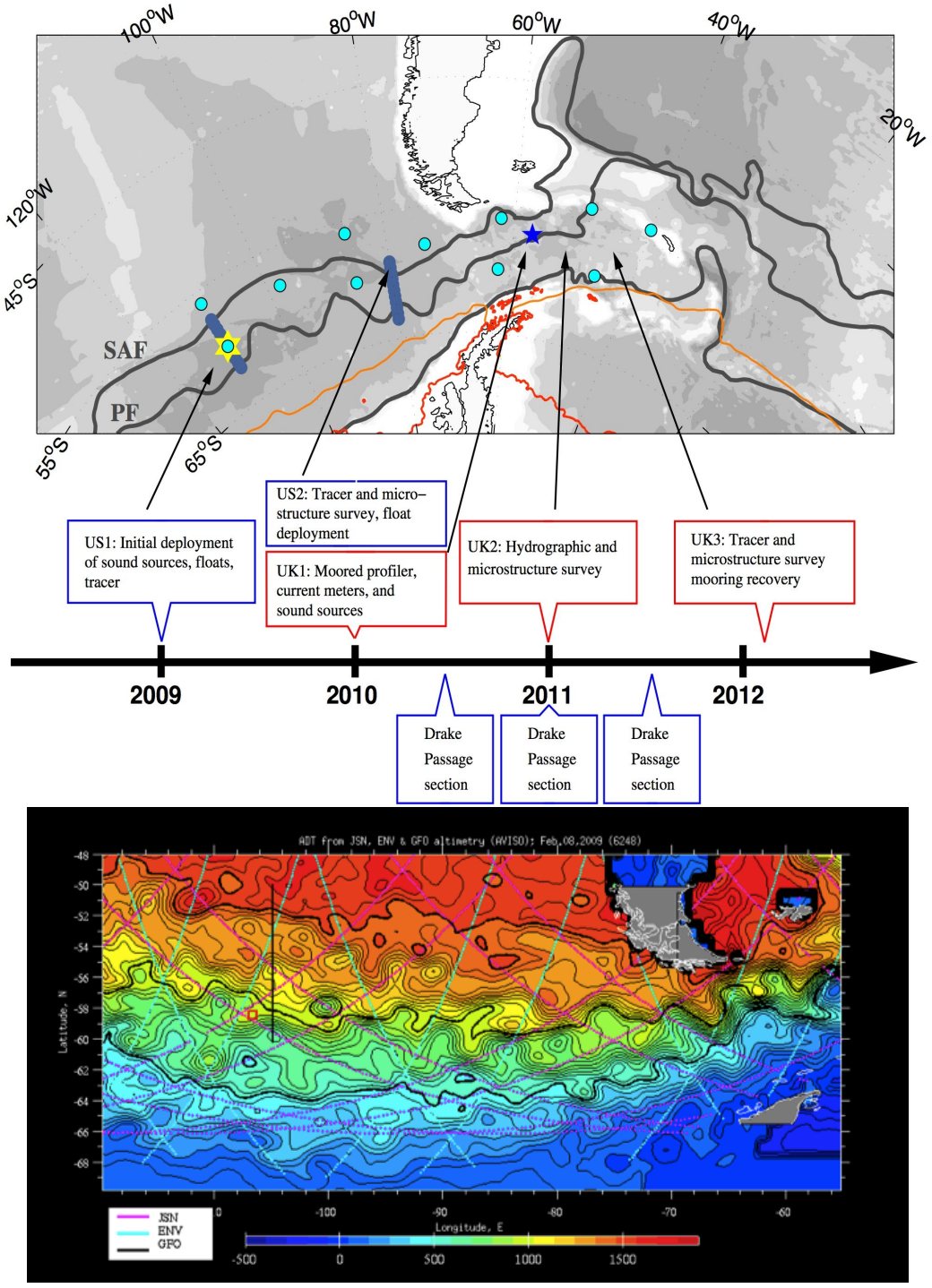

FIG. 14: (top) DIMES experiment schedule and (bottom) approximate location of tracer patch (red rectangle) on top of sea surface height (in millimeters), relative to an equilibrium surface, on the 8*th* of February 2009. Sea surface height from satellite altimetry. [Images from DIMES website].

methods (Fig. 3.8). High concentration patches are co-allocated with high probability density (correlation is more pronounced for specific tracer realizations as seen in figure 17, with accompanying discrepancies). It needs to be pointed out, that the tracer

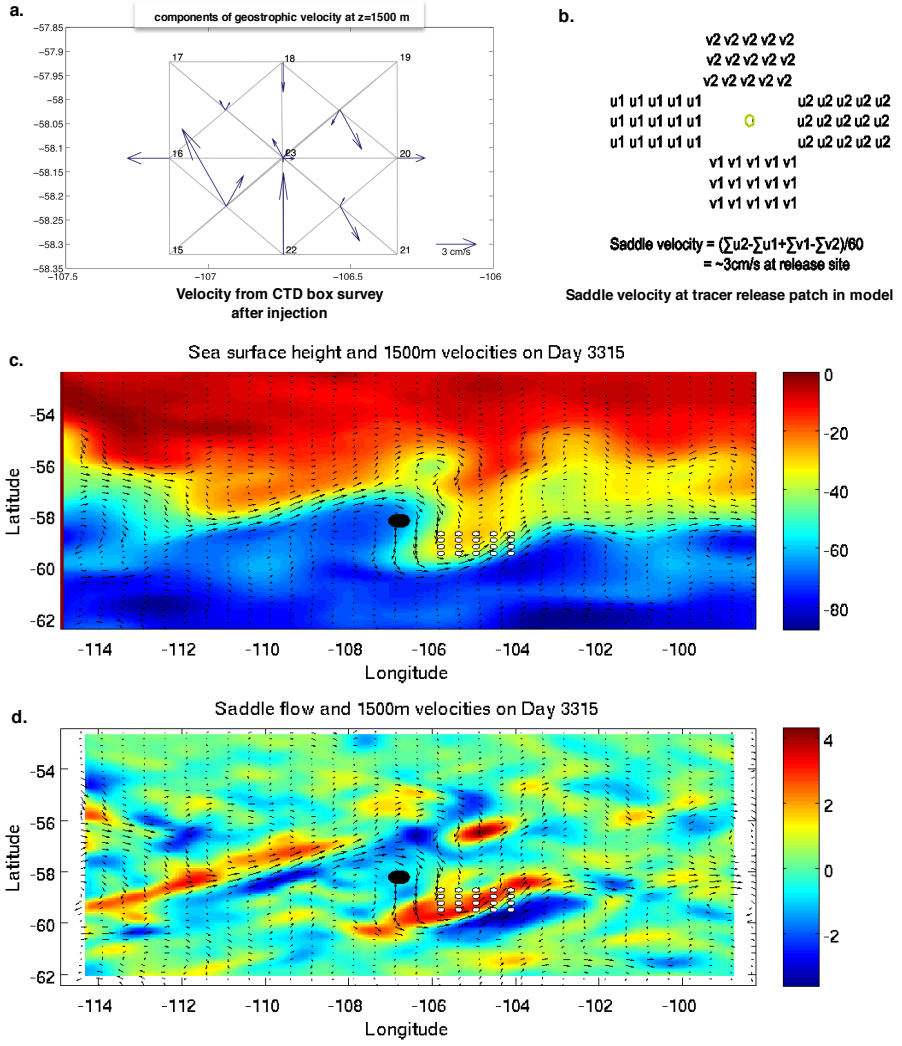

FIG. 15: Geostrophic velocity from CTD box survey after injection of the tracer at a depth of 1500 m (a.). Saddle velocity calculation at DIMES simulation initialization (b.) and estimation of equivalent climatology, OCCAM 1/12° sea surface height (cm) (c.) and saddle flow (cm s^{-1}) with overlying velocity vectors (d.), at tracer patch release location. [Images (a.) from DIMES website [*Ledwell*, 2009], (b.-c.-d.) courtesy of Martin Wadley].

mapping is constructed from annual instantaneous concentration combinations of the chemical tracer's realizations. The averaged effective probability densities are spatial ensembles of annual time averages of all monthly initializations, meant to provide average positions of material lines and their particles' attraction potential and/or delineate advection pathways of particles. In figure 19, the fraction of the tracer east of Drake Passage is computed. Even though, the concept of time averaged effective probability index (3.2.2) does not directly fit in the concentration of a chemical tracer's distribution definition, values are of approximately equal magnitude (0.14 - 2*nd*; 0.64 - 3*rd*; 0.90 - 4*th* year [in fraction of distribution east of DP for respective year of travel time]).

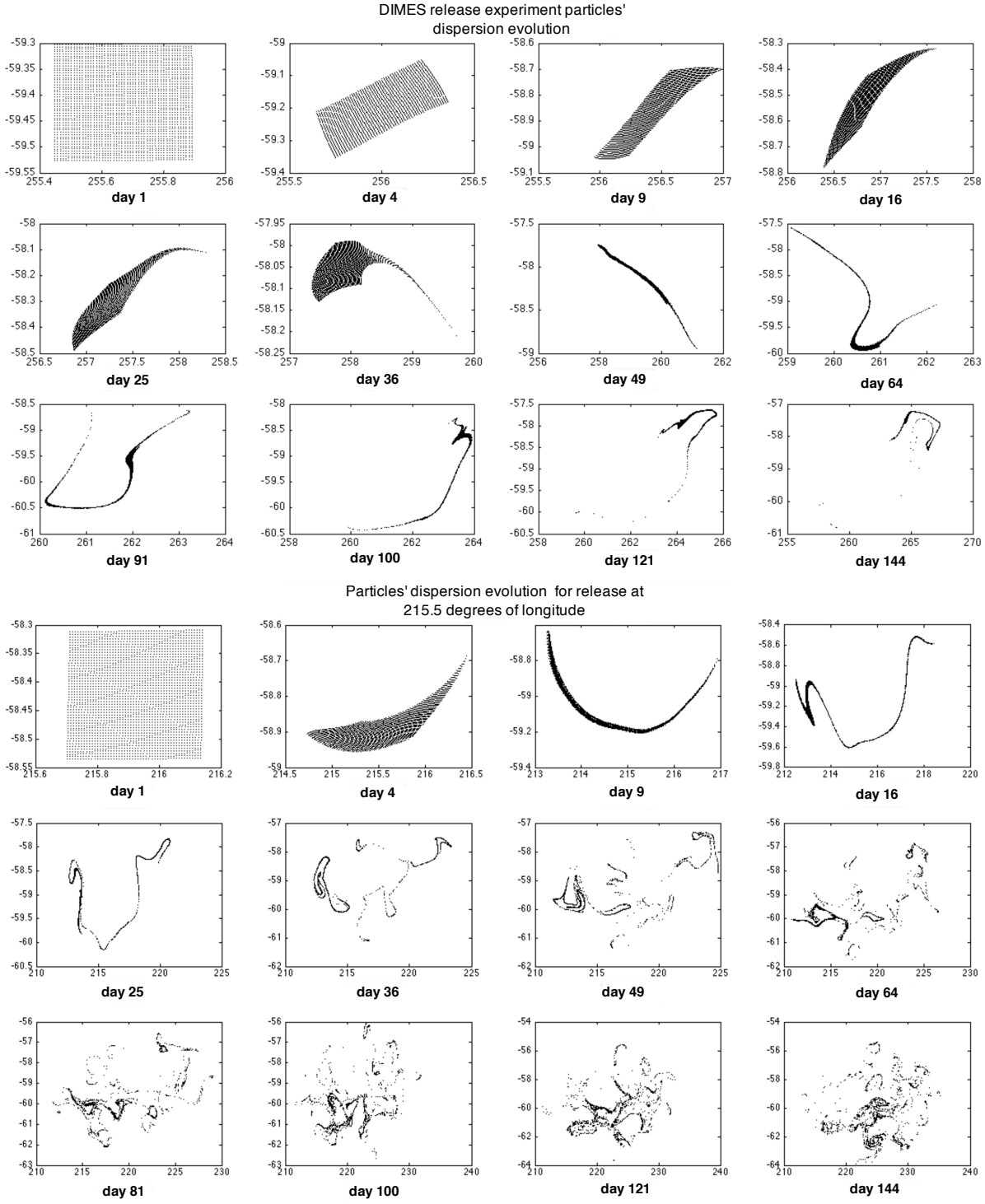

FIG. 16: Snapshots, for selected times, of high concentration particles streaks following the release of a cluster of particles on neutral density $\gamma^n = 27.9$ surface (top panel) DIMES release at $\sim 255.5°$ and (bottom panel) at $\sim 215.5°$ (in the vicinity of the Udintsev Fracture Zone).While filaments are quite coherent in time for the DIMES release, even after a significant amount of time (121 days), the case for the release in the more energetic region of UFZ, substantially differentiates from initial stirring-stretching structure after a period of 36 days. The transition to an uncorrelated 'chaotic' resembling state is already completed after 121 days (a possible re-organization of particles into streaks can be seen).

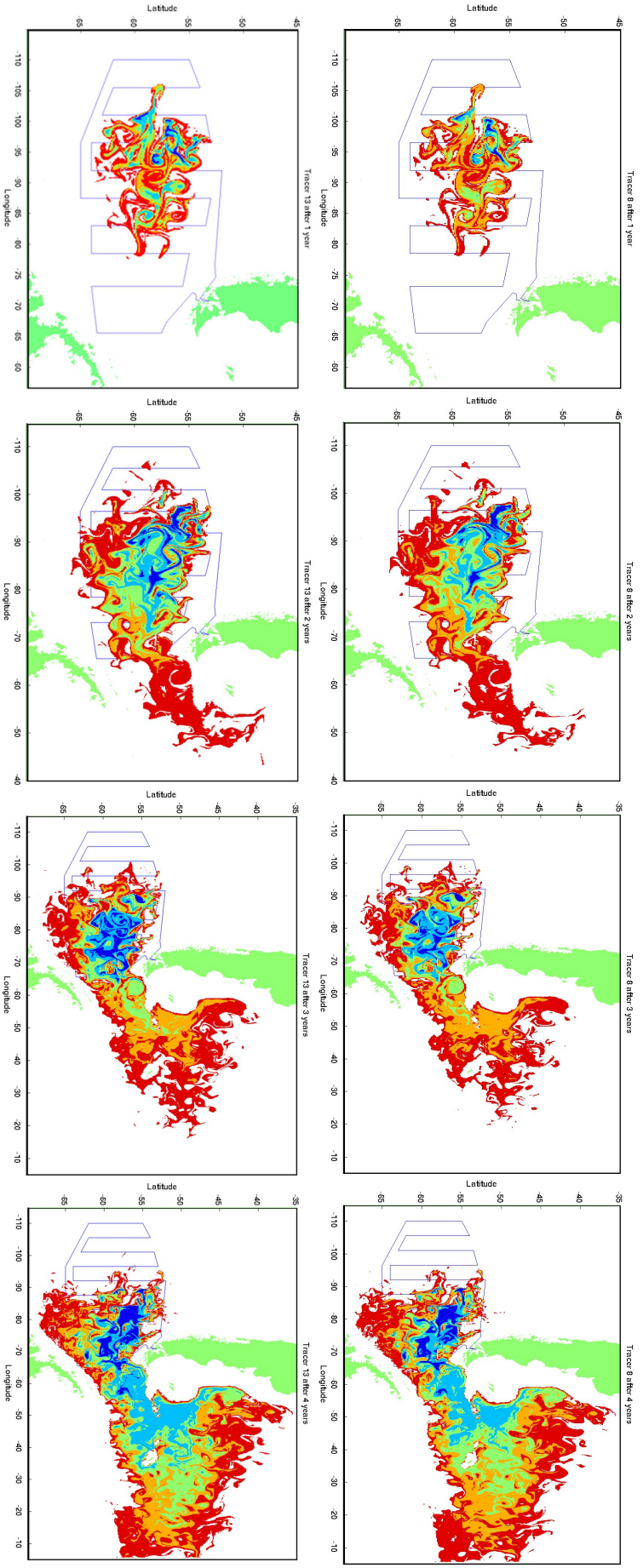

FIG. 17: Tracer evolution in the DIMES context for selected realizations in OCCAM 1/12° model (courtesy of Martin Wadley). Concentrations scale equivalently to a red (low) - blue (high) colour scale.

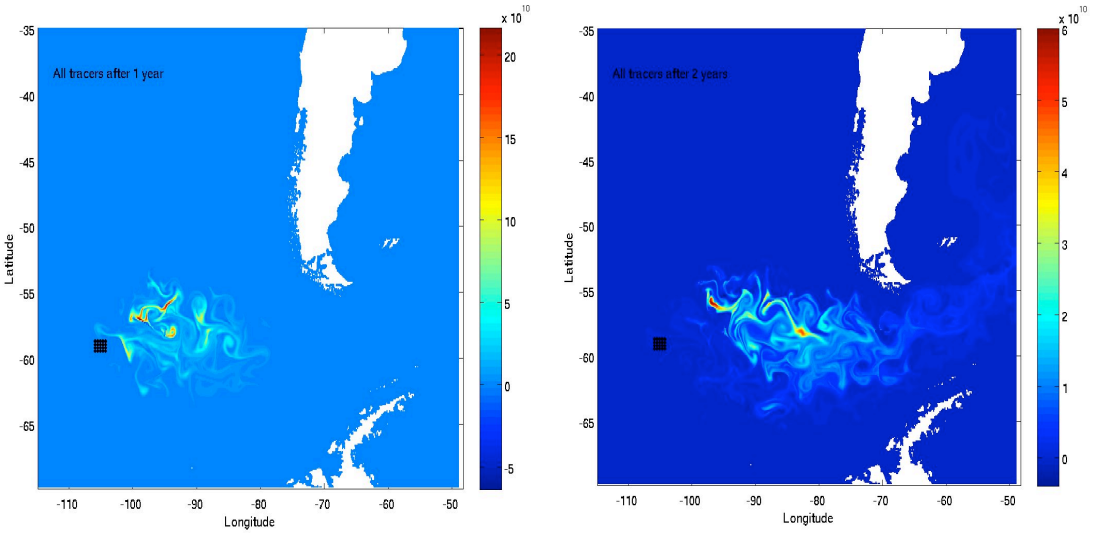

(a) (b)

FIG. 18: DIMES tracer concentration distributions in OCCAM 1/12° model after Martin Wadley for travel time periods of 1 and 2 years. [White areas depict land after GEBCO].

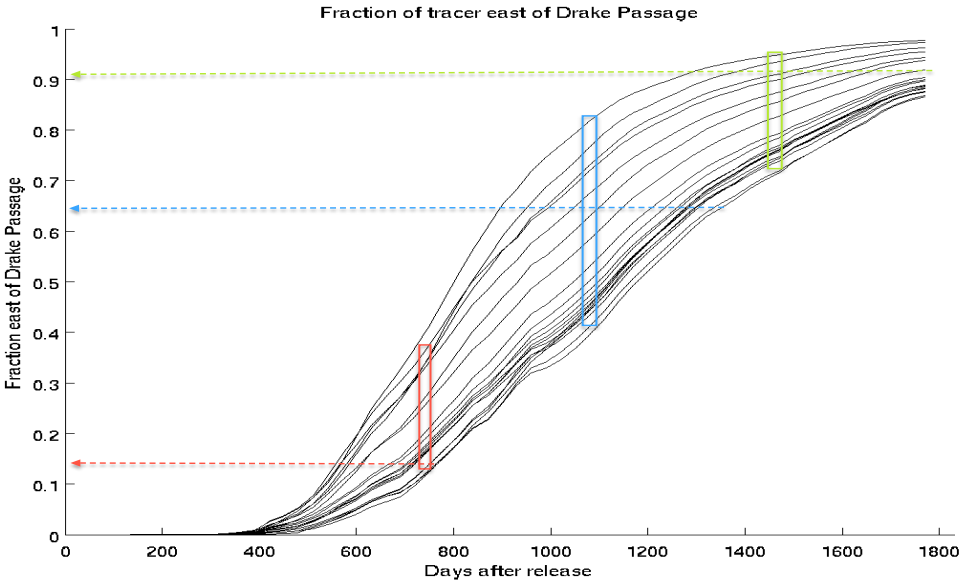

FIG. 19: Fraction of tracer concentration progression for all realizations east of Drake Passage in OCCAM 1/12° model after Martin Wadley. Rectangles denote variance range of tracer simulation realizations for respective travel time after initialization, 2 (red), 3 (blue) and 4 years (green). Horizontal dashed lines represent fractions computed from the effective probability density distributions (Fig. 3.8).

Appendix C

Here, the basic version of the numerical MATLAB code[13] used for the advection of particles on isoneutral surfaces is presented.

```
%      OCCAMTRACEMANY_2880_NRW_ISOPYCNAL_SOexp.M
%      Modified by Christos Mitsis 2007 by an earlier version of Sally Thorpe.
%      function [partlat,partlon] = occamtracemany_2880_nrm_isopycnal_SOexp(day, mm,...
%      yr, ndays, lon, lat, filestep, lev);

%------ THE PROGRAM ----------------------------------------------------------

       function [partlat,partlon]=occamtracemany_2880_nrw_isopycnal_SOexp(mdayi,...
                                                 mdayf,lon,lat,filestep,glevel)
% ------------------------------------------------------------------------------
% particles are being released in a different scheme than previous (linear .
% A cluster of 25kmX25km dimension is being originated consisting of thousand of
% particles. These are being released at DIMES proposed release location which is
% 105W, 60S. In order to define the the range of lat, lon in the cluster we
% need the latitudinal resolution(=111120*1/12(m)) and the longitudinal
% resolution depending on the latitude (=6370e3*cos(rad)*dxrad), where
% rad=lat*pi/180 (radians conversion) and dxrad is the models resolution
% translated in radians (=dxdeg*pi/180), dxdeg=1/12 for OCCAM 1/12.

% ------------------------------------------------------------------------------

%------ set this if using the random walk later on

%       rand('state',sum(100*clock));

%------ GRID RESOLUTION ------------------------------------------------------

%      nlimdeg is the northern limit of the input field in degrees,
%      (and similar for elimdeg, wlimdeg and slimdeg)
%      dxdeg and dydeg give the resolution of the grid in degrees;

       nlimdeg = -35; slimdeg = -78.0833; wlimdeg = 0.0833; elimdeg = 360;
```

[13] Free to replicated, copied, distributed and altered in any way.

```
33        dxdeg = 1/12;
34        dxrad = dxdeg*pi/180;
35        dydeg = 1/12;
36
37
38  % Check that the starting positions are inside the grid
39
40        if (~isempty(find(lon < wlimdeg)) || ~isempty(find(lon > elimdeg)) ...
41           || ~isempty(find(lat > nlimdeg)) || ~isempty(find(lat < slimdeg)))
42           disp('One or more starting position is outside the grid!');
43           q = input('Do you want to continue? 1 for Yes, 2 for No');
44           if q == 2
45              return;
46           elseif q == 1 % keep only those starting positions in grid
47             b = find(lon>wlimdeg&lon<elimdeg&lat<nlimdeg&lat>slimdeg);
48             lon = lon(b);
49             lat = lat(b);
50           end;
51        end;
52
53
54  % Initialise the output vectors now
55
56        partlat = ones(size(lat));
57        partlon = ones(size(lon));
58
59        disp('ok1')
60  %---- CALC FILENO ------------------------------------------------------
61
62  %     calculate modelday (in program) based on the actual modelday (mdayi)
63  %     which is the starting date on the files extracted from occam_run401. The
64  %     nloops are (mdayf-mdayi)/filestep.
65
66             modelday=mdayi + filestep;
67
68  %     find nearest model fileno
69
70        fileno = fix(modelday/filestep) * filestep;
71
72  %     need to see which side of the middle of the file period the start day
73  %     is to determine which vel files are needed
74
75        if modelday <= fileno + 0.5*filestep
76           fileno = fileno - filestep;
77        end;
78
79        fileno2 = fileno + filestep;
80
```

```
%      check for a valid starting date

       if fileno < mdayi || fileno > mdayf
          disp('Check the startdate: has to be between 1095 and 7300 ');
          return;
       end;

       disp('ok2')
%----- LOAD IN AND SORT OUT THE VEL FIELDS ----------------------------------

% path of data repositories
 dirpath = '/esdata/data/e024377/occam_run401/uv_gamma/';
 dirpathS = '/esscratch/env/e024377/occam/run401/SO_isop_exp/5dmeans/';

       load ([dirpath,'uvgammaN_glevel',num2str(glevel),'_mday',int2str(fileno),'to',...
       int2str(fileno2),'.mat'],'ug_n','vg_n');



%      remove singleton dimensions of u,v matrices to be consistent with 2-D matrix

       ufield1=ug_n;
       vfield1=vg_n;
       clear ug_n vg_n;

      load ([dirpath,'uvgammaN_glevel',num2str(glevel),'_mday',int2str(fileno2),'to',...
      int2str(fileno2+filestep),'.mat'],'ug_n','vg_n');


       ufield2=ug_n;
       vfield2=vg_n;
       clear ug_n vg_n;


%      also reorder arrays so they start from the north!!!!!!!

       ufield1=flipud(ufield1);
       vfield1=flipud(vfield1);
       ufield2=flipud(ufield2);
       vfield2=flipud(vfield2);


%      replace any land values with a nan - ALREADY DONE FOR THE PSEUDOFIELDS
%      change back to 0, should never have changed it!

       a = find(isnan(ufield1));
       ufield1(a) = 0; vfield1(a) = 0;
       ufield2(a) = 0; vfield2(a) = 0;
```

```
129
130       clear  a
131
132   %     jmt and imt are the dimensions (rows and columns respectively) of
133   %     the velocity matrices — hence jmt reps lat, imt lon
134
135         [jmt,imt] = size(ufield1);
136
137   %     Convert the velocities to m/s from cm/s, and combine to give a
138   %     speed matrix which will be used to determine land values:
139
140         ufield1 = 0.01*ufield1;
141         vfield1 = 0.01*vfield1;
142         speed  = sqrt(ufield1.^2 + vfield1.^2);
143
144         ufield2 = 0.01*ufield2;
145         vfield2 = 0.01*vfield2;
146
147         disp('ok3')
148   %———— CONVERT LON AND LAT TO I AND J FORMAT, CHECK STARTING POSITIONS ———
149
150         istart = (lon+(abs(wlimdeg)))*(1./dxdeg) +1;
151         jstart = (lat+(abs(nlimdeg)))*(-1./dydeg) +1;
152
153         ifix = fix(istart);
154         jfix = fix(jstart);
155
156   %     Check these are not on land — if so, ask whether to stop the prog
157
158         land = [diag(speed(jfix,ifix)) diag(speed(jfix+1,ifix)) ...
159                 diag(speed(jfix+1,ifix+1)) diag(speed(jfix,ifix+1))];
160         landc = find(isnan(land));
161
162         if ~isempty(landc)
163            disp(length(landc));
164            disp('particles are on land!');
165            q = input('Do you want to continue? 1 for Yes, 2 for No');
166            if q == 2
167               return;
168            end;
169         end;
170         clear land landc q
171
172         disp('ok4')
173   %———— NOW GO INTO THE TRACING LOOP ————————————————————————————————
174
175   %     This routine draws a trace starting from ISTART, JSTART for the
176   %     duration of the trace (NDAYS days). Input arrays are the u and v
```

```
177 %     components together with the speed field which is used only to check
178 %     for land (or submerged land) points.  NLIMDEG, DXDEG and DYDEG are
179 %     used to define the domain boundary and covering grid.
180
181 %     Calculate latresn in m : constant for the OCCAM grid
182
183       latresn = 111120*dydeg;
184
185
186 %---- Set up the first components of speed ------------------------------------
187
188 %     Derive current grid cell corners - used 'fix' earlier to round down to
189 %     the nearest integer
190
191       ip = ifix;
192       ip1 = ip + 1;
193       jp = jfix;
194       jp1 = jp + 1;
195
196 %     Info needed for the interpolation of the new velocities
197
198       delx = istart - ip;
199       dely = jstart - jp;
200
201 %     TSTEP is the number of seconds between trace steps. This should be
202 %     tuned to the largest value which does not significantly alter the
203 %     paths of the simulated drifters.
204 %     Sensitivity tests in the Scotia Sea showed 8640 s to be satisfactory.
205
206       tstep = 2880.;
207
208 %     nruns is the number of velocity fields to run through.
209 %     maxruns is the max number of runs through the tracing loop that
210 %     there'll be.
211 %     nsteps is the number of times the prog has to calculate a trace for
212 %     each field - constant here because the OCCAM fields are all 5 days
213 %     apart but would need changing if monthly fields are used: see POCM
214 %     version
215
216       ndays = mdayf-mdayi;
217       nruns = round(ndays/filestep) + 1;
218       maxruns = ndays * 86400/tstep;
219       nsteps = filestep * 86400/tstep;
220
221 %     This is needed for interpolating between the fields
222
223 %      time = [1 nsteps+1];
224
```

```
225 %     calculate the starting day in timesteps relative to the middle of
226 %     the file
227
228       startc2 = modelday - (fileno + 0.5*filestep);
229       startc2 = startc2 * 86400/tstep;
230
231 %     copied method from pocmtracemany_pseudo_*.m to interpolate to
232 %     get rid of for loops and reduce amount of interpolation
233 %     interpolate vel fields onto startc2 for now
234
235       gradu = (ufield2 - ufield1)/nsteps;
236       gradv = (vfield2 - vfield1)/nsteps;
237       intu = ufield1 + gradu*(startc2-1);
238       intv = vfield1 + gradv*(startc2-1);
239
240 %     now extract the corners of the grid cells
241
242       intu1 = diag(intu(jp,ip))';
243       intu2 = diag(intu(jp1,ip))';
244       intu3 = diag(intu(jp1,ip1))';
245       intu4 = diag(intu(jp,ip1))';
246
247       intv1 = diag(intv(jp,ip))';
248       intv2 = diag(intv(jp1,ip))';
249       intv3 = diag(intv(jp1,ip1))';
250       intv4 = diag(intv(jp,ip1))';
251
252 %     clear the interpolated fields
253
254       clear intu intv
255
256 %     calculate the components of velocity from the four surrounding
257 %     grid cell nodes
258
259       ucomp = (1.-delx).*(1.-dely).*intu1 + delx.*(1.-dely).*intu4 + ...
260               delx.*dely.*intu3 + (1.-delx).*dely.*intu2;
261
262       vcomp = (1.-delx).*(1.-dely).*intv1 + delx.*(1.-dely).*intv4 + ...
263               delx.*dely.*intv3 + (1.-delx).*dely.*intv2;
264
265       clear intu* intv*;
266
267       ri = istart;
268       rj = jstart;
269
270       rlat = lat;
271
272 %     counting indices
```

```
273
274         count3 = 1;
275 %     nextfile = fileno2;
276
277       disp('ok5')
278 %------ This is the loop that does the tracing...-----------------------------------
279
280         for count = 1:nruns
281
282 %       Now have another loop that runs for the number of time steps
283 %       between velocity fields
284
285 %       for the first field (ie when count = 1), use startc2 as first index
286
287             if count == 1
288                sc2 = startc2;
289             else
290                sc2 = 1;
291             end;
292
293 %       Now interpolate the two velocity fields onto each timestep - gets rid
294 %       of some of the for loops, increasing efficiency.
295 %       Only needs doing when the vel fields are changed.
296
297             gradu = (ufield2 - ufield1)/nsteps;
298             gradv = (vfield2 - vfield1)/nsteps;
299
300
301 %       initialise the u and v 3D matrices: faster this way
302
303
304             uvelblock = zeros(jmt,imt);
305             vvelblock = zeros(jmt,imt);
306
307
308             for count2 = sc2:nsteps
309
310 %       Calculate speeds in terms of 'gridnodes per sec'
311
312                   rad = rlat*pi/180; \%convert lat to radians
313
314                   speedi = ucomp./(6370e3*cos(rad)*dxrad);
315                   speedj = vcomp./latresn;
316
317                   if count3 > maxruns
318                      disp('Reached end of time');
319                      return;
320                   end;
```

```
321
322
323 % *** Get predictor value at 1/2 timestep
324
325 %     Calculate new position.  RJP has a minus in it so that with a
326 %     positive speed it goes northwards
327
328               rip = ri+(0.5*tstep)*speedi;
329               rjp = rj-(0.5*tstep)*speedj;
330
331 %     Derive current gridbox corners - use 'fix' to round down to the nearest integer
332
333               ip  = fix(rip);
334               ip1 = ip+1;
335               jp  = fix(rjp);
336               jp1 = jp+1;
337
338 %     Check that the particles haven't reached the edge of the grid.
339 %     If they have, change their last position to nans so that the prog
340 %     will ignore them in future.
341 %     The indices have to be different for after the first run through of
342 %     the loop.
343
344               a = find(jp == 0 | jp == jmt);
345               index = count3-1;
346               if count3 == 1
347                  index = count3;
348               end;
349
350               partlat(index,a) = nan;
351               partlon(index,a) = nan;
352
353               if isempty(a)==1;
354                   a=find(ip==0); b=find(ip==imt);
355                   partlon(index,a)=partlon(index,a)+wlimdeg;
356                   partlon(index,b)=partlon(index,b)+wlimdeg-elimdeg;
357                   rip(a) = rip(a)+1;
358                   rip(b) = rip(b)-imt;
359                   if rip(b)<1
360                    rip(b)=1+rip(b);partlon(index,b)=partlon(index,b)+wlimdeg;
361                 end;
362                   ip(a)=ip(a)+1;
363                   ip(b)=1;
364                   ip1=ip+1;
365
366               end;
367
368
```

```
369 %     Interpolate between the velocity fields at each of the 4 grid points
370 %     only for particles still going
371
372               pp = find(~isnan(partlat(index,:)));
373
374 %     Initialise the int vectors so there are nans wherever we don't
375 %     extract new info
376
377               intu1 = nan*ones(size(jp)); intu2 = nan*ones(size(jp));
378               intu3 = nan*ones(size(jp)); intu4 = nan*ones(size(jp));
379               intv1 = nan*ones(size(jp)); intv2 = nan*ones(size(jp));
380               intv3 = nan*ones(size(jp)); intv4 = nan*ones(size(jp));
381
382 %     Extract the vel data from the velblocks at level count2
383 %     calculate the vel fields for each timestep
384
385               uvelblock = ufield1 + gradu*(count2-1);
386               vvelblock = vfield1 + gradv*(count2-1);
387
388               intu1(pp) = diag(uvelblock(jp(pp),ip(pp)));
389               intu2(pp) = diag(uvelblock(jp1(pp),ip(pp)));
390               intu3(pp) = diag(uvelblock(jp1(pp),ip1(pp)));
391               intu4(pp) = diag(uvelblock(jp(pp),ip1(pp)));
392
393               intv1(pp) = diag(vvelblock(jp(pp),ip(pp)));
394               intv2(pp) = diag(vvelblock(jp1(pp),ip(pp)));
395               intv3(pp) = diag(vvelblock(jp1(pp),ip1(pp)));
396               intv4(pp) = diag(vvelblock(jp(pp),ip1(pp)));
397
398 %     Look for particles on land ---- all 4 components of u and v will be 0
399
400               onland = find(intu1==0 & intu2==0 & intu3==0 & intu4==0 & ...
401                             intv1==0 & intv2==0 & intv3==0 & intv4==0);
402
403 %     Replace landed particles later to stop the prog crashing
404
405 %     Info needed to interpolate to find the new velocities
406
407               delx = rip - ip;
408               dely = rjp - jp;
409
410 %     Interpolate to find the new velocities
411
412               ucomp = (1.-delx).*(1.-dely).*intu1 + delx.*(1.-dely).*intu4 + ...
413                       delx.*dely.*intu3 + (1.-delx).*dely.*intu2;
414
415               vcomp = (1.-delx).*(1.-dely).*intv1 + delx.*(1.-dely).*intv4 + ...
416                       delx.*dely.*intv3 + (1.-delx).*dely.*intv2;
```

```
417
418
419
420 % *** Calculate corrected values for full timestep
421
422 %     Calc corrected speeds
423
424                 speedi=ucomp./(6370e3*cos(rad)*dxrad);
425                 speedj=vcomp./latresn;
426
427 %     Calculate new position
428
429                 ri = ri + tstep*speedi;
430                 rj = rj - tstep*speedj;
431
432
433 %     Convert position from grid cell to lat and lon
434
435                 rlat = -(rj-1).*dydeg + nlimdeg;
436                 rlon =  (ri-1).*dxdeg + wlimdeg;
437
438 %     Store new positions in matrix
439
440                 partlat(count3,:) = rlat;
441                 partlon(count3,:) = rlon;
442
443 %     Replace all landed particles with nans now
444
445                 partlat(count3,onland) = nan;
446                 partlon(count3,onland) = nan;
447
448                 if isempty(find(~isnan(partlat(count3,:))))
449                    disp('All particles finished');
450                    return;
451                 end;
452
453
454
455 %  ------------------------------------------------------------------------
456 %  Check that the trace is still within the boundaries of the region.
457 %  Need to check that the particle isn't right at the edge of the region
458 %  either  - if it is the next step where ip1 and jp1 are calculated
459 %  cause the prog to crash
460 %  ------------------------------------------------------------------------
461 %  uncomment the following lines if you want the particles to finish when
462 %  they reach the longitudinal boundary limits
463
464 %           a = find( ri < 1 | ri > imt | rj < 1 | rj > jmt);
```

```
%           partlat(count3,a) = nan;
%           partlon(count3,a) = nan;

%-------------------------------------------------------------------------
%   comment the following lines if you wish the absence of the longitudinal
%   boundaries of the region so the particles will continue to follow ACC's path
%   as long as they do not cross the latitudinal boundary limits.

% convert longitude coordinates for particles reaching the eastern boundary limit
% from 360 to 0
          a = find(jp < 1   | jp > jmt);
          partlat(count3,a) = nan;
          partlon(count3,a) = nan;

          if isempty(a)==1;
               a=find(ri<1); b=find(ri>imt);
               partlon(count3,a)=elimdeg-partlon(count3,a);
               partlon(count3,b)=partlon(count3,b)+wlimdeg-elimdeg;
               ri(a) = imt-ri(a);
               ri(b)=ri(b)-imt;
                if ri(b)<1
                   ri(b)=1+ri(b);partlon(count3,b)=partlon(count3,b)+wlimdeg;
                end;

          end;

%-------------------------------------------------------------------------


%     Derive current gridbox corners

               ip  = fix(ri);
               ip1 = ip+1;
               jp  = fix(rj);
               jp1 = jp+1;


%     Initialise the vel vectors now with nans

               intu1 = nan*ones(size(jp)); intu2 = nan*ones(size(jp));
               intu3 = nan*ones(size(jp)); intu4 = nan*ones(size(jp));
               intv1 = nan*ones(size(jp)); intv2 = nan*ones(size(jp));
               intv3 = nan*ones(size(jp)); intv4 = nan*ones(size(jp));

%     Extract info for just the particles still in the running

               pp = find(~isnan(partlat(count3,:)));

```

```
513 %     Extract the vel data from the velblocks at level count2
514
515               intu1(pp) = diag(uvelblock(jp(pp),ip(pp)));
516               intu2(pp) = diag(uvelblock(jp1(pp),ip(pp)));
517               intu3(pp) = diag(uvelblock(jp1(pp),ip1(pp)));
518               intu4(pp) = diag(uvelblock(jp(pp),ip1(pp)));
519
520               intv1(pp) = diag(vvelblock(jp(pp),ip(pp)));
521               intv2(pp) = diag(vvelblock(jp1(pp),ip(pp)));
522               intv3(pp) = diag(vvelblock(jp1(pp),ip1(pp)));
523               intv4(pp) = diag(vvelblock(jp(pp),ip1(pp)));
524
525
526 %     Info needed to find new velocities
527
528               delx = ri - ip;
529               dely = rj - jp;
530
531 %      Linearly interpolate to find the new velocities
532
533               ucomp = (1.-delx).*(1.-dely).*intu1 + delx.*(1.-dely).*intu4 + ...
534                       delx.*dely.*intu3 + (1.-delx).*dely.*intu2;
535
536               vcomp = (1.-delx).*(1.-dely).*intv1 + delx.*(1.-dely).*intv4 + ...
537                       delx.*dely.*intv3 + (1.-delx).*dely.*intv2;
538
539
540
541               count3 = count3 + 1;
542               clear uvelblock vvelblock;
543               end;
544
545
546 %     recall the function in order to calculate the partlat partlon positions
547 %     for a particle released at the same position but at a velocity field which differs
548
549
550 %     Once the loop has gone through the number of steps between the
551 %     fields, need to get the next field to interpolate to.  Convert the
552 %     new fields to m/s and rotate too if they need it.
553
554 %     If the last file has been used return
555
556           if fileno + count*filestep == mdayf
557               disp('Run out of vel fields');
558               return
559            elseif rem(count2,nsteps) == 0
560               ufield1 = ufield2;
```

```
561                 vfield1 = vfield2;
562
563                 clear *field2;
564
565 %       load in the next fields
566
567         load ([dirpath,'uvgammaN_glevel',num2str(glevel),'_mday',...
568         int2str(fileno+(count+1)*filestep),'to',int2str(fileno+(count+2)*filestep),...
569         '.mat'],'ug_n','vg_n');
570
571
572 %       rename to u and vfield2,remove singleton dimensions and transpose to make input
573 %       consistent with program.
574 %       Also reorder arrays so they start from the north.
575
576          ufield2=ug_n;
577          vfield2=vg_n;
578          clear ug_n vg_n;
579
580         ufield2=flipud(ufield2);
581         vfield2=flipud(vfield2);
582
583
584 %       rename to u and vfield2, convert to m/s
585
586                 ufield2 = ufield2 * 0.01;
587                 vfield2 = vfield2 * 0.01;
588
589 %       replace land with nan; - ALREADY DONE FOR THE PSEUDOFIELDS
590 %       change back to 0
591
592                 a = find(isnan(ufield2));
593                 ufield2(a) = 0; vfield2(a) = 0;
594
595
596
597
598             end;
599
600             disp(['num_',int2str(count)])
601
602
603 end;
604
605 %       That's the end of the program!
```